Hahn-Meitner-Institut
Berlin

Annual Report 2001
Selected Results

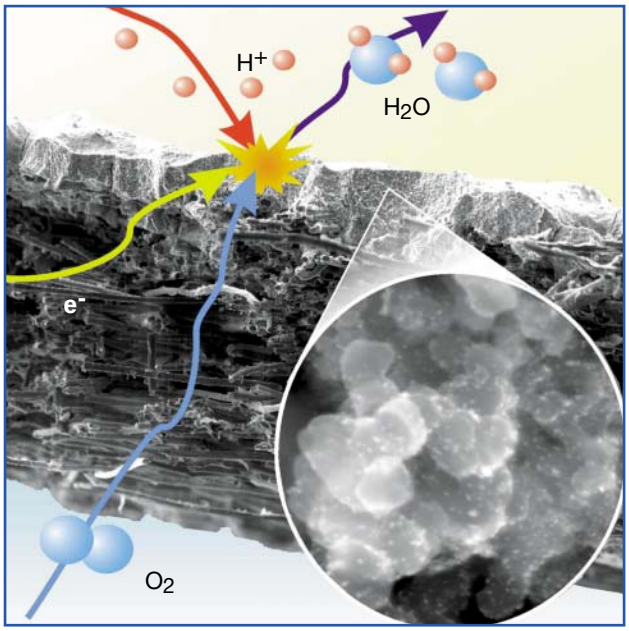

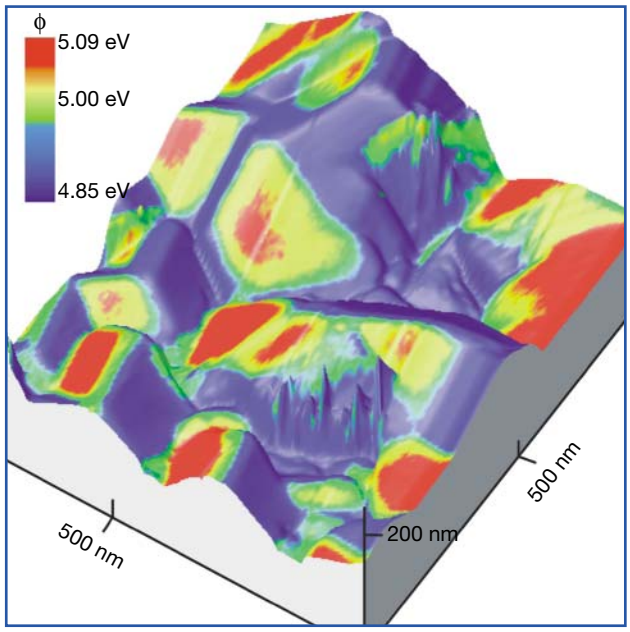

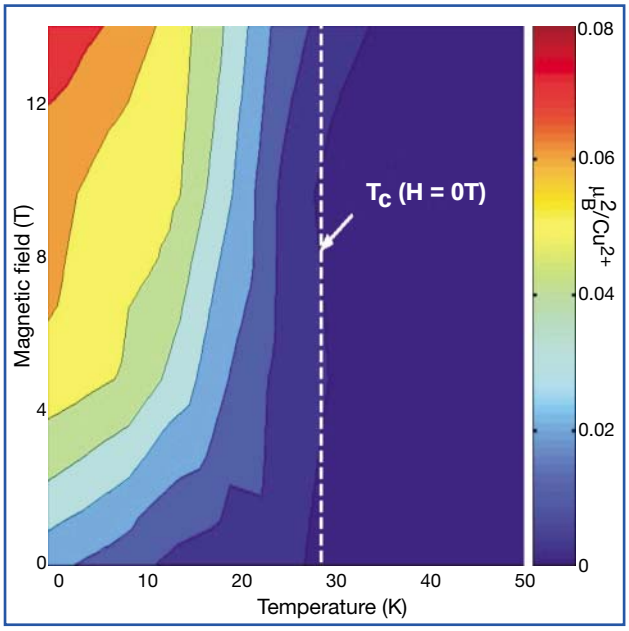

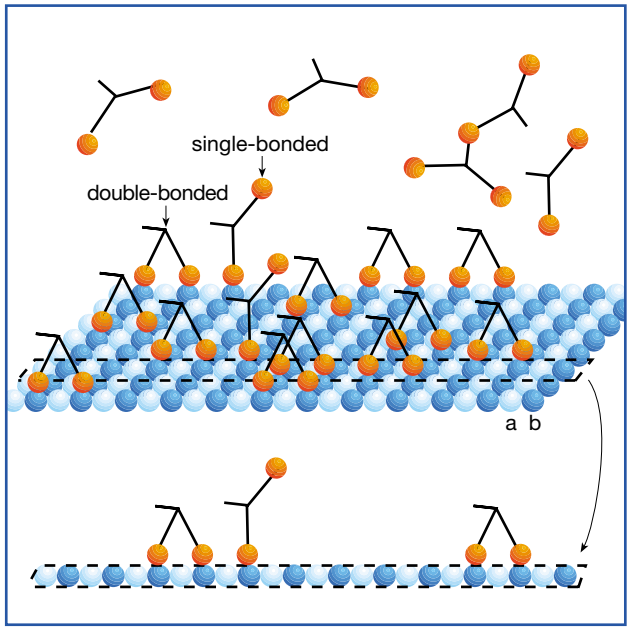

Hahn-Meitner-Institut
Berlin

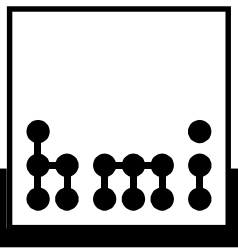

Annual Report 2001

Selected Results

Berlin 2002

Captions of cover images

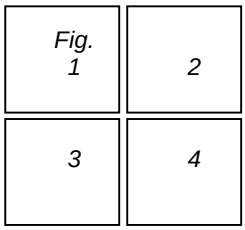

Fig. 1: SEM image of a gas diffusion cathode. The oxygen reduction occurs on catalytic nano particles which are incorporated into the high porous carbon black layer (enlarged insert).SE5.

Fig. 2: 3-dimensional representation of the surface of a $CuGaSe_2$ layer on a ZnSe(110) single crystal. The color scale represents the simultaneously measured work function using a Kelvin Probe Force Microscope. Differently oriented faces of single grains show different work function values. SE2.

Fig. 3: Neutron diffraction data for $La_{2-x}Sr_xCuO_4$ as a function of temperature and magnetic field. The figure shows the square of the ordered spin moment per Cu^{2+} ion as a function of temperature and applied magnetic field. The ordered moment squared is proportional to the observed neutron scattering signal. It first becomes significant below the zero-field superconducting transition temperature (T_c(H=0T)), and increases with decreasing temperature and increasing field. BENSC User Experiment performed with V2 (cold triple-axis-spectrometer).

Fig. 4: Schematic representation of the binding of kinesin dimers to a tubulin sheet. SF5.

1. Edition June 2002

Annual Report 2001
Selected Results
HMI-B 585

Hahn-Meitner Institut Berlin GmbH
Glienicker Str. 100
D-14109 Berlin (Wannsee)

Co-ordination:
Maren Achilles
Telefon: (030) 8062 2668
Telefax: (030) 8082 2047
e-mail: achilles@hmi.de

Table of Contents

Editorial V

Foreword VI

STRUCTURAL RESEARCH 1

Large scale facilities / User service 3

BENSC-Berlin Neutron Scattering Center 5
Antiferromagnetic order induced by an applied magnetic field in a high-temperature superconductor 8
Direct measurement of the spin hamiltonian and observation of condensation of magnons in the 2D frustrated quantum magnet Cs_2CuCl_4 9
Probing jump diffusion in crystalline solids with neutron spin-echo spectroscopy 10

ISL-Ion Beam Laboratory 11
High-energy PIXE using 68 MeV protons 13
Self-organization of $NiO/SiO_2/Si$ layer packages during irradiation with swift heavy ions 14
Lateral index-guided II-Vi laser diodes 16

NAA-Laboratory and Irradiation Service at BER II 18
Skeletal targeted radionuclide therapy with myeloablative 153Sm-EDTMP and melphalan in patients with relapsed multiple myeloma 19
Characterization of ochres stemming from European deposits by means of INAA 21

SF1 - Methods and Instruments 23
New solid state neutron optical devices 25
Software for development of new instruments, "Flight Simulator" for virtual instruments 26
Critical scaling in spin glasses 27
Stability and flexibility of proteins in solution 28
Self-assembly of biological model systems 29
Heuristic reconstruction of porous matter 30

SF2 - Magnetism 33
Magnetic phase diagram and chirality of the frustrated antiferromagnet $CsCuCl_3$ in Fields up to 17 Tesla 35
Coexistence of magnetism and charge density wave in Er5Ir4Si10 –a combined neutron and X-ray diffraction study 37
Specular and off-specular neutron reflectometry study of strongly coupled films of ferromagnetic Co and antiferromagnetic CoO 38
Cap layer influence on the spin reorientation transition of an ultrathin Co layer in Au/Co/X (X = UHV, W, Au) 40

SF3 - Materials 41
Rhenium distribution in the matrix of α Ni-Al-Ta-Re superalloy 43
MC simulation of the L12 order-disorder phase transformation 44
Microstructures of Ferrofluids studied by combined contrast variation using polarized neutrons 45
Evolution of the morphology in superalloys and nano-ceramics at high temperatures 47
Residual stress in polycrystalline materials and technical parts 48

SF4 - Structure and Dynamics 51
Spectroscopy of Si-Auger electrons from the center of heavy-ion tracks 52
Transmission of 3 keV Ne^{7+} through nanocapillaries in PET polymers: Evidence for capillary guiding 54
Radiation compaction of nanoporous Vycor Glass 55
Studies on metallic nanotubule formation in ion tracks 56
Bond lengths in $Cd_{1-x}Zn_xTe$ beyond linear laws 57
A new tool for proton beam eye treatment planning 59
Measurement of 3D dose distributions using BANG® polymer-gel dosimeters 60
Proton irradiation tests of the Rosetta ROLIS CCD detector electronics 61
Progress in heavy ion beam production 62
New features of the ISL-Accelerator-Control-System 64

SF5 - Theoretical Physics **65**
Magnetic systems of reduced dimension 67
Dipolar interactions in superconductor-ferromagnet heterostructures 68
Microcanonical thermodynamics 69
Axial and Landau gauge for a continuum electron in a homogeneous magnetic field 70
Semiconductor physics and photovoltaics 71
Biological physics 72
Soft condensed matter physics 73

SF6 - Trace Elements **75**
Analysis of metal-containing proteins by a novel method combining gel electrophoretic protein separation and SYXRFA 77
Regulation of selenium and selenoproteins in the mammalian organism 78
Changes in the structure of the metallothioneins in Alzheimer´s disease 79

SF7 - Nuclear Measurements **81**
The stopping power of ions in thin layers in dependence on the charge state distribution evolving from the ingoing charge state 83
Gamma-spectroscopy of Ca and Ne isotopes 85
Investigation of the structure of 11Be and 12Be 86
Structure studies of ^{15}C using the $^{9}Be(^{7}Li,p)$ reaction 87
Investigations of distinct effects in neutron transfer reactions: Elastic 2n-transfer $^{4}He(^{6}He,^{4}He)^{6}He$ and Nuclear rainbow scattering 88
Development of a large-area, high-rate, high-resolution MSGC detector for thermal neutron imaging 90

SOLAR ENERGY RESEARCH **93**

SE1 - Silicon Photovoltaics **95**
Pulsed EDMR – New insight into the mechanisms of recombination in thin crystalline silicon films 97
Amorphous/crystalline-silicon heterojunction solar cells 99
Thin organic layers: a new approach for functionalization of Si surfaces 100

SE2 - Heterogeneous Material Systems **101**
Multi-source evaporation of $Cu(Ga,In)S_2$ for thin-film solar cells 103
(Zn,Mg)O as window layer for Cd-free chalcopyrite solar cells 104
Analysis of recombination losses in chalcopyrite solar cells 105
Transport mechanism of solar cell grade polycrystalline $CuGaSe_2$ thin films 106
$CuGaSe_2$ by chemical vapor deposition (CVD) 107
Interdiffusion study at the ZnSe / $Cu(In,Ga)(S,Se)_2$ heterojunction by ERDA measurements 109
Kelvin probe force microscopy 110
Chemical and electrochemical deposition of chalcogenides for solar cells 111
Buffer layers, alternative sequential thin layer technology (ILGAR) 113
Eta-solar cell and other applications 115
Alignment of the endohedral fullerenes $N@C_{60}$ and $N@C_{70}$ in liquid crystals 117
Synchrotron-diagnostics for cost-efficient photovoltaic devices (CISSY) 118

SE3 - Technology **119**
Chalcopyrite solar cells and monolithically integrated test modules 121
Quality control and reliability of thin film solar cells 122
In-situ process monitoring 123
Doping 124

SE4 - Dynamics of Interfacial Reactions **125**
Time-resolved dynamics of hot electrons in InP(100) 127
Preparation and characterization of the n-SnO_2/p-InP heterocontact 128

SE5 - Solar Energetics **129**
Platinum-free catalysts for the reduction of oxygen 131
Interface engineering 134

SE6 - Electronic Structure of Semiconductor Interfaces **137**
TGM7, Transfer of a VUV monochromator to a BESSY II dipole beamline 139

Editorial

The scientific results from research and development of the Hahn-Meintner-Institute presented in this annual report give a representative inside into the activities and achievements of the last year, 2001.

Contributions are arranged along the departmental organization of the scientific divisions. Even though the results are of course based equally on the engaged work of the staff outside the scientific departments – from information technology over technical units to the administration. The activities directly connected to the user service at the large-scale facilities BER II / BENSC and ISL are summarized in separate chapters.

At the end of each text the reader finds a list of the responsible scientists as well as the project number and designation for internal purposes.

In addition to this annual report, HMI publishes a separate supplement, which contains the following statistical informations:

Listing of

- Publications
- Conference contributions and invited lectures
- Technology transfer and patents
- Academic education
- Co-operation partners and guests
- External funding
- Participation in external scientific bodies and committees
- Miscellaneous

Both the report and the separate supplement are available as download on the homepage of the Hahn-Meitner-Institute:

http://www.hmi.de/pr/druckschriften.html

or can be referred on request over the public relations office of the institute:

Hahn-Meitner-Institut Berlin GmbH
Öffentlichkeitsarbeit
Glienicker Strasse 100
D-14109 Berlin
e-mail: info@hmi.de

Annual reports covering various HMI activities in greater detail are

Statusbericht Strukturforschung 1997 – 2000
HMI-B 575

Status Report Solar Energy 1998 – 2001

BENSC Experimental Reports 2001
HMI-B 584

ISL Annual Report 2001
HMI-B 587

Foreword

With this report we present to the public selected results of the research and development activities in the Hahn-Meitner-Institute during the year 2001. We hope the reader will be convinced that at HMI cutting edge research was performed by both our own staff and the large community of external users of our facilities, and we are grateful for the boundary conditions and the resources setting the base for this success.

Looking at the activities in comparison to the past, programmatic re-orientations are getting visible. With Prof. Frey (SF5, Theory,,1.6.01) and Prof. Banhart (SF3, Materials, 1.1.02) distinguished representatives of the young generation took responsibility and are starting new scientific programs. This change of generation will continue with appointing new heads of the departments in both the divisions for Structural Research and Solar Energy Research in the near future.

It is important to underline that joint appointments with the universities remain key instruments to integrate the institute into its scientific surrounding. 2001 saw intensive discussions with the Humboldt-Universität and the Universität Potsdam to come to agreements similar to the most successful arrangements with both the Freie Universität Berlin and the Technische Universität Berlin. Final signing of cooperation agreements is scheduled for the summer of 2002.

In 2001, an important milestone was the very positive evaluation of the division for structural research based on the presentation of the results of the last four years to the Scientific Council, approving the programmatic strategy of the division and in particular the strong engagement in the user service at BENSC and ISL as one of the prime tasks of HMI as a Helmholtz Research Center.

Motivated by the rising request of the “bio-soft”-community for dedicated instruments at BENSC, work started to erect a new hall to house additional neutron instruments using the cold neutron source.

Even more challenging are the plans to further push the world-wide leading position of BENSC in providing highest magnetic fields for studying samples by neutron scattering. HMI proposes to install a High Magnetic Field Laboratory for Neutron scattering, NMFL, where fields up to 40 Tesla can be realized for neutron experiments. Conventional magnet technology will be combined with new technologies for neutron guiding and neutron detection both invented at HMI. NMFL is one out of nine projects of the next generation of large scale facilities for the sciences, presently evaluated by the German Wissenschaftsrat.

Another of these nine projects is the European Spallation Source ESS, where HMI acts as the leading laboratory to propose and develop the most suitable instrumentation.

The evaluation of the Solar Energy division is due for Spring 2002. Here also the long – term strategy of the division and the scientific orientation of upcoming joint appointments will be on the agenda.

Both scientific divisions took very successful efforts to use the potential of Berlins third generation source of synchrotron radiation, BESSY, for its scientific program. In a very fruitful collaboration with BESSY two especially designed insertion devices and several beam lines in 2001 could be pushed to near completion. First experiments are scheduled still before end of 2002. In 2001 the HMI staff working at BESSY could also move into a newly erected building at the BESSY site in Adlershof.

All these projects as well as all the achievements of last year are based on and depend upon the dedicated work of our staff and the user community of our facilities. Equally important is the steady support of our advisory boards and our funding agencies. Our thanks go to everybody for his share to keep and develop HMI as a place to do cutting edge science well noticed on the national and international scale.

On this basis we also feel well prepared to face the new scheme of program oriented funding of the HGF. We are confident that HMI is well positioned for the challenge and will successfully face the competition initiated by the new funding.

Division

SF Structural Research

(Structure and Dynamics in Condensed Matter)

The division Structural Research is formed by six departments which primarily use the three large scale facilities BER II / BENSC and ISL, and in future also BESSY. Although the study of the microscopic structure in condensed matter is the main field of research, the large scale facilities are also used for specific applications in health care and environmental proctection (eye tumor therapy with proton beams, activation anlysis with neutron beams).

The scientific program comprises three complementary issues: to provide a large national and international user community with top of the line research feasibilities at BENSC and ISL (and later on also at BESSY), to develop new methods and instruments, and to do in-house research with instruments and methods built and developed at HMI.

Methods developed at HMI are e.g. in the fields of electron microscopy, field ion microscopy, X-ray diffraction, neutron scattering instruments, and extreme sample environment (low temperatures in the mk range, magnetic fields of up to 15 Tesla).

The division Structural Research comprises 6 scientific departments:

SF1 Methods and Instruments
SF2 Magnetism
SF3 Materials
SF4 Strukture and Dynamics
SF5 Theoretical Physics
SF6 Trance Elements

and the group

SF7 Nuclear Measurement Technique.

The three first mentioned departments form the Berlin Neutron Scattering Center BENSC, SF4 is responsible for the operation and the development of the **Ion Beam Lab** and the **Eye Tumor Therapy**, and SF6 organizes the user service for the **Neutron Activation Analysis**.

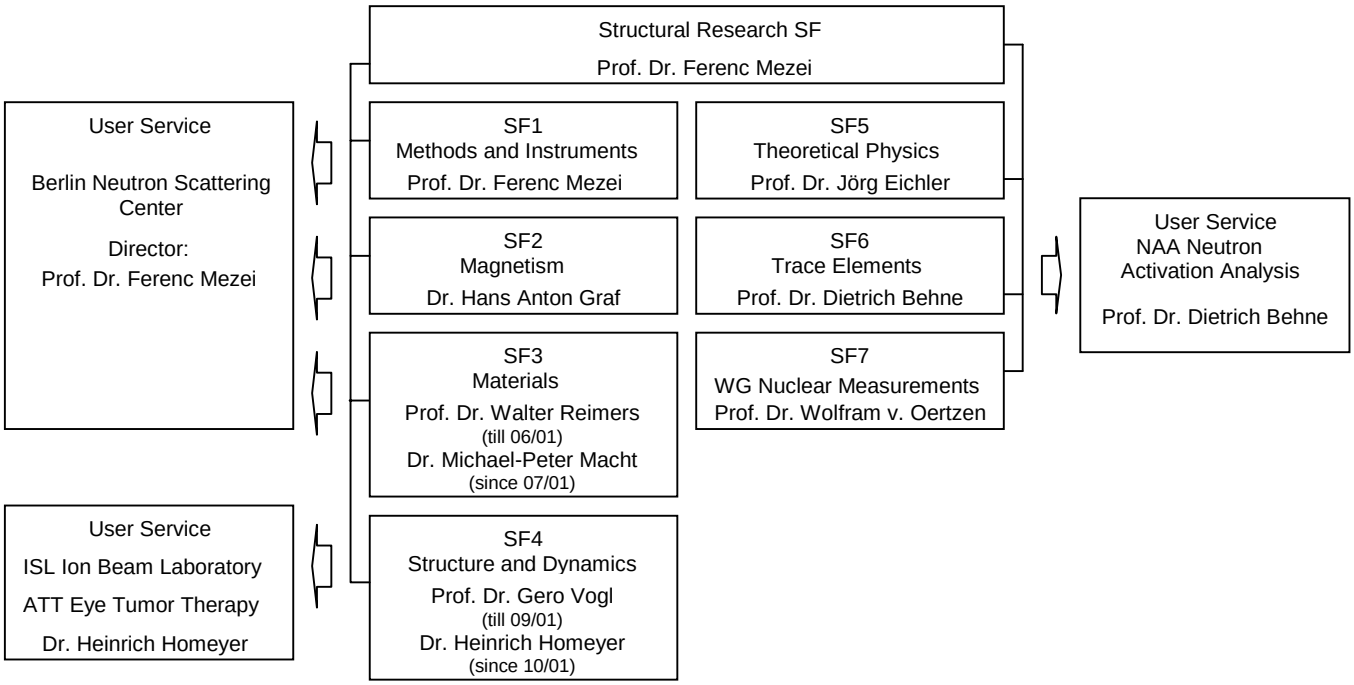

Large Scale Facilities / User Service

BENSC- Berlin Neutron Scattering Center

Director: Prof. Ferenc Mezei

It is the mission of the Berlin Neutron Scattering Center *(BENSC)* to develop and operate the scientific instruments at the Berlin research reactor BER II. About 70 % of the beam time at the most important instruments is made available to external scientific user groups from all over the world.

On a **regional and national scale** BENSC performs a principal task of the Hahn-Meitner-Institute:

Service for research groups

- from German Universities
- and from other public funded research institutions.

The relevant duties assigned to BENSC cover a broad range from contributions to scientific education up to performance of high ranking scientific research. An aim of increasing importance is

- scientific and technical support for industrial applications.

This support for industry is mainly based on co-operation agreements, where the partners produce the relevant samples and in return profit from the advanced analytical methods available at BENSC and from the highly specialized know-how of the BENSC staff.

On the **international scale** BENSC plays an important role in the round of European research centers. The growing international importance of BENSC is underlined by the fact that the number of short-term guest scientists from abroad exceeds the number of German visitors (see table 1) and has been stimulated by participating in the Access to Research Infrastructures Programmes of the European Commission.

The service orientation of BENSC requires a higher degree of reliable provision, preservation and development of know-how than this applies to rather basic research oriented institutions.

The leading role of BENSC for **sample environment at extreme conditions** is accepted worldwide: Experiments can be performed over a very large range of temperatures and/or magnetic fields. The temperature range for routine use is 15 mK to beyond 1200 K; and magnetic fields up to 17 Tesla have been made available to routine user operation. The unique Cryostat (1.5 K < T < 300 K) with a split pair superconducting magnet and a vertical field up to 17 Tesla is the world's leading magnet system in a neutron scattering facility and currently - and in the near future - available only at BENSC. A second magnet of this type is in the test phase and expected to be operational in summer 2002.

The advanced instrumentation and the unique sample environment capabilities attract renowned research groups Europe- and world-wide, and even from other powerful neutron sources. Three examples of highlight results from external user groups are included below.

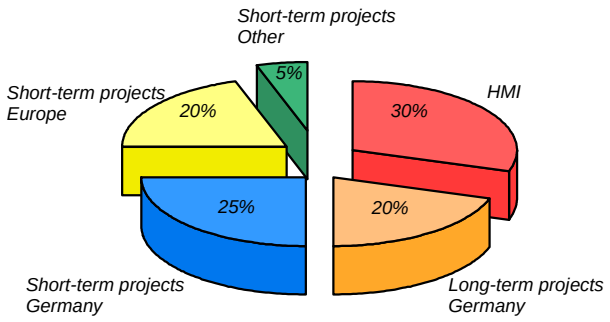

Fig. 1: Distribution of the BENSC instrument time

Profile of BENSC

The profile of BENSC is characterized by the exceptionally wide range of the **instrumentation**, which allows experiments to be performed in many areas ranging from basic to applied research. Several advanced BENSC instruments provide neutron intensities and resolutions competitive with the best available worldwide, including those operating at high flux reactors. Most of the instruments have the option of using polarized neutrons. Examples for unique instruments and instrument options are, e.g., ♦ the polarized neutron option SANSPOL, ♦ the multidetector option the time-of-flight spectrometer NEAT, and ♦ the novel spin-echo instrument (SPAN) with the unique wide-angle NSE option.

BENSC User Service

The BENSC user services provided for scientists of German universities and other national and international research institutions include

– Allocation of beam time to individual projects of external groups on the basis of peer reviewing by an international user committee and extensive scientific and technical support for the preparation, the experiments and the data evaluation

– Long-term scientific and technical projects on the basis of co-operation agreements, which mostly include the operation of instruments for which a contingent of beam time is allocated to the group

An amount of at least 50 % of the beam time of the 14 most important instruments operated by BENSC is reserved for individual scientific projects, 20% of the beam time are made available for long-term co-operation projects.

Long-term co-operations

Long-term co-operation projects are not only in the interest of the respective co-operations partners but also increase the manpower at BENSC and broaden the capacities for scientific support to the external users. In the pathbreaking field of soft matter research for instance, which until recently was not a main field of HMI's own scientific program, BENSC has established close collaborative links with the Institute of Biochemistry of the Technical University Darmstadt, the Iwan-N.-Stranski-Institut of the Technical University Berlin, and the Max-Planck-Institute of Colloids and Interfaces in Golm/Potsdam.

The most important long-term co-operation partners from the region of Berlin-Brandenburg are

- Technische Universität Berlin,
  Iwan-N.-Stranski-Institut für Physikalische und Theoretische Chemie,
  (Prof. G.H. Findenegg)
- Max-Planck-Institut für Kolloid und Grenzflächenforschung, Golm/Potsdam
  (Prof Dr. H. Möhwald)
- Technische Universität Berlin,
  Institut für Werkzeugwissenschaften und -technologie, Metallphysik,
  (Prof. W. Reimers)
- Technische Fachhochschule Berlin,
  (Prof. W. Treimer)

Other national long-term co-operation partners in 2001 are

- Institut für Kristallographie,
  Universität Tübingen
  (Prof. W. Prandl †)
- Institut für Biochemie
  Technische Universität Darmstadt
  (Prof. N. Dencher)
- Institut für Physikalische Biologie
  Universität Düsseldorf
  (Prof. G. Büldt)
- FB Materialwissenschaften
  Technische Universität Darmstadt
  (Prof. H. Hahn)
- Institut für Festkörperphysik
  Technische Universität Darmstadt
  (Prof. H. Wipf)
- Lehrstuhl für Experimentalphysik
  Universität Augsburg
  (Prof. A. Loidl)

Individual short-term research proposals of external users

It is the key issue of the BENSC user service to provide external groups with beam time and intensive scientific support for individual scientific experiments. This service is meant for both German groups and the international scientific community. The inclusion of new applications for beam time is decided by an Scientific Selection Panel in semi-annual selection rounds on the basis of scientific merit of the proposals.

Year 2001	**Germany**	**EU support** (EU Member and Associated States)	**Other EU +,** CH, USA, NIS Canada, Japan, Australia, India, Mongolia, …
250 Projects	**110**	**100**	**40**
450 Visits	**200**	**200**	**50**
330 Names	**140**	**140**	**50**

*NIS: New Independent States

Table 1: Results on the BENSC User Service. Number of projects, visits and scientists listed by country of home institution of principal proposer.

BENSC – A European neutron facility, Funds from the European Commission

The remarkably high number of guest scientists from member countries of the European Community have been stimulated by successfully applying for funds from the programs of the European Commission to support the transnational access to large scale facilities. BENSC and users of BENSC are presently supported by 500 000 € per year. In the new contract which became effective by the end of 2001 this sum was upgraded to 600 000 €. This EU funding program guarantees the support of external BENSC users until the beginning of 2004.

An analysis of the distribution of the beam time allocation for EU users demonstrates that a high number of users does not only come from countries which do not have a national research neutron facility, such as Italy, Spain or Greece. Strong user contingents also come from the UK and France to take advantage of options which are not available at their national neutron facilities or at the European neutron source, the ILL in Grenoble.

Human Potential Programme, Transnational Access to Research Infrastructures (IHP-ARI):

- Contract HPRI-CT 1999-00020 (2/2000-1/2003)
  (Total of 1500 000 Euro)
- Contract HPRI-CT 2001-00138 (11/2001-2/2004)
  (Total of 650 000 Euro)

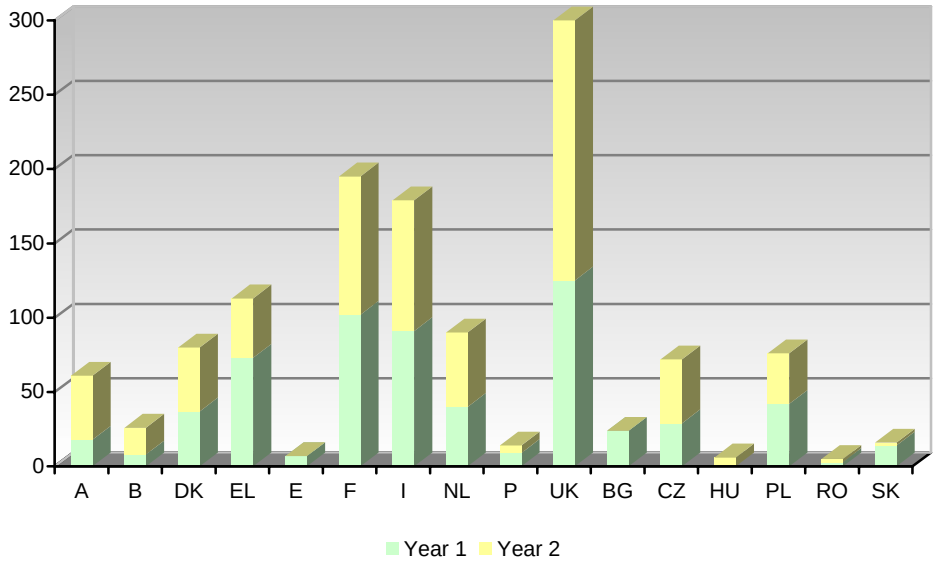

Fig. 2: Delivered Neutron Instrument Days under the current EU contract, grouped by country of the home institution of the group leader. International groups with principal proposer from ILL Grenoble are included under France.

Scientific results of the external users at BENSC

The scientific interim reports on most recent experimental results guarantee for a rapid dissemination of the results of external users of BENSC. These interim reports are published annually under the label of "BENSC EXPERIMENTAL REPORTS", and the year 2001 Volume, HMI-B 584 (ISSN 0936-0891), is distributed to all users of BENSC in June 2002 as cd rom and/or in printed form. The reports for 2000 and 2001 also available on the internet (http://www.hmi.de/bensc/report2000/start_en.htm). The year 2001 volume includes 240 reports of external and internal users, with 90 contributions on EU IHP-ARI supported projects. A rough split-up of the number of reports into the different fields of science is displayed in Fig.3.

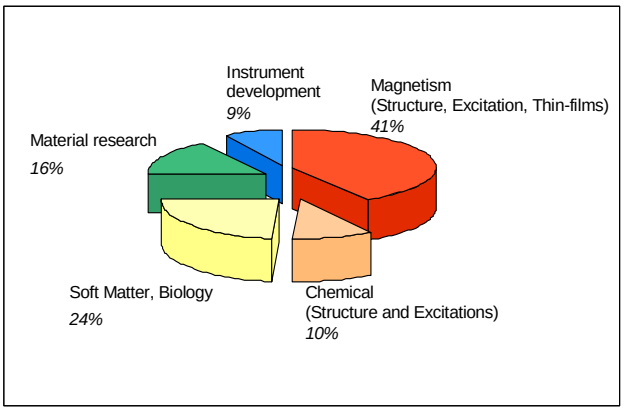

Fig.3: Fractions of Experimental Reports in HMI-B 584 listed by field of science

This rapid documentation system is complemented by oral and poster contributions to national and international conferences. An excellent example is the *International Conference on Neutron Scattering (ICNS '01)* which was held in Munich in September 2001. Staff members and external users of BENSC handed in 140 contributions, more than 16 % of the total number of conference contributions. More than 50 % of the BENSC contributions were provided by external users and the majority of the contributions to ICNS will be published in the peer reviewed conference proceedings (Appl. Phys. A) in 2002.

Publication in internationally renowned peer reviewed journals normally follows the experiments with a delay of 1 to 2 years. Since as a rule at least one collaborating BENSC scientist is among the authors the year 2001 publications of external users are included in the publication lists of the departments SF1, SF2 or SF3. A complete compilation of the year 2001 publication lists for all BENSC users is included in the volume "BENSC EXPERIMENTAL REPORTS 2001", HMI-B584, May 2002.

Antiferromagnetic order induced by an applied magnetic field in a high-temperature superconductor

One view of the high-transition-temperature (high-T_c) copper oxide superconductors is that they are conventional superconductors where the pairing occurs between weakly interacting quasiparticles (corresponding to the electrons in ordinary metals), although the theory has to be pushed to its limit. An alternative view is that the electrons organize into collective textures (for example, charge and spin stripes) which cannot be 'mapped' onto the electrons in ordinary metals. Understanding the properties of the material would then need quantum field theories of objects such as textures and strings, rather than point-like electrons. In an external magnetic field, magnetic flux penetrates type II superconductors via vortices, each carrying one flux quantum. The vortices form lattices of resistive material embedded in the non-resistive superconductor, and can reveal the nature of the ground state—for example, a conventional metal or an ordered, striped phase—which would have appeared had superconductivity not intervened, and which provides the best starting point for a pairing theory.

Magnetic neutron diffraction experiments were performed with the cold neutron triple-axis-spectrometer V2 to measure the spin ordering in single crystals of underdoped $La_{2-x}Sr_xCuO_4$ (x=0.10). The superconducting CuO_2 planes were aligned in the scattering plane, and magnetic fields (up to 14.5 T) were applied perpendicular to these planes.

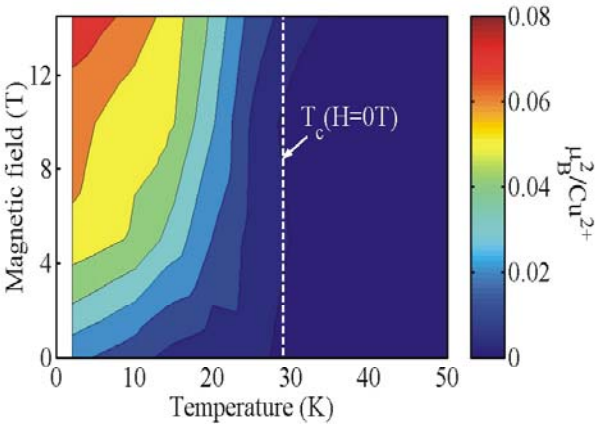

Fig. 1: Neutron diffraction data for $La_{2-x}Sr_xCuO_4$ as a function of temperature and magnetic field. The figure shows the square of the ordered spin moment per Cu^{2+} ion as a function of temperature and applied magnetic field. The ordered moment squared is proportional to the observed neutron scattering signal. It first becomes significant below the zero-field superconducting transition temperature (T_c(H=0T)), and increases with decreasing temperature and increasing field. BENSC User Experiment performed with V2 (cold triple-axis-spectrometer).

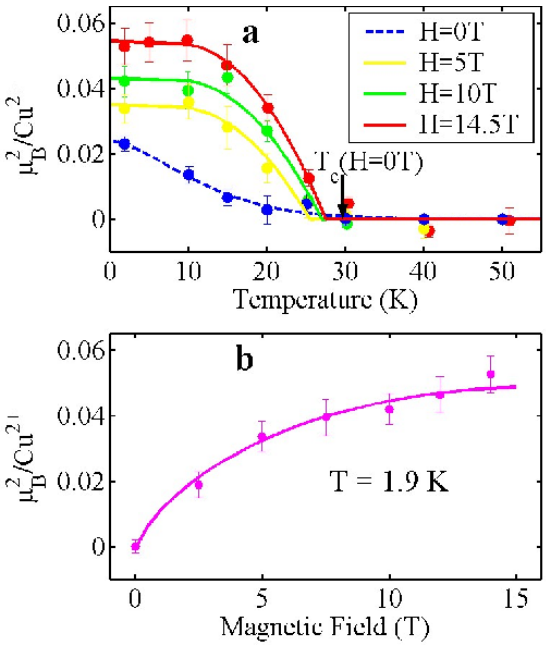

Fig. 2: The dependence on temperature and magnetic field of the ordered spin moment squared in $La_{1.9}Sr_{0.1}CuO_4$. (a) The temperature dependence. The zero-field signal (blue circles) increases gradually below T_c (H=0T). The dashed line is a guide to the eye. Also plotted is the field-induced signal (equal to the signal measured in field minus the zero-field signal) for fields of H=5T (yellow circles), 10 T (green circles) and 14.5 T (red circles). The solid lines through the data are fits to mean field theory. (b) The field-induced signal as a function of field at T=2K (magenta circles). The solid line is a fit to the data as predicted by theory.

The new finding of this experiment is that external magnetic fields markedly increase the intensity of incommensurate elastic peaks which occur in the superconducting phase. The applied field that imposes the vortex lattice thus also induces 'striped' antiferromagnetic order. Ordinary quasiparticle models can account for neither the strength of the order nor the nearly field-independent antiferromagnetic transition temperature observed in these measurements.

B. Lake, H. M. Ronnow, N. B. Christensen, G. Aeppli, K. Lefmann, D. F. McMorrow, P. Vorderwisch, P. Smeibidl, N. Mangkorntong, T. Sasagawa, M. Nohara, H. Takag and T. E. Mason.
Nature 415, 299 - 302 (2002)

Direct measurement of the spin Hamiltonian and observation of condensation of magnons in the 2D frustrated quantum magnet Cs_2CuCl_4

A new experimental method has been successfully applied to measure the spin Hamiltonian of the spin-1/2 Heisenberg antiferromagnet Cs_2CuCl_4. This is a frustrated quantum magnet that has recently been shown to display a very unusual quantum spin liquid state. The excitations are not spin-1 magnons as observed in other unfrustrated 2D quantum magnets but instead are spinons carrying a fractional spin of ½, as predicted by a resonating-valence-bond theory.

By applying strong magnetic fields (up to 12T) a transition from the fractional quantum spin-liquid phase to the fully-polarized phase is induced, transforming the system into an effective ferromagnet. In this phase all quantum fluctuations are quenched by the external field, the strongly-interacting quantum system behaves like a classical magnet and the excitations are conventional magnons.

Inelastic neutron diffraction experiments were performed with the cold neutron triple-axis-spectrometer V2 to measure the magnon dispersion relation. Measurements were made with a large Cs_2CuCl_4 crystal mounted in the (0,k,l) scattering plane. In the experiments with the VM-1 vertical cryomagnet and dilution insert magnetic fields up to 12T (much larger than the saturation field B_c =8.44T) and temperatures below 0.2K were used.
The measured one-magnon dispersion relation gives the exchange couplings directly. Considerable dispersion along both [0k0] and [00l] directions in the *bc* plane indicates strong 2D character (see figure). The exchange couplings are found to form an anisotropic triangular lattice with small Dzyaloshinskii-Moriya terms.

Upon decreasing the field the magnon energies reduce by the additive Zeeman energy. At the critical field B_c=8.44T the gap closes at the dispersion minima and Bragg peaks appear at the corresponding wavevectors below B_c indicating transverse (off-diagonal) long-range order. This order is an example of Bose-Einstein condensation in a dilute gas of magnons.

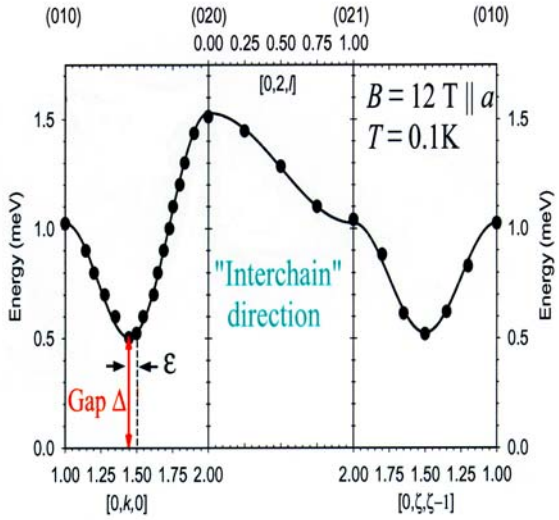

Fig 1: Magnetic dispersion relations in the saturated phase (B=12T || a), T < 0.2 K) along symmetry directions in the 2D plane. The solid line is a fit to the theoretical dispersion and thus gives directly the coupling parameters.

The method is generally applicable and could be used to reveal exchanges and quantum renormalizations for a broad range of systems: random magnets, quantum antiferromagnets or spin glasses.

R. Coldea, D. A. Tennant, K. Habicht, P. Smeibidl, C. Wolters, Z. Tylczynski.
Phys. Rev. Letters 88, 13, 137203, (2002)

Probing jump diffusion in crystalline solids with neutron spin-echo spectroscopy

Neutron spin-echo (NSE) spectroscopy reaches the longest times in inelastic neutron scattering. This method was used for the first time to give direct access to the jump-like motion of atoms on lattices, which up to now has been the domain of quasielastic neutron scattering (QNS). In a pioneering experiment it was showed that NSE delivers the information on the time behavior of diffusing atoms in a most direct manner and has the potential to observe diffusivities which, up to now, could only be studied on ^{57}Fe with Mössbauer spectroscopy. The potential of the method was demonstrated on the model system NiGa, where both the jump vector and the residence times on the different sublattices are known and the incoherent cross sections of the constituents are such that Ni diffusion can be observed without any interference from Ga atoms.

NiGa crystallizes in the CsCl structure and the atomic motions are directly related to the local order since the diffusing atom —in order to avoid a long distance next-nearest neighbor (NNN) jump on the regular lattice— may be forced to jump to a nearest neighbor (NN) site on the "wrong" sublattice and create a point defect (see Fig. 1). NSE spectroscopy determines the intermediate scattering function $S(\mathbf{Q},t)$, which for the structure of NiGa, with only two sublattices, reads :

$$S(Q,t) = \sum_{i=1}^{2} w_i(\vec{Q}) \exp(M_i(\vec{Q})\, t).$$

At fundamental Bragg reflections the results are trivial and identical for all possible jump vectors. Around superlattice reflections, however, it is possible to clearly distinguish between different jump vectors and decide between conflicting jump models from measurements at only two positions in reciprocal space.

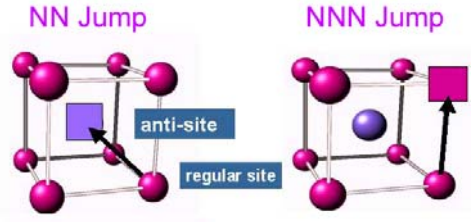

Fig.1 : At the unit cell with CsCl structure a Ni atom may perform a NN jump into a vacancy on a Ga site (purple square) or a NNN jump into a vacancy on the Ni sublattice (pink square)

The samples were two NiGa single crystals, with 51.5 and 52.5 at.% Ni respectively. The measurements were performed at 1100°C and 1130°C on the NSE spectrometer SPAN of BENSC with a wavelength of 6.5 Å. The scattered neutrons were detected simultaneously by two detector benches positioned at 94 and 130 deg.

Figure 2 shows the spectra obtained from the $Ni_{52.5}Ga_{47.5}$ sample at 1130°C. Two model curves are drawn in, one for model based on NN jumps and one for NNN jumps. For the spectrum obtained at $2\Theta = 94^{o}$ a good agreement is obtained for both jumps. However, at the second scattering angle $2\Theta = 130^{o}$, which corresponds to a wave vector the vicinity of a superlattice point, only the NN model agrees with the experiment.

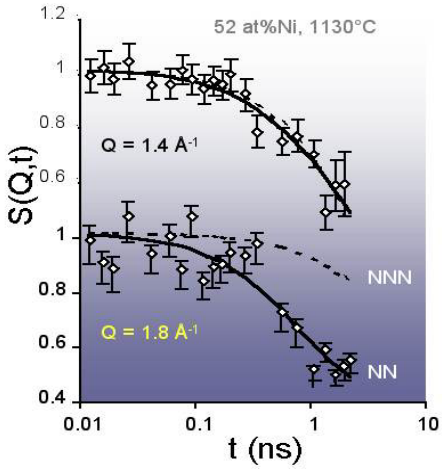

Fig. 2: *Intermediate scattering function s(Q,t) measured on the Ni52.5Ga47.5 single crystal at 1130°C. The two spectra were obtained in a simultaneous measurement at $2\Theta = 94^{o}$(top) and 130^{o}(bottom). The lines represent the time correlation functions calculated for NN jumps (solid line) and NNN jumps (dashed line).*

It is remarkable that an unambiguous decision between two opposed diffusion models can be obtained on the basis of two spectra only and that the information on the residence times can be obtained in a very direct manner. NSE proved to be as efficient for diffusion studies as the time-domain variant of Mössbauer spectroscopy, nuclear resonant scattering of synchrotron radiation (NRS) on ^{57}Fe, with the difference that NSE is *applicable to a wide range of systems*. From Fig. 2 it becomes obvious that NSE competes with Mössbauer spectroscopy also in terms of resolution. The spectrum corresponds to a diffusivity of 4.4 10^{-12} $m^2 s^{-1}$ and shows an effect of 50%. Considering that a 10% effect can be resolvable, diffusivities in the 10^{-13} m^2 s^{-1} range should be easily accessible and this will permit to penetrate the domain of Mössbauer spectroscopy. The pronounced difference in the time correlation for different jump vectors in the present experiment shows that diffusional dynamics on the 1–100 ns scale are accessible to neutron scattering, hence providing a powerful tool, which offers a resolution comparable to Mössbauer spectroscopy without being restricted to a single element. Information on the mean residence times that diffusing atoms spend on different sublattices is obtained in a very direct manner from individual spectra. This immediate access to the different time scales is expected to push the understanding of complicated diffusion mechanisms.

M. Kaisermayr, C. Pappas, B. Sepiol, G. Vogl. Phys. Rev. Lett., 87, 175901, 2001

ISL - Ion Beam Laboratory

The ion beam laboratory ISL is exclusively dedicated to ion beam applications-technologies. ISL provides beams of light and heavy ions from various accelerators, and combinations of accelerators, with energies ranging from 10 eV to several 100 MeV. More than 65% of the total beam time is given to outside users. They have access to the ISL via a Program Advisory Committee, PAC, which meets twice a year, and decides on applications for beam time solely on the basis of the projects scientific merits.

The visiting users can either use permanently installed target areas, or install their own technical equipment.

Scientists and technicians at ISL offer their specific expertise resulting from a broad scientific program in structural and material research as well as from their involvement in the technical applications of ion beams.

With the therapy of eye tumors, and the irradiation of polymeric foils, ISL also contributes to direct medical and technological applications.

Operations in 2001

In October 2001, the PAC meeting approved 14 new experiments, 17 others were prolonged. In total, 50 projects have been active in 2001.

Due to enforced ion source developments, several long term awaited beams could be placed at the users‘ disposal: 650 MeV Xe-ion beams, first two weeks of beam time with 350 MeV Au-beams and extremely stable, high intensity Kr-beams, all produced with the Supernanogan, the new ECR-ion-source of the RFQ-injector. Though considerable

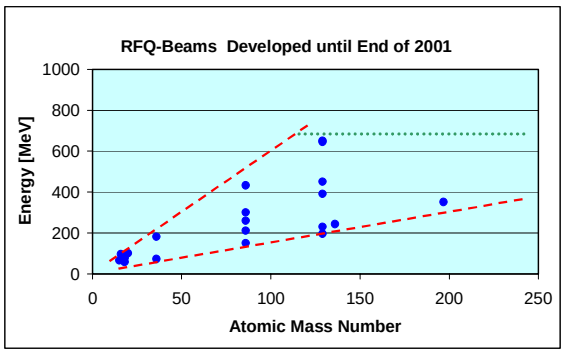

Fig. 1: Ion Beams Developed with the RFQ-Injector. A new highest energy (650 MeV Xe) and a new highest mass (Au) have been produced in 2001

efforts were still necessary to improve the performance and the tuning procedures of the RFQ-injector (see Progress in heavy ion production), the high mass injector has become an extremely important part of ISL enabling us to produce the above mentioned ion beams. A summary of all beams produced with the RFQ-injector is shown in Fig. 1.

Beams were delivered to 11 different target stations. In particular the new target station enabling Auger electron spectroscopy at UHV conditions has been used for a couple of long-periods of beam time.

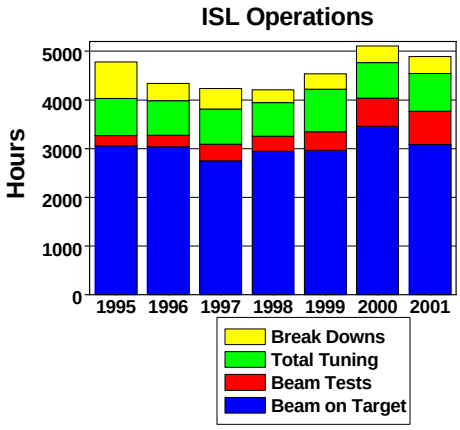

Fig. 2: ISL Operations
Last year’s eam on target value reached the long term average of 3000 h per year. Considerable amount of time was used for beam tests, in particular for high current, extremely stable heavy ion beams, Xe-beams with the highest energy possible (6 MeV/N), and the development of the first Au ion beams, all of them produced with the RFQ-injector.

The commissioning of the new target station and the new beam species took increased amounts of beam testing time. Nevertheless, the long-term average of about 3000 hours of beam-time per year was produced in 2001 (see Fig 2). The break down time could be kept rather low as well as the total tuning time.

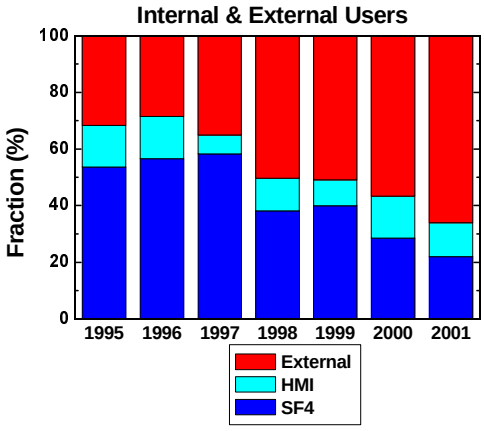

Fig. 3: User Facility ISL
From 1997 to 2001, outside users increased their share of the beam time at ISL continuously.

This excellent accelerator performance allowed the stable operation of the outside users´ programs, in particular the therapy of ocular melanomas with high-energy protons. 68 patients were treated in 10 therapy sessions.

Outside users increased their share of beam time in 2001 as shown in Fig. 3. It is expected that the development of beams of high energy and high ion masses (Au-beams) will create additional demands, in particular for the new target areas to be installed in 2002, for experiments related to the project "Ion Tracks in Solids"

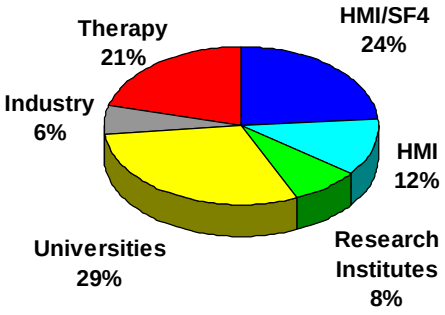

Fig. 4: ISL users

It is interesting to monitor where the different users come from: This is displayed in Fig. 4. About 30 % of the users come from universities. Together with the tumor therapy project, a joint effort of the HMI and the Universitätsklinikum Benjamin-Franklin of the Freie Universität Berlin, university groups take nearly 50 % of the beam time. The part "HMI" means HMI departments other than SF4.

The graph showing the fraction of beam time used for the different scientific fields active at ISL reflects the increasing importance materials modification (see Fig. 5). The share used for medical applications stays relatively constant since the beginning of the therapy program (1998). Fluctuations are due to varying amounts of beam time used for research and development.

In 2001 the total beam time for ion beam analyses decreased due to the fact that less low energy beam time (hydrogen profiling using ^{15}N-beams) had been asked for. On the other hand, the use of fast and heavy ions as analytical tools has been intensified.

Elastic Recoil Detection Analyses (ERDA) with Xe projectiles concerned materials relevant for the construction of photovoltaic devices, including the rear-contact metal, Si-based as well as chalcopyrite absorbers, compounds for buffer and window layers. In total, close to 80 % of the activities involved collaborations with internal and external photovoltaic groups. The analytical contributions to the developments greatly improved the production processes for the different layers.

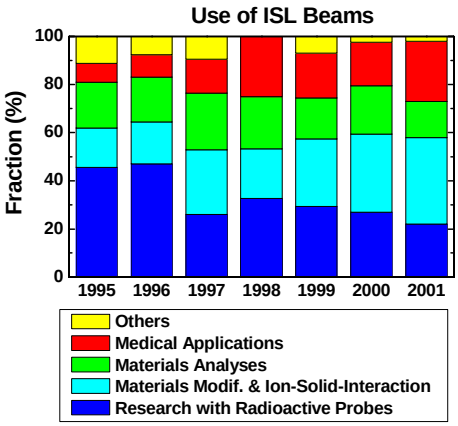

Fig. 5: Use of ISL beam
Specific changes of the fractions of beam time used for the different scientific activities can be observed. The increasing fraction for materials modification reflects the start of the project "Ion Tracks in Solids"

Increasing interest from museums, university institutes and private art collectors resulted in more beam time for High Energy PIXE analyses. At ISL, this method has been developed to a high perfection, in particular for items of cultural heritage. Thus, collaborations with restorers and archaeologist to exploit this new method are funded by the EU COST G8 project.

The amount of beam time used for direct technical and industrial applications stayed constant. The mayor project was the irradiation of polymeric foils for the production of microfilters. In addition, several shorter runs involving irradiations of eletronic components with different ion species and energies have been carried out. In collaboration with the DLR, Institute for Space Sensors & Planetary Research, Berlin Adlershof, CCD cameras for the Rosetta Mission of the ESA were tested under proton irradiation.

H. Homeyer
(SF4.05b ISL Accelerator Operations)

High-energy PIXE using 68 MeV protons

Since several years, high energy PIXE (Proton induced X-Ray Emission) is applied successfully to objets d'art and archaeological findings. This work continued as an ongoing service during the year under report: About 60 % of the experimental time was dedicated to solve art historical or archaeological questions (see figure) in collaboration with German research institutes and universities. For a common project with the Kunsthistorisches Museum, Vienna, concerning the "Hoard of Tulln", a short-term scientific mission was allocated by the EU which will be performed next year, as the EU granted the money for 2002.

Another 40 % were used to improve the method, expanding it to new fields and for progresses in the quantification of the analysis. For the latter, we collaborate with the University of Guelph to test the evaluation program GUPIX for the high proton energies used at ISL.

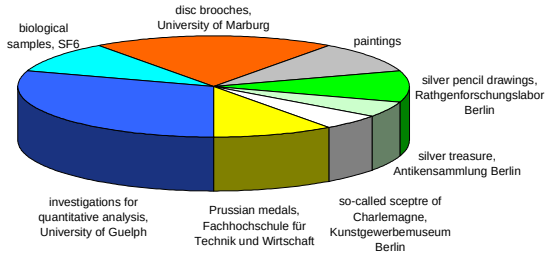

Fig. 1: Distribution of the high-energy PIXE beam time to the different collaborations. 60 % of the beam time was dedicated to objets d'art and archaeological items.

A. Denker
(SF4.05 b ISL Accelerator Operations)

PIXE analysis of the medal „Hoher Orden vom Schwarzen Adler" 21.338a, German Historic Museum Berlin

In the frame of a thesis describing "*gap-filling on enamel illustrated by three medals of the German Historic Museum Berlin*" the medals were analyzed by high-energy PIXE at the ISL. The main issue of the thesis was to find a suitable material for the completion of the medals. To examine their usability under museum conditions, commercial products were tested as well as materials commonly used in conservation. A questionnaire was sent to German and international conservation institutes supported by a detailed literature research in order to determine a praxis-oriented selection of materials. Following to a test on the light ageing properties of all materials, a grit section test was carried out on mock-ups to examine the adhesive properties of selected conservation materials on gold and enamel. To specify the composition of the mock-ups, the composition of the medals was analyzed using micro X-ray fluorescence (for the enamel) and high-energy PIXE (for the support). Only materials with positive test results were used for gap-filling on the medals themselves.

Fig. 1: Condition at the time of analysis (before conservation) front.

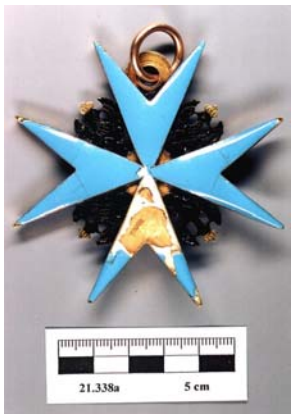

Fig. 2: Condition at the time of analysis (before conservation) back.

In case of all three medals it was not possible to take samples for analysis. Hence non-destructive methods needed to be used. The aim of the PIXE measurements was the determination of the metal composition, especially whether the medals consisted of massive gold or were only gilded. Further the quantitative composition of the metal and the solder had to be determined. As example for the analytical results, medal 21.338a is presented, the findings of the other medals are similar: The medal 21.338a consists of a massive gold/silver/copper alloy. The central medallion and the rest of the medal differ in composition. The alloy of the medallion contains about 60 % gold, 15 % silver and 10 % copper. The rest of the medal was made of an alloy with about 75 % gold, 15 % silver and 25 % copper.

A. Denker in collaboration with K. Ebert, Main area of studies: Conservation /archaeological cultural asset
University of Applied Sciences (Fachhochschule für Technik und Wirtschaft Berlin)
(SF4.05b ISL Accelerator Operations)

Self-organization of $NiO/SiO_2/Si$ layer packages during irradiation with swift heavy ions

During our investigations of swift heavy ion induced atomic transport processes in NiO/SiO_2 thin-film-systems we observed a new self-ordering phenomenon of the NiO toplayer [1]. We have irradiated $NiO/SiO_2/Si$ layer packages with Ar-, Kr- and Xe-ions of some MeV/amu energy at large tilt angles (small angles of beam incidence). For sufficiently large tilt angles the surface reorganizes completely and a regular lamellae structure becomes visible.

The samples were prepared using thermally oxidized silicon wafers (thickness of the SiO_2 layer: 240 nm) as the substrate material, covered with a 130 nm thick NiO layer deposited by reactive magnetron sputtering. X-ray diffraction (XRD) revealed a micro-crystalline (111)-texture of the NiO top-layer with an average cristallite size of 40 nm. The irradiations were performed with the cyclotron of the Ion Beam Laboratory at the Hahn-Meitner-Institute using tilt angles ranging from $\theta = 0°$ and $\theta = 85°$, with θ being the angle between the incident ion-beam and the normal of the sample surface. The N_2-cooled samples were irradiated with 90 - 230 MeV Ar-, Kr- and Xe-ions at fluences of $\phi = 1.7\times10^{13}$ - $1.3\times10^{15}/cm^2$.

After irradiation the surface-roughness of the samples with a tilt angles larger than $\theta \approx 60°$ rose by a factor of up to 30. We have therefore investigated the surface after irradiation with different fluences by means of Scanning Electron Microscopy (SEM). A series of perspective SEM images taken from the edges of the Xe-irradiated samples is shown in Figure 1.

At low fluences first cracking of the surface can be observed (a). The cracks are oriented perpendicular to the beam direction. Increasing fluence leads to further opening of the cracks at the surface and their penetration into larger depths of the NiO layer, until the SiO_2 layer is reached (b). Further irradiation then leads to shrinking of the NiO "stripes" in between the cracks and an increase of their height (c,d). Finally, at higher fluences, lamellae with a typical distance of $\lambda = 1$ - 3 μm, a height of 0.5 - 1 μm and a width of about 100 nm have formed (e,f).

Microspot-RBS (Rutherford Backscattering) and PIXE (Particle Induced X-ray Emission)-mapping performed by means of the 2.2 MeV proton-microprobe of the Max-Planck-Institut for nuclear physics in Heidelberg (with a beamspot size of $1.4\ \mu m \times 1.4\ \mu m$) revealed, that all Ni from the former continuous NiO layer is now located in the lamellae, while no Ni is left in between. Since no significant loss of oxygen was observed for the irradiations carried out with $\theta = 0°$ - 60°, we conclude that the lamellae consist of NiO (or at least a nickel suboxide). XRD measurements performed on the irradiated samples point at an amorphous structure of the lamellas.

The observed cracking is due to the uni-axial tensile stresses induced by the nuclear track formation in the top layer. Grinfeld et al. [3] have shown that surfaces of stressed solids are unstable against periodic perturbations. The lamellae formation itself can than be understood in terms of the so-called hammering effect first observed by Klaumünzer, et al., in metallic glasses [3].

References

[1] Feyh, A., et al.:
Phys. Rev. Lett., 2002, submitted
[2] Grinfeld, M.A.:
Dokl. Akad. Nauk. SSSR 290, 1986, p. 1358
[3] Gutzmann, A. and Klaumünzer, S.:
Nucl. Instrum. Methods B 127/128, 1997, p. 12

A. Feyh, B. Schattat, W. Bolse (Institut für Strahlenphysik, Universität Stuttgart); A. Jasenek (Institut für Physikalische Elektronik, Universität Stuttgart) in collaboration with S. Klaumünzer (HMI)
(SF4.05b ISL Accelerator Operations)

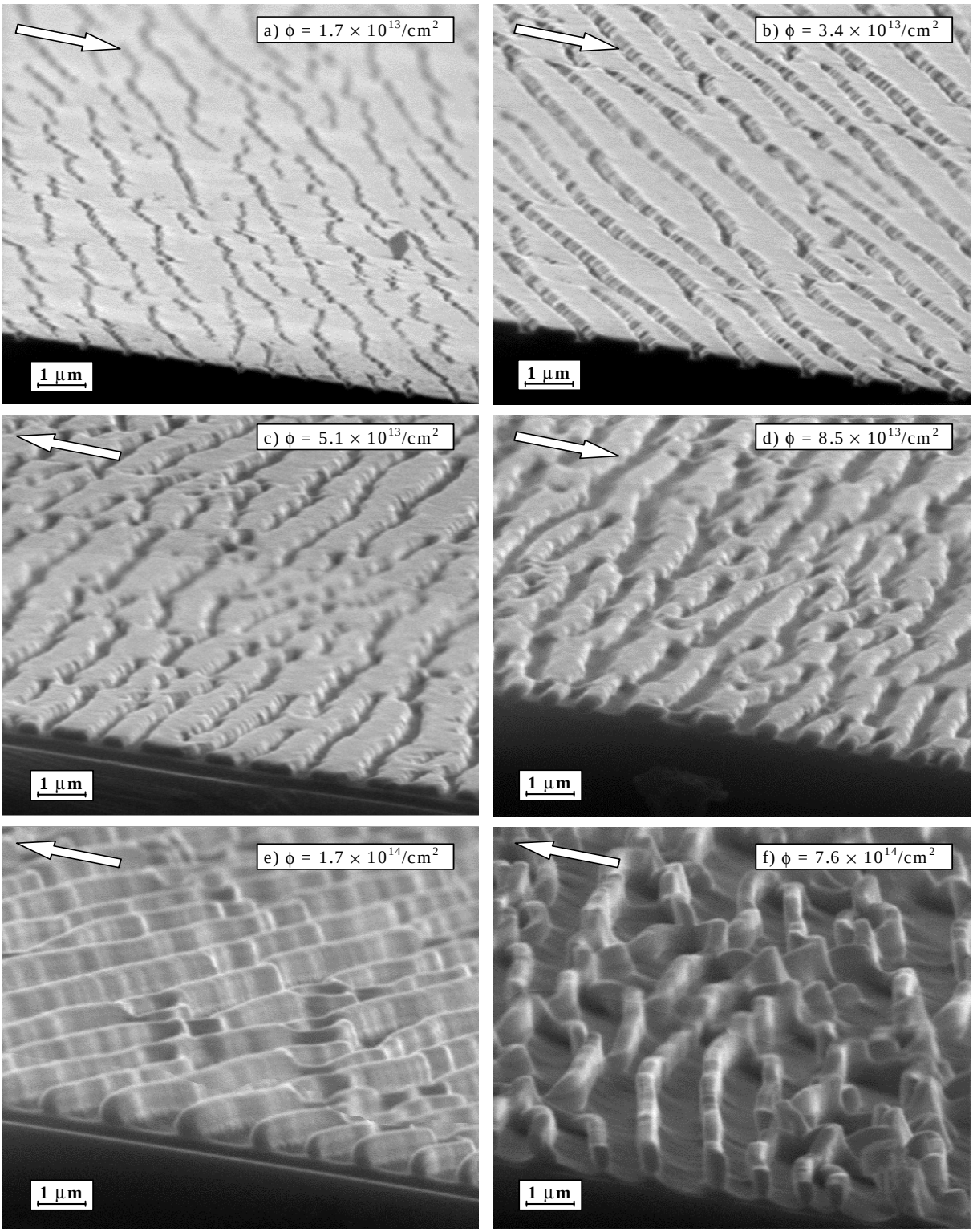

Fig. 1: Samples irradiated with 230 MeV Xe-ions of $\phi = 1.7 \times 10^{13}$ - 7.6×10^{14}/cm^2 and $\theta = 75°$.

Lateral index-guided II-VI laser diodes

Implantation-induced disordering is applied to define lateral waveguides in ZnCdSe and ZnCdSSe single quantum well lasers. Due to the intermixing-induced lateral difference of the refractive index, the optical and electrical characteristics are significantly improved. A reduction of the threshold current density from 276 A/cm^2 to 96 A/cm^2 for ZnCdSe LDs and from 447 A/cm^2 to 153 A/cm^2 for ZnCdSSe LDs was achieved.

Till this day, ZnSe-based heterostructures are the only available material system for semiconductor lasers emitting in the green spectral range. For many practical applications, such as laser TV and polymer optical fibre (POF) communication, a high output power and a long lifetime are required.
To increase their presently limited device lifetime [1], a reduction of structural defects [1, 2], optimized laser design, and improved contacts [3] are indispensable.
An optimized laser design should reduce the lateral current spread and provide a guiding of the light wave. This can be achieved by a laterally selective implantation-induced disordering (IID), which already has been proven as a powerful tool for III-V devices [4]. For II-VI materials, only a few applications of IID exist [5, 6]. A reduction of the threshold current density for ZnCdSe- and ZnCdSSe- single quantum well lasers by a factor of three using an optimized IID technology [7].

Lateral wave guiding by implantation-induced disordering: Lateral modulation of the refractive index can be produced by super-lattice or quantum well intermixing induced by suitable annealing atmospheres [8] or by ion implantation [6, 9]. The vacancies generated by both methods lead to a drastically enhanced Cd diffusion resulting in a complete intermixing of the sample structure, sufficient for the required change of the refractive index [6, 9]. Furthermore, the IID has the second advantage, that the implantation itself induces deep impurities. Such impurities lead to a large resistivity of the implanted material. Therefore, the implanted regions act as current guides, which means, that they suppress the current spread.
While vacancy-generating atmospheres need a process temperature exceeding 400 °C [4], ion implantation only increases the temperature near the path of the injected ion. Therefore, the region where defects are generated can be easily controlled. To achieve an effective intermixing of the laser structure, the energy of the ions has to be adjusted to create a maximum amount of vacancies in and near the active region. We used N_2^+ molecule ions or Ar^+ ions at an acceleration voltage of 2.5 MV and a dose of $1 \cdot 10^{15}$ /cm^2 for implantation.

Sample structure: Separate confinement heterostructure (SCH) single quantum well (SQW) lasers grown by molecular beam epitaxy on n-GaAs substrates are used to study electrically pumped lasing. The structure consists of a ZnCdSe or a ZnCdSSe quantum well embedded in ZnSSe waveguide and cladded by ZnMgSSe. A ZnTe/ZnSe multi quantum well structure is used for the p-contact. The emission wavelength is around 520nm at room temperature. Lateral confinement is defined by the widths of the Pd(10 nm)/Pt(50nm)/ Au(100 nm) contact stripes. The threshold current density is 276 (±10) A/cm^2 for the ZnCdSe quantum well and 447(±10) A/cm^2 for the ZnCdSSe quantum well.
Such lasers are gain guided. The operating voltage is as high as 6…7 V. The lasers are tested for a duty cycle of 0.5 %. The wavelength and the light output from one facet are measured by a silicon wavelength/ powerhead and a optical multimeter. Lifetime measurements are carried out under cw conditions.

Results and discussion: The advantage of the implantation-induced index guiding becomes evident by a comparison of the threshold current density of as-grown and laterally intermixed lasers. A very strong decrease of the threshold current density to 96 (±10) A/cm^2 and 153 A/cm^2 is observed for such laterally structured implanted lasers. This reduction leads to values of the threshold current density even lower than the best value of 176 A/cm^2, reported for homoepitaxially grown II-VI quantum well lasers by Katayama et al. [10]. The reduction of the threshold current density is accompanied by an increase of the slope of the L-I characteristics. For implanted lasers we obtain an increase of the differential quantum efficiency from 2.9 % to 4.1 % for ZnCdSe-lasers, and from 4.0 % to 9.1 %, respectively [11, 12].
Far field patterns were recorded for different operation currents. An almost homogenous illumination of the CCD camera was recorded below the threshold current density. For implanted lasers we observed a reduced number of higher modes during laser operation even for currents seven times above the threshold. This constant emission characteristic is induced by the lateral index-guiding generated by IID.
Due to the more efficient operation of the implanted lasers, IID also lead to an increased device lifetime. The total lifetime under cw-operation slightly above the threshold current was at least doubled.

Conclusions: We demonstrated laterally index-guided lasers generated by a structured implantation-induced disordering. A reduction of the threshold current density down to 96 A/cm^2 are achieved and the corresponding differential quantum efficiency is doubled up to 9.1 %. The obtained results reveal the potential to achieve commercially relevant lifetimes of green lasers.

Acknowledgements: The authors appreciate expert assistance of Dr. Johann Krauser (Hahn-Meitner-Institute, Berlin) for ion implantation and support by the Deutsche Forschungsgemeinschaft (DFG).

References

[1] Kato, E., Noguchi, H., Nagai, M., Okuyama, H., Kijima, S., and Ishibashi, A.:
Elec. Lett. 34, 1998, p. 282
[2] Ishibashi, A.:
J. Cryst. Growth 159, 1996, p. 555

[3] Kijima, S., Okuyama, H., Sanaka, Y., Kobayashi, T., Tomiya, A., and Ishibashi, A.:
Appl. Phys. Lett. 73, 1998, p.235
[4] Holonyak, Jr., N.: U.S. Patent 4 511 408 (1985), see also Deppe, D.G., Guido, L.J., Holonyak, Jr., N., Hsieh, K.C., Burnham, R.D., Thornton, R.L., and Paoli, T.:
Appl. Phys. Lett. 49, 1986, p. 510
[5] Yokogawa, T., Merz, J., Luo, H., Furdyna, J., Jau, S., Kuttler, M., and Bimberg, D.:
Jpn. J. Appl. Phys. 34, 1995, p. 1159
[6] Kuttler, M., Straßburg, M., Türck, V., Engelhardt, R., Pohl, U.W., Bimberg, D., Behringer, M., Hommel, D., Nürnberger, J., and Landwehr, G.:
J. Cryst. Growth 184/185, 1998, p. 566
[7] Schulz, O., Strassburg, M., Pohl, U.W., Bimberg, D., Itoh, S., Nakano, K., Ishibashi, A., Klude, M., and Hommel, D.:
Phys. stat. sol. (a) 180, 2000, p. 213
[8] Kuttler, M., Straßburg, M., Türck, W., Pohl, U.W., Bimberg, D., Kurtz, E., Landwehr, G., and Hommel, D.: Appl. Phys. Lett. 69, 2647 (1996), see also Kuttler, M., Straßburg, M., Stier, O., Heitz, R., Pohl, U.W., Bimberg, D., Kurtz, E., Nürnberger, J., Behringer, M., and Hommel, D.:
Appl. Phys. Lett. 71, 1997, p. 243
[9] Straßburg, M., Kuttler, M., Pohl, U.W., Bimberg, D., Behringer, M., and Hommel, D.:
Proc. 2nd ISBLLED, 1998, p. 425
[10] Katayama, K., Yao, H., Nakanishi, F., Doi, H., Saegusa, A., Okuda, N., Yamada, T., Matsubara, H., Irikura, M., Matsuoka, T., Takebe, T., Ishine, S., and Shirakawa, T.:
Appl. Phys. Lett. 73, 1998, p. 102
[11] Agrawal, G.P., Dutta, N.K.:
Semiconductor Lasers, van Nostrand Reinhold, New York, 1993
[12] Strassburg, M., Schulz, O., Pohl, U.W., Bimberg, D., Itoh, S., Nakano, K., Ishibashi, A., Klu-de, M., and Hommel, D.:
IEEE J. Select. Topics Quant. Electr. 7, 2001, p. 371

O. Schulz, T. Rissom, M. Straßburg, U.W. Pohl, D. Bimberg (Technische Universität Berlin);
M. Klude, D. Hommel (Universität Bremen);
S. Itoh, K. Nakano, and A. Ishibashi (Sony Corporation, Tokyo, Japan) in collaboration with the department SF4 (HMI).
(SF4.05b ISL Accelerator Operations)

NAA-Laboratory and Irradiation Service at BER II

The laboratory for neutron activation analysis (NAAL) at the BER II provides radiation services for universities, scientific institutions and industry. Typical fields of applications are:

- Trace elements analysis with neutron activation analysis (NAA) for example in biology, medicine, geology and archeology. Certification of reference materials.
- Irradiation experiments, such as isotope production for medical applications, sources for Mößbauer spectroscopy and production of tracers for industrial applications.

The operation and further development of the irradiation devices at BER II and of the NAA measuring systems are a central task of the department SF6.

Irradiation devices

Four irradiation devices are available for different applications.

DBVK: rotatable irradiation device in the reactor core
DBVR: rotatable irradiation device in the Be-reflector of the reactor core
TBR: dry irradiation device outside the Be-reflector
SRT: fast rabbit system

DBVK and DBVR are used for long term irradiation experiments. Up to nine aluminium containers can be irradiated simultaneously.
Short time irradiation experiments are carried out by means of TBR and SRT.

Device	$\Phi_{thermal}$ [1/cm^{2}s]	Φ_{fast} [1/cm^{2}s]	Containers
DBVK	1,5E+14	4,3E+13	9
DBVR	7,5E+12	1,9E+10	9
TBR	3,4E+12	2,2E+10	1
SRT	4,4E+11	3,9E+10	1

In 2001 extensive neutron flux measurements in the irradiation devices DBVK and DBVR have been performed in collaboration with the Radiochemistry Department of the TU München. The aim of the study was to find out whether in these devices quantitative element determination by NAA can be carried out by means of the k_0-method. In this procedure the multi-element standards are replaced by a neutron flux monitor and the levels of the elements to be determined are calculated from the nuclear data of their isotopes and the neutron flux during activation. This approach requires a constant, well-known neutron spectrum. The results showed that in the case of the DBVK corrections have to be made which account for the changes in the neutron spectrum during the relatively slow transport of the samples to and from the irradiation position.

Irradiation experiments 2001

A total of 1762 samples were irradiated in 2001. 60 % of the irradiation experiments, are performed with the DBVK or DBVR. With these devices it is possible to irradiate up to 24 samples simultaneously in one aluminium container.

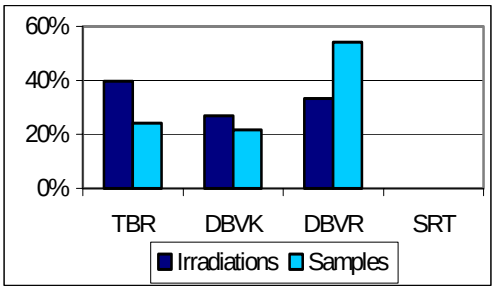

Fig. 1: Use of the irradiation devices in 2001. During 277 irradiations with DBVK, DBVR and TBR totally 1762 samples were irradiated.

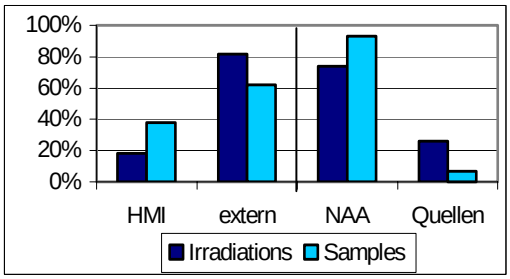

Fig. 2: Quotas of external and internal users and of neutron activation analysis and activation for different purposes

External users

Universities:
FU Berlin
HU Berlin
TU München
University München
University Marburg
University Potsdam
University Tübingen
University Mainz
University Leipzig
University Erlangen
University of Cyprus
University Modena

Research Institutes:
Rathgen Research Laboratory, Berlin
BAM, Berlin
National Institute of Health, Bethesda, USA
GSF, Neuherberg, Institute of Inhalation Biology
MPI, Marburg
IIF, Leipzig

D. Alber (SF6.01 Analysis of trace elements and metalloproteins by NAA and other methods)

Skeletal targeted radionuclide therapy with myeloablative 153Sm-EDTMP and melphalan in patients with relapsed multiple myeloma

In an attempt to intensify myeloablative treatment of multiple myeloma by adding radiation preferentially to the bone marrow, bone seeking electron-emitting agents have been proposed. First dose escalation studies in patients using [^{166}Ho]Holmium-DOTMP or [^{153}Sm]Samarium-EDTMP in combination with high-dose melphalan demonstrated a high rate of complete remissions. From the various compounds theoretically useful for such a treatment (^{90}Y-EDTMP, ^{90}Y-DOTMP, ^{153}Sm-EDTMP, ^{166}Ho-DOTMP, ^{186}Re-HEDP, ^{188}Re-HEDP) ^{153}Sm-EDTMP was preferred for such kind of treatment at the department of Nuclear Medicine of the University of Tübingen since the first studies seem to indicate, that a low energy beta-emitter is less toxic while equally effective and because of the lower renal uptake of ^{153}Sm-EDTMP compared to ^{186}Re-HEDP.

In contrast to bone pain palliation - an indication for which ^{153}Sm-EDTMP is licensed in Germany (Quadramed®, Schering, Berlin, Germany) - where a standard dose related to the body weight is given, in high dose treatment bone uptake of the radiopharmaceutical (which is quite variable) has to be determined beforehand to adjust the treatment dose in order to achieve a standardized radiation dose in the bone marrow.

First experiments using the Schering material unfortunately resulted in a dramatically reduced bone uptake of the treatment dose compared to the test-dose. This could be attributed to the difference in EDTMP injected (fig. 1). It thus turned out, that the commercial ^{153}Sm-EDTMP containing at least 24 mg EDTMP per GBq ^{153}Sm (1 day before official calibration) was not useful for high dose treatment requiring up to 100 GBq ^{153}Sm-EDTMP (50% bone uptake, 100 kg). Thus a ^{153}Sm-EDTMP with higher specific activity had to be prepared. For this purpose a EDTMP-kit (Multibone®, Iason, Graz, Austria), licensed in Hungary and Turkey for labeling with ^{153}Sm was used.

This kit contains 20 mg EDTMP and one can label up to 500 mg Sm with one vial according to the manufacturer. Since the uptake studies indicated, that 1 GBq ^{153}Sm per mg EDTMP would be sufficient to ensure good bone uptake, supply of ^{153}Sm with a specific activity of more than 40 GBq/g when arriving in Tuebingen as well as transformation of this material into $SmCl_3$ dissolved in physiological saline with neutral pH were the remaining crucial points.

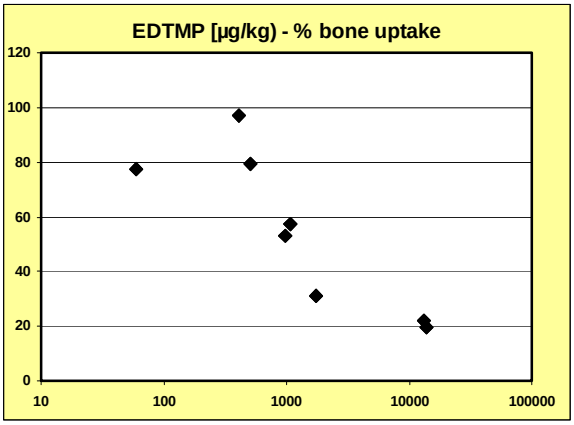

Fig.1: ^{153}Sm-EDTM uptake (y-axis) vs. amount of EDTMP injected (x-axis)

First calculations indicated that using a neutron flux of $2*10^{14}$ 1/cm^{2}s, reached in the DBVK of the research reactor at the HMI ^{153}Sm with a specific activity of about 80 GBq/mg ^{153}Sm at EOB could be produced by 3 d irradiation. Thus targets containing about 2 mg as well as lower amounts of enriched $^{152}Sm_2O_3$ were produced and test irradiations were performed confirming the previous estimates. Results are given in the following table.

Mass Sm_2O_3 [mg]	Irradiation duration [h:mm]	Activity GBq@EOB calculated	Activity GBq@EOB measured	Specific Activity GBq/mg@EOB measured
1.07	2:00	3.75	4.94	4.62
1.40	18:50	38.3	35.2	25.1
0.46	20:46	14.3	14.8	32.2
2.14	72:13	163.0	149.0	69.6
0.44	0:30	0.450	0.669	1.52
2.32	72:11	176.5	162.2	69.9

The work up of the Sm_2O_3 targets was established basing on the experience of the colleagues from the Institute of Isotopes Co. (IZOTOP) in Budapest, the manufacturer of the Multibone®-kit, who also produce ^{153}Sm (even so with lower specific activity) for labeling. Briefly the target material is dissolved in 4 ml conc. HCl, which is then evaporated at 180 °C. Thereafter the $SmCl_3$ is dissolved in 10 ml H_2O which is evaporated at 180 °C. Then the $SmCl_3$ is dissolved in 1-4 ml 0.9% NaCl for labeling. Three main problem had to be solved: Avoiding contamination during cracking of the target, avoiding destruction or irreversible binding to the vessel of the $SmCl_3$ during the work-up and limiting radiation exposure to the hands of the person performing the work-up.
Finally stable labeling yields of > 95 % using one kit per 500 mg Sm could be achieved (Fig. 2).

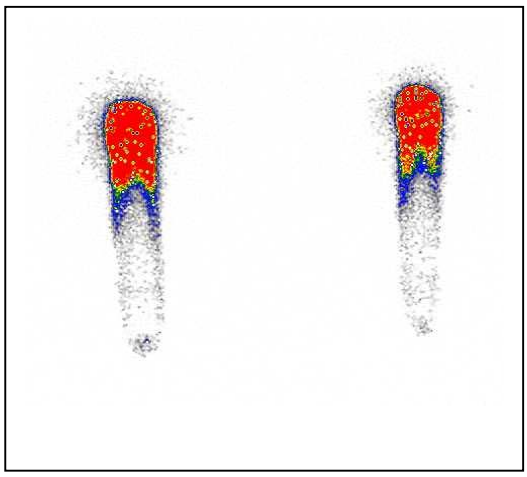

Fig. 2: ITLC of ^{153}Sm-EDTMP (Paper, PBS pH 7.4)

First applications in myeloma patients demonstrated reproducibility of the bone uptake if the amount of EDTMP was equal in test and treatment dose, as well as sufficient bone uptake (fig. 3). Myelosuppression occurred rapidly as well as initial tumor response.

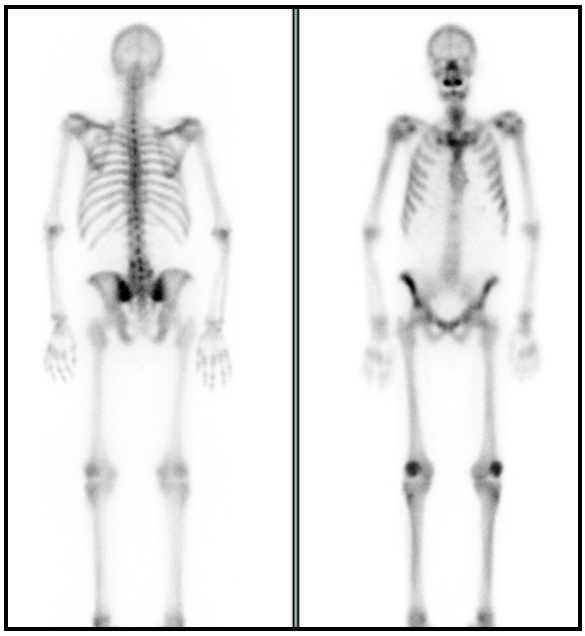

Fig. 3: Gamma camera scan of a myeloma patient 7d after administration of 55 GBq 153Sm-EDTMP (55 % bone uptake, calculated from urinary excretion)

B. M. Dohmen (University of Tübingen, Department of Nuclear Medicine) in collaboration with D. Alber (SF6.01 Analysis of trace elements and metalloproteins by NAA and other methods)

Characterization of ochres stemming from European deposits by means of INAA

Ochres or natural colored earths are the result of the weathering of rocks containing iron. Their colors range from the very clear French ochre and transparent Gold ochre to darker, more opaque shades of orange and red (Fig. 1). Due to their worldwide occurrence they are widely employed since Paleolithical times, e.g. for cave paintings, ceramics decoration, roman wall paintings, etc.

Fig. 1: Paintings samples of some ochres; 1. Bolus, Germany, 2. Terra di Sienna, burnt, Ardennes, France 3. French ochre, Vaucluse, 4. Havanna ochre, North Italy, 5. Terra di Sienna, burnt, Toscana, Italy, 6. Terra di Sienna, natural Toscana, Italy, 7. Terra di Sardegna, 8. Terra di Pozzuoli, Campania, Italy, 9. Amberg yellow, Oberfranken, Germany, 10. Gold ochre, Sachsen, Germany.

There are a lot of questions about their terminology, mineralogical origin (deposits) and manufacture process. Till now, there are no extensive studies concerning the geochemical differences between modern ochres which are used nowadays and historical European ones.

In the present study, 27 earth pigment samples from known deposits were considered: 12 of them belong to an old pigments collection of Rathgen Forschungslabor, Berlin and 15 have been offered by pigments manufactures.

Involved in this investigation were ochres from France (Ardennes, Niévre, Vaucluse), Italy (North Italy, Toscana, Sardegna, Campania) and Germany (Sachsen, Oberpfalz, Oberfranken).

INAA employed about 20mg of the samples which were irradiated in the reactor BERII. For the determination of the isotopes with short halflifes, the samples were irradiated for one or two minutes at the position of the TBR and a second irradiation was performed with the DBVR for two days. The samples were irradiated together with multi elemental standards and reference materials. After appropiate decay time, the emitted gamma-rays were measured with high purity germanium detectors.

The concentrations of 10 elements (Fe, Ti, V, Sb, Ce, Rb, Sc, Tb, Yb, Zn) were considered for statistical analyses using SPSS V8.0. like in figure 2 which shows the correlation of Zinc with Iron.

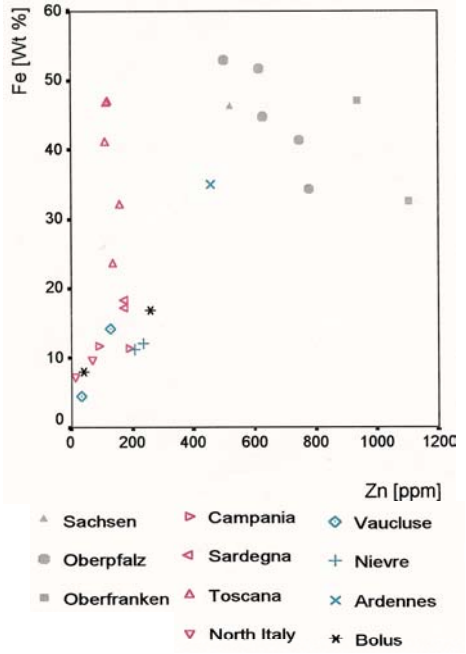

Fig. 2: Concentrations of Iron and Zinc in ochres from different geographical regions

The results demonstrated, that INAA is a suitable method to characterize pigments with different origins. The minerals of different deposits could be similar as it was put in evidence using other analythical methods: XRD, FT-IR, but some concentrations of main and trace elements remain specific.

Ochre contains iron which is found in the form of natural iron oxides, where iron is partially substituted by other transition metals like Ti, V, Zn, etc. The degree of substitution of iron with other metals is characteristic for each deposit (Fig 2).

Trace elements concentrations can be considered another characteristic of an ochre deposit. Indeed during the processing (milling, stirring, burning, etc.) the concentrations of the main elements are altered, whereas the concentrations of the trace elements are not affected.

Further studies on a greater number of samples will provide more information about the mineralogical characteristics of the ochre deposits. A systematic comparative study of European quarries, using raw pigment samples taken directly from deposit is required.

I. Behnert (Rathgen Research Institute, Berlin) in collaboration with D. Alber (SF6.01 Analysis of trace elements and metalloproteins by NAA and other methods)

Department

SF1 Methods and Instruments

New solid state neutron optical devices

Important issues for the development of neutron optical elements are the polarization and collimation of neutron beams. One of the most difficult problems is the analysis of polarization a neutron beam with a high divergence by using supermirrors. For this purpose large amounts of supermirrors are needed and the set up requires diameters of a few meters. With the solid state neutron optical elements developed at BENSC [1] this can be done in a much more compact way.

A solid state radial bender for the polarization analysis of neutrons over a wide angular range was built and tested at the reflectometer V6 and the neutron mirror instrument V 14 at BENSC [2]. It consists of a bent stack of Si wafers each of them coated with a polarizing supermirror and an absorbing layer. The stack consisted of 19 channels which were tilted against each other by an angle of 0.19°, and thus a total angular interval of 3.8° could be analyzed. There is no limitation for expanding this angle to much larger values and up to a full circle.

The device was put onto the detector arm of a reflectometer with the bending axis of the bender

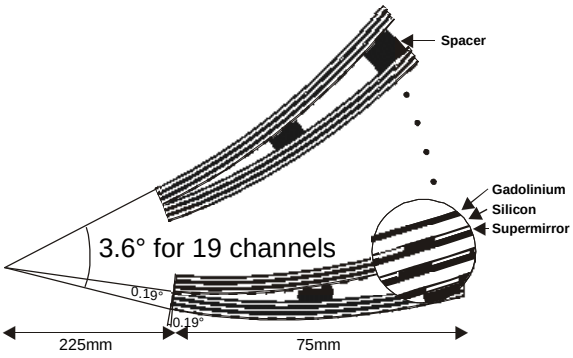

Fig. 1 Drawing of the radial bender with four of the 19 channels shown.

parallel to the sample axis. With an incoming polarization of 98.7 %, a total flipping ratio of 70, and a transmission of 60 % of the spin up component were measured.
Rotating the detector arm around the sample axis without a sample inserted shows that the expected angular range of more than 3° can be analyzed. The transmission has an angular dependence due to an imperfect mechanical set up of the bender. This effect does not occur for the direction parallel to the channels where the geometry allowed for covering a range of 9.5° to be analyzed.
With such benders neutron spins can be analyzed for very large solid angles in two dimensions for small samples.

Secondly we developed, built and tested at V14 a radial collimator. Here a supermirror coated 75 mm long collimator channel was opened at the downstream end by inserting a thin slab of a silicon wafer. Since we used a polarising supermirror as wall coating it is possible to measure the transmission of the radial collimator with purely absorbing and with reflecting walls for geometrically exactly the same set up. This could be done because the spin down component interacts with a collimator with purely

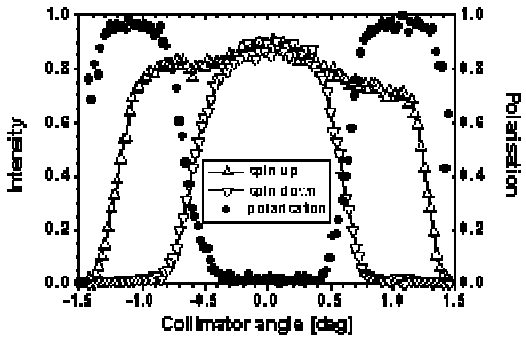

Fig. 2 Transmission coefficient for the two spin states for neutrons with a wavelength of 4.72 Å through a radial collimator channel formed by Si wafers coated with a FeCo-Si supermirror followed by a Gd layer, measured in a magnetic field of 300 Oe.

absorbing walls since the supermirror coating is transparent for it while the spin up component reacts with the supermirror coating and is reflected from the walls. Fig. 2 shows the transmission for the two spin components. The spin down component is reflected with high intensity only within an angular interval of ± 0.4° with a maximum intensity at 0° because this is where the lowest amount of silicon is in the flight path. Beyond 0.4° the intensity drops to zero at an angle of ± 0.78°. The spin up component interacts with the walls which reflect it up to 1°. Due to the wall inclination of ± 0.37° neutrons are transmitted up to ± 1.37°. The transmitted intensity is 89 % at 0° and drops to about 75 % at the critical angle of the supermirror.

Such solid state neutron optical devices, including also non radial benders and collimators which were developed in the last years, are smaller and lighter than their conventional counterparts. They have very well defined channels and are mechanically simple. In addition they can handle broader wavelength bands than FeCo-Si coatings which are hit by neutrons from air and hence they are better applicable at spallation sources

References

[1] Krist, Th.; Kennedy, S J; Hicks, T J; Mezei, F Physica B 241-243 (1998) 82-85

[2] Krist, Th.; Fritzsche, H. and Mezei, F. Appl. Phys. A 74 (2002) 1-3

Th. Krist, J. Hoffmann, S.-J. Cho, P. Schubert-Bischoff, F. Mezei (SF1.01 BENSC-Activities)

Software for development of new instruments, "Flight Simulator" for virtual instruments

Computer simulations play a major role in the development of modern technology, for example in the development of cars or training of pilots. Similarly, the planning and design process of neutron instruments or entire neutron facilities needs to be based on detailed and accurate "neutron-flight simulation" studies in order to be able to find the best solutions. By Monte Carlo (MC) methods, it is possible to build virtual neutron scattering instruments and thus obtain accurate estimates of their performance or to optimize the layout of individual components including the moderators.

In this framework the MC simulation software VITESS (Virtual instrumentation for ESS) has been developed at HMI, supported by the HGF-ESS and the SCANS projects. It consists of independently executable program components (e.g. guide, chopper, polarizer, sample, etc.) running in a pipe. The virtual instrument is built by listing the components of the real instruments and giving details of their positions and properties. This is done on a graphical user interface (GUI). It can be run on Linux, Unix, and Windows systems. The performance of VITESS is validated by comparison to other packages and experiments.

In 2001 the versions 2.0 and 2.1 of VITESS including new modules ('Fermi chopper', 'polarizer', 'flipper', 'reflectometer sample', etc), improvement of existing modules, new and extended sample instruments, and a more user friendly graphical user interface were released. Polarisation, gravity and absolute flux values were included into the simulation.

Up to now the package has been downloaded by more then 100 scientists from all over the world in order to improve existing instruments or to develop new ones on existing or planned sources.

As examples for applications, a comparison of reflectometers at different sources and target stations as well as the simulation of a polarizing beam splitter are given:

Reflectometers installed on different target stations / moderators proposed for ESS were simulated and for comparison a similar instrument at the ILL was simulated. The time needed to measure an entire D2O spectrum with a given accuracy were calculated (Fig. 1, Table 1).

Source	r=0.03	r=0.08
Reactor (ILL)	3700 s	160 s
SPSS 10 Hz, 1 MW	710 s	110 s
SPSS 50 Hz, 5 MW	170 s	25 s
LPSS 16.7 Hz, 5 MW	370 s	32 s

Table 1: Measurement times of a D_2O sample at different sources.

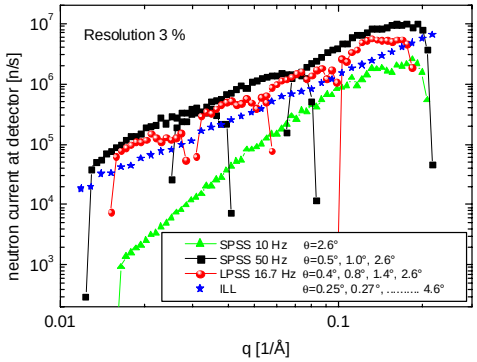

Fig. 1: Reflected neutron current from different sources as function of q at instruments of resolution 3 %, assuming a sample with total reflectivity in the whole q-range

As a result it was demonstrated that the ESS source will be superior to the best reactor sources. For high resolution reflectometers, the 50 Hz short pulse target station (SPTS) is the best choice, whereas for low resolutions the 16.7 Hz long pulse target station (LPTS) provides similar results. In both cases, the 10 Hz SPTS is the least favourable pulsed source, as its power is too low. This contributed to the decision for the long pulse station for ESS instead of the 10 Hz short pulse station.

High reflectivity supermirrors allow for sophisticated neutron optical systems which work with multiple reflections (for example polarizing cavities, beam splitters). Polarizing cavities are highly efficient broad wavelength band polarizer systems. Beam splitter polarizing cavities for example yield a practically ideal separation into one spin "up" and one spin "down" neutron beam, which can supply two different instruments (implemented at BENSC).

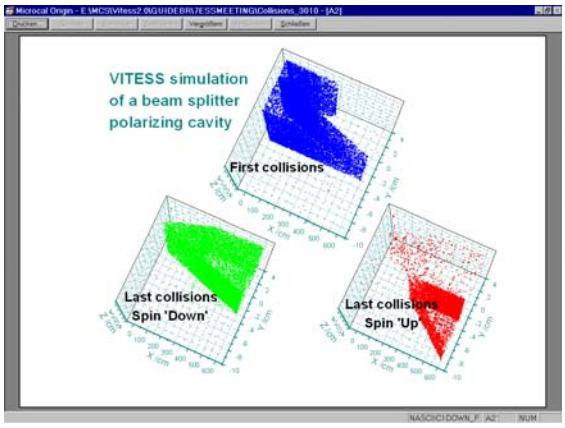

Fig. 2: Recent Monte Carlo simulations for the optimization of polarizing cavity systems and their application at ESS.

F. Mezei, K. Lieutenant, G. Zsigmond
(SF1.02 Spallation)

Critical scaling in spin glasses

The glass transition, characterized by a dramatic slowing down of the dynamics without any noticeable change in the spatial order, is a wide spread phenomenon, that affects systems as different as disordered magnets, polymers and biological substances. It is still controversial whether the glass transition is a gradual freezing or a phase transition due to a critical instability. The difficulty is the absence of an observable conventional static order parameter in the low temperature phase, a key quantity in the study of phase transitions. In this situation the observation of scaling relations, which are the direct consequence of the homogeneity hypothesis in the vicinity of a critical instability, can reveal the crucial signature of a phase transition. New Neutron Spin Echo (NSE) results provide for the first time compelling evidence for scaling relations between different physical quantities in spin glasses, which are the simplest realizations of glassy systems from the experimental as well as from the theoretical point of view.
The sample, $Au_{0.86}Fe_{0.14}$, is a classical metallic spin glass with strong ferromagnetic correlations. These correlations amplify the magnetic scattering in the forward direction and improve the signal over noise ratio. The NSE data were collected at the high resolution spectrometer IN15 of ILL and at the wide angle NSE spectrometer SPAN of BENSC.

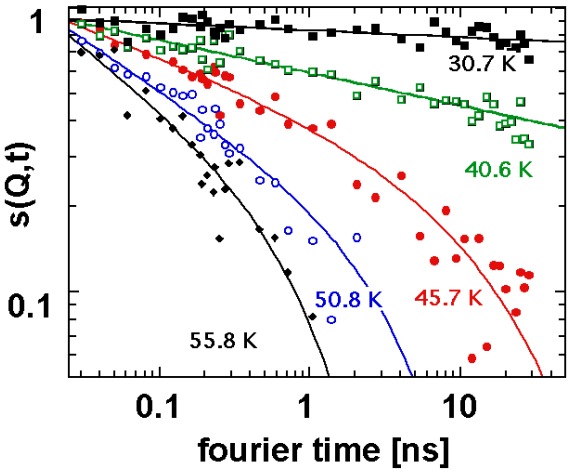

Fig. 1: Temperature dependence of the intermediate scattering function s(Q,t) of $Au_{0.86}Fe_{0.14}$. The spectra were collected at Q = 0.04 Å^{-1} at the Neutron Spin Echo spectrometer IN15 (ILL).

Fig. 1 shows the intermediate scattering function s(Q,t) of $Au_{0.86}Fe_{0.14}$ at Q = 0.04 Å^{-1} plotted in a log-log scale. The spectra span a dynamic range of three orders of magnitude and the time dependence of s(Q,t) is impressively similar to that found in large scale simulations, revealing a phase transition in three-dimensional Ising spin glasses. The simulations showed that, as T_g is approached from above S(Q=0, t) is strongly non-exponential and its decay is well described by the so-called Ogielski function, an empirical formula $t^{-x}\exp((-t/\tau(T))^{\beta})$ with β tending to 1/3. The most important point of further data analysis is, however, dynamic scaling, which predicts a simple power law decay t^{-x} with $x = (d-2+\eta)/2z$, where d is the system dimensionality, η the static Fisher exponent and z the dynamic exponent. Scaling thus relates exponents determined by completely independent dynamic and non-linear macroscopic susceptibility measurements.

For $T \le T_g$ we found $s(Q,t) \propto t^{-x}$ and the lines on Fig, 1 represent the best fits to the data with x=0.116±0.007 and 0.025±0.005 at T=40.6(~T_g) and 30.7 K, respectively. Above T_g, the power law decay holds only at short times and the data are well described by the Ogielski function shown by the continuous lines. The simple power law decay found at and below T_g was confirmed by revisiting historical CuMn 5 % results. Below T_g, the spectra of CuMn 5 % were combined with macroscopic dynamic (ac) susceptibility measurements. These data also show a power law decay below T_g~27,5K, which extends over an impressively large range of at least 9 orders of magnitude in time as shown in Fig. 2.

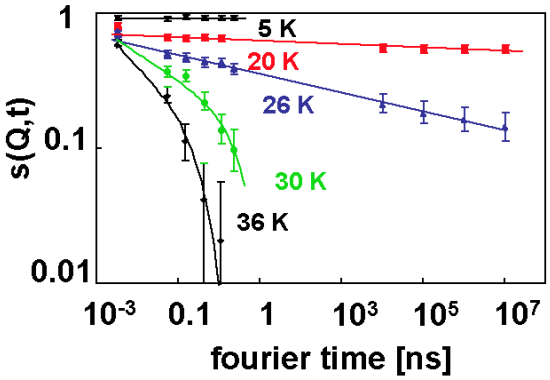

Fig. 2: *Revisiting historical s(Q,t) data on CuMn 5%. The continuous lines correspond to a simple power law decay below T_g and to the Ogielski function above T_g.*

Most remarkably the observed exponent x≈0.12 is in full agreement with the value predicted by critical scaling.
These results represent the first verification of scaling in spin glasses relating quantities of very different nature and measured by different methods on very different time scales. This agreement is a most compelling evidence for a phase transition in spin glasses at T_g. In addition, the existence of a phase transition also implies that the non-exponential temporal relaxation in these spin glasses is an intrinsic, homogeneous feature.

C. Pappas, F. Mezei, G. Ehlers, I.A. Campbel
(SF1.03 Collective Dynamics and Diffusion)

Stability and flexibility of proteins in solution

Biologically functional proteins, in a sufficiently hydrated state or in aqueous solution, have a unique three-dimensionally folded structure, which is stable under physiological conditions like temperature, pressure, hydration, salinity, etc., but becomes unstable if the environmental conditions are changed sufficiently, and undergoes a transition from the folded (F) to the unfolded (U) state. Some organisms, so-called extremophiles, live preferentially under extreme environmental conditions. Thermophilic bacteria, for instance, which live at temperatures from 70 °C to above 100 °C, produce proteins known as thermozymes which are adapted to these comparatively high temperatures. Because they do not unfold under these conditions, they remain functional, whereas at lower temperatures they are often less active. Contrary to this, mesophilic homologues having similar folded structure and high sequence homology, start to unfold near 60 °C and therefore loose functionality already at this lower temperature. Increased thermostability has not only been related to specific structural features such as shorter loop regions, additional hydrogen bonds and salt bridges or stronger internal hydrophobicity, but also to dynamic properties. The change of conformational entropy ΔS during the unfolding transition is directly related to the difference between dynamical fluctuations of folded and unfolded states. We have employed quasielastic neutron scattering (QENS) techniques,

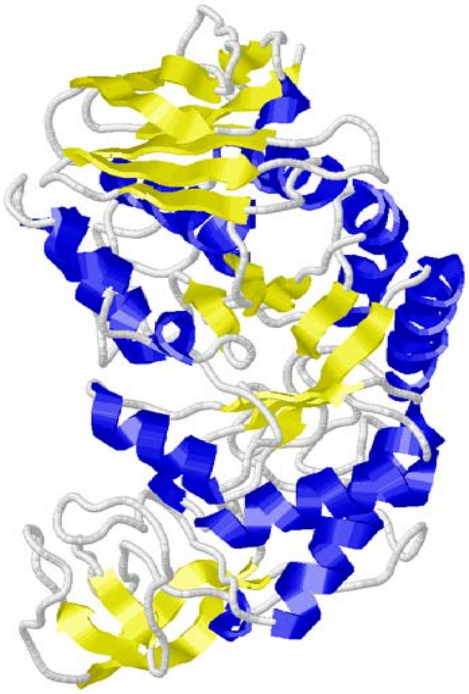

Fig. 1: Structure of the thermophilic enzyme α-amylase from Bacillus licheniformis (BLA; PDB-entry: 1BLI).

in order to compare the dynamic properties of a mesophilic (BAA) and a thermophilic (BLA) α-amylase on the pico-second time scale. Internal molecular equilibrium fluctuations have been studied in

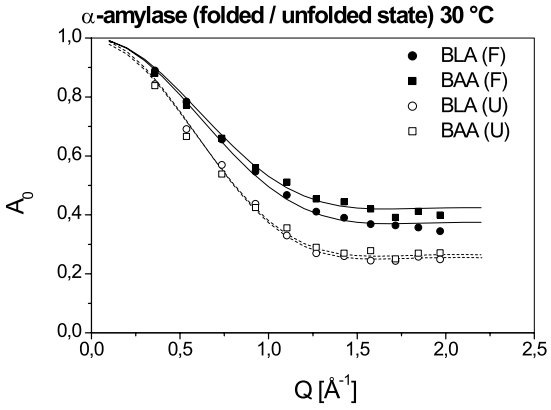

Fig. 2: EISFs (A_0) as a function of momentum transfer Q for both enzymes, BLA and BAA, at 30°C, in the folded (F) and unfolded (U) states.

solutions of the two α-amylase homologues, to investigate the relationship between thermal stability and internal equilibrium fluctuations. Fairly similar rates of slowly exchanging amide protons indicate approximately the same free energy of stabilization ΔG_{stab} for both enzymes. The QENS data shown in Fig. 2 concern however the much faster pico-second dynamics of the folded states at room temperature. With respect to motions on these shorter time scales, the thermophilic enzyme is characterized by an unexpected higher flexibility as compared to the mesophilic counterpart. In particular the pico-second dynamics revealed a higher degree of conformational freedom for the thermophilic α-amylase [1].
Compared to the mesophilic homologue, the results indicate a higher conformational entropy (resulting in a lower EISF [2], see Fig. 2) of the folded state and thus a smaller ΔS of unfolding for the thermophilic enzyme. We have therefore proposed a new mechanism as the reason for a higher temperature of unfolding, i.e. for higher thermal stability. This mechanism is characterized by entropic stabilization and by a flattening of the curvature of ΔG_{stab} as a function of temperature.

References
[1] J. Fitter, R. Herrmann, T. Hauß, R. E. Lechner, N. A. Dencher, Physica B 301, 1-7 (2001)

[2] R. E. Lechner, in: J. Colmenero, A. Alegría and F. J. Bermejo (Eds.), Proceedings of the Quasielastic Neutron Scattering Workshop QENS'93, San Sebastián, Spain 1993 (World Scientific, Singapore 1994) pp. 62-92.

J. Fitter, R. Herrmann, N. A. Dencher, Inst. für Biochemie, Techn. Univ. Darmstadt; T. Hauß, Inst. f. Phys. Biol., Universität Düsseldorf; in co-operation with R. E. Lechner
(SF1.03b Diffusion and material transport in condensed matter)

Self-assembly of biological model systems

Controlled design of supported lipid bilayers which serve as models for biomembranes is a central challenge for the development of biosensors [1]. These bilayers are also excellent tools for basic biophysical studies on the interaction of membranes with interfaces or structural changes as effected by membrane active molecules (proteins, DNA, detergents). Under optimal conditions a hybrid biomembrane of a polymer adsorbed lipid monolayer, resembling a soft membrane surface with an aqueous interface, and a free floating lipid bilayer in the fluid state may be obtained (Fig.1). We were able to successfully assemble in a first step a hybride biomembrane system via fusion of small uni-lamellar vesicles to polymer-coated substrates (silicon single crystals). The self-assembly process of this membrane at the solid-liquid interface was monitored in situ by neutron reflectometry [2] and the recorded reflectivity curves were analyzed on the basis of a multilayer model for the refractive index taking the data step by step. By contrast variation via D_2O/H_2O exchange and the use of deuterated components (e.g. d54-DMPC, d-PS) the experimental resolution could be distinctively enhanced. We found that a first lipid monolayer (DMPC) of 16 Å thickness was irreversibly adsorbed to the hydrophobic polymer cushion (polystyrene, PS) from aqueous solution of the vesicles within 8h. This layer was then covered by another lipid bilayer (d=32 Å) in a very slow diffusion governed process. No further adsorbed layers were observed within 4 weeks.

On the basis of the above results, we conducted first neutron reflectivity experiments on a more complex system, namely on the interaction of a membrane active peptide (amyloid-β) from solution with the precursor of the hybrid biomembrane, i.e. a d54-DMPC monolayer adsorbed to a hydrophobic d-PS cushion. The experiments were motivated by current neutron diffraction studies on the interaction of the neurotoxic β-amyloid peptide, Aβ (25-35) where the C-terminus of the peptide was located in the core of the phospholipid bilayers, in the case of stacked lipid multilayers [3]. The neutron reflectivity experiments were especially designed to gain further information on the adsorption of Aß to lipid membranes under as close as possible physiological conditions. Thus the contrast scenario of the neutron reflectivity experiments was chosen to highlight the protonated peptide. Therefore, we prepared a spin-coated polymer film (d=292 Å) of deuterated polystyrene (d-PS) on a silicon block and adsorbed a monolayer (d=17 Å) of deuterated lipids (d54-DMPC) from a solution of small unilamellar vesicles (0.58 mg/ml) to it. The polymer supported lipid layer was almost invisible against D_2O (Fig. 2, top: the Kiessig interference fringes of the hybrid membrane are very much suppressed due to a lack of contrast at the membrane/liquid interface. The situation changed after injection of Aß into the liquid subphase (Fig. 2, bottom). Fig. 2 shows that mainly the amplitude of the Kiessig oscillations increased while there was no significant change of the minima positions. This proofs directly that Aß is

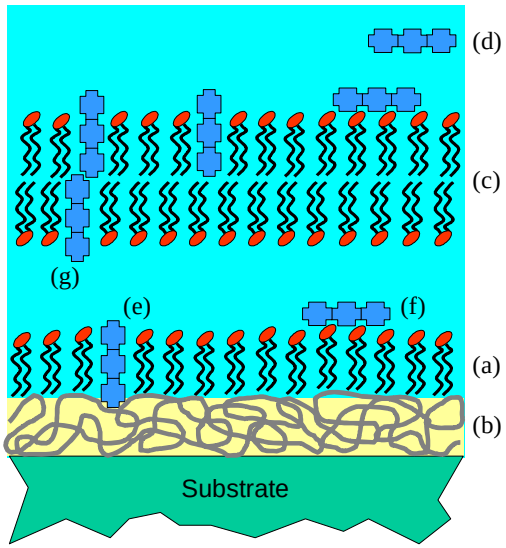

Fig. 1: Schematic diagram illustrating a supported lipid monolayer (a) on a polymer cushion (b) in equilibrium with a free floating lipid bilayer (c) at the solid-liquid interface. Different possible binding sites (e-g) of a water soluble peptide (d) are indicated.

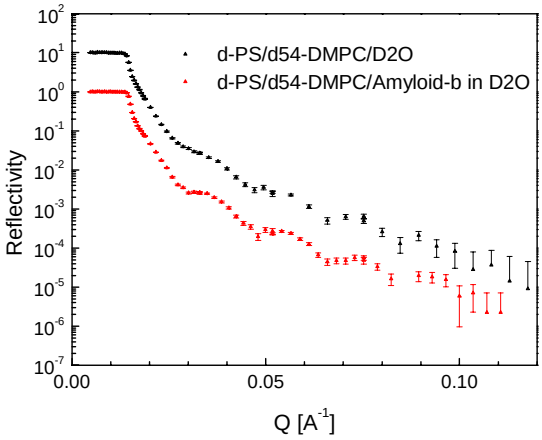

Fig. 2: Neutron reflectivity of the polymer supported lipid layer against the liquid phase before and after binding of Aβ. The curves are offset on the y-axis for clarity.

not adsorbed to but inserted into the polymer supported lipid layer, such as depicted in Fig.1, situation (e).

References

[1] E. Sackmann, Science, 271, 43-48 (1996)

[2] T. Gutberlet, R. Steitz, J. Howse, I. Estrela-Lopis and B. Klösgen, Applied Physics A, accepted for publication (Sep. 2001)

[3] S. Dante, T. Hauß, N. A. Dencher, Biophysical Journal, submitted (2002)

R. Steitz, S. Dante T. Gutberlet, T. Hauß, B. Klösgen, S. Schemmel
(SF1.03c Superstructures and competitive Interactions)

Heuristic reconstruction of porous matter

Neutron scattering techniques allow the quasi direct observation of adsorption and condensation in porous solids. The final goal of this work is the three-dimensional simulation of these phenomena by use of neutron scattering data.

The first step towards this goal is the 3D reconstruction of the mesoporous solid. A binary 3D model, the bits of which represent a random distribution of the two phases of the material, is subjected to an evolution process: random interchanges of the phases are assessed and selected according to “material descriptors” until, by and by, the model is adapted to these descriptors, which are of statistic nature and which are derived from experiments. As an example, Fig. 1a depicts the reconstruction for a two-point probability distribution which was calculated from the SANS data of a mesoporous silica-gel by autocorrelation. As a second descriptor the pore-size distribution was used (Fig. 1b).

It was deduced by means of the “non-local density-functional theory” from measurements of the sample’s nitrogen uptakes under varying pressure (provided by BAM for the nitrogen boiling-point). Conjointly, the descriptors force the evolution algorithm to reconstruct the pore structure as shown in Fig. 2; it is considered a statistically relevant model of the real material and can be used, for instance, to calculate characteristic parameters such as the mean value of the wall thickness or the interface of the phases with respect to size and shape.

Evolutionary reconstruction by means of statistical descriptors is a general method which can be adapted to various optimization tasks. Unfortunately, “blind” evolution suffers from its enormous time consumption. Therefore we studied heuristic control criteria; i.e. general strategies of mutation and selection, or applicationspecific thumbrules to reduce the time consumption by restricting the search space. For the reconstruction of porous matter, the “neighborhood heuristics” proved to be particularly efficient; it avoids generating isolated single bits thus reducing the run-time by roughly two orders of magnitude (from days to hours on a modern PC).

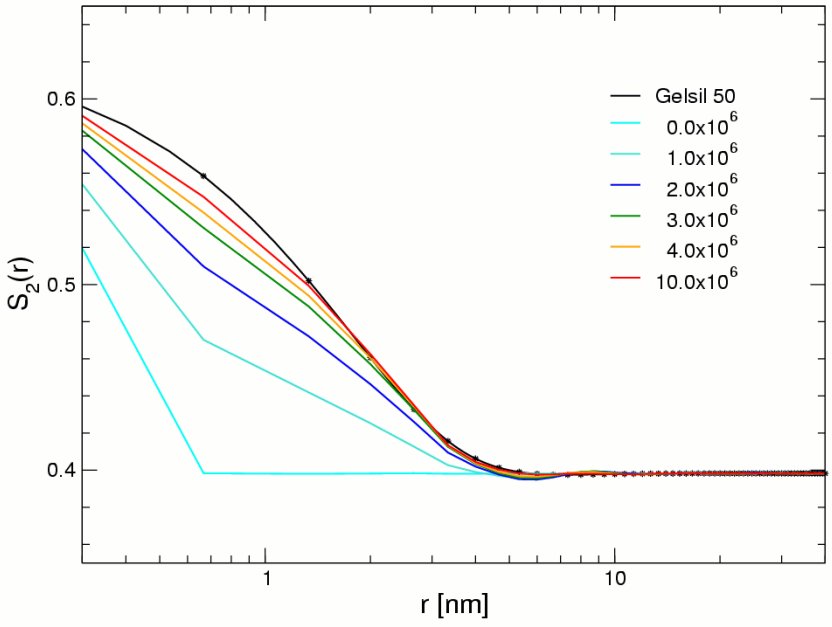

(a)

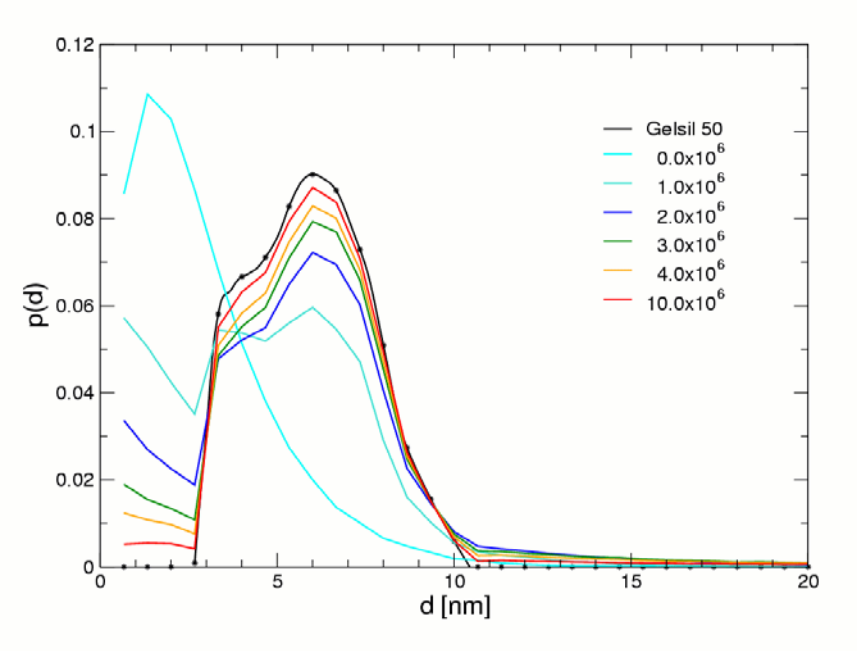

(b)

Fig. 1: Simultaneous approximation of statistical descriptors during the reconstruction of Gelsil-50:
(a) two-point probability distribution (black) as calculated from small-angle neutron-scattering;
(b) pore-size distribution (black) as deduced from the nitrogen adsorption-isotherm measured at the nitrogen boiling point. The evolution starts from the blue curves; after 10 million mutations, the reconstructed pore structure exhibits the red distributions, i.e. a best approximation of the pore structure with respect to the two descriptors is achieved within acceptable error bounds.

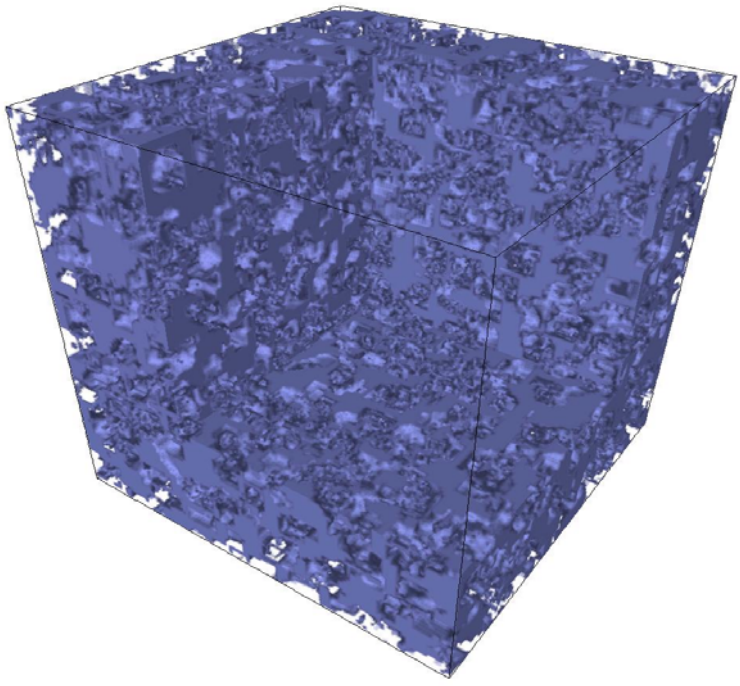

.

Fig. 2: Binary 3D model of the pore structure as reconstructed by an evolution strategy that adapts the model to the statistical descriptors of Fig. 1. The model uses 1203 bits to represent a Gelsil-50 cube of 80 nm edge-length.

N. Eschricht, F. Mädler (Subdivision Information Technology) in collaboration with E. Hoinkis
(SF1.03b Diffusion and material transport in condensed matter)

Department

SF2 Magnetism

Magnetic phase diagram and chirality of the frustrated antiferromagnet $CsCuCl_3$ in Fields up to 17 Tesla

The nature of phase transitions of frustrated systems can be novel and different to that of phase transitions of conventional unfrustrated magnets. Geometrical frustration is e.g. realized in systems with an antiferromagnetic coupling of adjacent spins arranged on a triangular lattice. Hexagonal $CsCuCl_3$ is one of these systems with the triangular lattice in the *ab*-plane. It is not possible to minimize all interactions individually and a canted 120° spin structure is formed on each triangular plaquette. A consequence of the canted spin structure is the appearance of a chiral degree of freedom where one has a twofold degeneracy according to a possible right or left handed rotation of the spins on the basic triangle as shown in Fig. 1.

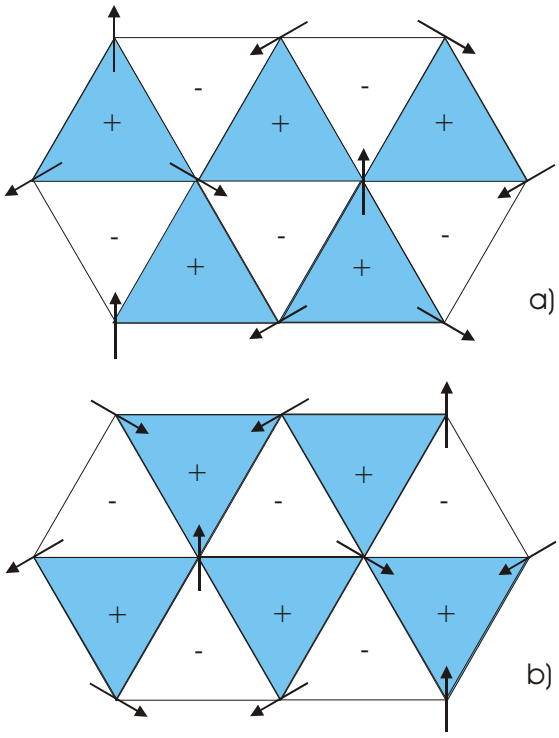

Fig.1: 120° spin structure of frustrated triangular-lattice antiferromagnet. Opposite chirality are as shown in a) and b).

The magnetic interaction along the *c*-axis is predominantly ferromagnetic and an additional Dzyaloshinskii-Moriya interaction – possible by the low symmetry in the local structure due to a Jahn-Teller distortion – accounts for an incommensurate magnetic helix in the *c* direction. Anomalies in the field-dependent magnetization at low temperatures stimulated many experimental and theoretical studies during the last decade. It is now understood that these anomalies, which cannot be accounted for by classical theory, are a consequence of quantum fluctuations at low temperatures and thermal fluctuations at higher temperatures [1]. Therefore, $CsCuCl_3$ is one of the rare systems where extraordinarily large effects of fluctuations on the magnetic structure can be studied. In particular, the phase diagrams in the H-T plane show various magnetic structures which, in addition, depend strongly on the direction of the applied field. During the last year the availability of the superconducting VM1 magnet together with the Dysprosium booster enabled us to study the magnetic phases by magnetic neutron diffraction applying fields to a single crystal in the *ab*-plane up to field strengths of 17 Tesla. The complete phase diagram obtained is shown in Fig.2. We observe four different magnetic phases below 10.65 K. The three phases below 16-17 Tesla are incommensurate and a commensurate spin arrangement is observed only for high fields.

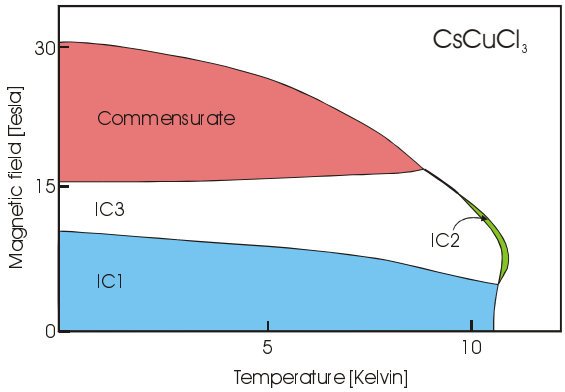

Fig. 2: Magnetic phase diagram of $CsCuCl_3$ with the field in the ab-plane. IC1, IC2, and IC3 indicate different incommensurate structures. The structure of phase IC2 was studied earlier [2].

IC1 phase

In zero field, magnetic Bragg intensities can be detected at 1/3 1/3 *Q* originating from the triangular spin arrangement in the *ab* plane tripling the unit cell and the regular spiral along *c*. As already studied earlier the value of *Q* decreases continuously with applied field and new magnetic satellites occur at 1/3 1/3 2*Q*. This behaviour reflects the elongation of the spirals and a distortion where spins close to the field direction move together and spins opposite to the field spread apart. Our recent experiments demonstrate clearly that the average ordered moment increases with applied field. At the lowest temperatures this may be explained by the fact that the ordered spins on the triangular frustrated lattice suffer a large moment reduction which becomes partially lifted by the applied field. At higher temperatures the rise in intensity is much more pronounced and one has to consider a reduction of the thermal fluctuations by the field as well.

IC3 phase

All our observations point to a qualitative change of the spin structure above roughly 1/3 of the saturation field: the value of *Q* for the magnetic Bragg reflections at 1/3 1/3 *Q* and 1/3 1/3 2*Q* becomes nearly independent on the field (in the central part of

IC3), the intensity ratio I(1/3 1/3 *Q*)/I(1/3 1/3 2*Q*) stays roughly constant, and the magnetization increases with a reduced slope d*M*/d*H* in comparison to the behaviour in IC1. Up to now we were not successful to distinguish between different models proposed for the spin structure within phase IC3. A very interesting feature is the observation of an asymmetry generally above 14.5 Tesla in the peak intensities of the reflections at 1/3 1/3 *Q* and 1/3 1/3 -*Q* observed when approaching the commensurate phase as shown in Fig.3. The same asymmetry is still present after one has cycled through the commensurate phase and remains upon field reduction even down to zero field. The asymmetry only vanishes after heating above and subsequently cooling below the magnetic ordering temperature. We relate the observed asymmetry to a domain effect of the chirality within the *ab*-plane. The magnetic spiral in $CsCuCl_3$ is characterized by a so-called propagation vector [1/3 1/3 *Q*] where the z-component *Q* is determined by the sense of rotation of the spins along the hexagonal chain axis. This "chain chirality" should be fixed to the crystal structure i.e. to the Jahn-Teller distortion. Therefore, our observations which cannot distinguish between [1/3 1/3 *Q*] and [-1/3 -1/3 -*Q*] indicate a change in the distribution of domains related to different chiralities on the triangular lattice in the *ab*-plane induced by the applied field. A similar domain effect was reported for $CsMnBr_3$, however, by using polarized neutrons.

C-phase

In the commensurate phase all spins along the *c*-axis are aligned ferromagnetically. The spins in the *ab*-plane still occupy three different sublattices.
The phase diagram derived from our neutron diffraction experiments at $CsCuCl_3$ resembles that of frustrated ferromagnetically stacked TLA systems [3] surprisingly well, despite the fact that the magnetic structure of $CsCuCl_3$ is more complex due to the Dzyaloshinskii-Moriya interaction. We clearly find a lifting of the moment reduction by the applied field. These effects which have not yet been considered theoretically in these systems will be studied in more detail in the next future. The domain effects evident in the asymmetric peak intensities apparently make "chirality" visible for the first time with unpolarized neutrons in these systems [4]. This can open new possibilities to study the field dependence of chirality in order to get a better understanding of the nature of the phase transitions and the new chiral universality class.

References

[1] Nikuni, T., Jacobs, A.E.: Phys. Rev.B57,1998, 5205

[2] Schotte, U.; Kelnberger, A., Stüßer, N.: J. Phys.: Cond. Mat.10,1998, pp.6391-6404

[3] Suzuki, N.; Matsubara, F.: Phys. Rev.B55,1997, 12331

[4] Stüßer, N., et al., J. Phys.:Cond. Mat., in press

N. Stüßer, U. Schotte, A. Hoser
(SF2.01 Bulk Magnetism)

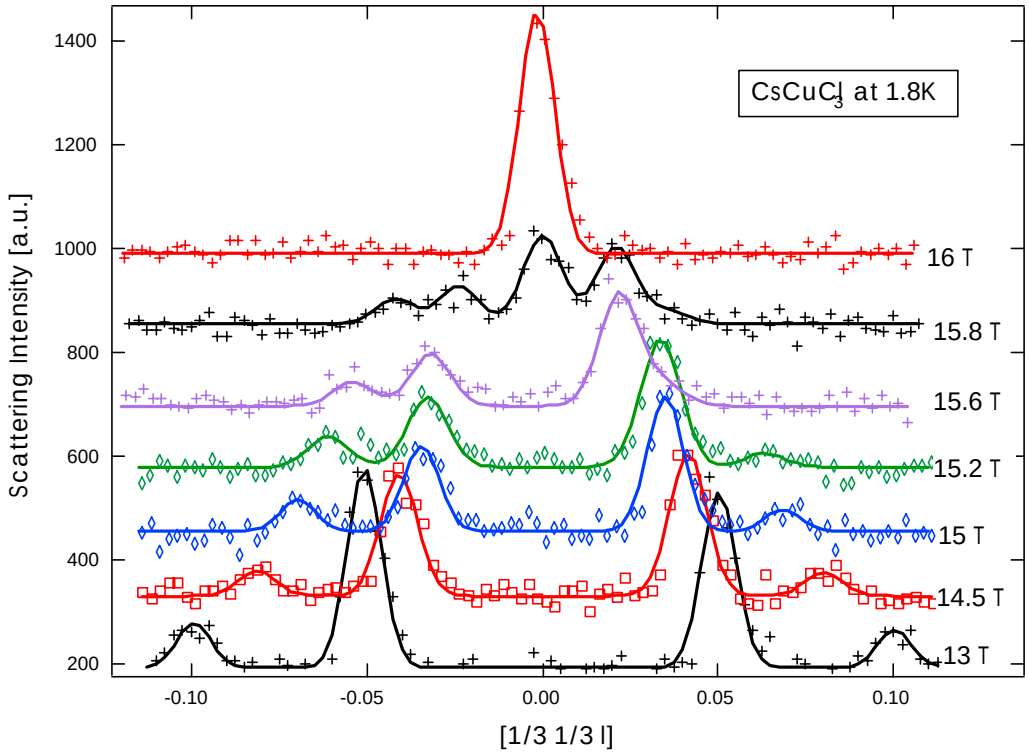

Fig. 3: Diffraction patterns along [1/3 1/3 l] close to the IC-C phase transition. Asymmetry in peak intensities is clearly visible with increasing field.

Coexistence of magnetism and charge density wave in $Er_5Ir_4Si_{10}$ – a combined neutron and X-ray diffraction study

The tetragonal 5-4-10 series of intermetallic rare-earth (RE) compounds $RE_5Ir_4Si_{10}$ all show a charge density wave (CDW) ordering at about 100 K [1]. It has been shown by high intensity x-ray diffraction on single crystals, that the CDW order occurs along the *c*-axis in the case of $Lu_5Ir_4Si_{10}$ [2] and of $Er_5Ir_4Si_{10}$ [3]. In addition, for the magnetic rare-earth ions magnetic ordering is found around 3 K. Since the magnetic interactions are carried by the conduction electrons, which in turn take part in the CDW, it is interesting to investigate the possible interplay between the CDW and the magnetic order.

Here, we present a combined neutron and X-ray diffraction study on $Er_5Ir_4Si_{10}$. We were able to prove for the first time that both cooperative ordering phenomena coexist with no apparent interaction.

In $Er_5Ir_4Si_{10}$ the CDW transition at 155 K involves the development of a combined commensurate [**q**=(0,0,1/2)] and incommensurate [**q**=(0,0,1/4±δ)] superlattice. Upon cooling below 55 K the incommensurate CDW locks-in (δ=0), leading to a superstructure of periodicity 4**c* along the *c* axis. On further cooling, $Er_5Ir_4Si_{10}$ exhibits two successive magnetic transitions at T_{N1} = 2.8 K and T_{N2} = 1.4 K [3]. We have determined the magnetically ordered structure below 2.8 K by neutron diffraction on powder and single crystal samples using the diffractometers E2 and E6 at BENSC [4]. Several magnetic Bragg reflections of type (h/2 k/2 0) are observed, yielding a doubling of the unit cell in the basal plane, i.e., perpendicular to the CDW. The corresponding magnetic structure is depicted in Fig. 1. Detailed data analysis yields different values for the ordered moments on the inequivalent Er positions. Single crystal diffraction data taken at 0.07 K indicate additional weak magnetic reflections of type (h/4 k/4 0) and hence another doubling of the magnetic unit cell in the basal plane below T_{N2}.

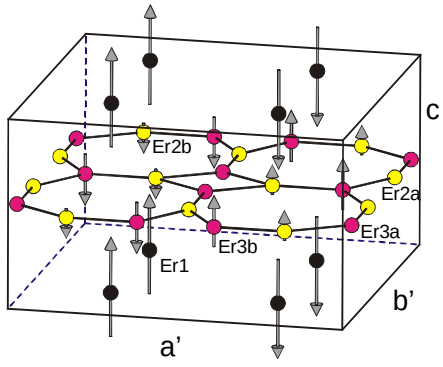

Fig. 1: Magnetic structure model for antiferro-magnetic $Er_5Ir_4Si_{10}$ below 2.8 K as determined by neutron diffraction at BENSC. Only Er ions are shown. The ordered moments are $|\mu|$ = 9.0, 1.4, 2.0 μ_B for Er1, 2b, 3b, respectively. For symmetry reasons, the moments on Er 2a and 3a are zero.

In order to check for the coexistence of CDW and magnetic ordering, we have carried out combined resonant magnetic X-ray scattering and X-ray diffraction on a single crystal of $Er_5Ir_4Si_{10}$ at the Xmas beamline (BM28) at the ESRF, Grenoble.

Choosing an energy of the incident X-rays of 8.361 keV, i.e. at the L_{II}-edge of Er, we were able to identify a few Bragg reflections of magnetic origin like (3/2,3/2,0) below T_{N1}. We have determined the temperature dependence of the intensity of these reflections and of several CDW superlattice reflections, like (4,4,1/4) between 1.7 K and 4 K. The results are shown in Fig. 2. The intensity of the magnetic Bragg reflections observed by X-rays resembles the curve determined before by neutron diffraction [4] and vanishes above T_{N1} = 2.8 K. In contrast, the intensities of the CDW superstructure reflections are constant when passing the magnetic transition. Since both data sets have been taken on the same crystal in the same experiment, this unambiguously shows that the CDW superstructure coexists with the magnetic ordering and that it is unaffected by the magnetic transition [5].

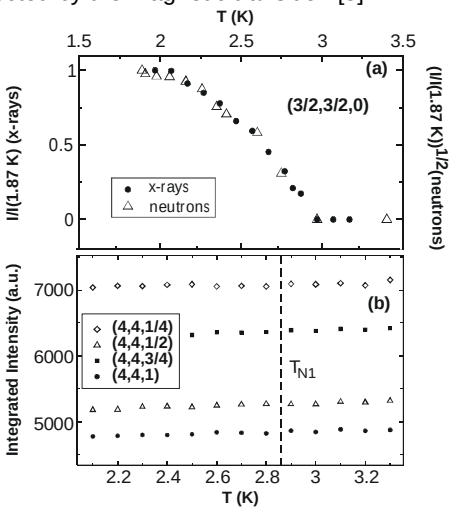

Fig. 2: Temperature dependence of the intensity of (a) magnetic and (b) CDW superstructure reflections around the antiferromagnetic transition temperature.

References

[1] H.D. Yang *et al.*, Phys. Rev. B 43 (1991) 7688

[2] B. Becker *et al.*, Phys. Rev. B 59 (1999) 7266

[3] F. Galli *et al.*, Phys. Rev. Lett. 85 (2000) 158

[4] F. Galli, R. Feyerherm, R.W.A. Hendrikx, S. Ramakrishnan, G.J. Nieuwenhuys, J.A. Mydosh, Phys. Rev. B 62 (2000) 13840

[5] F. Galli, R. Feyerherm, R.W.A. Hendrikx, E. Dudzik, G.J. Nieuwenhuys, S. Ramakrishnan, S. Brown, S. van Smaalen, J.A. Mydosh, submitted to Phys. Rev. B (2002)

R. Feyerherm, E. Dudzik (SF2.04 BESSY Activities)

Specular and off-specular neutron reflectometry study of strongly coupled films of ferromagnetic Co and antiferromagnetic CoO

A characteristic shift of the magnetic hysteresis loop away from zero-field has initially been found in ferromagnetic (FM) Co particles having an antiferromagnetic (AFM) CoO coating. This phenomenon which has been called exchange bias (EB) is often observed after field cooling AFM/FM systems below the Néel temperature T_N. In the past two decades, EB has intensively been studied in thin films [1] where it has a high potential for technological applications. Especially, a detailed understanding of the involved reversal processes is of interest for magnetic storage technology. In at least some EB systems different reversals for the increasing and decreasing field branch can readily be identified by the shape of the hysteresis loop; and it is well established now that reversal asymmetry is of crucial importance to elucidate unidirectional behavior in this large group of magnetic systems.

Magnetization curves belong to the fundamental macroscopic properties characterizing ferromagnetic materials. The specific type of reversal is determined by various subtle contributions such as exchange interaction or magnetic anisotropy. Magnetization can be reversed either by rotation or domain wall (DW) motion. For single thin layers, nucleation and DW motion is the dominant mechanism because it is energetically more favorable. For granular soft magnetic materials, the relevant mechanism can strongly depend on the direction of magnetocrystalline anisotropy or material composition. For double layers such as AFM/FM systems, reversal may drastically change due to the coupling at the interface. Recent investigations have shown that depending on the particular system both DW motion and rotation can be preferred. Because polarized neutron reflectometry (PNR) provides a ready means to not only measure the in-plane magnetization parallel but also perpendicular to the external field we have been able to elucidate the mechanisms responsible for asymmetry of the magnetization curve of a CoO/Co exchange bias system.

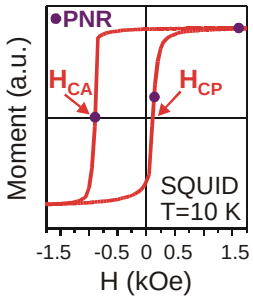

Fig. 1: Magnetic hysteresis loop for the biased state at T=10 K (after cooling in a field H^{COOL}=+4000 Oe from T=300 K).

In situ oxidation [2] was used to prepare [Co(16.4 nm)/CoO(2 nm)/Au(3.4 nm)]$_{20}$ multilayer samples [3]. Magnetic properties were characterized by magnetometry using a superconducting quantum interference device (SQUID) and by PNR. A magnetization curve performed at T=300 K shows no shift and has small coercivities H_C of less than 20 Oe. At this temperature, which is sufficiently above the blocking temperature T_B=180 K for EB in this particular type of CoO/Co system, there is virtually no coupling between CoO and Co (unbiased state). On the other hand, in the biased state (T=10 K) the hysteresis loop is considerably shifted away from zero field (EB field H_E=-393 Oe) featuring different coercivities H_{CA} =-895 Oe and H_{CP} =+110 Oe for decreasing and increasing fields, respectively (Fig.1). Using the product of the EB field H_E, the Co magnetization and the Co thickness as a measure of the interfacial energy ΔE a value of 0.9 erg/cm^2 (T=10 K) is obtained. This is one of the highest values ever reached [1].

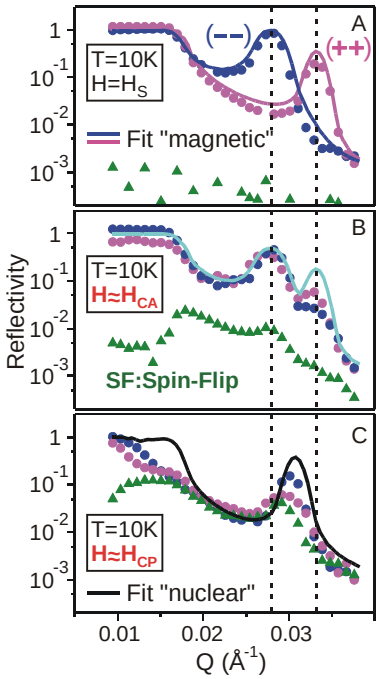

Fig. 2: Specular PNR profiles corresponding to three characteristic fields in the hysteresis loop of the biased state. A: magnetization saturation, B: coercivity at decreasing fields $H \approx H_{CA}$, and C: coercivity at increasing fields $H \approx H_{CP}$.

PNR experiments were performed with the standard setup of the reflectometer V6 at the Hahn-Meitner-Institut Berlin with neutron wavelength λ=0.466 nm. θ-2θ specular reflectivity scans with normal wave vector $|\mathbf{Q}|=4\pi \sin\theta / \lambda$ were recorded for all four cross sections: (++), (--), (+-) and (-+). The two non-spin-flip (NSF) cross sections, (++) and (--), yield information on the nuclear structure and the in-plane magnetization of the sample parallel to the external fields. For the two spin-flip (SF) cross sections, (+-) and (-+), the neutron polarization is changed due to interaction with the sample. These intensities are exclusively of magnetic origin and correspond to the in-plane magnetization perpendicular to the external field.

Neutron reflectivity profiles corresponding to three characteristic fields in the magnetization curve of the biased state are shown in Fig. 2. Solid lines are fits to the NSF reflectivity using a simulation procedure which is based on the Parratt formalism. We focus on reflectivity profiles within a small range of wave vector Q featuring only one characteristic peak. In this range, peak positions for (++) and (--) reflection profiles can considerably differ depending on different magnetic contributions to the neutron potential. For magnetization saturation (Fig. 2A), each of the two NSF reflectivity profiles is characterized by one dominant peak, only. These peaks are clearly separated from each other. Apart from a background of less than 10^{-3}, there is no significant contribution in the SF profiles which is expected for the sample magnetization completely aligned in-plane with the external field.

For $H \approx H_{CA}$ (Fig. 2B), both NSF profiles now clearly exhibit two peaks at the same positions as observed in the Fig.2A. Obviously, the sample now mainly consists of domains with magnetization pointing either parallel or antiparallel to the sample field. That is, almost identical cross sections for (++) and (--) neutrons correspond to an almost equal distribution of domains with parallel or antiparallel magnetization. This behavior is further illustrated by the fit curve which represents an intuitive model simply adding half of the calculated intensity of the (++) and (--) profiles of the saturated state (Fig.2A). The resulting net magnetization of the observed domain configuration is zero. It can therefore be concluded that the observed configuration with magnetization pointing either parallel or antiparallel to the sample field originates from a reversal which is mainly due to DW motion.

For the opposite coercivity H_{CP} (Fig. 2C), both NSF profiles clearly show only one dominant peak at a changed position (which is between the peak positions in Fig.2A and Fig.2B). This position is very close to the peak found by the simulation procedure including only nuclear contributions to the neutron potential (solid line in Fig. 2C). Additionally, the reflectivity in the SF profile is of the same magnitude as in the NSF profiles. This unambiguously proves that the main part of the magnetization has been rotated in the plane of the sample perpendicular to the external field. Contrary to the behavior found for $H \approx H_{CA}$, the reversal mechanism in the increasing field branch ($H \approx H_{CP}$) is obviously due to rotation.

For the unbiased state (T=300 K), PNR profiles (not shown here) unambiguously prove a reversal which is due to rotation on both sides of the hysteresis loop.

Off-specular scattering provides additional insight into the microscopic nature of the reversal processes (Fig. 3). For magnetization rotation, relatively strong diffuse scattering can be observed close to an exit angle of $\theta_f = 0.4^o$ (Fig. 3C). This diffuse intensity which is not present for magnetization saturation (Fig. 3A) and DW motion (Fig. 3B) indicates the formation of domains in the ferromagnetic Co layers. That is, the rotation of magnetization appears not to be uniform during the reversal process. The lateral extension of the magnetic domains is related to the value of the diffuse scattering vector ΔQ.

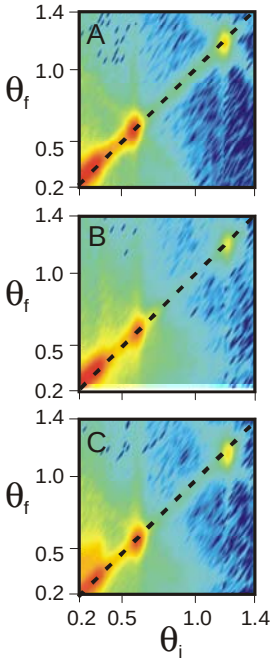

Fig. 3: Diffuse (off-specular) neutron scattering as a function of incident angle θ_i and exit angle θ_f corresponding to three characteristic fields in the hysteresis loop of the biased state (same as in Fig. 2). Dashed lines correspond to the specular reflectivity shown in Fig. 2.

In summary, in the unbiased state (T=300 K) magnetization reversal is mainly due to rotation on both sides of the hysteresis loop whereas in the biased state (T=10 K) rotation is the dominant mechanism only for increasing fields. For decreasing fields which is in the direction opposite to the bias (antiparallel to H^{COOL}), the mechanism changes to a reversal which is due to DW motion. That is, in the biased state the AFM strongly affects the reversal of the FM in the direction opposite to the bias whereas for the return into the bias direction the AFM does obviously not have any significant effect. An appreciable energy barrier for reversal may be provided only opposite to the bias direction probably due to formation of a DW in the AFM. A drastic change of magnetic behavior observed exclusively opposite to the pinning direction is most naturally expected for a system of strong unidirectional anisotropy.

References

[1] *For a review, see*: Nogués, J.; Schuller, I. K.: J. Magn. Magn. Mater., 192 (1999), 203-232.

[2] Gruyters, M.; Riegel, D.: J. Appl. Phys. 88 (2000), 6610-6613.

[3] Gierlings, M.; Prandolini, M.; Fritzsche, H.; Gruyters, M.; Riegel, D.: Phys. Rev. B 65 (2002), 092407.

M. Gruyters, M. Gierlings, D. Riegel
(SF2.02 Magnetism in thin films)

Cap layer influence on the spin reorientation transition of an ultrathin Co layer in Au/Co/X (X = UHV, W, Au)

Ultrathin films with dominant perpendicular magnetic anisotropy (PMA) are of particular interest in respect to both the exploration of the microscopic origin of magnetocrystalline anisotropy and the application in data recording as a means of achieving the highest areal densities. Films may show a spontaneous magnetization perpendicular to the film plane which rotates into the plane with increasing temperature or with increasing film thickness. This so called spin reorientation transition (SRT) at the critical temperature T* or critical thickness d* is due to competition between the surface anisotropy which may favor a perpendicular state and the volume contribution (essentially the shape anisotropy) always favoring an in-plane magnetization. It also depends on the materials used for the substrate and cap layer.

In order to gain further insight into the microscopic origin of the magnetic anisotropy we have studied systematically the temperature and thickness driven SRT of thin epitaxial Co films in Au(111)/Co/X (X= UHV, W, Au) by means of magneto-optical Kerr effect (MOKE), SQUID magnetometry, polarized neutron reflectometry, and x-ray experiments at the synchrotron. Some results on the critical thickness d^*_{Co} obtained at 300 K prior and after coverage with W and Au overlayers are summarized in table 1. A comparison of the measured magnetic phase diagrams (versus d* and T) demonstrates that the difference between the reorientation thickness d^*_{Co} in Au(111)/Co/W and Au(111)/Co/Au strongly increases with decreasing temperature and amounts to ~ 10 Å at T = 10 K [R. Sellmann et al., Phys. Rev. B 63 (2001) 224415, and Phys. Rev. B 64 (2001) 054418].

In addition, x-ray magnetic circular dichroism (XMCD) vector magnetometry provides evidence that the SRT also depends on the thickness of the Au cap layer. Whereas a 20 Å capping exhibits a pure in-plane magnetization at 300 K, the same Co film with a thinner Au cap layer shows a significant out-of-plane component. For the first time, these findings were linked to the observation of a cap-thickness induced variation of the orbital moment of Co. Using the magneto-optical sum rules we determined an enhancement of the Co orbital moment from 0.13 μ_B per atom for 2 nm Au to 0.18 μ_B for 1 nm Au cap (Fig. 1). The orbital moment anisotropy appears directly linked with the occurrence of the SRT observed here. Following the treatment by Bruno we obtain from the data in Fig. 1 for the spin-orbit magnetic anisotropy energy 1.25 10^{-4} eV per Co atom. This energy is still larger than the spin-spin dipole interaction of about 9 10^{-5} eV per Co atom. The data in Fig. 1 therefore explains, within this simple qualitative model, the observation of out-of-plane components as the Au cap thickness decreases.

Au(111)/Co	Au(111)/Co/W	Au(111)/Co/Au
d_{Co}^* = 9.6 Å	12.8 Å	14.5 Å

W(110)/Co	W(110)/Co/Au	
no SRT	8.5 Å	

Table 1: Critical Co layer thickness d^*_{Co} of the spin reorientation transition in various trilayers.

H. Maletta in collaboration with J. Langer, R. Sellmann; Stanford Synchrotron SSRL, USA: J. Hunter Dunn; University of Uppsala, Sweden: A. Hahlin, O. Karis, D. Arvanitis (SF2.04 BESSY Activities).

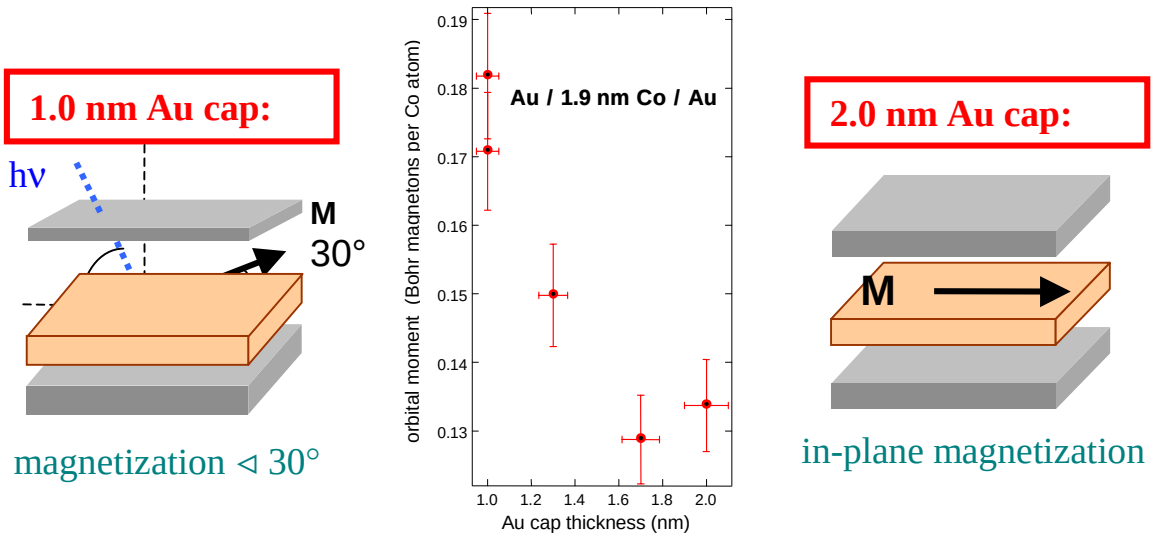

Fig. 1: Orbital moment per Co atom versus Au cap thickness as determined after application of the XMCD sum rules. For all regions the spin moment was found to be constant, 1.7(2) Bohr magnetons per Co atom. The orientation of the mean Co magnetization M is also displayed schematically.

Department

SF3 Materials

Rhenium distribution in the matrix of α Ni-Al-Ta-Re superalloy

Modern Ni-base superalloys are materials used as blades in power plant turbines where they have to resist for long times high mechanical stress at temperatures of around 1000 °C. The strength of these materials under service conditions is mainly determined by precipitates of the ordered intermetallic γ' phase Further improvement of the mechanical properties can be achieved through solid solution hardening of the matrix γ phase. However, how exactly Re improves the high temperature creep strength depends on its atomic distribution. In order to measure the chemical composition on a nanometer scale the field ion microscope (FIM) with three dimensional atom probe (3DAP) was used which is presently the only method providing both, high detection sensitivity independent of the kind of element and atomic scale spatial resolution.

Fig. 1 displays the reconstructed positions of Al, Re and Ta atoms as measured by means of 3DAP. The microchemical information is obtained from concentration depth profiles which can be constructed from these data. In such depth profiles clustering of Re on the nanometer scale becomes visible as a deviation from the homogeneous distribution. Fig. 2a shows a concentration depth profile of Re obtained in the γ phase. This plot seems to indicate local clustering of Re at positions where the 2σ error limit is exceeded. However, a clear distinction of what is mere statistical scatter and what are true Re clusters cannot be made at this point. In any case the usual χ^2-test of these data indicates that the Re is indeed not randomly distributed. Such test, on the other side, does not give evidence on the spatial distribution and strength of the detected heterogeneity. These details can be evaluated using advanced statistical methods like the here developed wavelength dependent filtering (WDF) method which is based on a Fourier analysis of the data. With this even small quasi-periodic deviations from a statistically random, i.e. homogeneous, distribution can be detected by comparison of the variances σ^2 of a random distribution with those of the experimental data after averaging over a systematically increased length scale L. This method provides the characteristic properties, wave length and amplitude, of the prominent Fourier component of the fluctuation. Fig. 2b presents a plot of the reduced variance $\Sigma^2(L) = (\sigma^2_{exp} - \sigma^2_{ran}) / \sigma^2_{ran}$ together with the expected statistical uncertainty. The maximum of Σ^2 at L = 20 nm indicates precipitates with a mean concentration of about 8 at.% Re and an average mutual distance of about 20 nm. Inspection of the concentration depth profile suggests about 1 nm width of the precipitates. This investigation quantifies for the first time Re heterogeneities in the γ-matrix of a Ni-Al-Ta-Re superalloy. Obviously the special thermal treatment which was applied for this alloy caused the clustering of Re which results in an improved high temperature creep resistance.

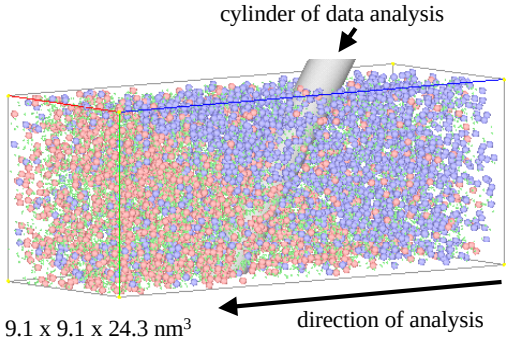

Fig. 1: 3 dimensional elemental mapping of Re atoms (blue), Ta atoms (red) and Al (green) of a Ni-Al-Ta-Re (Re31) alloy as derived from 3DAP data. The volume shown has the dimensions of 9.1 x 9.1 x 24.3 nm^3 (about 2x10^5 atoms) and contains both phases, γ' and γ. A cylindrical region of 4 nm diameter running across the γ/γ' interface is indicated. This figure represents only part of the complete 3DAP-measurement involving a total of 2x10^6 atoms.

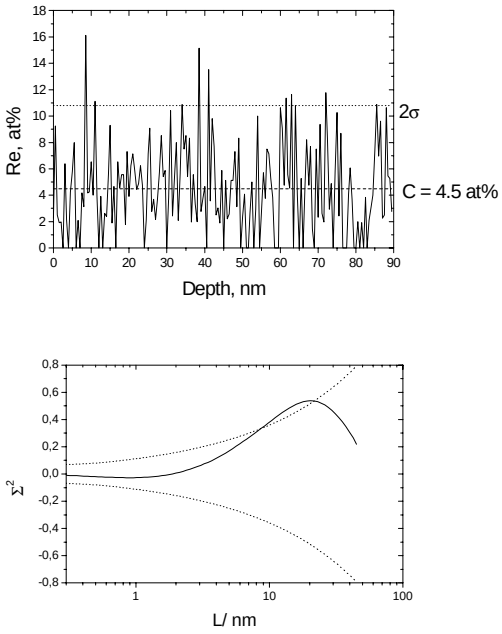

Fig. 2: a) Concentration depth profile of Re in the γ. The dashed line indicates two standard deviations. Possible Re clusters are visible at a depth of about 10 nm, 40 nm, and possibly 70 nm. b) WDF analysis of the Re distribution. The reduced deviation $\Sigma^2(L)$ between the variances of the measured concentration distribution and those of the corresponding random distribution is plotted versus the logarithm of the effective averaging length L. The position and height of the maximum in this plot quantify the average distance between and the mean concentration of the Re clusters.

N. Wanderka, V. Naundorf (SF3.01 Microstructure and Kinetics of Phase Transitions in Metallic Alloys)

MC simulation of the $L1_2$ order-disorder phase transformation

The stability of the ordered intermetallic phases determines the applicability of many technically important materials. By Monte Carlo technique the processes of formation and destruction of such phases under non-equilibrium conditions can be simulated. We investigated the ordering and disordering of an $L1_2$ intermetallic in detail. The ordering process was described with a atomic exchange mechanism based on a fcc Ising model.

The temperature dependence of the stationary degree of long-range-order parameter $S_\infty(T)$, i.e. the equilibrium phase diagram of the $L1_2$ order-disorder transformation was calculated assuming appropriate pairwise atomic interaction parameters V_1, V_2, V_3 and V_4. The simulations were performed from two initial states of order: (i) the completely disordered state and (ii) the completely ordered state, i.e. starting the simulation from the low and from the high temperature state of order. In addition the effect of heavy ion irradiation on the ordered phase was modelled by simulating overlapping cascades.

The time evolution of atomic arrangements evolves differently for the two initial conditions. When starting from a completely ordered state, the equilibrium state with partial degree of order is achieved very fast. In this case no new ordered domains are nucleated, and therefore no antiphase boundaries (APB) appear.

Results for thermal ordering from an initially completely disordered state into the $L1_2$ structure demonstrate the importance of APBs. Ordered domains of equivalent variants nucleate randomly at different places independently from each other. APBs form when ordered domains grow and intersect. For a complete transformation from order to disorder, all the APBs have to be removed. This is a slow process when compared to the growth of an ordered region into a disordered environment. Two different evolutions of the APBs were found. Most simulations yielded the same average LRO parameter, irrespective of the initial state of complete order or complete disorder, i.e. all APBs anneal completely. In order to demonstrate the details of the evolution of APBs, we have plotted the simulation results in a 3D data presentation. Figure 1 shows examples of the evolution of the APBs during the late stage of the ordering kinetics. If the APBs are curved they shrink and anneal with time. At 5000 mcs a single-phase state of $L1_2$ order is reached belonging to one order variant without any APB. In some simulations the structure did not approach the equilibrium values even after 10000 mcs. Figure 1b demonstrates the corresponding APB evolution. Here the dominant APBs after 1000 mcs are plane. Such APBs are stable because the driving force for annihilation is much smaller than of the curved APBs and do not change with increasing mcs.

Plane APBs have been found in the $L1_2$ ordered Cu_3Au during the disorder-order transformation experimentally. By means of HRTEM the atomic arrangement could be imaged directly. In these investigations the corresponding superlattice reflection symmetries show the difference between the structure containing curved or plane APBs.

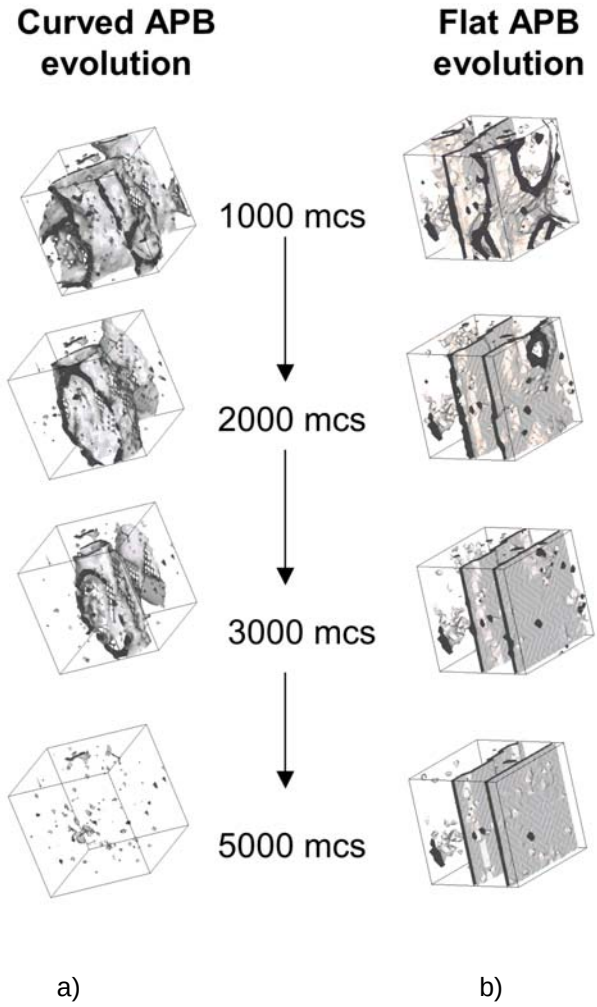

Fig. 1: *Evolution of the APBs during the late stage of the ordering process of the $L1_2$ structure (1000 – 5000 mcs). Initial state had be the completely disordered. At the left side the complete annealing of curved APBs is demonstrated resulting in a homogeneously ordered $L1_2$ structure. At the right side, an example of the evolution of a flat APBs is shown. This structure is stable and does not anneal with increasing MC simulation steps.*

C. Abromeit in collaboration with S. Matsumura [Kyushu University, Japan] (SF3.01 Microstructure and Kinetics of Phase Transitions in Metallic Alloys)

Microstructures of Ferrofluids studied by combined contrast variation using polarized neutrons

Small Angle Neutron Scattering (SANS) is used as a non destructive technique for the analysis of nano-structures in modern materials. This nano-analytical technique allows composition, density and magnetization fluctuations to be identified on a length scale between 0.5 and 300 nm. Macroscopic averages of the nano-structural parameters are obtained and correlated with basic material properties in magnetic and ceramic nanomaterials, in amorphous and partly crystallised materials and in magnetic liquids.

In polydisperse multiphase systems identification of the constituents by SANS is a puzzling task which requires proper labelling techniques. For magnetic materials we have shown that application of polarized neutrons (SANSPOL) is such a labelling technique. The scattering length density, illustrated in Fig.1 by different colors for the central magnetic core of a composite particle depends on the neutron polarization states (+) or (-), respectively. Two scattering curves are measured alternatively by switching the neutron polarization from (+) to (-) which differ solely as a result of the different magnetic contrasts. In addition, the "color" of the surrounding matrix can be adjusted using mixtures of isotopes (such as H and D with different signs of scattering lengths) in such a way that either the core or shell of the composite appears to be transparent for neutrons. This combined contrast variation allows magnetic and nonmagnetic particles to be distinguished and density-, composition-, and magnetization profiles to be precisely determined.

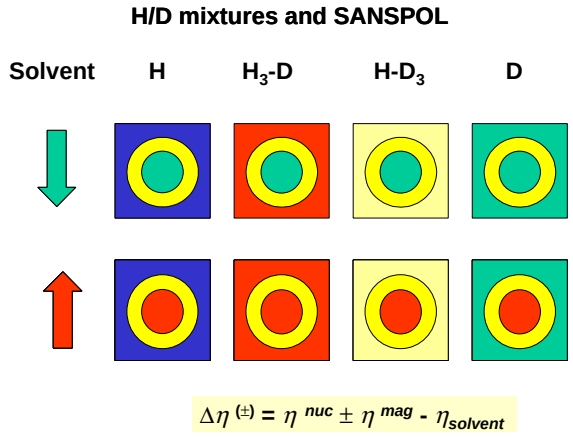

Fig. 1: Illustration of the scattering contrasts for polarized neutrons in a particle with a magnetic core and a nonmagnetic shell in different isotope mixtures of the solvent.

This technique was used for structure investigations of magnetic colloids. In such "Ferrofluids" nanoscaled magnetic particles are stabilized against coagulation either by electrostatic repulsion or by coating the core with organic chain molecules acting

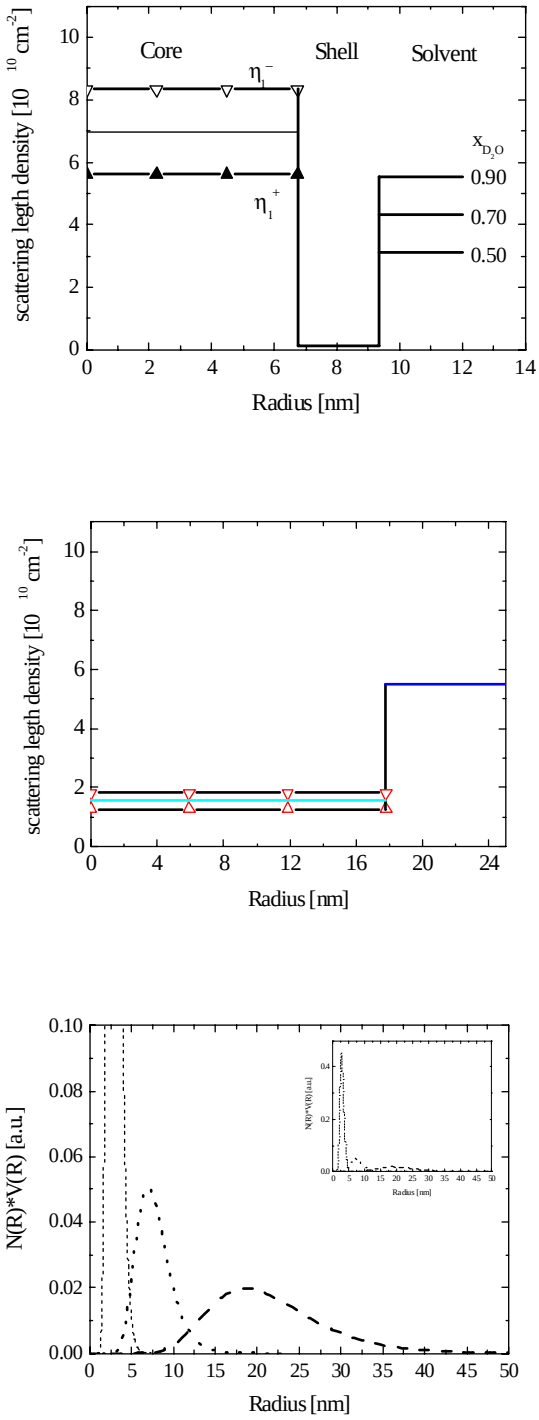

Fig. 2 Scattering length density profiles for SANSPOL of core-shell particles a) and aggregates b) and size distributions c) of Fe_3O_4 based FF with Laurin-acid/Malipal double layer surfactants in D_2O/H_2O as carrier liquids. The inset enlarges the size of the micet.

as surfactants. Currently great effort is undertaken to prepare new bio-compatible Ferrofluids for potential biomedical applications, for which the knowledge of the microstructure is a prerequisite. In the frame of the DFG Priority Program 1104 we investigate Ferrofluids where magnetic materials (Co, Magnetit, Ba-Hexaferrite), shell forming surfactants (mono- and bi-layers) and carrier liquids (water, organic solvents) have been systematically varied. Structure and composition of core and surrounding shell, size distribution of particles as well as the magnetic structure have been determined at different concentrations. As a common feature three different components were identified, magnetic core – shell particles, free organic shell molecules and magnetic aggregates. Typical scattering length density profiles and size distributions are shown in Fig. 2. The average core size depends on the material and preparation condition whereas the shell thickness seem to be characteristic for the surfactant material and the solvent. In all cases the shell of the composite particle was found to be impenetrable for the solvent. The magnetic ordering of diluted systems corresponds to non-interacting ferromagnetic single domain particles. In some systems small amounts of aggregates with a typical size of 2-4 times the core radius are formed due to imperfect screening. The densities and magnetization of this aggregates are reduced probably by inclusions of surfactant molecules.

The set-up of inter-particle interactions under the influence of magnetic field was studied in Ferrofluids with higher Co-concentrations (5 vol. %). Strong field induced correlations are clearly reflected by a low-Q peak in the SANS curves of Fig.3. All curves are well described using the same structure factor S(Q) corresponding to a hard sphere interaction. The hard spheres radius R_{hc} = 8.65nm. is by a factor of about 1.5 larger than the total radius of the composite particles. No evidence for an anisotropic structure factor was found which implies a dense packing of the particles rather than formation of chains as predicted for dipole interactions. Data analysis of a detailed study of field-induced ordering is in progress.

A. Wiedenmann, A. Hoell, M. Kammel
(SF3.05 Structure Investigations in Nanomaterials using SANS)

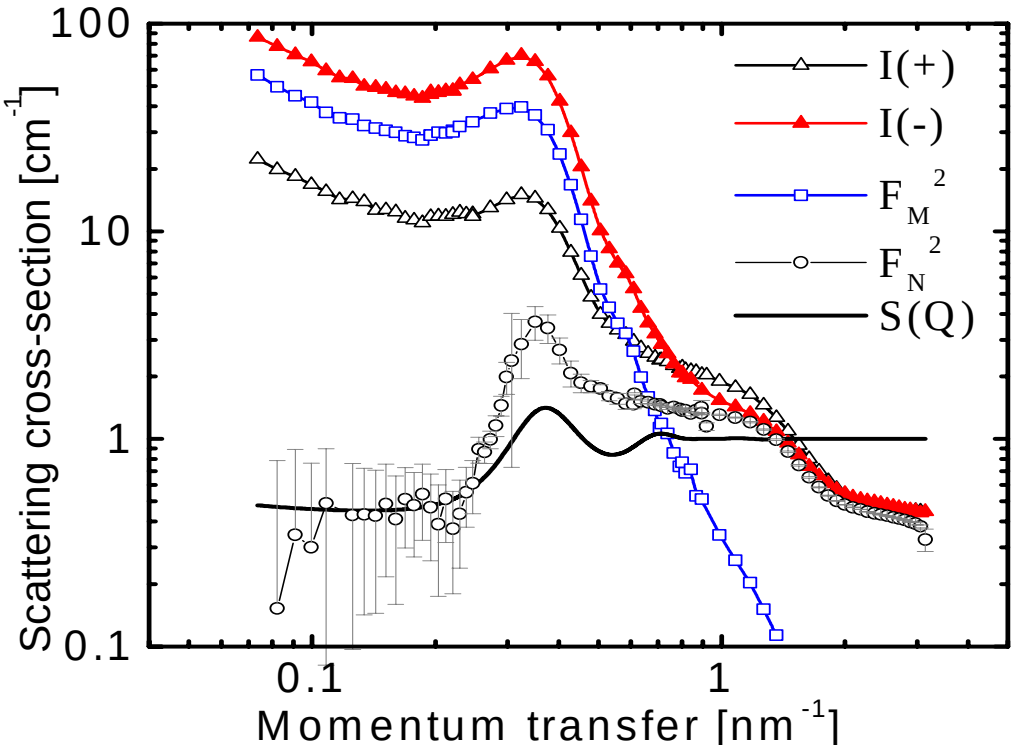

Fig.3: SANSPOL intensities $I^+(Q\perp H)$ (solid triangles) and $I^-(\mathbf{Q}\perp\mathbf{H})$ (open triangles) of 5vol% Co-Ferrofluids in C_7D_8 and magnetic (squares) and nuclear (circles) contributions from non-polarized neutrons. The solid line represents the common structure factor S(Q) for hard spheres.

Evolution of the morphology in superalloys and nano-ceramics at high temperatures

In-situ annealing on the SANS instrument V4 allowed the evolution of the morphology at high temperatures to be analyzed. SANS investigations of γ'-phase precipitate microstructure in Ni based superalloys have been continued in collaboration with Dr. Mukherji (TU Braunschweig). The experiments performed on specially prepared Re-containing alloys single crystal brought new insights concerning shape, size, and distribution of the precipitates in the vicinity of the solvus line. The structural parameters have been obtained in great detail using the previously developed model fitting technique (see Fig.1, solid lines). The pattern of Fig. 1 with a pronounced temperature dependence shows clearly the dissolution of precipitates and the temperature range of their homogenization. The detailed SANS-data evaluation lead to the conclusion that the dissolution occurs inhomogeneously above 1000º C. Diffusion-driven effects, which were observed on some of the Re-containing samples, will be studied in more detail in further experiments.

The sintering behavior of zirconia ceramics doped with 0, 4, 10, and 12 mol-% yttria was investigated by in-situ time-resolved SANS. Nanocrystalline powders were produced by Chemical Vapor Synthesis (CVS) pressed into greenbodies and sintered at temperatures between 300°C and 1200°C. Fig. 2 shows the average particle sizes for selected temperatures. It can be concluded that a slight particle growth already starts at very low temperatures, but only significantly accelerates at temperatures around 1000°C. However, the increase of the relative density of the samples (i.e. the disappearing of pores) already occurs at a lower temperature.

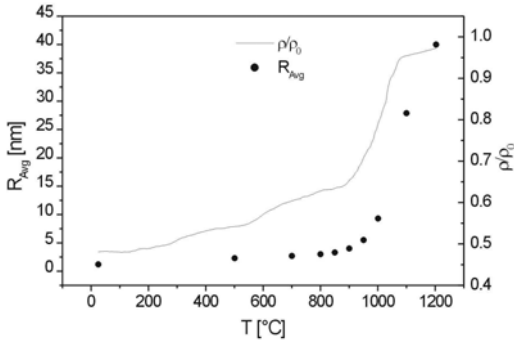

Fig.2: Average particle size RAvg, and relative density ρ/ρ0 determined by dilatometer experiment

P. Strunz, U. Keiderling A. Wiedenmann
(SF3.05 Structure Investigations in Nanomaterials using SANS)

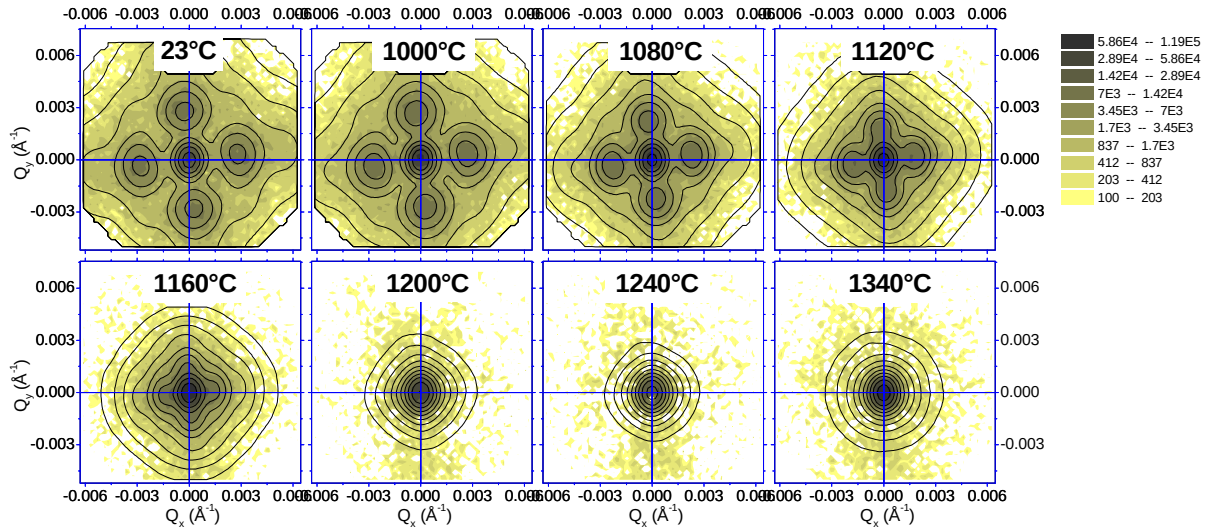

Fig.1: Cross-section in a logarithmic scale for SCA433 superalloy (heat treatment: 1285°C/4h/ air cooling and 1100°C/0.25h/ air cooling) at different temperatures. Color maps are the measured data and the iso-intensity lines denote the fit of the optimum mode.

Residual stress in polycrystalline materials and technical parts

The research project deals with the analysis of residual stresses in polycrystalline materials, which are known to influence the mechanical properties of technical parts to a large extent. Diffraction methods using X-rays, neutrons or synchrotron radiation permit the non-destructive determination of the macro- and micro residual stress state at the surface as well as in the volume of the material by analyzing both, the shift and the broadening of the diffraction lines. For this reason, the diffraction equipment at the Hahn-Meitner-Institute provides the necessary tools for complementary residual stress-, texture and microstructure analysis within different depth zones below the surface.

Mechanical surface processing is known to give rise to complex residual stress fields in the near surface region of polycrystalline materials and their analysis by means of non-destructive diffraction methods has become an important topic in materials science. Because the information depths achieved by X-rays, neutrons and/or hard synchrotron radiation usually differ from each other by orders of magnitude, stress evaluation within the near surface region up to some millimetres requires the application of complementary methods.

Fig. 1 shows a front view of the ETA- diffractometer for surface gradient analysis, which has been developed in a cooperation between the HMI and the company SEIFERT in Ahrensburg. This new type of 5-circle diffractometer permits a direct rotation of the sample around the diffraction vector **g** for a fixed orientation (φ,ψ) with respect to the sample reference system. Therefore, it is well suited for the analysis of textures, the microstructure and steep residual stress gradients in any diffraction geometry and –mode.

Using appropriate optical elements in the primary (polycapillary semi-lens) and the diffracted beam (Soller+secondary monochromator) for grazing incidence diffraction, the analysis of residual stress gradients is possible even in very thin layers of about 100 nm thickness (Fig. 2). The investigations refer to a small poly-Si-layer deposited and laser recrystallizated on a glass substrate. Due to the differences in the coefficients of thermal expansion between the film and the substrate ($\alpha_{substrate} < \alpha_{Film}$), strong tensile stresses arise in the film, which relax towards the free surface.

Fig. 1: The 5-cirle diffractometer XRD 3003 ETA for the analysis of steep near-surface gradients of residual stress, texture and microstructure [1].

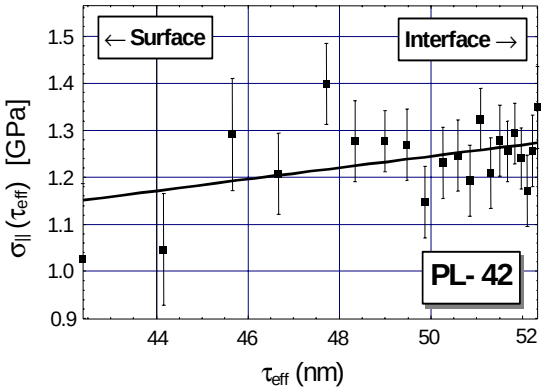

Fig. 2: Depth distribution of the in-plane residual stress $\sigma_{\parallel}(\tau)$ in a thin boron-doped poly-Si-film (110 nm) deposited on a glass substrate[1].

In order to analyze the residual stress state in the intermediate zone between the surface and the volume of the material, favorite use can be made of energy dispersive diffraction methods (ED-XRD) performed in the reflection mode. Depending on the material, the transition zone concerns a range between about 10 µm and 1 mm, where the conventional X-ray methods are no longer and the neutron methods are not yet sensitive. To achieve the

[1] The sample was delivered by the department SE1 (silicon photovoltaics) of the Hahn-Meitner-Institute.

necessary penetration depths τ, radiation energies up to 60 keV should be used.

Because highly collimated white synchrotron radiation provides a series of advantages compared with a conventional high energy X-ray tube (high photon flux, short measuring times, small gauge volume), a new materials science beamline is currently established at the BESSY II storage ring. The white radiation up to an energy of about 60-80 keV will be provided by a 7T multipole wiggler.

The diffractometer system, which was built by SEIFERT, is shown in Fig. 3. It is mounted on a linear y-z stage in order to align the system with respect to the beam. Its basic unit consists of a θ-θ' diffractometer operating in the vertical plane. For sample manipulation two units are available, which can be exchanged for each other depending on the measuring problem. For small samples the basic diffractometer can be equipped with an Eulerian cradle segment which is mounted on the Θ-axis (cf. Fig. 3). For large and heavy samples up to 50 kg, the cradle segment can be replaced by a X-cradle segment with its rotation axis perpendicular to the diffraction plane (not shown in Fig. 3).

Fig. 3: Multipurpose diffractometer for residual stress-, texture and microstructure analysis at BESSY [2].

A decisive advantage of ED-XRD methods is given by the multitude of reflections hkl recorded simultaneously in one spectrum, which provide additional information because they comprise different penetration depths τ(hkl). Therefore, efforts have been made to adapt different methods developed so far for the angle dispersive X-ray stress analysis to the energy dispersive case.

The example in Fig. 4 refers to an ED residual stress analysis at a ground steel plate. A high energy W-tube was used for the investigations. The strain depth profile analysis was performed in the scattering vector mode [3], where the spectrum is recorded after stepwise rotation around the diffraction vector.

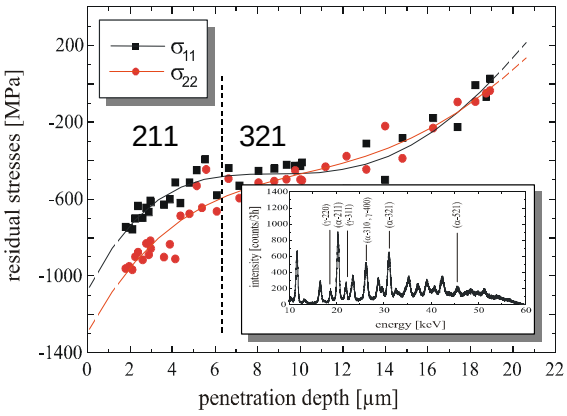

Fig. 4: Laplace stress depth profiles $\sigma_{ii}(\tau)$ (i = 1,2) in a ground steel sample obtained from the 211 and the 321 reflection by means of the scattering vector method [2].

In the present case, high compressive residual stresses $\sigma_{11}(\tau)$ and $\sigma_{22}(\tau)$ are observed immediately below the surface, which rapidly decrease with depth. Besides the steep gradients, significantly higher compressive stresses within the first 6 µm are found in the transverse direction (σ_{22}), which agree with the common ideas of residual stress formation due to uniaxial grinding.

References

[1] Ch. Genzel, W. Reimers, A. Haase. A New Type of X-Ray Stress and Texture Diffractometer for the Analysis of Complex Near Surface Residual Stress Fields. ICRS-6, Oxford, 10.-12.07.2000, Proc. Vol. 1, S. 74-81.

[2] Ch. Genzel, C. Stock, B. Wallis, W. Reimers. The Application of White Radiation to Residual Stress Analysis in the Intermediate Zone between Surface and Volume. Nucl. Instrum. Meth. A 467–468 (2001), 1253 – 1256.

[3] Ch. Genzel. Entwicklung eines Mess- und Auswerteverfahrens zur röntgenographischen Analyse des Eigenspannungszustandes im Oberflächenbereich vielkristalliner Werkstoffe. Habilitationsschrift, Humboldt-Universität zu Berlin, 2000.

Ch. Genzel, C. Stock
(SF3.02 Strain and Stress in Materials and Technical Parts)

Department

SF4 Structure and Dynamics

Spectroscopy of Si-Auger electrons from the center of heavy-ion tracks

One of the most important problems in the fields of ion-solid and laser-solid interactions is to gain knowledge about charge neutralization and electronic relaxation mechanisms in the case of dense electronic excitations. Hot electrons as well as charged regions on a nanoscopic scale trigger the subsequent atomic motion and rearrangement inside ion tracks. In this work, we have produced such highly excited electron systems inside tracks of swift heavy ions. High resolution Auger spectroscopy provides the tool to investigate the electron dynamics in the close surrounding of the ion path inside silicon targets and on a time scale of up to $5 \cdot 10^{-14}$ s.
Electron spectra haven been taken for heavy ions as well as for electrons of equal velocity incident on amorphous and single crystalline Si targets. The experiments have been performed under UHV conditions at operating pressures of about 10^{-10} mbar in the new ISL cyclotron beamline TF. The atomically clean target surfaces, either amorphous Si or Si(111) with 7x7 reconstruction, were characterized by Auger-electron spectroscopy and low-energy electron diffraction (see Fig. 1) before and after the ion-irradiation runs.
Various LVV-Auger electron-structures are identified and these peaks show a broadening as well as a shift towards lower energy when the charge of the projectile is increased. As an example, the Si L^1VV-Auger structure (initially with a single vacancy in the L_{23} shell) is displayed in Fig.2 after background subtraction. The electron induced reference spectra are indicated by open plot symbols. It is seen that these two spectra for amorphous Si (a-Si, shown as circles) and crystalline Si (c-Si, shown as triangles) are very similar, pointing to comparable valence density-of-states. The spectra due to fast Xe^{31+} ions (marked with solid symbols) are due to the same inner-shell vacancy-configuration. Thus, deviations from the electron reference spectra may only be due to local electron-density reductions or excitations in the Si valence-band. It is seen that both ion-induced spectra are in fact broadened and shifted with respect to the reference.
The line shift points to a nuclear-track potential due to positive charges inside the ion track [1] and the broadening indicates a high electron temperature that modifies the Fermi-Dirac distribution [2]. The comparison of the ion induced Auger-electron spectra for amorphous and crystalline Si gives, for the first time, evidence for phase effects in the short-time dynamics of ion tracks. Charge neutralization seems to be significantly slower in amorphous than in crystalline Si targets, leading to deceleration of ejected electrons. Transport theoretical calculations for Auger electrons in Si are under way and will allow for a quantification of the observed effects.

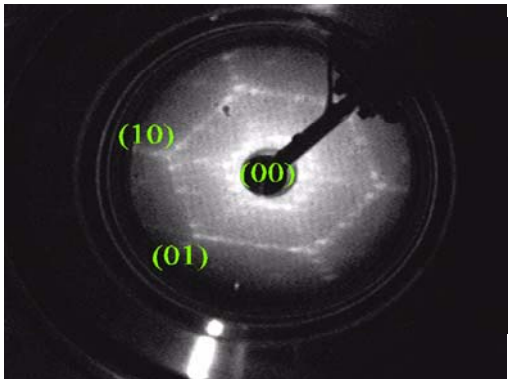

Fig. 1: Low-energy Electron Diffraction pattern of the Si(111) surface with 7x7 reconstruction.

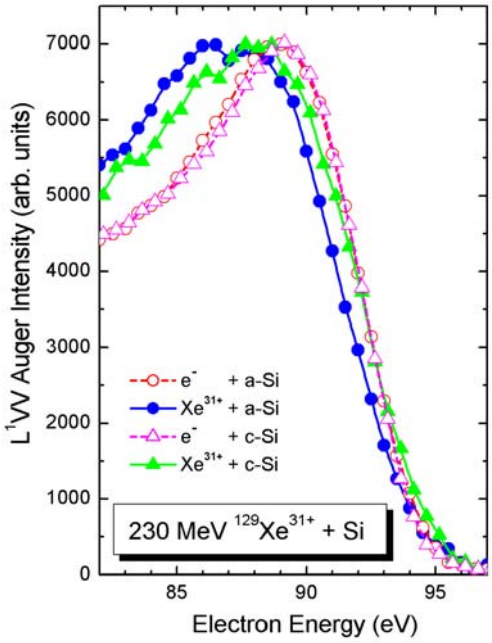

Fig. 2: Auger electron spectra for amorphous and crystalline Si irradiated by electrons and heavy ions.

References
[1] Xiao, G. et al:
Phys.Rev.Lett. 79, 1997, pp.1821

Schiwietz, G. et al:
Phys.Rev.Lett. 69, 1992, pp.628

G. Schiwietz, G.; G. Xiao, G.:
Nucl. Instr. Meth. B107, 1996, pp.113

[2] Schiwietz, G. et al:
Europhys. Lett. 47, 1999, pp.384

G. Schiwietz, K. Czerski, M. Rösler, M. Roth, F. Staufenbiel in collaboration with P.L. Grande (Universidade Federal do Rio Grande do Sul, Instituto de Física, Porto Alegre, Brazil)

(SF4.01a Atomic Dynamics: Ion Impact)

Transmission of 3 keV Ne^{7+} through nanocapillaries in PET polymers: Evidence for capillary guiding

Recently, we started experiments in which slow highly charged ions are transmitted through capillaries of 100 nm diameter in a 10 µ thick foil obtained by etching ion tracks in a PET (Mylar) polymer. We measured the transmission of 3 keV Ne^{7+} ions whose final charge state was analyzed including neutrals by means of an electrostatic deflector. In our experiments, particular emphasis was given to the comparison of angular distributions obtained with insulating material (Mylar) and metals.

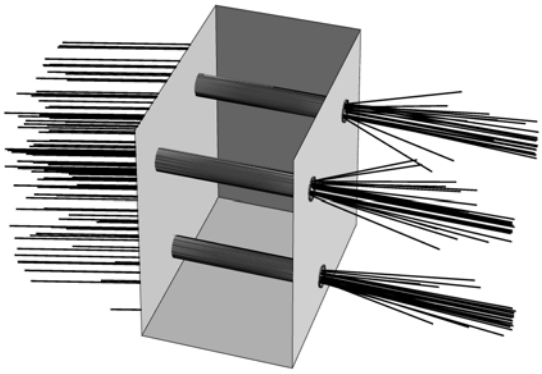

Fig. 1: Trajectories of ions guided through capillaries in a tilted foil.

In particular, transmission measurements were made where the foil was tilted with respect to the incident beam direction as shown in Fig. 1. The angular distributions of the transmitted Ne^{7+} ions for PET are found to be essentially different from those obtained with metals. In the latter case when the capillaries are covered with Ag, the Ne^{7+} angular distribution is rather narrow (FWHM of 1^0) and ion transmission vanishes when the foil is tilted (Fig. 2). On the contrary, for the 5^0 tilted Mylar foil, the angular distribution of the Ne^{7+} is found to be relatively broad (FWHM of 4^0 - 6^0) and the maximum is shifted by 5^0.

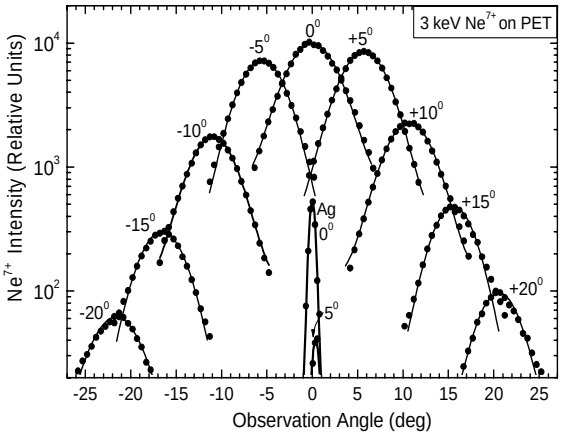

Fig. 2: Angular distributions of Ne^{7+} ions transmitted through capillaries in PET. The tilt angle is indicated. Also plotted are data for capillaries in Ag showing that the angular distributions are quite different from those for PET.

Similar effects were found for tilt angles as large as 20^0. The latter observation suggests a "guidance" of the Ne^{7+} ion within the insulator (PET) capillary, i.e. multiple scattering events alter the main propagation direction of the Ne^{7+} ions along the capillary axis. This observation is surprising, since multiple scattering events are expected to change the charge state of the projectile, i.e., highly charged ions scattered by, e.g., 5^0 are neutralized when emerging from the surface.

The present finding of ion guidance provides evidence that the inner walls of the capillaries are charged and close collisions with the surface involving electron capture into the projectile are suppressed. The charge deposition occurs by means of a self-organizing process, which allows charge up until a certain maximum value where the electric field becomes so high that the ions are deflected and further charge deposition is inhibited. This scenario has been confirmed by measuring the time dependence of the process. Experiments have shown that the guiding effect did not appear immediately after the ion beam first hit the foil. The measured time constants for the build-up and the decay of the guiding field were in agreement with simple model assumptions for the charge deposition process on the capillary walls.

Our preliminary model indicates that the description of the observed capillary guiding is a challenging theoretical tasks that involves ordering phenomena by a self-organizing process. Capillary guiding has considerable potential for obtaining information about the interaction of multiply charged ions with insulators, and controlling the transport of highly charged ions within regions of mesoscopic dimensions.

References

[1] Stolterfoht, N.; Bremer, J.H.; Hoffmann, V.; Hellhammer, R.; Petrov, S.; D. Fink, D.; Sulik, B.:
Phys. Rev. Lett., 88, 2002, 133201

[2] Pešić, Z.; Lebius, H.; R. Schuch, R.; Víkor, Gy.; Hoffmann, V.; Niemann, D.; Stolterfoht, N.:
Nucl. Instrum. Methods Phys. Res. Sect. B 164, 2000, pp. 511-516

N. Stolterfoht, J.H. Bremer, V. Hoffmann, R. Hellhammer, A. Petrov, D. Fink in collaboration with B. Sulik (On sabbatical leave from the Institute of Nuclear Research, Debrecen, Hungary)
(SF4.01a Atomic Dynamics: Ion Impact)

Radiation compaction of nanoporous Vycor Glass

Along its trajectory a swift heavy ion in matter induces a cylindrical trail of dense electronic excitations. If a substantial fraction of this excitation energy is rapidly converted into atomic motion a thermal spike may form within about 0.5 ps. In this hot ion track, which is a few nanometers wide and many micrometers long, a thermo-elastic stress field of cylindrical symmetry appears [1,2]. If a fluid track forms in a material containing numerous pores of nanometer size it is expected that the track matter flows into the pores releasing the track's overpressure. The existence of this effect has been demonstrated by irradiating Vycor with 340 MeV Xe ions [3]. Vycor (Corning Glass Works, glass code 7930) is a silicate glass (96 % SiO_2) with numerous tiny pores having typical radii of about 2 nm. The average mass density of Vycor in the near-surface region is ρ_v = 1.2 g/cm^3. The density of the backbone material is ρ_b = 2.18 g/cm^3, i. e. the average volume fraction of the pores in the near surface region is about 0.45.

The samples had a size of $10 \times 10 \times 1.5$ mm^3 and a central area of 5×5 mm^2 was uniformly irradiated at T_i = 300 K with 70 MeV ^{40}Ar, 260 MeV ^{86}Kr, and 340 MeV ^{129}Xe ions, respectively. At various fluxes the height depression h was measured ex-situ as the difference of the specimen height between the bombarded and the unbombarded area. In Fig. 1 the surface depression is plotted versus flux Φt for 340 MeV ^{129}Xe ions. Due to the small ion fluxes Φ pore shrinkage by macroscopic beam heating can be safely ignored. Mass loss by decomposition of SiO_2 is also negligible because the possible decomposition products SiO and Si are black whereas the samples remained transparent during irradiation.

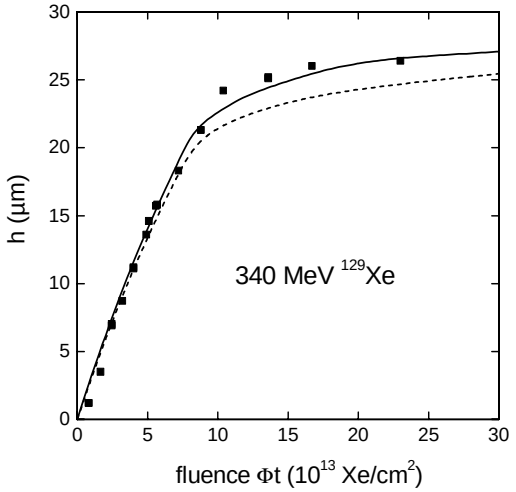

Fig. 1: Surface height depression h versus ion flux Φt for 340 MeV Xe ions.

Using Lagrangian co-ordinates (z-axis being oriented parallel to the surface normal) mass conservation reads

$$\frac{\partial \rho}{\partial t} + \rho \frac{\partial v}{\partial z} = 0 . \qquad (1)$$

Complete pressure relaxation yields for the compaction velocity gradient $\partial v/\partial z$

$$\frac{\partial v}{\partial z} = - \frac{1.16\ \alpha (1+\nu) \Phi\ S_e'}{eC\ \rho} \qquad (2)$$

where uniform irradiation in the xy-plane has been assumed. α is the coefficient of linear thermal expansion, ν the Poisson number, C the specific heat, and S'_e the fraction of the electronic energy loss converted into heat in the track core. Equation (2) is valid only as long as complete pressure relaxation can take place, i.e. when pore filling starts to be completed at $t = t_{crit}$ pressure relaxation has to be replaced by shear stress relaxation. Then the compaction velocity approaches zero [3]. The solutions of eqs. (1) and (2) are

$$\rho(z,t) = \begin{cases} \rho_v \exp(-BtS_e') & \text{for } t < t_{crit} \\ \rho_s & \text{for } t > t_{crit} \end{cases}$$

$$v(z,t) = \int_0^z BS_e' \exp(BtS_e')\, dz'$$

with $B = -1.16\alpha(1+\nu)\Phi/(e\rho_v C)$ and the saturation density ρ_s = 2.26 g/cm^3 of irradiated SiO_2. The time t_{crit} depends on z' and is defined self-consistently by taking $\rho(z', t_{crit}) = \rho_s$. The height depression is given by

$$h(t) = \int_0^{R_{pv}} \left(1 - \frac{\rho_v}{\rho(z,t)}\right) dz \qquad (3)$$

with R_{pv} being the projected ion range in the unirradiated material. The dashed line in Fig. (1) is the result of a numerical integration of eq. (3). The solid line is a calculation with includes additional pore filling at the end of the ions' path by the nuclear energy loss. The good agreement between theory and experiment provides strong support for the idea that particle tracks can be considered as thermo-elastic inclusions. Because of its reference to mechanical equilibrium the pore filling mechanism will work in any material as long as crystallisation effects do not interfere.

References

[1] Trinkaus, H.; Ryazanov, A.I.:
Phys. Rev. Lett. 74 (1995) 5072-5075

[2] Trinkaus, H.:
Nucl. Instr. Meth. B146 (1998) 204-216

[3] Klaumünzer, S.:
Nucl. Instr. Meth. 166/167 (2000) 459-464.

S. Klaumünzer, G. Schumacher, N. Darowski
(SF4.01a Atomic Dynamics: Ion Impact)

Studies on metallic nanotubule formation in ion tracks

It has been suggested to develop nanoelectronic devices on the basis of etched tracks in polymers. From several possible strategies we selected the production of metallic (Cu, Ag, Ni) and polymeric (PMMA, PAN) nanotubules as basic elements for that purpose. For example, by combination of concentric metal-insulator-metal tubules we want to produce nanosized condensers. Polymeric tubules can be prepared by simple adsorption of polymer solutions on the inner track walls, or by in situ polymerization of monomer solutions within the tracks. In order to accomplish the production of conducting tubules by chemical deposition of metals onto the inner walls of etched ion tracks in polymers, the commercial recipes available in the galvanic industry have to be modified.

It turned out that several of the recommended preparatory steps (such as „Conditioning“ and „Generation“) are useless or even detrimental in our case, as polymeric surfaces are highly sensitive to the alkaline ambience used there. The only step that is really important – and necessary! – is the formation of a high density of nucleation centers on the polymeric surface, at which the metal atoms can precipitate („activation“). This can be accomplished either chemically by the use of the well-known $SnCl_2$ or Pd complex salt activators, or physically by the introduction of radiation defects via laser or ion beam irradiation.

Especially the last possibility appears to be most promising for future applications, as it enables one to tailor the metal deposition along the track axis quite precisely. It has turned out that the impact of medium-energy (30 to 300 keV) medium-heavy (Ne, Ar) ions at fluxes around $10^{14...15}$ cm^{-2} is most efficient for the nucleation center formation on polymers such as PI, PET, and PSiO. It appears that electronic energy transfer mechanisms rather than nuclear ones are responsible for that surface activation. The mechanism involved appears to be radiation-induced bond breaking that leads to superficial polymer oxidation in ambient atmosphere, which enables metal bonding according to the principle scheme:

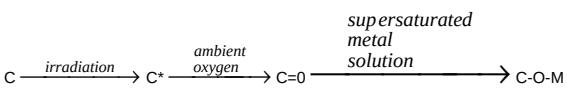

with M being a metal atom. It appears that this ion-induced polymer surface activation enables one to obtain a higher density of nucleation centers than the conventional chemical activation, which leads to somewhat smaller metal crystallites, and hence to smoother deposited layers with reduced surface roughness, see Fig.1.

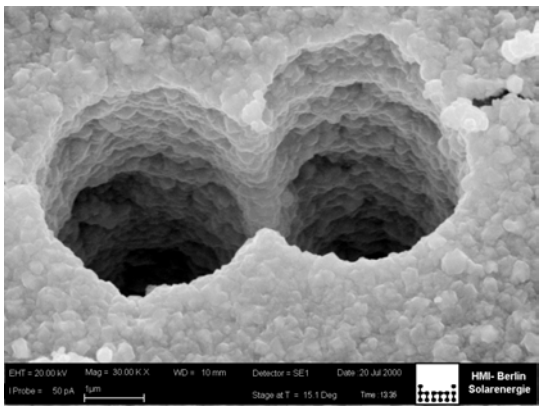

a)

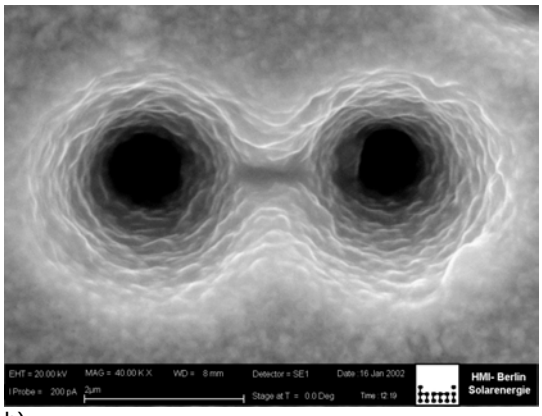

b)

Fig. 1: Ag deposition onto the inner walls of etched tracks in PI. SEM view into the interior of the tubules. Comparison of (a) conventional surface activation by nucleation center formation using a $SnCl_2$ solution, and (b) ion-induced surface activation using a 300 keV Ne^+ beam at 10^{14} cm^{-2}.

Furthermore, the limited range of the postirradiation allows one to restrict the metal tubule formation to the surface-near track region only. Two such short tubules on front and back side of an ion track can be used as transparent electrical contacts for embedded sensor materials.

A. Petrov, D. Fink, M. Müller in collaboration with V. Rao (Universität Mangalore, India), W. Fahrner (Fernuniversität Hagen, Germany), A. Schulz (SDK Technik GmbH, Quedlinburg, Germany), M. Behar (UFRGS Porto Alegre, Brazil)
(SF4.01a Atomic Dynamics: Ion Impact)

Bond lengths in $Cd_{1-x}Zn_xTe$ beyond linear laws

We have studied the local structure around the constituent atoms in the mixed system $Cd_{1-x}Zn_xTe$ with different composition x. In an earlier study this system was already investigated with Te as central absorbing atom alone and only at the Te L_{III}-edge [1]. For $Ga_{1-x}In_xAs$, as the textbook example of ternary alloys with zincblende structure, it was found that on an atomic scale bond lengths deviate strongly from the virtual-crystal approximation (VCA, Vegard's law) [2]. Using K-edge absorption on all three constituents, we have now extended the investigation to much lower concentrations, and to all constituent elements, and were able to extract considerable details from simultaneous fits up to the second shell. In addition, we have complemented the extracted experimental bond lengths with calculations of the lattice relaxation within the framework of the density functional theory using the WIEN97 code [3].

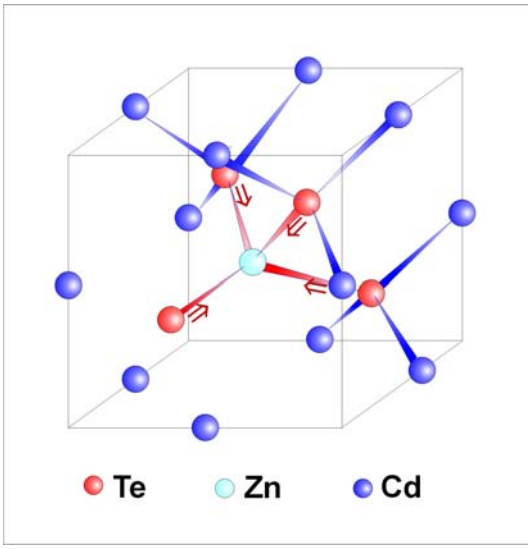

Fig. 1: Illustration of the local lattice relaxation with the incorporation of a Zn atom, replacing a Cd atom in a CdTe lattice. In the case of a Cd atom replacing a Zn atom in a ZnTe lattice the forces are in the opposite direction.

We have measured the absorption fine structure in the fluorescence yield mode at the E4- (in the case of Zn) and the X1- (in the case of Te and Cd) beamline of HASYLAB at DESY. In the case of Zn, the fluorescence was detected using a standard NaI:Tl scintillation counter and employing critical absorption. In the case of Cd and Te, the higher energies of the respective K-edges allowed us to measure the absorption in transmission with an ionization chamber as well as in fluorescence mode detected with the 5-segment Ge-detector. The crystals of $Cd_{1-x}Zn_xTe$ with the various x values were obtained from the Institute of Physics, HU Berlin [3]. Samples with x=0 and x=1 and samples with 2 % Zn were obtained from Crystec GmbH [5]. The transmission was measured on powdered samples mixed with graphite or PE. The analysis of the observed absorption spectra was done following the standard FEFF procedure [6].

Using all three constituents as central absorbing atom, the local bond strength is found to dominate over the averaging of the bulk known as the virtual crystal approximation. This is reflected in the well-defined first neighbor Te-shell to the absorbing cation Zn or Cd over the whole concentration range in terms of width, amplitude, and position, while in the case of Te, the absorption spectra are best fit with a superposition of two distinct bond lengths, whenever both, Te-Zn and Te-Cd, bonds are involved.

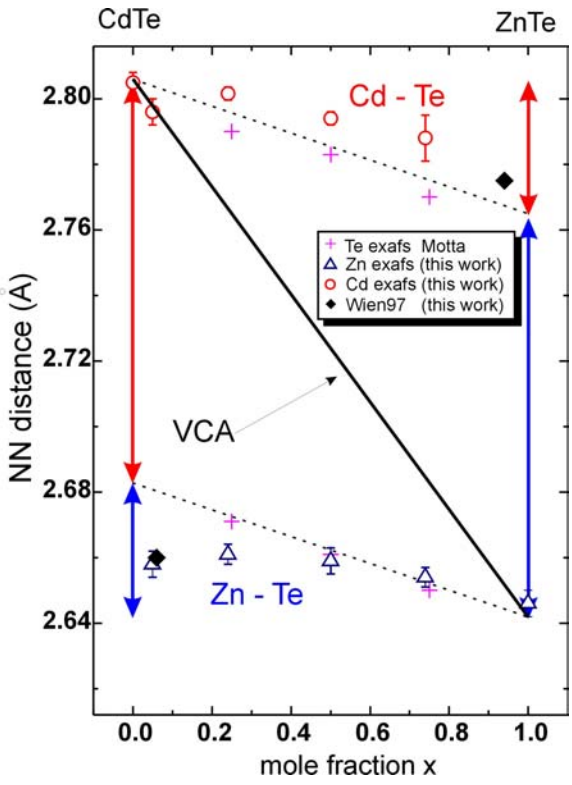

Fig. 2: Local bond length of Cd – Te (circles) and Zn – Te (triangles). The local bond lengths deviate strongly from Vegard's law (VCA) as given by x-ray diffraction data [1] and are significantly less than a quarter of the bond-length difference of the pure systems (compare the arrows). Calculated values (WIEN97, diamonds) support the experimentally observed strong local nature of the cation-anion bond.

In general, the local bond lengths deviate only slightly from their 'natural' values determined in the pure binary components ZnTe and CdTe. The deviations are significantly less than a quarter of the difference of the lengths in the binary systems as predicted by a simple radial force constant model [6] (see Fig. 2). For the second shell, bimodal anion-anion distances are found while the cation-cation distances already follow the virtual crystal averaging of the lattice (Fig. 3).

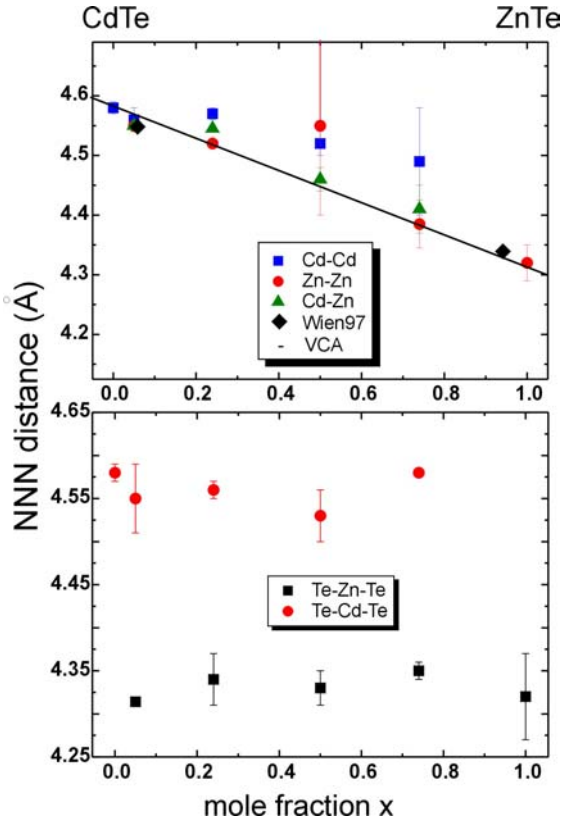

Fig. 3: Second-neighbor distances. The cation-cation distances (top) together with the calculated results follow the VCA, and the anion-anion distances (bottom) are bimodal depending on the type of cation in-between.

The strong local nature of the Zn-Te bond observed in CdTe at low Zn concentration as well as for Cd-Te in ZnTe (extrapolated to low Cd concentration) has prompted us to perform appropriate ab-initio calculations based on the DFT theory. The linearized augmented plane wave (LAPW) method was used, as implemented in the WIEN97 program package, and equilibrium atomic lattice positions were calculated for the scenario of 1 Zn atom in a supercell of 32 atoms in a CdTe lattice, or 1 Cd atom in a ZnTe lattice, resp. with the fixed lattice constants taken from experiment. The input parameters were set up in accordance with calculations on As in CdTe by Lany et al. [7].

Relaxations along the symmetry directions of the first-, second-, and third-shell atoms were allowed until the calculated forces were below 0.02 eV/Å. The resulting distances for the first shell are 2.660 Å for Zn embedded in a supercell of CdTe, which is 5.2% shorter than the Cd-Te bond length of the surrounding lattice, and 2.775 Å for Cd embedded in a supercell of ZnTe, which is 4.9 % longer than the respective Zn-Te bond length of the surrounding lattice. Both results are in good agreement with the experimental values (see Fig. 2 for the first shell and Fig. 3 for the second shell).

Acknowledgement: This work was partly supported by the Bundesminister für Bildung und Forschung under the grant 03MK4HMI8. The authors are grateful to the HASYLAB staff at DESY, in particular to N. Haack and E. Welter. We thank H. Rossner for his advice on analysis and fitting of the data. Special thanks go to S. Lany from the University in Saarbrücken for his advice in setting up the input parameters for our WIEN97 calculations.

References

[1] Motta, N.; Balzarotti, A.; Letardi,P.; Kisiel, A.; Czyzyk, M.T.; Zimnal-Starnawska, M.;M. Podgorny, M.: Journal of Crystal Growth 72, 1985, pp. 205

[2] Mikkelsen, J.C.; Boyce, J.B.: Phys. Rev. Lett. 49, 1982, pp. 1412

[3] Blaha, P.; Schwarz, K.; Luitz, J.: WIEN97 (Karlheinz Schwarz, TU Wien, Austria,1999), ISBN 3-9501031-0-4, Institut für Physik, Präparationslabor Sölle, Humboldt-Universität zu Berlin, D-10115 Berlin

[4] Newville, M.; Livins, P.; Yacoby, Y.; Rehr, J.J.; Stern, E.A.: Phys. Rev. B47, 1993, 14126

[5] Rehr, J.J.; Mustre de Leon, J.; Zabinsky, S.I.; Albers, R.C.: J. Am. Chem. Soc.113, 1991, pp. 5135

[6] Shih, C.K.; Spicer, W.E.; Harrison, W.A.; Sher, A.: Phys. Rev. B 31, 1985, pp. 1139

[7] Lany, S.; Blaha, P.; Hamann, J.; Ostheimer, V.; Wolf, H.; Wichert, Th.: Phys. Rev. B 62, 200, pp. 2259

V. Koteski, H. Haas, E. Holub-Krappe, N. Ivanovic, H.-E. Mahnke
(SF4.01.c Formation and transformation of local structures)

A new tool for proton beam eye treatment planning

Planning proton beam radiotherapy of the eye requires special features of the planning software. Up to now, the only existing program for this purpose, EYEPLAN, is used with very good success since 1975. However, the program shows some limitations that may cause problems for certain patients:

1. the program allows only spherical eyeball models,
2. the program is model-based, no diagnostic data input is possible,
3. the anatomic structures of the model (except for the tumor) are fixed.

In cases with a large eyeball deformation, the EYEPLAN may fail to place anatomic structures at the right position, leading to partial wrong dose calculations for tissues with a high radiation complication risk such as the lens or the optic nerve. To improve this point for the HMI proton therapy, a routine procedure has been established in collaboration with the Universitätsklinikum Benjamin Franklin (UKBF) to obtain high-quality X-ray computer tomography (CT) scans with a well-determined fixation of the patients eye. A dedicated program, JDISPLAY, has been developed in collaboration with the Department Medizinische Informatik of the UKBF to provide visualization of these CT scans and measurement tools and allow a comparison with the EYEPLAN model of the tumor eye. Using this program, the eye model can be verified quite easily and corrections may be obtained to modify the eye model to get the best possible approximation to reality.

The program is designed to work with medical image data formats (i.e. DICOM and ACR-NEMA). In Fig. 1, a screen capture of JDISPLAY shows an example where an overlay of the model and diagnostic data is created. The alignment of both images is done to fit the detected centroids of the marker clip positions. Fig. 2 shows in a different example the comparison of the projected tumor eye model with the patients CT data. The overlay shows a good agreement between the positions of tumor, sclera, cornea, lens and optic nerve.
The JDISPLAY tool is in use for treatment planning since October 2001.

C. Derz, J. Heese in collaboration with J. Bernarding (Univ. Klinikum Benjamin Franklin, Abt. Medizinische Informatik, FU Berlin)
(SF4.03 Eye Tumor Therapy)

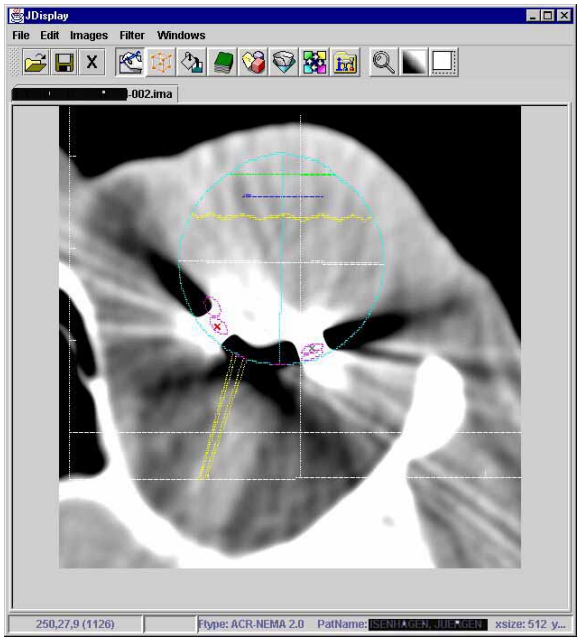

Fig. 1: Alignment of eye model and CT slice with the marker clip positions.

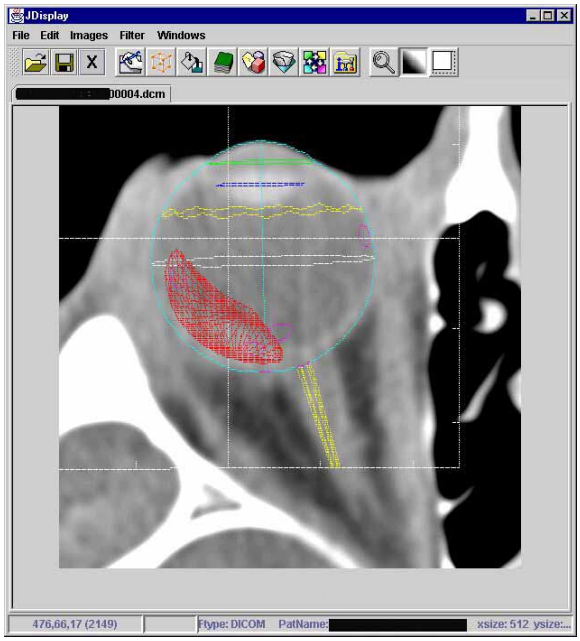

Fig. 2: Comparison of the eye model and diagnostic data.

Measurement of 3D dose distributions using BANG® polymer-gel dosimeters

Polymer gels can be used to visualize three-dimensional dose distributions of ionizing radiation: the gels are tissue-equivalent, phantom and detector material are identical. An irradiation can be performed in a short time and then be analyzed whereas 3D-diode scans in water tanks with high spatial resolution are very time-consuming. BANG® polymer gels provided by MGS Research, Inc. (Madison, CT) are used in conventional radiotherapy in the verification process of dynamic irradiations. BANG gel is composed of aqueous gelatin infused with acrylamide and N, N'-methylene-bisacrylamide monomers, and made hypoxic by nitrogen saturation. Irradiation of the gel causes localized polymerization of the monomers, which, in turn, reduces the transverse NMR relaxation times of water protons. The dose dependence of the NMR transverse relaxation rate, R_2, is reproducible and linear. Magnetic resonance imaging (MRI) may be used to obtain accurate 3D dose distributions. Since the radiation-induced polymers do not diffuse through the gelatin matrix, the dose distributions recorded by BANG gels are stable for a certain period of time. Since the light-scattering properties of the polymerized regions are different from those of the clear, non-irradiated regions, the dose distributions are visible as seen in Fig. 1.

The goal of this project is to explore the use of BANG gels in proton radiotherapy where, in contrast to conventional megavoltage radiotherapy two complications occur:

1. a very high spatial resolution is needed, affecting the obtainable signal/noise ratio
2. the proton depth dose distributions show a strong LET-dependence

BANG gels have been irradiated with several proton doses. The MRI scans have been performed at the 1,5 T Siemens Magnetom Vision at the Charité in Berlin-Mitte using a head coil. The first results obtained with these gels show promising results, however, the signal/noise ratio needs to be improved to allow a better spatial resolution. Thus, more efforts have to be made to find optimum MRI sequences for the analysis of the irradiated gels.

S. Stiefel, J. Heese, J. Heufelder in collaboration with G. Grebe, M. Roll (Technische Fachhochschule Berlin, Abt. Medizinische Physik); M. Pfaender, L. Lüdemann (Charité, Humboldt Universität Berlin, Abt. Strahlentherapie und Radiologie)
(SF4.03 Eye Tumor Therapy)

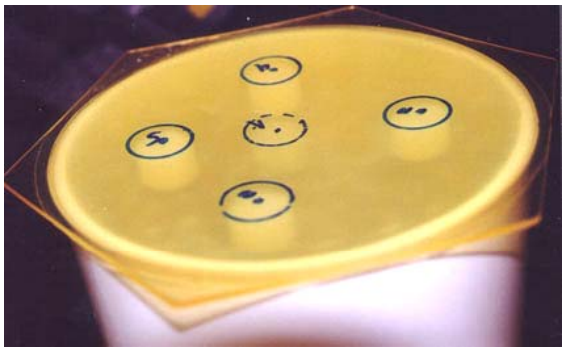

Fig. 1: BANG polymer gel phantom photographed after irradiation. Visible are the marked entrance regions of the proton beams applied with different doses.

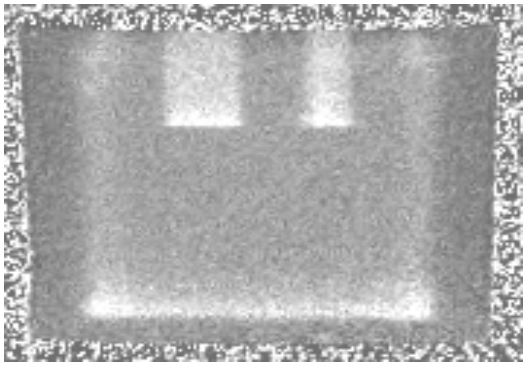

Fig. 2: Relaxation rate R_2 in a sagittal slice of the phantom showing two unmodulated proton irradiation areas. The image has been calculated from a MRI spin-echo scan with TE_1= 70 ms, TE_2=140 ms, TR = 1000 ms. The Bragg peaks at the end of the proton range are clearly visible.

Proton irradiation tests of the Rosetta ROLIS CCD detector electronics

ROLIS-D is a light-weight and compact wide-angle camera which will be operated on the Rosetta landing device during the descent phase from the Rosetta Orbiter to the nucleus of comet 46P/Wirtanen, and during the operational phase on the surface of the nucleus. Proton radiation captured inside the radiation belts of the earth, and protons ejected into the solar wind by solar flares have been identified as the dominating constituents of the Rosetta radiation environment. In order to verify the proper operation of all ROLIS-D sub-units, and to document degradations in performance caused by radiation, proton radiation step-stress units (series of cumulative irradiation steps and accompanying test measurements) were carried out for all those sub-units that are potentially sensitive to this irradiation, and the behavior of which was not known with sufficient certainty.

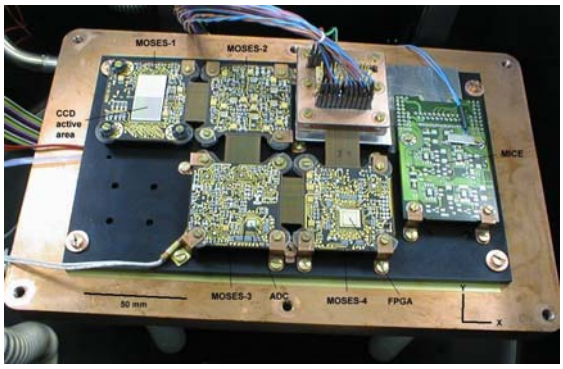

Fig.1: MOSES detector electronics mounted inside the thermal vacuum chamber for functional tests and performance measurements after proton irradiation.

The irradiation was performed at one of the high-energy target areas of the ISL. At this target station, the beam leaves the vacuum of the beam-line through a thin foil. For protons, a 50 µm thin Kapton foil is used. The objects to be irradiated remain in normal atmosphere, hence there are no restrictions to size or sensitivity of the device. The tests of the components required not a high-energy monoenergetic proton beam, but a continuous spectra with an intensity maximum at a quite low energy. To achieve this, Plexiglas absorbers were introduced in the beam and the resulting spectra were monitored by a particle detector.

Each unit received its individual proton energy dose steps which are characteristic for the whole mission. Typical fluxes were $2 \cdot 10^{10}$ to $1 \cdot 10^{11}$ protons / cm^2, corresponding to total absorbed energy doses of max. 12 – 60 krad (Si) for the different electronic parts.

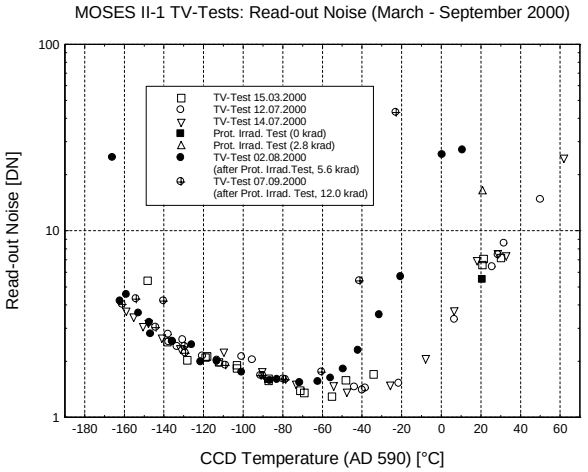

Fig. 2: Read-out noise of the MOSES detector electronics as a function of CCD temperature and increasing total energy doses induced by proton irradiation. Note that the read-out noise returns to normal values at approx. –70°C even after 12 krad of radiation of the whole detector electronics including the CCD, whereas at room temperature an increase by more than a factor of 10 can be observed

After each irradiation step the complete detector electronics was mounted into a thermal vacuum chamber where the performance and the functioning was tested. Although the principle functions of the imaging electronics were maintained even after a total absorbed energy dose of 12 krad (Si) directly on the unprotected CCD (Thomson THX7888A), a significant and irrevocable increase in the dark current generation and the read-out noise was observed. In contrast to this, the LED array (LEDs directly bonded / chip-on-board) did not show any significant degradations larger than approx. 6 % decrease in their fluxes even after an absorbed dose of 60 krad (Si) of proton irradiation (measurements only at room temperature).

A. Denker, H. Homeyer in collaboration with H.-G. Grothues, M. Tschentscher, H. Michaelis (DLR Institute of Space Sensor Technology & Planetary Exploration)
(SF4.04 Ion Beams for Technology)

Progress in heavy ion beam production

RFQ-Injector

A new coupling system has been tested successfully on one RFQ-stage. The **coupling loop** provides transformation of the high resonator impedance to the 50 Ohm impedance of the connected amplifier system. In contrast to the old system, the new design avoids induced self oscillation within a part of the RFQ-frequency-band.

Several openings of the RFQ-tank revealed changes of the surfaces of the **RFQ-electrodes** resulting from sputtering of particles which are not transmitted. By cutting out those fractions of the beam which cannot be bunched into the window of phase acceptance of the RFQ, the sputtering at the electrodes can be reduced. This reduction is realized by a **chopper** which has been installed in front of the RFQ. Now, about two thirds of the out-of phase particles are deflected onto a plate in front of the RFQ.

The **tuning of the RFQ parameters** (RF-phases and amplitudes as well as the parameters of the injection elements (phase and amplitude of the bunchers) has been improved considerably due to progress in diagnostics and control system. Now, the tuning can be monitored by a fast energy analyses of the accelerated beam. This particularly important for beams with the second RFQ-structure operating in transport mode. All RF-phases and amplitudes influence the energy centroids and energy distributions of the accelerated ions. This behavior is demonstrated in Fig. 1. With the newly installed energy diagnosis, the energy of RFQ-beams can be tuned exactly before injecting into the cyclotron.

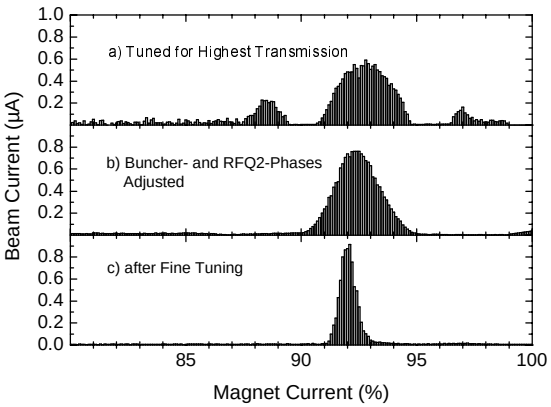

Fig. 1: Analysed Beam after RFQ-Acceleration. The first analysis after tuning for highest transmission shows a broad energy distribution (a). Coarse tuning of the most critical phases reduces the side bands (b). Small energy widths can be obtained by fine tuning all influencing elements (c).

Ion Sources

Following the results of detailed calculations and measurements, the ion optics of the injector platform was redesigned and rebuilt. In addition, we installed the latest version of the supernanogan ECR-ion-source and improved the vacuum system

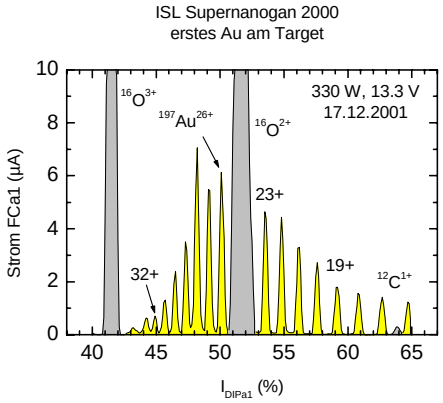

Fig.2: Charge State Distribution for Au-Ions. Au-ions are now offered at ISL. With charge state 26, beams of 350 MeV are produced with high intensity.

at extraction. In order to obtain the necessary long and short term stability several measures have been taken, including better stabilization of the gas flow, new materials for the extraction lens, air conditioning and cooling temperatures. As a result, very stable Kr-beams, highly charged Xe-beams (charge state 26) and most importantly Au-beams have been produced. The charge state spectrum of Au-ions with a microwave power of 300 W is shown in Fig. 2. We expect that stable Au 32^{+} beams allowing the production of energies higher than 600 MeV are possible in the near future.

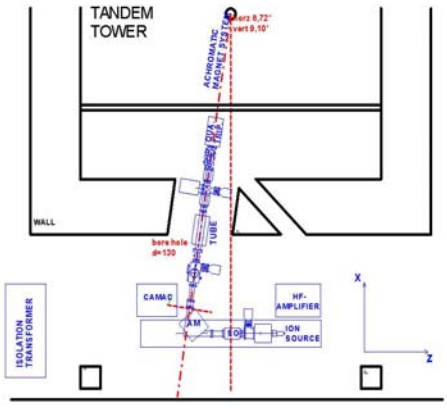

Fig. 3: A schematic view on the second ion source and the new beam line from above. SO and AM are the solenoid and the analysing dipole.

Experiences with the existing ECR ion sources have shown that the production of highly charged heavy ions, in particular metallic ions, needs extensive tuning times to finally reach the necessary equilibrium to obtain a high beam current stability. Thus, a second ECR ion source will lead to a reduction of the injector tuning time, since one source can be tuned for the next beam while the other is still in operation.

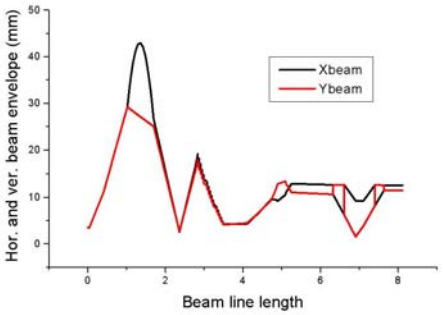

Fig. 4: Injection from the second ECR Source. After the analysis, the ions are accelerated. At inflection into the existing beam line the beam is parallel beam in both directions.

The installation of a second 14.5 GHz ECR ion source on a 150 kV platform in an adjoining room of the former tandem tower has been started. The layout is shown in Fig. 3. The acceleration tube has to be installed inside the thick wall originally necessary for radiation shielding when the building housed the 8 MV Tandem accelerator. The constraints imposed by the new site required elaborate beam optics calculations. As shown in Fig. 4, the required parallel beam in both, x- and y-direction, has been achieved.

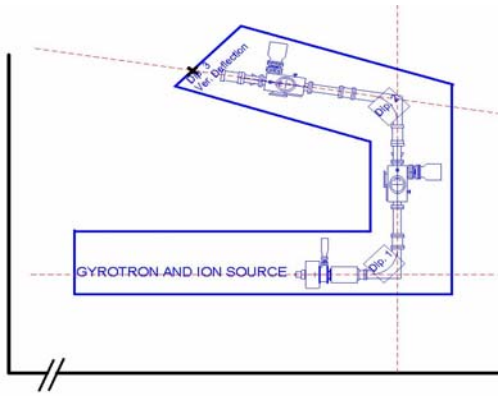

Fig. 5: Injection Line for a superconducting ECR Ion Source
The injection into the existing beam line is marked by a cross in the middle of the quadratic room of 7.5X7.5 m².

In order to exhaust to the full power of the RFQ-injector charge to mass ratios of 1/4.7 for elements up to U are necessary to produce the highest possible energy of 6 MeV/N after the cyclotron. This goal can only be achieved with ECR ion sources operating at higher RF-frequencies. First studies for the installation of a respective source have been started.
For the production of 50+ Uranium with sufficiently high beam currents (100 pnA), 28 GHz and magnetic confinement fields up to 4 Tesla seam to be necessary [1]. Such high magnetic fields can only be generated by superconducting magnets.

A few prototypes of superconducting ECR ion sources are operating (SERSE at Catania) [1] or are starting operation (VENUS of the 88" cyclotron at LBL, Berkeley) [2].

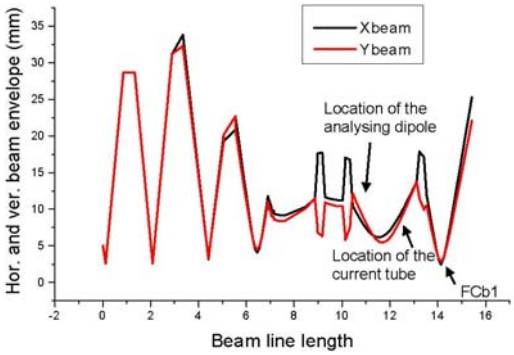

Fig. 6: The transverse beam envelopes. As indicated, the envelopes show a small beam diameter at the position of the analysis dipole and the tube.

Similar to the second source, the location and the connection of a new superconducting source to the existing installation is the first problem to overcome.
A possible realization on a high voltage platform on the floor above the existing source is shown in fig. 5. be. It offers the largest space behind the source for the RF-injection. Beam transport calculations show that the beam is narrow enough to pass the small gap of the existing analyzing dipole and diverges at the position of Faraday cup FCb1 as required by the existing injection beam line (Fig.6). On the hand, the long beam transport system and the corresponding power needed for the operation may lead to further constraints. Detailed design studies to determine the total space needed for the source, microwave system and total will carried out in 2002.

References
[1] Gammino, S.; Ciavola, G.; Celona, L.: Rev. Sci. Instr., Vol. 72, No 10, October 2001

[2] Lyneis, C.M. et al, VENUS: The Next Generation ECR Ion Source, Proc. Cyclotron Conf. 2001

H. Homeyer, P. Arndt, W. Busse, A. Denker, W. Pelzer, A. Meseck, Ch. Rethfeldt, J. Röhrich
(SF4.05a Accelerator Development)

New features of the ISL-Accelerator-Control-System

The proposed seamless upgrade of the control system for the continuously running ISL accelerator facility has reached the status of first practical applications.

The old ISL control system dates from the late 1970's and was originally designed for the VICKSI accelerator complex. It is based on a single server processor and software which was developed in-house. The new system will provide distributed processors and data bases, with modern graphics and as much commercial software as possible. In the first approach the CAMAC fieldbus will persist until new technologies are integrated for immediate use. The choice taken in the course of the 1990's consists of an OpenVMS cluster with workstations and X-Terminals for the presentation and human interaction level, with servers for the distributed data bases and transaction libraries, with rt-VAX's as front end servers for concurrent access to the fieldbus hardware (cf. Fig.1), with PVWave (Visual Numerics Inc.) to provide graphics for data evaluation as an intermediate step and with Vsystem (VISTA Inc.) as the basic control system software which

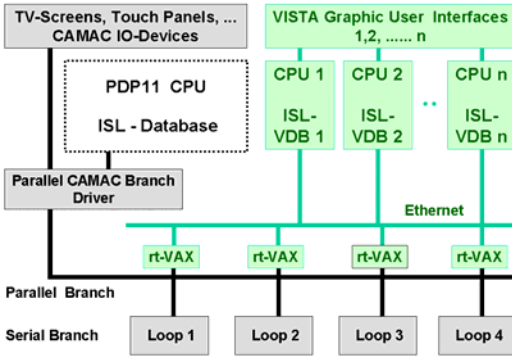

Fig. 1: Schema of the ISL-Control System Upgrade.
The VISTA Databases (VDB) are distributed among several CPU's, supporting Graphic User Interfaces on X-Terminals and handling the CAMAC communication by remote procedure calls to Serial Highway front end servers (rt-VAX's). Simultaneous access to the Serial Highways from either the Parallel Branch or the rt-VAX's is coordinated by hardware semaphores.

supports distributed data bases along with access and transaction libraries in its middle layer. The common API for application programming is transparent with regard to remote network. In the application layer Vsystem incorporates a drawing tool for graphical applications and a bunch of general application programs such as scripting and alarm handling, all of which can be live linked to respective accelerator parameters. - Both versions of the ISL control system will be operating in parallel for some interim time.

New Control System Applications

The new control system allows the implementation of graphical information displays as shown in fig.2, giving a complete live overview of the status of accelerator sections of interest. Graphical features like specific colors for a 'normal', 'warning' and 'alarm' status, trend charts and active text or bars support the ergonomic information which is presented to the operators or machine physicists.

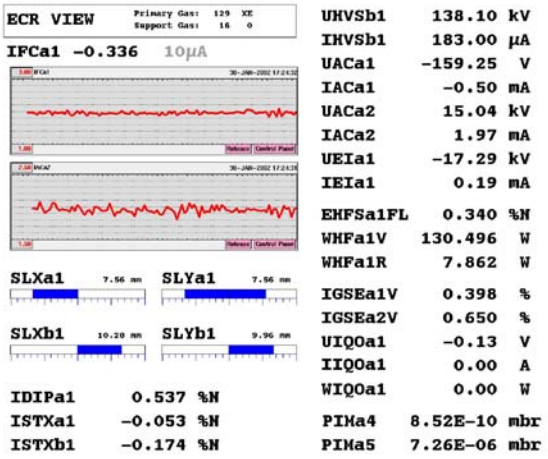

Fig. 2: Typical Vista Graphic User Interface. Trend Charts, Active Text and Bars display the actual status of the ECR Ion Source of the RFQ injection beamline.

As Vsystem is a multi-platform implementation allowing remote access in a heterogeneous network through a common transparent API, useful remote applications can be developed for remote monitoring and control of a large facilities like the HMI Ion Beam Laboratory. For remote visualisation and archived data access a first Linux Application Server was installed (fig.3). It collects and archives device data and generates 24h trend charts which can be viewed via the Internet. It also supports WAP-Handy data exchange and sends alarm messages when requested.

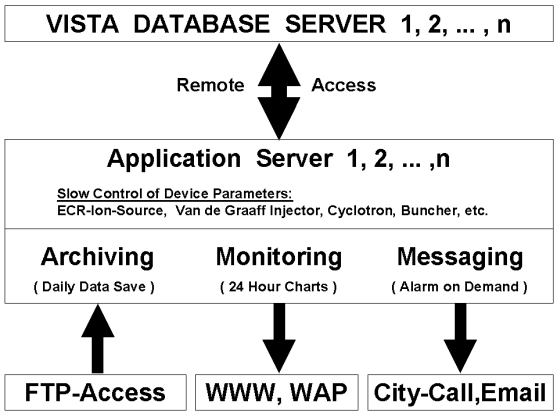

Fig. 3: Linux Application Server supporting the monitoring of the ISL-Facility.

W. Busse, C. Rethfeldt, M. Birnbaum, D. Draht, R. Grünke, D. Hildebrand, J. Reinicke
(SF4.05a Accelerator Development)

Department

SF5 Theoretical Physics

Magnetic systems of reduced dimension

Investigations of magnetic properties of thin films and multilayers, with particular emphasis on the role of collective excitations (spin waves).

There is considerable experimental and theoretical interest in the way the reorientation of the magnetization of thin magnetic films depends upon the temperature and film thickness. In our work, we have enlisted the help of the many-body Green's functions theory (GFT) in order to throw some light on this problem. The choice of such a method was guided by the requirement of being able to go beyond the mean-field theory (MFT) that is usually applied. This is of considerable importance because it turns out that collective excitations in the form of spin waves (magnons) are much more important for thin films than for bulk magnetic materials.

The Hamiltonian for the model consists of an isotropic Heisenberg exchange interaction, single-ion anisotropies, the magnetic dipole-dipole coupling and an external magnetic field.

In previous papers [2, 3], which deal with the magnetic reorientation transition of ferromagnetic multilayers, only the lowest-order Green's functions were used. In order to obtain a closed system of equations one had to decouple the higher-order Green's functions. For the exchange interaction terms, use was made of the Tyablikov decoupling (RPA), which we have shown in reference [1] to be a very good approximation in simple exactly solvable cases; for the anisotropy terms the Anderson-Callen decoupling was applied, which is only a satisfactory approximation for small anisotropies.

The essential progress in our recent work [4] came about from taking higher-order Green's functions explicitly into account. An exact treatment of the terms coming from the anisotropy is then possible because there exist relations among products of spin operators which lead to closure of the hierarchy of the equations of motion for the Green's functions. Terms coming from the exchange interaction, however, still have to be decoupled in a RPA-like fashion.

In the figure, a comparison of Curie temperatures for a spin $S = 1$ ferromagnetic monolayer demonstrates the superiority of the exact treatment of the anisotropy over the Anderson-Callen decoupling and the mean-field theory. The Anderson-Callen decoupling is only good for small anisotropies K_2, whereas MFT violates the Mermin-Wagner theorem ($T_{Curie} \rightarrow 0$ for $K_2 \rightarrow 0$). MFT approaches the exact values for large anisotropies, which is physically reasonable, because this corresponds to the Ising limit.

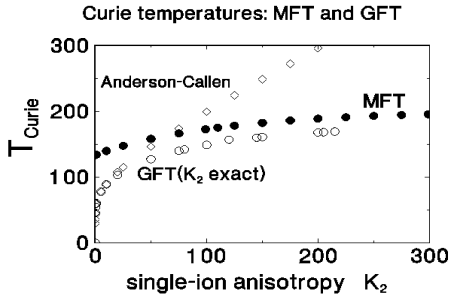

Fig.1: Comparison of Curie temperatures calculated with the exact (GFT) treatment of the anisopy terms, the Anderson-Callen decoupling and mean-field theory (MFT).

In collaboration with P. Henelius (Stockholm), we have also begun an investigation of the quality of the Green's function theory by comparing with results of 'exact' Quantum Monte Carlo (QMC) methods for an Heisenberg model with single-ion anisotropy .

References

[1] A. Ecker, P. Fröbrich, P.J. Jensen, and P.J. Kuntz, J. Phys., Condens. Matter 11, 1557 (1999).

[2] P. Fröbrich, P.J. Jensen, and P.J. Kuntz, Eur. Phys. J. B 13, 477 (2000).

[3] P. Fröbrich, P.J. Jensen, P.J. Kuntz, and A. Ecker, Eur. Phys. J. B 18, 579 (2000).

[4] P. Fröbrich, P.J. Kuntz, M. Saber, Ann. Physik, 5, 387 (2002).

P. Fröbrich, P.J. Kuntz, A. Ecker
(SF5.01a Magnetic Systems of Reduced Dimension)

Dipolar interactions in superconductor-ferromagnet heterostructures

In this work, we consider the role played by the long-range-dipolar interaction in heterostructures composed of superconducting and ferromagnetic materials.

This work focusses on the interaction between superconductivity and ferromagnetism in heterostructures composed of superconducting/ferromagnetic/superconducting (SC/FM/SC) layers, which have been produced and experimentally investigated for many different combinations of materials, e.g. V/Fe, V/Ni, Mo/Ni, Pb/EuS, EuO/Al, Nb/Gd, see [1,2,3].

There are three main reasons which lead to competition between superconducting order and ferromagnetic order in bulk materials, namely the superconducting pair breaking effects induced by the localized magnetic moments and the suppression of the RKKY exchange interaction between the magnetic moments, due to the presence of the Cooper pairs, these two effects being present in s-wave and d-wave superconductors, and also the interaction of the long-range dipolar field of the magnetic moments with the superconducting electrons, which also leads to Cooper-pair breaking, this effect being present in all superconductors, irrespective of the nature of the paring.

The two first effects are mitigated in SC/FM/SC heterostructures, as there is no bulk coexistence of magnetism and superconductivity, except possibly due to the proximity effect, which is negligible in ferromagnetic insulators, e.g. in EuS. One is thus naturally led to consider the interaction between the dipolar fields and superconductivity in these heterostructures, and as a starting point [4], we have considered systems in which the thickness of the ferromagnetic layers is much smaller than the thickness of the superconducting layers (i.e. the number of atomic mono-layers of one material is much smaller than the other). The picture below shows a schematic view of one such heterostructure, where the relative dimensions of the two substructures, the superconducting and the ferromagnetic one, are emphasized.

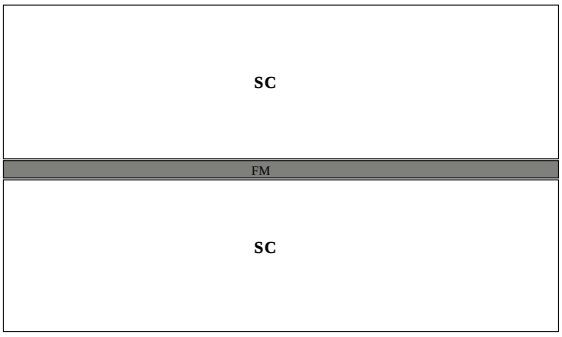

In this case, and for a type I superconductor, one can consider that superconductivity is not affected by the dipolar field, the dipolar field configuration being nevertheless changed by the repulsion of the field from the superconductors, due to the Meissner effect. Working in the London approximation, we have determined the dipolar field configuration and its energy, and we have found that for wavelengths larger than the London penetration depth of the superconductor, the field configuration has a two-dimensional form, as the magnetic flux is confined to the ferromagnetic layer by the presence of the superconducting layers. The picture below shows the result of the calculation of the dipolar energy kernel for the SC/FM/SC layer in the London approximation as a function of the wave number k. The long-dashed plot is the ordinary three-dimensional dipolar kernel and the short-dashed plot the two dimensional one. The result of our calculation is given by the continuous gray plot (the plot being given in units of the inverse London penetration depth). It is seen that this calculation interpolates between the two dimensional result for small wave-numbers (large wavelengths) and the three-dimensional result for large wave-numbers (small wavelengths), the cross-over length being the London penetration depth, here equal to one.

This effect leads to a change in the expression of the longitudinal magnetic susceptibility of the ferromagnetic layers and could have a pronounced effect at a phase transition between the para-magnetic/ferromagnetic states, provided that a magnetic material is found with a low enough Curie temperature such that the material of which the superconducting layers are made is already in the superconducting state at this temperature. EuS, being a magnetic insulator and having a Curie temperature of 16.5 K stands as an ideal choice for the constituent of the magnetic layer, another possibility being the use of layers of La/Gd [5].

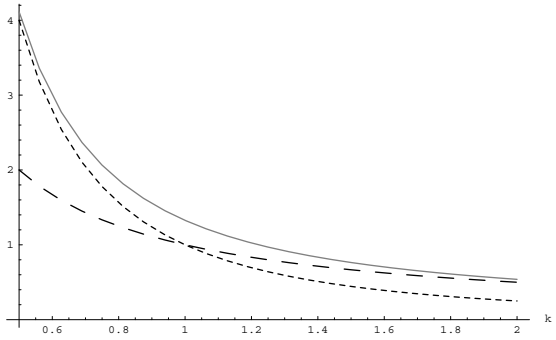

References

[1] B. Y. Jin and J. B. Ketterson, Adv. Phys. 38, 189 (1989).

[2] W. Zinn, B. Saftic, N. Rasula, M. Mirabal and J. Kohne, J. Magn. Magn. Mater. 35, 329 (1983).

[3] H. K. Wong and J. B. Ketterson, J. Low Temp. Phys. 63, 139 (1986); H. K. Wong, B. Y. Jin, H. Q. Yang, J. B. Ketterson and J. Hilliard, ibid. 63, 307 (1986).

[4] J. E. Santos, E. Frey and F. Schwabl, Phys. Rev. B 63, 054439 (2001).

[5] H. Zabel, (private communication).

J. E. Santos, E. Frey (SF5.01a Magnetic Systems of Reduced Dimension)

Microcanonical thermodynamics

Microcanonical description of phase-transitions in "Small", non-extensive systems as nuclei, cluster and astrophysical systems.

Phase transitions and Second Law in finite systems.

Boltzmann's principle $S(E,N,V) = \ln W$ relates the entropy to the geometric area $e^{S(E,N,V)}$ of the manifold of constant energy in the (finite-N)-body phase space. By its definition $S(E,N)$ as a high dimensional integral it is everywhere multiply differentiable. In contrast to the believe of Schrödinger one can deduce from the principle all thermodynamics and especially all phenomena of phase transitions and critical phenomena. The topology of the curvature matrix $C(E,N)$ (Hessian) of $S(E,N)$ determines regions of pure phases, regions of phase separation, and (multi-)critical points and lines. Thus, $C(E,N)$ describes all kinds of phase-transitions with all their flavor. They are linked to convex (upwards bending) intruders of $S(E,N)$, where the canonical ensemble defined by the Laplace transform to the intensive variables becomes multi-modal, non-local, and violates the basic conservation laws (it mixes widely different conserved quantities). At such points the one-to-one mapping of the Legendre transform gets lost. These convex intruders in $S(E)$ correspond to negative heat capacities and have been recently experimentally verified in nuclear fragmentation [1,2].

These findings were a quite remarkable verification of the non-canonical behavior of real systems. Within Boltzmann's principle, Statistical Mechanics becomes a *geometric* theory addressing the whole ensemble or the manifold of points in phase space [4,5] which are consistent with the few macroscopic conserved control parameters, energy, number of particles, eventually volume and magnetization. Moreover, this interpretation leads to a straight derivation of irreversibility and the Second Law of Thermodynamics out of the time-reversible microscopic mechanical dynamics. It is the whole ensemble that spreads irreversibly over the accessible phase space not the single N-body trajectory. To overcome the constancy of the phase space measure due to Liouville, a special "measure" is introduced, the box-counting, which is interpreted as a consequence of the large redundancy of macroscopic theories like thermodynamics. This is all possible in contrast to recent "proofs" of the Second Law without invoking the thermodynamic limit, extensivity, or concavity of $S(E,N,V)$ and also without invoking any cosmological constraints. Without the thermodynamic limit or at phase-transitions the systems are usually not self-averaging, i.e. do not have a single peaked distribution in phase space. It is further shown that non-extensive Hamiltonian systems at equilibrium are described by Boltzmann's principle and not by Tsallis non-extensive statistics, c.f. next section. Details are found in ref. [3].

Phase transitions in closed rotating self-gravitating systems.

The microcanonical properties of a system of N classical particles interacting via Newtonian gravity as a function of the total energy E and, for the first time, of the total *angular momentum* L, are discussed. A very rich phase diagram is found: At large E the gravitational system is in a homogeneous gas phase. At low E there are several collapse phases: at small $L = 0$ there is a single star phase and for larger L there are several phases with two stars (double star systems). At intermediate angular-momenta we even find rotating homogeneous rings and also multi-star systems. Thus the microcanonical statistics shows a very rich and realistic scenario of a self-gravitating system. It thus proves to be superior to any canonical or non-extensive statistics based on the canonical ensemble [6]. Details in refs. [7,8].

References

[1] A. Chbihi, O. Schapiro, S. Salou, and D.H.E. Gross. Experimental and theoretical search for a phase transition in nuclear fragmentation. Eur. Phys. J. A, 5:251-255, (1999); http://xxx.lanl.gov/abs/nucl-th/9901016.

[2] M. D'Agostino et al. Negative heat capacity in the critical region of nuclear fragmentation: an experimental evidence of the liquid-gas phase transition. Phys. Lett. B, 473:219--225, 2000.

[3] D.H.E. Gross. Microcanonical thermodynamics: Phase transitions in "Small" systems, volume 66 of Lecture Notes in Physics. World Scientific, Singapore, 2001.

[4] D.H.E. Gross. Geometric foundation of Thermo-Statistics, Phase Transitions, Second law of Thermodynamics, but without Thermodynamic Limit, PCCP 2002, in print,cond-mat/0201235.

[5] D.H.E. Gross. Ensemble probabilistic equilibrium and non-equilibrium thermodynamics without the thermodynamic limit. In Foundations of Probability and Physics, ed. A. Khresnikov, XIII, p. 131-146, World Scientific 2001.

[6] D.H.E. Gross. Non-extensive Hamiltonian systems follow Boltzmann's principle not Tsallis statistics. - Phase Transitions, Second Law of thermodynamics, Physics A, 2002, in print,cond-mat/0106496.

[7] O. Fliegans and D.H.E. Gross. Effect of angular momentum on equilibrium properties of a self-gravitating system. Phys. Rev. E in print, 2002, http://xxx.lanl.gov/abs/cond--mat/0102062.

[8] V.E. Votyakov, H. Hidmi, A. De Martino and D.H.E. Gross. Microcanonical mean-field thermodynamics of self-gravitating and rotating systems. 2002, preprint: cond-mat/0202140.

D. Groß, H. Hidmi, A. De Martino, E. Votyakov
(SF5.01b Microcanonical Thermodynamics)

Axial and Landau gauge for a continuum electron in a homogeneous magnetic field1

A hydrogen-like atom placed in a homogeneous magnetic field represents one of the simplest possible atomic systems. However, its quantum mechanical treatment constitutes an exceedingly difficult task. While solutions have been obtained for a large number of special situations, it is fair to say that the full problem still awaits a theoretical description.

The problem has been mostly treated for extremely strong magnetic fields occurring in neutron stars and white dwarfs or in the study of chaotic behavior prevalent in highly excited Rydberg states, which are magnetically dominated already for field strengths of a few Teslas. The renewed interest derives from the attempts to form anti-hydrogen in a Penning trap by radiative recombination of antiprotons with positrons and from experiments in an electron cooler ring, where a magnetically guided beam of bare heavy ions merges an electron beam of almost the same velocity so that electrons are radiatively captured into a Coulomb bound state. In contrast to most theoretical treatments, which have dealt with bound or quasi-bound states, both cases of interest require the consideration of continuum electrons.

The process of radiative recombination requires a quantum description in order to correctly accommodate photon emission. However, it should be instructive to visualize the corresponding classical trajectories. While we have a good notion of how classical trajectories of continuum electrons look in a Coulomb field alone or in a homogeneous magnetic field alone, we find it difficult to imagine trajectories in a combined Coulomb and magnetic field. A quite surprising trajectory is shown in Fig. 1, signalling chaotic behavior. The upper part of the figure is a projection on a plane containing the vector of the $\boldsymbol{B}$ field, the lower part is a projection on a plane perpendicular to the field.

In a quantum treatment, it is advantageous to express the homogeneous magnetic field $\boldsymbol{B}$ by an auxiliary potential, the *vector potential* $\boldsymbol{A}$. However, there are several possible choices for the vector potential, all of them yielding the *same* magnetic field. These choices are denoted as *gauges* and are physically completely equivalent.

The gauge universally applied for an atom placed in a magnetic field $\boldsymbol{B}$ is the *axial gauge* defined by

$$\boldsymbol{A}^{(a)} = -(\boldsymbol{r} \times \boldsymbol{B})/2 \qquad (1)$$

which has the advantage that the angular momentum in the direction of the field is a constant of the motion. Another gauge, now mostly used in the context of solid state physics, is the *Landau gauge* introduced by L.D. Landau in his seminal 1930 paper with the vector potential constructed as $A_x = -B_y$ and $A_y = A_z = 0$, where $\boldsymbol{B}$ defines the z direction.

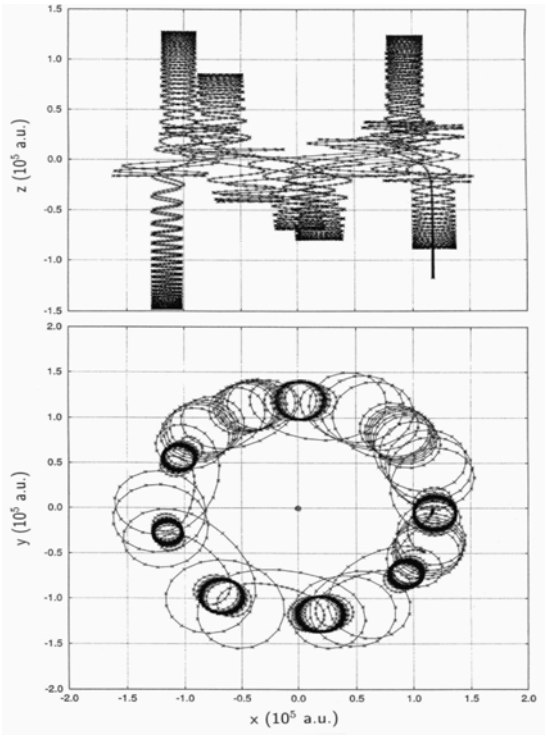

Fig. 1: Classical trajectory of an electron in the combined field of a bare nucleus with charge $Z = 6$ and a magnetic field in the z direction of $B_z = 42$ mT. The upper part shows the projection in the x-z plane, while the lower part shows the projection in the x-y plane. The electron has an asymptotic kinetic energy of $E_{\parallel} = 0.1$ meV in the direction of the field and of $E_{\perp} = 0.0$ meV perpendicular to the field.

In order to define differential cross sections for a reaction in a magnetic field, it is necessary to consider asymptotic plane-wave states in the limit of vanishing field strengths B . So far, all attempts to construct asymptotic plane waves have been performed in the axial gauge, which is suitable for localized states but meets with serious difficulties when trying to define scattering states in a homogeneous infinitely extended magnetic field.

In this work, after discussing the conventional axial and the Landau gauge we have demonstrated that the latter, in contrast to the former, allows for a simple construction of asymptotic states that tend to plane waves in the limit of vanishing field strength. Although the full quantum theory of a (non-localized) continuum electron placed in a combined Coulomb and magnetic field is still unsolved and will require enormous computational effort, we have shown a way that should lead to a more consistent and efficient treatment.

J. Eichler, Y. Yoshihama, N. Toshima
(SF5.01c Atomic Collisions)

[1] Phys.Rev. A65, 033404 (2002)

Semiconductor physics and photovoltaics

Theoretical studies, for photovoltaic applications, on the transport of charge carriers in semiconductors, on the growth of thin semiconductor films and on stresses in mesoscopic semiconductor structures.

Localized interface states in abrupt semiconductor heterojunctions have been studied within a tight-binding model. The intention was to provide a microscopic foundation for the results of similar studies which were based on the Keldysh two-band model within the envelope-function approximation. In a two-dimensional description, the tight-binding Hamiltonian has been constructed such that the Dirac-like bulk spectrum of the two-band model is recovered in the continuum limit. Localized states in heterojunctions have been shown to occur under conditions equivalent to those of the two band model. In particular, shallow interface states have been identified in noninverted junctions with intersecting bulk dispersion curves. As a specific example, the GaSb-AlSb heterojunction has been considered. The matching conditions of the envelope-function approximation have been analyzed within the tight-binding description.

Fluid dynamics studies have been resumed for the new design of a closed-space vapor transport reactor by Aixtron for HMI department SE2, which will be used for optimizing the processing of 1"x1'' semiconductor samples. With the given radiation heating power and ambient temperatures around the reactor we expect a very *encouraging temperature difference* of some 100^{o} to evolve across the narrow gap between the material dispensing container and the substrate site. We find however that the temperature on the substrate site may well be *homogenuous only within some* 10^{o}, depending on the unknown homogenity of the heating, which contributes to the inhomogenity of the deposited substrate. The blocks of amorphous graphite in the reactor must have for their purpose, the equilibration of temperatures laterally, have a thickness of some 2 cm which leads to loss of heat to their sides. We have discussed the use of other, thinner materials (Ag, Cu) with better heat conduction but the consequences for the chemistry in the reactor is as yet not clear. In preparation for fluid dynamics calculations which include chemical reactions we have prepared a routine that allows the flexible representation of surface reactions in the licensed CFD code.

In the construction of optical devices that manipulate photons at the blue and violet range of the spectrum, for example lasers using GaN, multi-quantum-wells of GaN/AlGaN are widely used. Photons from GaN are reflected by the AlGaN walls many times before they emerge. The crystalline flaws in GaN and AlGaN degrade the optical properties of device. Flaws in the form of micro-cracks often appear in AlGaN as it is grown epitaxially on GaN. These micro-cracks are clearly visible in the scanning electron microscope (SEM) images. These cracks arise because of the tensile stress induced in the epitaxial AlGaN by the GaN substrate due to the mismatch of their lattice constants. Although it is not yet possible to measure the depths of these flaws using atomic force microscope (AFM), nevertheless it is of great interest to know if the cracks penetrate into the underlying GaN as they then would influence the optical properties of GaN. Since the presence of micro-cracks affect the stress distribution in AlGaN, we have investigated the theoretical implication for the stress on the surface of AlGaN when the cracks penetrate into GaN. The stress distribution of a typical sample surface was calculated by the elasticity theory using the finite-element (FE) method. It was found that the stresses on the AlGaN surface from a FE calculation change smoothly as the cracks penetrate into GaN, see Fig. 1.

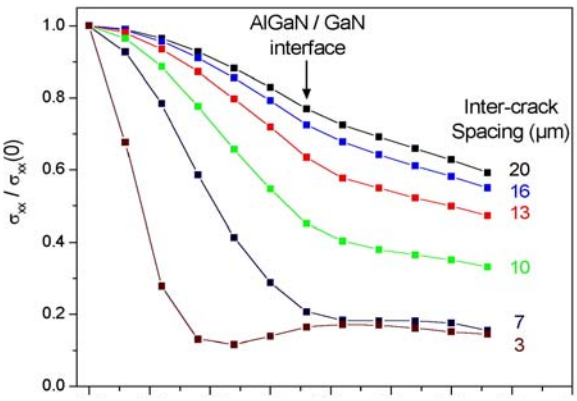

Fig. 1: The variation of stress on the AlGaN surface as a function of crack depth.

Hence we conclude that the cracking of GaN does not leave a signature behind in the stress distribution of the AlGaN surface.

U. Wille, W. Fritsch, Q. Liu, T. Weis
(SF5.02 Semiconductor physics and photovoltaics)

Biological physics

Binding dynamics of motor proteins and molecular complex

Theoretical studies of the "binding dynamics" of motor proteins and molecular complex to related biopolymer.

Complex phenomena in eukaryotic cell like mitosis, transport, cell movement and growth are based on the interaction of cellular components such as enzymes, cytoskeletal filament and related regulatory proteins.
An interesting process where all these components interact is the "binding dynamics". Such dynamics, involving a continuous adsorption and desorption kinetics of complex molecules on a substrate, is intrinsically off-equilibrium and shows interesting collective features which have been extensively investigated in our group.
More specifically, we have modeled the cooperative binding dynamics of ligands to a substrate, such as dimeric motor proteins to microtubules (see Fig. 1) or larger macromolecular complex like tropomyosin to actin filaments. We used numerical and analytical methods, e.g. lattice dynamics and reaction -diffusion models [3]. We analyzed the different phases of the system that occur during the relaxation kinetics and characterized them by their scaling behavior. We also discussed the effect of the cooperativity on the equilibrium binding stoichiometry (i.e. the mean total number of bound monomers per lattice site) and the relative consequences in the interpretation of 3-D images obtained by cryo-electron microscopy in microtubule-kinesins "decoration" experiments. Such experiments are crucial to understand the dynamics of kinesins motor proteins moving along microtubule.

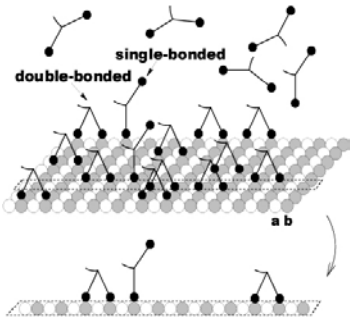

Fig.1: Schematic representation of the binding of kinesin dimers to a tubulin sheet.

References

[1] A. Vilfan, E. Frey, F. Schwabl, M. Thormählen, Y.-H. Song and E. Mandelkow. J. Molec. Biol. 312, (2001) 1011-1026.

[2] A. Vilfan, E. Frey and F. Schwabl. Europhys. Lett. 56, (2001) 420-426.

[3] See the java applet in the internet: http://www.tcm.phy.cam.ac.uk/~av242/decoration/

E. Frey, A. Parmeggiani
(Biological Physics)

Intracellular Ca^{2+} dynamics

Theoretical studies on the control of Ca^{2+} concentration in living cells.

The cell organelles like the nucleus, mitochondria or the endoplasmic reticulum (ER) in living cells are embedded in the cytosol. The endoplasmic reticulum and the mitochondria are used among other functions as Ca^{2+} stores. Living cells control the concentration of Ca^{2+} in the cytosol by release and uptake of Ca^{2+} by these intracellular storage compartments and by Ca^{2+} binding proteins, so called buffers.
The exchange of Ca^{2+} between the ER and the cytosol is controlled by channels and pumps. Upon opening of a channel, Ca^{2+} is released into the cytosol. Pumps transport Ca^{2+} against the concentration gradient back into the ER.
In recent years, biological research focussed on the elementary events of that dynamics. There is a hierarchy of events starting from the opening of single channels, via the concerted opening of small groups of channels to oscillations or travelling waves concerning the whole cell.
Our research aims at building up a model capable of covering the complete hierarchy. Recently, we developed an algorithm to incorporate spatial discreteness of channel clusters and stochasticity of channel behavior [1] into whole cell simulations. The ongoing research incorporates buffers into that model.
A topic of ongoing research is the question for the origin of long period oscillations. Periods of up to 2 minutes are observed in experiments but the dynamics of a single channel would predict periods in the range of 30s only. One hypothesis is that long period oscillations might be due to low nucleation probabilities for global events. We could show by simulations using the above mentioned algorithm with buffers incorporated, that that might be indeed the case (see Fig. 1).

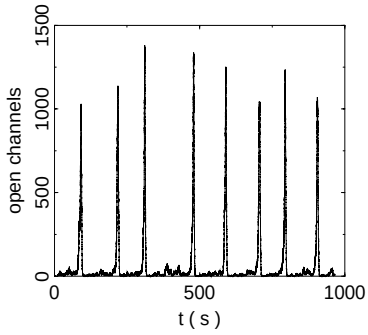

Fig. 1: Simulated long period oscillation.

References

[1] M. Falcke, L. Tsimring, H. Levine, Phys. Rev. E 62 (2000) 2636

M. Falcke, E. Frey (Biological Physics)

Soft condensed matter physics

Liquids of arbitrarily curved and looping flux lines in type-II superconductors

We have derived a hydrodynamic model for a liquid of arbitrarily curved and looping flux lines in type-II superconductors using a mapping of the vortex liquid onto a fictitious liquid of relativistic charged quantum bosons in 2+1 dimensions.

In the mixed phase of type-II superconductors, the magnetic field penetrates the sample in an array of vortex lines. For more than thirty years, the mixed phase was believed to be a single crystalline phase (Abrikosov lattice). Vortex matter has been a very active field of research since the discovery of high-temperature superconductivity. Thermal fluctuations, intervortex interactions, anisotropy due to a layered structure and interaction with quenched disorder reveal a very rich phase diagram which consists of various crystalline, glassy, and liquid phases. The experimental accessibility of these phases (and the transitions between them) and the theoretical challenges that they bring about render vortex matter a model system for the study of fundamental problems of both equilibrium and dynamic properties of systems of fluctuating, interacting extended objects.

The melting of the Abrikosov lattice is now well established both experimentally and theoretically. The nature of the resulting liquid phase remains, however, unclear. Is it a single phase? Is there a transition within the liquid phase? Most theoretical studies so far have been based on a mapping of the statistical mechanics of flux lines onto that of (non-relativistic) two-dimensional quantum bosons pioneered by D. R. Nelson. In this approach, flux lines are directed along the direction of the external magnetic field. Recent theoretical investigations (Z. Tesanovic, 1999) and numerical simulations (A. Sudbo et al., 1999), however, have suggested that overhangs of the lines and closed flux loops may play an important role in the properties of the liquid. A recent experiment (F. Bouquet et al., 2001) looking at measurements of magnetization and specific heat provides evidence for the existence of a liquid-liquid transition at high magnetic fields (above 20 Tesla). This transition appears to be in accord with the theoretical prediction by Tesanovic, Sudbo and collaborators of a vortex loop "blow out" (dubbed the Φ transition) in the liquid where closed loops of every size proliferate and thread the entire sample yielding an effective vanishing of the flux-line tension.

In collaboration with Prof. M. C. Marchetti (Syracuse University, U.S.A.), we have derived a long-wavelength, coarse-grained (hydrodynamic) description of a liquid of flux lines with overhangs and closed loops (Phys. Rev. B 64, 054518, (2001)). The starting point is a relativistic quantum analogy between flux lines and lines of time evolution of two-dimensional charged quantum bosons. Thermal fluctuations of the vortex lines correspond to quantum fluctuations of the bosons. The areal density of the vortex lines corresponds to the charge density of the bosons. The flux-line tension corresponds to the boson mass. The external magnetic field which sets up the mixed phase corresponds to the chemical potential of the charged boson liquid which controls the average charge density. Vortex loops appear naturally and correspond to boson-antiboson creation and annihilation events. In the end, boson degrees of freedom are integrated out and yield a physically transparent model in terms of vortex degrees of freedom. Our model, compared to similar previous models, has the advantage of treating both "field-induced lines" and "vortex loops" on equal footing. It also involves a finite penetration depth (of course, much longer than the coherence length) as opposed to the infinite penetration depth approximation used in previous models. We have calculated the Gaussian correlators of the various density fields involved and we have shown that loops and overhangs change the structure factor quite drastically at finite wavelengths.

Directed-line models based on the non-relativistic boson analogy have been particularly useful in describing vortex arrays pinned by correlated disorder (columnar defects). Uncorrected disorder (random point defects) , on the other hand, enhances the wiggling of the flux lines and leads beyond the regime of applicability of those models. Our model provides an appropriate framework for studying this kind of disorder and that is an very interesting direction for future work along with its ramifications with respect to the aforementioned Φ transition.

Dynamics of dense colloidal liquids

For multi-component mixture obeying overdamped colloidal (Brownian) dynamics, a mode-coupling approximation leads to partial density correlation functions which are completely monotone. The ling-time limit of these functions, equivalent to the Debye-Waller factor of the system, fulfills a maximum property. The existence of power series for both small frequencies and short times is shown.

Density correlation functions are convenient tools to characterize the dynamics of liquids or disordered systems. They can be measured experimentally, e.g. by inelastic neutron scattering, or can be determined from computer simulation techniques. On the other hand, one can calculate them from theory, but in the case of strongly interacting systems, one typically has to invoke certain approximations in order to obtain the desired results. There are, however, some general properties of such correlation functions directly related to the time-evolution of the system. It is a non-trivial point to show that all approximations involved in deriving a theory's equation of motion indeed preserve these general properties.

One example are overdamped colloidal suspensions obeying Smoluchowski dynamics. One knows from general grounds that in such systems, density correlation spectra must be positive, and the correlation functions themselves are known to be completely monotone, i.e., they can be written as a su-

perposition of decaying exponentials only. An approximate theory calculating such quantities should aim to reproduce these properties, since they are direct consequences of the structure of the time-evolution operator. However, the concept of complete monotonicity is quite subtle, and is therefore nontrivial that a given approximation does not destroy it.

At high densities, colloidal systems on the other hand are known to undergo glassy dynamics, provided crystallization can be suppressed for sufficiently long time. In these cases, the mode-coupling theory of the glass transition (MCT) has been successful in describing much of the experimental facts. For one-component, i.e. monodisperse systems, the theory has been shown to give results for the density correlation functions, which indeed reproduce the above mentioned features. However, little is known about multi-component, or polydisperse, mixtures.

The aim of the project was to generalize the known proofs of the general properties of MCT solutions in the case of one-component systems to that of multi-component mixtures. In particular, we showed that the structural relaxation can be represented as a continuous sum of decaying exponentials, i.e. that the density correlation functions indeed are completely monotone. Furthermore, the long-time limits can be obtained by a simple iteration procedure that does not involve the solution of the complete dynamical equations. In addition, a short-time expansion of the density correlation functions is demonstrated to be convergent for short times, and similarly, a power series for small frequencies is shown to exist.

Light-induced phase transitions in two-dimensional colloidal crystals

Colloidal suspensions are ideal model systems for studying the influence of external periodic potentials on the nature of phase transitions in two dimensions. We have developed a theory based on a dislocation mediated melting scenario explaining recent experimental results.

Two-dimensional melting and the mathematically related systems, such as for example the normal-to-superfluid transition and planar paramagnet to ferromagnet transition, described by the XY model are striking examples of the increased importance of thermal fluctuations in low dimensional systems. In contrast to their bulk, three dimensional analogs, where, typically, fluctuations only lead to quantitative modifications of mean-field predictions, here the effects are qualitatively different.

Landau's order parameter expansion predicts that the direct transition from a solid to a liquid should always be first order. In two dimensions (2d), however, fluctuations can suppress the transition temperature so far below its mean-field value that order parameter amplitude fluctuations (except in the form of topological defects) play no role, and Landau's mean-field analysis is qualitatively wrong. In this case a two-stage melting process mediated by the unbinding of dislocations and disclinations provides an alternative scenario with two successive continuous phase transitions with an intermediate hexatic phase instead of a single direct first order transition. A periodic embedding medium for the 2d solid (e.g. a crystal substrate or a laser potential) leads to commensurability effects and engenders an enormous variety of interesting phenomena.

Colloids confined between smooth glass plates provide an ideal model system for experimental studies of 2d melting. In this system individual particles can be imaged, allowing a direct observation of topological defects and measurement of real-space correlation functions. Murray et al. and Zahn et al. have given strong experimental evidence for a two-stage melting mechanism in such systems.

In collaboration with D. Nelson and L. Radzihovsky, we have demonstrated that particles confined to two dimensions (2d) and subjected to a one-dimensional periodic potential exhibit a rich phase diagram, with both ''locked floating solids" and smectic phases. The resulting phases and phase transitions are studied as a function of temperature and potential strength. We have identified a reentrant melting behavior as a function of the potential strength. Our results lead to universal predictions consistent with recent experiments on 2d colloids in the presence of a laser-induced 1d periodic potential. Some of our results are presently tested by experimental investigations by C. Bechinger and collaborators in Konstanz. Currently, we are interested in further exploring the phase diagram and incorporate effects due to incommensurability between the laser potential and the lattice spacing. We expect to find a multitude of new and interesting phases.

References

[1] L. Radzihovsky, E. Frey, and D. R. Nelson, Phys. Rev. E 63, 031503 (2001).

[2] C. Bechinger and E. Frey, J. Phys.: Condensed Matter 13, R321 (2001).

P. Benetatos, T. Franosch, E. Frey
(Soft Condensed Matter Physics)

Department

SF6 Trace Elements

Analysis of metal-containing proteins by a novel method combining gel electrophoretic protein separation and SYXRFA

The analytical methods used in the department for the determination of trace elements in biological samples include neutron activation analysis (NAA), atomic absorption spectrometry (AAS) and inductively coupled plasma mass spectrometry (ICP-MS). They are now in routine use and only a few studies have to be carried out for further improvement of certain steps of these procedures.

The greatest challenge in the analytical field has to be faced in the development of methods for the identification and analysis of trace element- containing proteins. As the properties of most of these compounds are not yet known, information on their presence in a biological sample can only be obtained by protein separation and determination of the element content in the isolated fractions. Biological materials contain several thousands of different proteins, and methods which allow separation with the highest degree of resolution are therefore required. For this reason we have chosen gel electrophoretic procedures in which the proteins migrate in an electric field and are isolated due to differences in their molecular masses or in their isoelectric points.

A novel method for the determination of trace element-containing proteins is being developed in which synchrotron radiation X-ray fluorescence analysis (SYXRFA) is used in conjunction with the different techniques of polyacrylamide gel electrophoresis (PAGE), isoelectric focusing (IEF) and two-dimensional IEF / PAGE. With these procedures the separated proteins are present in a plane gel matrix or are blotted onto a plane membrane. Measurement of the trace element distribution among the proteins may therefore be best achieved by the use of an analytical technique which allows the element determination by surface scanning. A XRFA device is being set up at the BAMline of BESSY (collaboration with the BAM Berlin). Pilot studies have been carried out at BESSY and at HASYLAB on known metalloproteins and on metal-containing compounds in human tissues after separation by SDS-PAGE. In this way information has been obtained on various factors which may influence the analysis such as X-ray beam diameter, sample geometry, radiation background or contamination by trace elements present in separation media and blot membranes. The determination of several metal-containing proteins such as the copper/zinc superoxide dismutase via analysis of their metal content (s. Fig. 1) has shown the suitability of this novel method which will open up new ways in metalloprotein research.

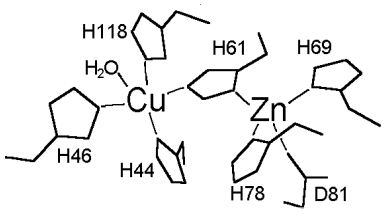

Active center of the Cu,Zn-SOD

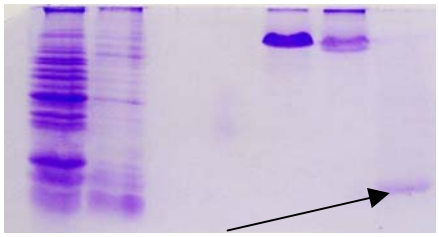

SOD protein band on a gel matrix isolated by SDS-PAGE

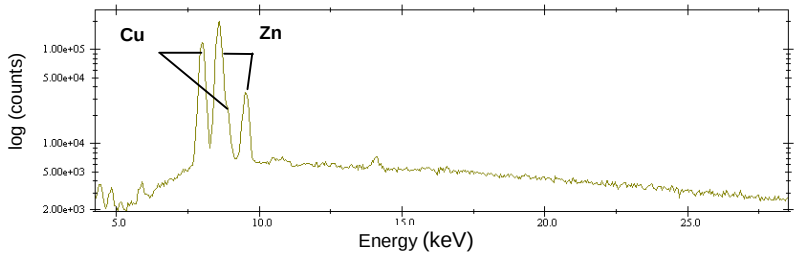

SYXRFA spectrum of the Cu,Zn-SOD

Fig. 1: Analysis of the copper/zinc-containing superoxide dismutase (SOD) by means of SDS-PAGE protein separation and scan of the two metals by SYXRFA

D. Behne, D. Alber, G. Weseloh, C. Wolf, M. Kühbacher (SF6.01 Analysis of Trace Elements and Metalloproteins by NAA and other Methods)

Regulation of selenium and selenoproteins in the mammalian organism

The research carried out in this project included a study within a project of the EU-Biomed program on the regulation of selenoprotein metabolism. This study has now been completed, and the conclusions drawn from its findings may help to answer several open questions on the biological significance of selenium in mammals including man and on the health effects of inadequate selenium intake.

In numerous tracer experiments and analyses of the tissue selenium levels by NAA in selenium-deficient and selenium-adequate rats we were able to show the existence of regulation mechanisms by which in periods of insufficient selenium intake the organism strives to maintain the levels of this element in certain tissues such as the brain, the endocrine and the reproductive organs. This regulation is achieved by preferential supply of these tissues with the element from the small amounts still contained in the deficient diet but also by a redistribution of the metabolized element which in selenium deficiency is excreted to a much lesser extent and is instead transported back to these high priority organs. Accordingly, the feeding of rats with a selenium-deficient diet over several generations led to a drastic drop in the selenium concentration below the limit of detection in low priority tissues such as liver, skeletal muscle and heart muscle while the central nervous system still contained more than 50 % of the concentration of selenium-adequate control animals. Based on the results of these studies we were able to arrange the tissues into several groups, with the body compartments at the lowest level of priority in group 1 and those at the highest level in group 5 (s. Table 1).

By measuring the distribution of the element among the selenium-containing proteins in the different tissues of the deficient and the control animals, we could then show that there is also a hierarchy at a molecular level. In most of the tissues investigated the element was preferentially incorporated into two selenoproteins, the phospholipid hydroperoxide glutathione peroxidase and an 18 kDa selenoprotein whereas two other selenoenzymes, the cellular

1.	Blood cells, blood plasma, diaphragm, heart, liver, seminal vesicle, skeletal muscle
2.	Eye, kidney, lung, pancreas, prostate, small intestine, skin, spleen, stomach, thymus, uterus
3.	Adrenal, ovary, testis
4.	Corpora lutea, pituitary, thyroid
5.	Brain, spinal marrow

Table 1: Levels of priority in the selenium supply tothe tissues of the rat

glutathione peroxidase and the plasma glutathione peroxidase, were at the lower end of this hierarchy. The main findings of these studies are summarized in the scheme in Fig. 2. It shows that during the first stages of selenium depletion there is above all a decrease in the selenium concentrations in the tissues at the lowest priority level such as the heart, the liver and the skeletal muscle and here first a decrease in glutathione peroxidase. With progressing depletion these pools are emptied almost completely. In the organs with high priority, however, the concentrations of certain selenoproteins are maintained even in severe selenium deficiency, a fact which can be taken as an indication of the biological importance of these compounds. The existence of this hierarchy can explain the findings described in the literature that in selenium deficiency or a combined low selenium and low vitamin E state lesions appear first in the heart, the liver and the skeletal muscle. The studies on the ranking order in the selenium distribution have also revealed several other low priority tissues which may be affected in selenium deficiency. The results therefore supply valuable information for future research with regard to further sites in which selenium-related diseases are likely to occur and to the selenoproteins which may play a role in their pathogenesis.

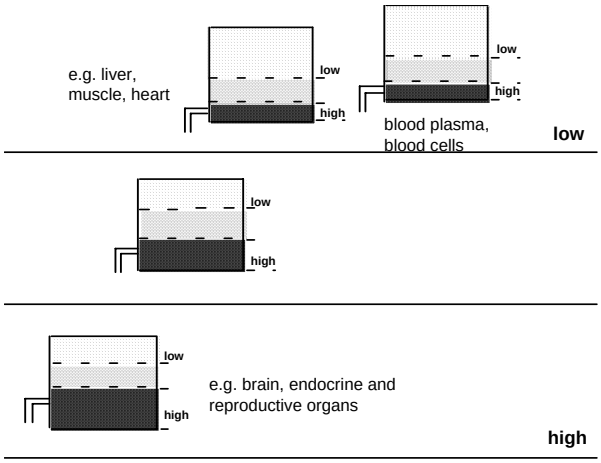

Fig. 2: Levels of priority in the selenium supply to tissues and selenoproteins. Regulatory mechanisms ensure preferential supply of selenium to high priority organs and within the tissues to certain selenoproteins represented by the darkly shaded areas. Consequently selenium depletion leads above all to a decrease in the concentrations of the low priority selenoproteins represented by the most lightly shaded areas, especially in the tissues which are last in this hierarchy

A. Kyriakopoulos, D. Behne, H. Bertelsmann, B. Hoppe, A. Richarz (SF6.02 Molecular Trace Element Research: Selenoproteins and Metalloproteins)

Changes in the structure of the metallothioneins in Alzheimer's disease

As brain cells are especially susceptible to damages due to free radicals and oxidative stress, and trace elements are known to be involved in the production of free radicals as well as in the protective systems against these damages, the elucidation of the role of trace elements and their different binding forms in neurodegenerative diseases is of great interest. An investigation has been carried out in which we compared the patterns of several metals and metal-containing proteins in post mortem samples from up to 10 different brain regions from 11 patients with Alzheimer's disease (AD) and 5 non-AD controls. The total element concentrations determined for iron, selenium and zinc by NAA and for cadmium and copper by AAS in samples from several brain regions were not significantly different between these two groups. Alterations were, however, observed in the pattern of the elements contained in the metallothioneins.

Metallothioneins (MT) are cysteine-rich proteins of low molecular mass which bind metals such as zinc, copper, cadmium, lead, silver and mercury via their cysteine groups. They exist in several isoforms MT-1, MT-2, MT-3 and MT-4. Their biological significance is due to their functions in various important processes including copper and zinc homeostasis, heavy metal detoxification, radical scavenging and antioxidative protection. The isoform MT-3, which is predominantly present in the brain, seems to play a significant role in the brain cell metabolism, and it has been discussed that a reduction in its expression may be related to the pathogenesis of AD.

The trace elements contained in the MT in brain samples from AD patients and healthy controls were determined by separation of the brain cytosols using size exclusion chromatography and on-line detection of the element profiles in the protein fractions by ICP-MS. Fig. 3 shows the distribution of copper and zinc among the fractions containing the Cu/Zn-superoxide dismutase (SOD), MT-3 and MT-1/MT-2 in untreated samples and in the samples treated with the reducing agent dithiothreitol (DTT). Without DTT, the concentrations of both copper and zinc in the MT-1/-2 and MT-3 fractions were significantly decreased in the AD patients. After DTT treatment, however, they were found to have risen again and the differences between AD and control samples were no longer statistically significant. This effect could be attributed to a decrease in the number of metal-binding sites of the MT in AD due to increased oxidation of the cysteine residues which could partly be reversed in vitro by addition of the reducing agent. It can therefore be concluded that the significant difference between AD and control brains is not due to lowered concentrations of MT but to a higher percentage of oxidized MT. This finding strongly supports the hypothesis discussed in the literature that oxidative processes play an important role in Alzheimer's disease. It also shows that this analytical approach of investigating the different element species is of much greater clinical significance than the determination of total trace element concentrations and may contribute to the elucidation of the pathogenesis and the pathological processes of this disease.

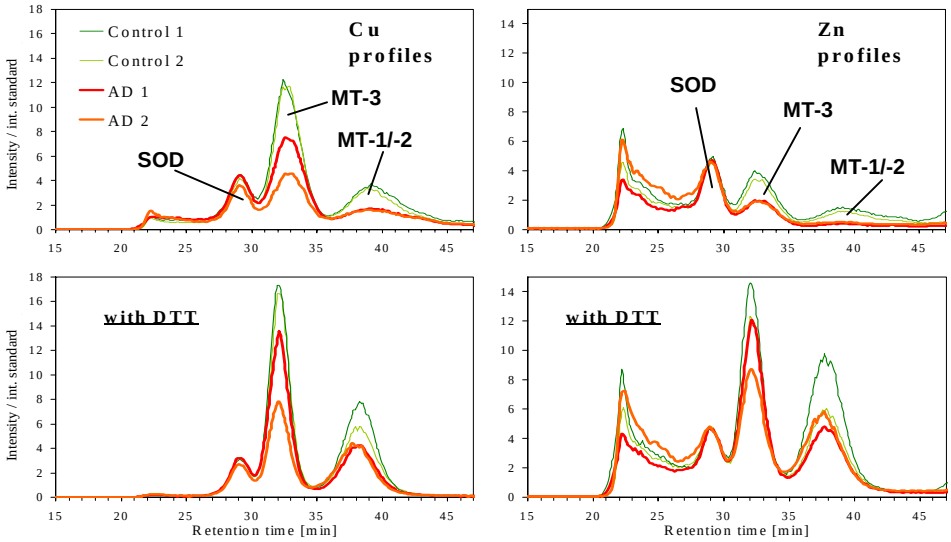

Fig.3: Copper and zinc profiles in fractions of brain cytosols from AD patients and non-AD human controls after size exclusion chromatographical protein separation of untreated samples and samples treated with DTT.

D. Behne, A. Kyriakopoulos, C. Wolf, A. Richarz, H. Bertelsmann (SF6.03 Clinical Applications)

Work Group

SF7 Nuclear Measurements

The stopping power of ions in thin layers in dependence on the charge state distribution evolving from the ingoing charge state

Even though the stopping of ions in matter is a subject of interest since almost a century, only since a few years there exist some theoretical microscopic descriptions of this process. For protons one can use the Bethe-Bloch formula, for thick targets there exist several tables and semi-empirical methods like the stopping tables of Northcliff-Schilling or the code Trim of Biersack-Ziegler-Litmark. But regarding thin targets, where the initial charge state dependent evolution of the charge state distribution, f(q,d), before reaching the region of dynamic equilibrium, can not be neglected, one has to treat the slow-down process microscopically. Therefore charge state dependent stopping powers, S(q), are needed. Combining these with the fraction of the corresponding charge state, the energy loss even in thin targets can be calculated: $S(d) = \int S(x)\,dx = \int \sum_q f(q,x) \times S(q)\,dx$.

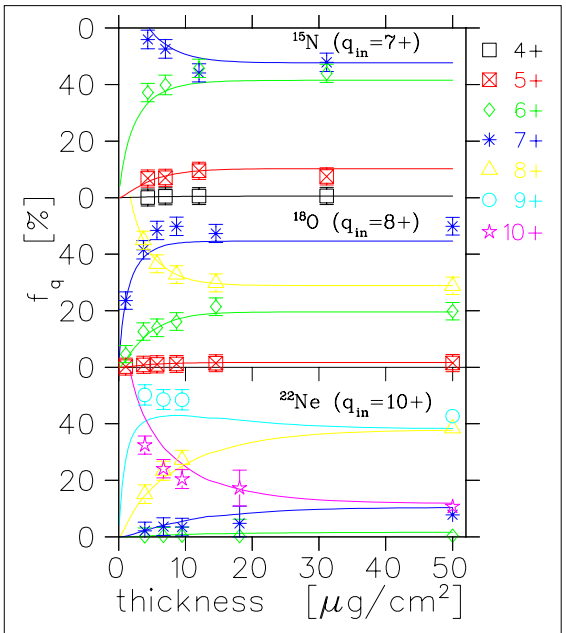

Fig. 1: Evolution of the charge state distributions of $^{15}N^{7+}$, $^{18}O^{8+}$ and $^{22}Ne^{10+}$ ions in Carbon at 2 MeV/u in dependence on the layer thickness.

We have measured both, the charge state evolution f(q,x) as well as the charge state dependent energy loss S(q) for all relevant incoming and outgoing charge states. Therefore we use the magnetic spectrometer Q3D with its excellent energy resolution of $\delta E/E = 5\ 10^{-4}$. From the charge state fractions after penetration through carbon foils of different thickness (3 µg/cm^2 to 20 µg/cm^2) one can obtain the cross sections for the charge changing processes, like ionization, electron capture, excitation or decay, by solving the rate equations. Using those cross sections to model the passage of the ion through the target, one can eliminate the modification of the measured energy loss $DE(q_i=q_f)$ by those ions, which suffered charge exchange and hence lost more energy or less energy compared to the investigated charge state, and so extract charge state dependent stopping powers S(q) for 'frozen' charge states [1,2].

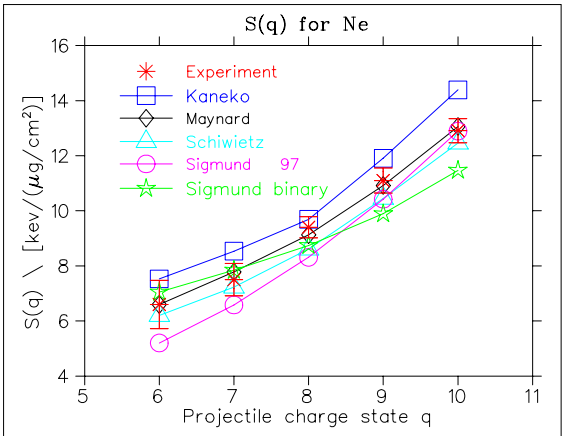

Fig. 2: Comparison of the extracted S(q) values of ^{22}Ne ions at 2 MeV/u with five theoretical descriptions.

The stopping and charge exchange of three kinds of projectiles in thin carbon foils have been investigated until now: neon, oxygen and carbon at an incident energy of 2 MeV/u.

Fig. 1 shows for the isotopes ^{15}N, ^{18}O and ^{22}Ne an example of the experimental results for the evolution of the charge state distribution with increasing layer thickness starting from an incoming ion charge of $q_{in} = Z$ (such data were also measured for other q_{in} values). The lines represent results for the charge state fractions obtained from the solution of the rate equations using cross sections for electron loss and capture from microscopic calculations (see ref. [1]).

The analysis of the neon data is completed, fig. 2 shows the charge state dependent stopping powers, S(q), for the charges 6^+ to 10^+ (red stars). The data were used to test different theories (fig. 2). Sigmund [3] (circles) developed a theory to calculate the stopping of swift heavy ions as a function of the projectile charge q. Excitation and ionization of target electrons are described within Bohr's classical theory. The effect of projectile electrons is taken into account mainly via screening of the Coulomb interaction. Kaneko [4] (squares) derived an analytical formula for the electronic stopping power for swift lithium- and beryllium-like ions based on first-order perturbation theory. The bound electrons attached to ions in the ground state were described by the Hartree-Fock-Slater determinant. Schiwietz and Grande [5] (triangles) developed the code CASP to calculate with a simple method the impact-parameter dependence of the electronic energy loss of bare ions. This perturbative convolution approximation is based on first order perturbation theory, which is only valid for fast projectiles with low charges. But

using Bloch's stopping-power result and a simple scaling, they could overcome the restriction to low charge states and derived a unitary convolution approximation. Maynard et al [6]

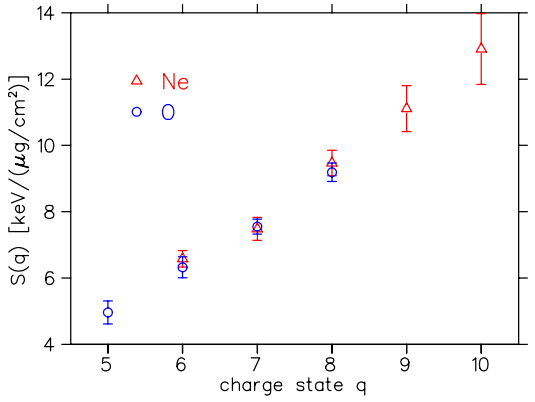

Fig. 3: Comparison of charge state dependent stopping powers S(q) of ions with different nuclear charge number Z (here neon and oxygen) for the same charge state.

(diamonds) expressed the stopping power of swift heavy ions within the convergent kinetic Lindhard theory (CKLT), based on a modified Bloch correction term, devoted to correctly describe the close collision contribution to the energy-loss process. As expected, the first order perturbation theory of Kaneko overestimates the stopping power. Those values can be considered as an upper limit. The calculations of Schiwietz underestimate the data, because there are still some polarization corrections needed, which will be included soon. The procedure of Sigmund seems to use a too strong screening function, as the slope is steeper as compared to the others. The best agreement with our data is obtained with the theory of Maynard.

Fig. 3 shows the stopping powers for neon and oxygen ions. Same charge states for different Z-values differ by the number of screening electrons. More data will give us the possibility to test different models for screening functions.

References

[1] A. Blazevic, H.G. Bohlen and W. von Oertzen, Phys. Rev. A 61, 32901 (2000).

[2] A. Blazevic, H.G. Bohlen and W. von Oertzen, in press, Nucl. Instr. and Meth. in Phys. Res. B (2002).

[3] P. Sigmund and A. Schinner, J. Europ. Phys. D12, 425 (2000), and P.Sigmund and A.Schinner, Phys. Scr. T92, 222 (2001).

[4] T. Kaneko, Phys. Rev. A 49, 2681 (1994).

[5] G. Schiwietz and P.L. Grande, Nucl. Instr. and Meth. in Phys. Res. B153, 1 (1999).

[6] G. Maynard et al., Nucl. Instr. and Meth. in Phys. Res. A464, 86 (2001).

H.G. Bohlen, W. von Oertzen in collaboration with A. Blazevic*, P. Pirzadeh (TU Darmstadt)
(SF7.01a ERDA and Interaction of Ions with Matter)

Gamma-spectroscopy of Ca and Ne isotopes

γ-Spectroscopy of ^{40}Ca and ^{42}Ca

In a recent study we found in the ^{32}S + ^{24}Mg system an enhanced population of the deformed K=4$^-$ side band in ^{48}Cr in the binary fusion-fission case of ^{8}Be emission from the compound nucleus ^{56}Ni compared with the uncorrelated emission of 2 α-particles from the compound nucleus, which is understood as fusion-evaporation reaction [1].
In order to establish this effect and to extend it to the comparison between the binary emission of ^{12}C and the uncorrelated emission of 3 α-particles in 4N-nuclei, we performed an experiment bombarding a thin ^{24}Mg target with a 139 MeV ^{28}Si beam from the XTU tandem accelerator at LNL. To identify the γ-rays from the differently deformed bands in the nuclei of interest, events with at least 2 γ-rays registered in the Ge-detector array GASP were recorded. In order to distinguish the different reaction mechanisms, the emitted light particles were detected in the Si-detector ball ISIS.
In the recent experiment the number of events in the ^{12}C and the 3α channel, respectively, is almost the same. Indeed, as also reported in Ref. [1] and refs. cited therein, in the case of the fusion-fission channel (^{12}C) the subsequent emission of LCP (here in particular the emission of one and two protons, respectively) is much stronger in comparison to the fusion-evaporation channel (3α).
The crucial point of that kind of analysis of γ-particle coincidences is that the level scheme of the investigated nucleus has to be well understood. Since the main focus of interest is on ^{40}Ca, which can be populated by the binary channel ^{28}Si + ^{24}Mg → ^{52}Fe → ^{40}Ca + ^{12}C as well as by the evaporation channel ^{52}Fe → ^{40}Ca + 3α, the first step was to obtain detailed information about the level scheme of ^{40}Ca.
From this experiment 19 new levels and 25 new transitions for ^{40}Ca for excitation energies up to 21 MeV were found. We found no connecting transitions between the positive and negative parity bands. Assuming two steep, well separated valleys with large values of β_3 of opposite sign, would explain why there are no decays between negative and positive parity states, in contrast to the case in heavy nuclei.
Another nucleus of interest for the investigation of different populations of deformed bands for different reaction mechanism is ^{42}Ca, which can be populated via the exit channels ^{42}Ca + ^{8}Be + 2p and ^{42}Ca + 2α + 2p. We expect a structure related to ^{40}Ca based on 6p4h and 10p8h configurations. From this experiment 6 new levels and 5 new transitions for ^{42}Ca for excitation energies up to 13 MeV were found.
The detailed analysis of the population of the different bands for the different reaction channels in ^{40}Ca and ^{42}Ca as well as for ^{44}Ti is still in progress.

References

[1] S. Thummerer et al., J. Phys. G 27, 1405 (2001).

γ-Decay of octupole bands in ^{21}Na and ^{21}Ne

In studies of the structure of the lightest nuclei in the sd-shell often the observation of negative parity states has led to suggestions that they are associated with clustering. Correspondingly the structure of the negative parity states is associated to octupole deformations and to intrinsically reflection asymmetric shapes. A particular case which has been recently discussed is the system consisting of ^{16}O, an α-particle and a valence neutron. The well known doublet structure of ^{20}Ne is there mirrored in two doublets of bands with K=3/2 and K=1/2 in ^{21}Ne.
There are particular features in the γ-decay connected to reflection asymmetric (octupole) shapes. We are interested in the structure of the rotational bands in ^{21}Na and ^{21}Ne and their comparison in an mirror symmetry concept and corresponding decay properties, which can be associated with clustering. In Ref. [1] the known states of ^{21}Ne have been grouped into rotational bands: the negative parity states are placed in parity doublets with intrinsic parity violation corresponding to an octupole (molecular) structure. The aim of the present work was to search for these two main bands as parity-doublets with *K* values of 1/2 and 3/2.
We report here on the results of the ^{7}Li + ^{16}O reaction at an energy of 27 MeV obtained in an experiment with a ^{10}BeO-target deposited on a thick backing (4 mg/cm^2 Pt and 35 mg/cm^2 Au). The γ-spectra have been obtained using the GASP-detector array at the Tandem Accelerator of LNL.
The K=3/2$^+$ band is clearly seen in the data, whereas from the K=3/2$^-$ band and the K=1/2 bands only the depopulation of the band heads can be observed. We interprete this result as due to α-clustering, with large values of β_3 of opposite sign. We thus can explain, why there are no decays between negative and positive parity states.
There are also 16 other transitions, which end up in the 5/2, 7/2 and 9/2 state of the K=3/2$^+$ band, respectively. These transitions are not forming an additional rotational band structure. The highest lying states populated in the recent reaction are at a maximum excitation energy of 8.2 MeV.
In ^{21}Na, where only the K=3/2$^+$ band was observed in the present experiment, the scheme was extended by the 4419 keV state and its depopulating γ-rays. The mirror symmetry of ^{21}Na and ^{21}Ne led to a very similar band structure and life time for the 5/2$^+$ state.
To extend the search for molecular bands in ^{21}Ne and also ^{20,22}Ne, we recently performed an experiment with the reaction ^{18}O + ^{13}C at GASP.

References

[1] W. von Oertzen, Eur. Phys. J. A 11, 403 (2001).

S. Thummerer, W. von Oertzen, H.G. Bohlen, B. Gebauer, T. Kokalova, S. Torilov, A. Tumino and collaborations (SF7.01b Nuclear Spectroscopy)

Investigation of the structure of ^{11}Be and ^{12}Be

In the neutron-rich isotopes ^{11}Be and ^{12}Be we found in previous work [1] a number of higher lying excited states with the property, that their excitation energies follow a linear J(J+1)-dependence (J spin of the state) indicating the structure of a rotational band. The slope of the line is inversely proportional to the moment-of-inertia Θ . The obtained Θ-values are very large and correspond to extreme deformations of ^{11}Be and ^{12}Be. They can be interpreted even as molecular structure. A similar result has been obtained also by Freer *et al.* for ^{12}Be [2]. We have populated these states using a two-neutron transfer reaction, e.g., ^{9}Be(^{14}N,^{12}N), for ^{11}Be and a three-neutron transfer reaction ^{9}Be(^{15}N,^{12}N) for ^{12}Be. In both cases it was important to start with ^{9}Be as a core, because this nucleus has already in its ground state a pronounced molecular structure.

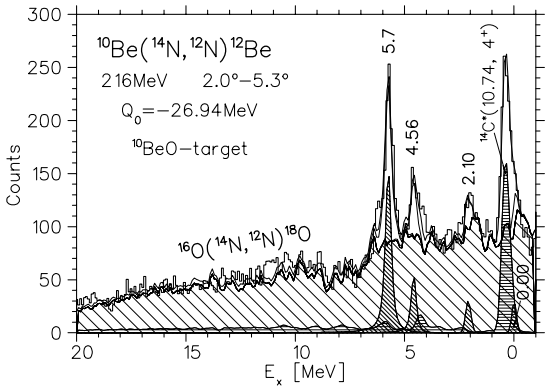

Fig. 1: ^{12}Be-states populated in the ^{10}Be(^{14}N,^{12}N) two-neutron stripping reaction.

The attempt to populated the molecular states in ^{11}Be by a one-neutron transfer reaction on ^{10}Be, e.g. ^{10}Be(^{14}N,^{13}N), failed: only four states, all different from the molecular band members, were populated. Three of them are known to have single particle character. We concluded from this result, that these states have the structure of a ^{10}Be core and one neutron in a shell model orbit outside. In contrast to this, the molecular states do not have a configuration with a ^{10}Be ground state core, but a 2α-cluster structure as it exists in the ^{9}Be ground state.

We have investigated now the structure of ^{12}Be in the same way and studied the population of ^{12}Be states using the two-neutron transfer reaction on ^{10}Be: ^{10}Be(^{14}N,^{12}N)^{12}Be, the spectrum is shown in fig. 1. The target material was ^{10}Be-Oxide, therefore a strong background from ^{16}O appears in the spectrum. It could be fitted correctly using a spectrum measured separately on ^{16}O (widely hatched area), the used target material was V_2O_5 in this case. A strong contamination line of $^{14}C_{4+}$ (E_x=10.74 MeV) from ^{12}C is observed near the ground state of ^{12}Be, a corresponding spectrum was also measured on ^{12}C. Taking these background contributions correctly into account, there remain only four peaks in the spectrum. They correspond to the known states of ^{12}Be at 0.00 MeV, 2.10 MeV, 4.56 MeV and 5.7 MeV excitation energy. All of them do not belong to a molecular rotational band of ^{12}Be, which would start at about 6.4 MeV. We do not observe any significant peak in the spectrum for excitation energies higher than 6 MeV up to 20 MeV. A similar sensitivity to the core configuration is met here for ^{12}Be as in the case of ^{11}Be: molecular states with a 2α-cluster structure are not populated in the 2n-transfer on a ^{10}Be core.

In December 2001 we studied the population of ^{11}Be states in a two-proton pick-up reaction on ^{13}C. Fig. 2 shows a spectrum of the ^{13}C(^{12}C,^{14}O)^{11}Be reaction (the peaks marked in yellow come from a 5% ^{12}C contamination). Only three states at 0.32 MeV, 2.70 MeV and 3.90 MeV are clearly observed (a peak at 5.3 MeV has only a low significance), but no other state at higher excitation energy up to the observed range of 20 MeV. We find also in this reaction, that the nine members of the molecular rotational band of ^{11}Be are not populated due to their different structure (see above). The analysis of the data and of the angular distributions of the observed states is in progress.

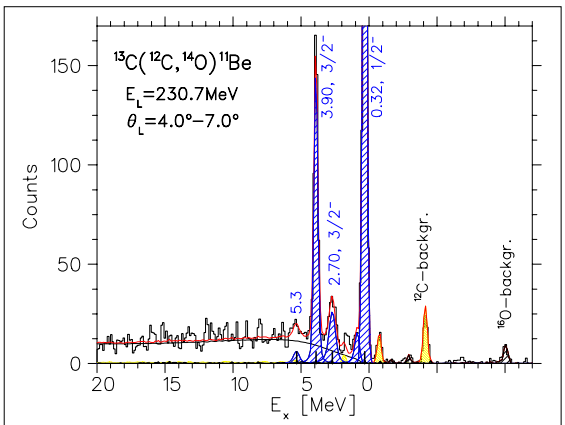

Fig. 2: ^{11}Be-states populated in the ^{13}C(^{12}C,^{14}O) two-proton pick-up reaction.

References

[1] H.G. Bohlen et al., Proc. Int. Conf. ENPE, Sevilla, ed. B. Rubio et al., AIP Conf. Proc. 495, 303 (1999).

[2] M. Freer et al., Phys. Rev. Lett. 82, 1383 (1999).

H.G. Bohlen, W. von Oertzen, B. Gebauer, in collaboration with S.M. Grimes (Ohio University, Athens, USA), R. Kalpakchieva (FLNR, JINR, Dubna, Russia, and Bulgarian Academy of Science, Sofia, Bulgaria), T. Kokalova, T.N. Massey, M. Milin, Ch. Schulz, S. Thummerer, A. Tumino
(SF7.01b Nuclear spectroscopy)

Structure studies of ^{15}C using the ^{9}Be(^{7}Li,p) reaction

As proposed already in 1997 by von Oertzen [1], neutron-rich carbon isotopes may form molecular structures at high excitation energies through the clustering into three α-particles (trimers) with the extra neutrons as valence particles, which provide the binding. These structures correspond to the extension of the molecular structures in ^{11}Be and ^{12}Be (see preceeding page) by one more α-particle.

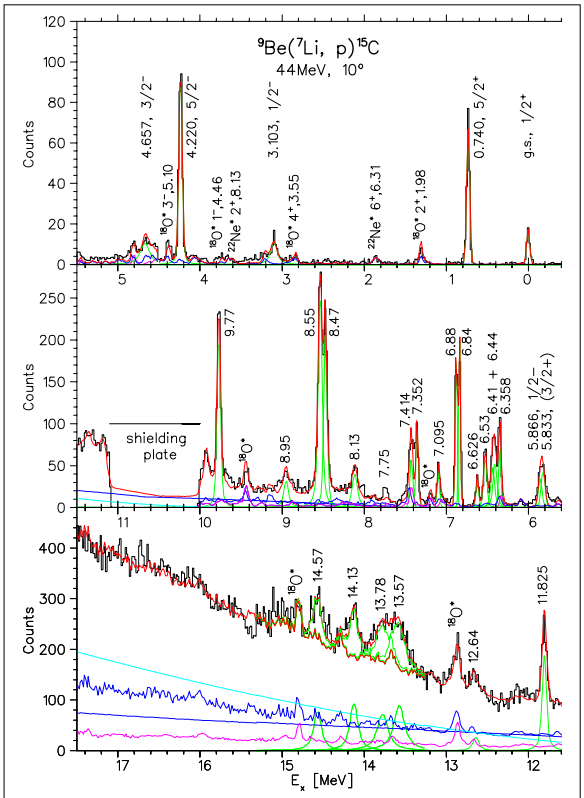

Fig. 1: Spectrum of ^{15}C-states obtained in the ^{9}Be(^{7}Li,p) reaction at E_{Lab}=44 MeV and θ_{Lab}=10°.

We have measured the ^{9}Be(^{7}Li,p)^{15}C reaction at the Q3D magnetic spectrograph of the Munich Tandem Laborarory to study the structure of ^{15}C and, in particular, search for new high-lying states with possible molecular structure. States are known in ^{15}C up to 11.8 MeV, but molecular structures are expected rather at about 15 MeV excitation energy [1]. Fig. 1 shows the spectrum obtained at 10° with 5 settings of the magnetic field to cover the range of excitation energies from the ground state to 17.5 MeV. All the known states of ^{15}C could be identified in the spectrum (except between 9.8 MeV and 11.2 MeV, where a shielding plate was inserted against the elastic line). In addition to the known states five new states were observed at the excitation energies 12.64 MeV, 13.57 MeV, 13.78 MeV, 14.13 MeV and 14.57 MeV with widths between 50 and 150 keV. In this region of excitation energy different background contributions of four kinds exist: the (^{7}Li,p) reaction on the contaminations (i) ^{16}O (dark blue fluctuating line) and (ii) ^{12}C (pink line), and (iii) the three-body (dark blue continuous line) and (iv) four-body (light blue line) phase space distributions. Above 14.6 MeV no significant peak is observed up to the end of the spectrum (17.5 MeV), although there is much more energy available due to the positive Q-value of +9.093 MeV.

The four new states between 13.57 MeV and 14.57 MeV fall close to the expected region of molecular states and may be candidates for this structure. A molecular band with a K=1/2 or 3/2 band head at 13.57 MeV fits the observed excitation energies. States in the region of 5.8 – 12 MeV show a dependence of cross sections on spins J, which is typical for a rotational band. Fig. 2 shows the tentative spin assignments for the states, which may form a rotational band built on the known 1/2$^-$ state at 5.866 MeV (a neutron hole state in the 1p1/2 shell). The present results are preliminary and the analysis is continued.

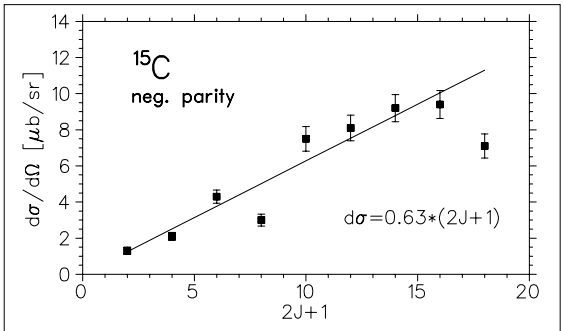

Fig. 2: Tentative spin assignments for states, which may form a rotational band built on the 1/2$^-$ state at 5.866 MeV. The cross sections show a dependence on the spins J proportional to 2J+1 (except for 7/2$^-$ and 17/2$^-$).

References
[1] W. von Oertzen, Z. Phys. A 357, 355 (1997).

H.G. Bohlen, W. von Oertzen, S. Thummerer, T. Kokalova, M. Milin, A. Tumino in collaboration with Y. Eisermann, G. Graw, R. Hertenberger, H.J. Maier, H.-F. Wirth (LMU München), Th. Faestermann (TU München)
(SF7.01b Nuclear spectroscopy)

Investigations of distinct effects in neutron transfer reactions: Elastic 2n-transfer ^{4}He(^{6}He,^{4}He)^{6}He and Nuclear rainbow scattering

Using the framework of the coupled reaction channels (CRC) the elastic scattering and the elastic transfer in the system ^{6}He + ^{4}He measured at low energies [1] and at E_L=151 MeV [2], have been analyzed. This system has so far been analyzed without explicitly taking into account the interference with the elastic transfer process. Here it is shown that the structure observed at E_L=151 MeV in the backward range of the angular distributions is influenced by the interference of the elastic 2n-transfer with a two-step process passing through the 2^+ excitation in ^{6}He.

The backward rise in the angular distribution of the elastic channel evidenced in the experimental data is the signature of the well known elastic transfer process.
The present analysis takes into account the two-step transfer via the inelastic excitation added to the elastic transfer process. The calculations are done in the framework of the coupled reaction channel (CRC) approach [3].
For the wave functions of ^{5,6}He and the structural aspects we can rely on the previous study [4], in addition the di-neutron ("cluster") approximation for the transitions via the inelastic channel will be considered. The generalized double-folded potential for the real potential has been used, and the density dependent BDM3Y-Paris effective nucleon-nucleon (NN) interaction [5] has been chosen for the optical potential in the incident and exit channels for the CRC calculations.

The coupling scheme is illustrated in Fig.1. The coupling routes are the following: a) Elastic two-neutron one-step, solid line, b) cluster 2n-transfer with the "indirect" route via the 2^+ state, dash-dotted line. The results of these calculation are shown in Fig.2.

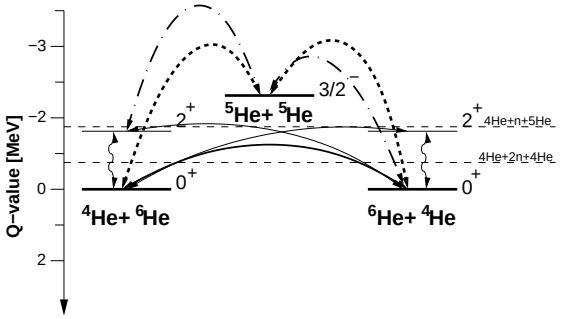

Fig.1: Coupling diagram for the one- and two-neutron transfer and inelastic excitation in the system ^{6}He + ^{4}He. The one- and two-step processes in the two-neutron transfer, the transitions via the ground state and the ^{6}He$_{2+}$ state are indicated.

For the CCBA-coupling scheme the "collective" form factor for the 2^+ state allows an exact solution of the coupling equations in inelastic scattering and multi-step Born approximation for the transfer. The strength of the quadruple coupling in this case has been taken from the literature.

We have also made calculations for the 2n-transfer without the "indirect" route in the microscopic basis. We find a dominance of the one-step 2-neutron transfer contribution by one order of magnitude, and there is a destructive interference between the one- and two-step amplitudes.

The same calculations have been performed for the low energy data [1] measured at E_{cm} = 11.6 MeV and E_{cm} = 15.9 MeV, and it is shown that the structure observed in the angular distributions is due to the interference of the elastic transfer process.

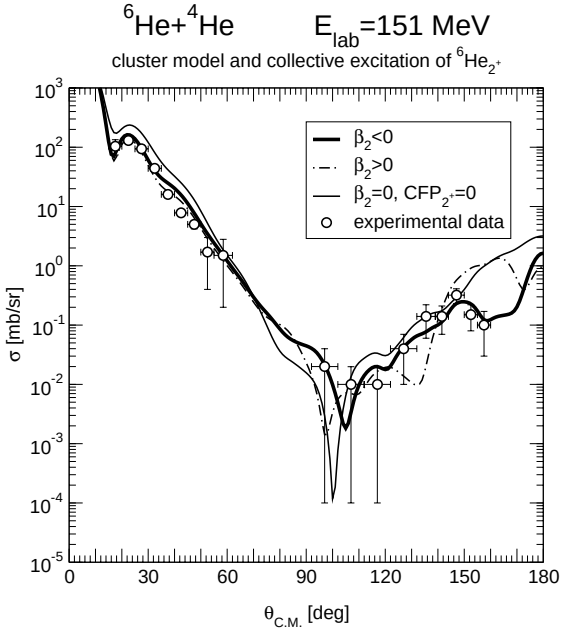

Fig.2: Angular distributions of the elastic scattering of ^{6}He + ^{4}He at E_{lab} = 151 MeV from Ref. [2] and results of calculations. The curves show the following calculations: a) thin curve, - elastic transfer with the 2n-cluster, b) dot-dashed - elastic transfer with the indirect route and β_2>0, c) full heavy curve as b) with β_2<0.

Further investigations have been performed for nuclear rainbow scattering. Elastic scattering of light heavy-ion systems like ^{16}O+^{16}O show clearly refractive effects, which are known as nuclear rainbow scattering and show the characteristics of Airy pattern. Our results on the systematic investigation of these effects in ^{16}O+^{16}O [6] allowed to determine the energy dependence of the interaction potential for both, (i) a parametrized form of the optical potential and (ii) calculating the real part of the potential from an effective nucleon-nucleon interaction and density distributions of the scattering partners. The potential is called in the latter case Folding Potential (FP). In both cases the imaginary part is described by a Woods-Saxon volume plus derivative term [6].

It is interesting now to investigate also the one-neutron transfer channel for refractive effects, since the density distribution changes in the transfer process,

which may modify the Airy pattern. Spectra of this reaction channel were simultaneously measured together with the elastic scattering data. The spectra of the $^{16}O(^{16}O,^{17}O_{gs})^{15}O$ reaction show the population of only two strong lines in ^{15}O, the $1/2^-$ ground state and the $3/2^-$ excited state at 6.18 MeV excitation energy, both states correspond to single neutron holes in the closed shells of ^{16}O. The former state shows in the angular distributions a reduced nuclear rainbow effect at large scattering angles, whereas it is not observed for the $3/2^-$ state. Correspondingly, a slightly increased absorption is needed for the ground state ($1/2^-$) transition and stronger absorption for the excited state [7].

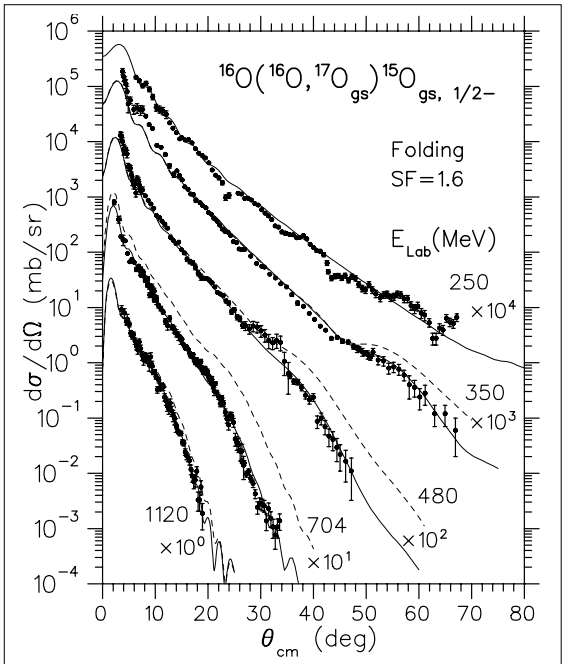

Fig. 3: Angular distributions of the 1n-transfer reaction $^{16}O(^{16}O,^{17}O_{gs})^{15}O_{gs}$ at five energies between 250 MeV and 1120 MeV.

Fig. 3 shows the angular distributions of the ^{15}O $1/2^-$ ground state transition at five incident energies between 250 MeV and 1120 MeV. The curves represent calculations using the folding potential together (i) with the imaginary part of the entrance channel (dashed curves) and (ii) with an imaginary part, which is increased to fit the data (solid lines), the real part is unchanged. The full angular distributions can be well described in this way [7], including the refractive enhancement at 350 MeV, 480 MeV and 704 MeV incident energy. All the curves are normalized with a constant spectroscopic strength factor SF=1.6, which corresponds to values from the literature.

The increase of the absorption is best characterized by the volume integral J_W per interaction pair of the imaginary part for the three different exit channels (fig. 4). It is obvious that the deep $3/2^-$ hole in ^{16}O increases the absorption strongly. The very consistent description of the data in several respects shows the predictive power of the applied method.

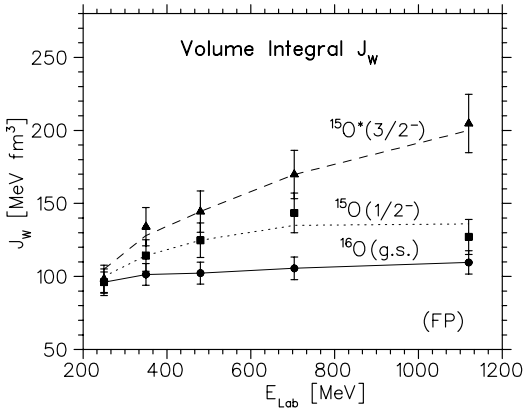

Fig. 4: Volume integral J_W of the absorptive part of the optical potential in dependence on the incident energy E_{Lab} for the elastic $^{16}O+^{16}O$ scattering (solid line) and the 1n-transfer to the ^{15}O ground state (dotted line) and the neutron-hole state $^{15}O(3/2^-)$ at Ex=6.18 MeV.

References

[1] R. Raabe, A. Piechaczeck, A. Andreev et al., Phys. Lett. B458, 1 (1999).

[2] Yu.Ts. Oganessian, V.I. Zagrebaev, J.S. Vaagen, Phys. Rev. Lett. 82, 4996 (1999), and Phys. Rev. C 60, 044605 (2000).

[3] I.V. Krouglov, W. von Oertzen, Eur. Phys. J. A6, 501 (2000).

[4] I.V. Krouglov, M. Avrigeanu, W. von Oertzen, Eur. Phys. J. A12, 399 (2001).

[5] Dao T. Khoa, G.R. Satchler, W. von Oertzen, Phys. Rev. C 56, 954 (1997).

[6] Dao T. Khoa, W. von Oertzen, H.G. Bohlen and F. Nuoffer, Nucl. Phys. A 672, 387 (2000).

[7] H.G. Bohlen, Dao T. Khoa, W. von Oertzen et al., Nucl. Phys. A (2002), in press.

I.V. Krouglov, M. Avrigeanu, W. von Oertzen,
H.G. Bohlen, Dao T. Khoa
(SF7.01b Nuclear Spectroscopy)

Development of a large-area, high-rate, high-resolution MSGC detector for thermal neutron imaging*

At the European Spallation Source ESS, i.e. the most powerful of the next generation high-flux pulsed neutron sources, in comparison with present generic instruments at ILL or ISIS for high-rate experiments an increase of the detector counting rates by factors 50-150 is expected. This is due to (i) a two orders of magnitude higher thermal neutron flux at the moderators and (ii) an additional flux gain at the sample by a factor of 5-10 due to improved neutron optics, with (iii) some of the intensity gain being sacrificed again for higher resolutions. Thus, e.g. in single-crystal protein diffraction, the efficient investigation of very complex sub-millimeter samples in small time frames will come within reach if fast and efficient large-area detectors and/or detector arrays are available which combine a MHz count rate capacity per detector segment, sub-microsecond time-of-flight (TOF) resolution and two-dimensional sub-millimeter position resolution.

In order to meet these requirements, large-area (57 cm x 0.57 cm) fourfold segmented hybrid low-pressure microstrip gas chamber (MSGC) detectors are being developed [1], based a thin composite ^{157}Gd/CsI neutron converter foils, sandwiched between two low-pressure gas gaps of 4.5 mm depth and two MSGC plates (Fig. 1). The converter is made by RF-sputtering of 0.5-1.5 µm thick ^{157}Gd layers either side on a 6 µm thick Aramid support foil and coating with <1 µm thick layers of columnar CsI, which is grown by thermal evaporation in an Ar atmosphere [2]. The ^{157}Gd thickness is adapted to deliver maximum detection efficiency for cold to thermal neutrons. After neutron capture, followed by emission of fast (29-182 keV) conversion electrons from ^{157}Gd, a well-localized detectable cluster of eV secondary electrons (SE) is emitted from one of the CsI coated converter surfaces. With the thin ^{157}Gd converters TOF resolutions of <10 ns and about 60% detection efficiency can be reached for thermal neutrons [1]. In the low-pressure two-stage gas multiplication mode used in the present MSGC, with the exponential gas multiplication starting at the converter surfaces in parallel-plate mode and further amplification in microstrip mode in the strong fields between the alternating microstrip anodes and cathodes, the sensitive detector volume is restricted to the converter surfaces, and the SE clusters are pre-amplified without parallax errors. This mode of operation is possible due to the high reduced field strength E/p achievable in low-pressure operation in the constant field region, which extends from the converter up to ~ 0.5 mm above the MSGC plate [1]. It delivers high gains, fast pulses and very good position and TOF localization [1,3].

Thus, the position and TOF resolution and count rate limits caused by the commonly used gaseous neutron converter ^{3}He are overcome. The latter are due to (i) the range of the proton and triton ions in ^{3}He/quench gas mixtures, emitted after neutron capture in the reaction n + ^{3}He $\rightarrow$ p(573 keV) + t(191 keV), and (ii) the cm-depth of the conversion gap needed for good detection efficiency. This depth causes parallax errors and bad TOF resolutions limited by the thermal neutron transit time of 4.55 µs/cm.

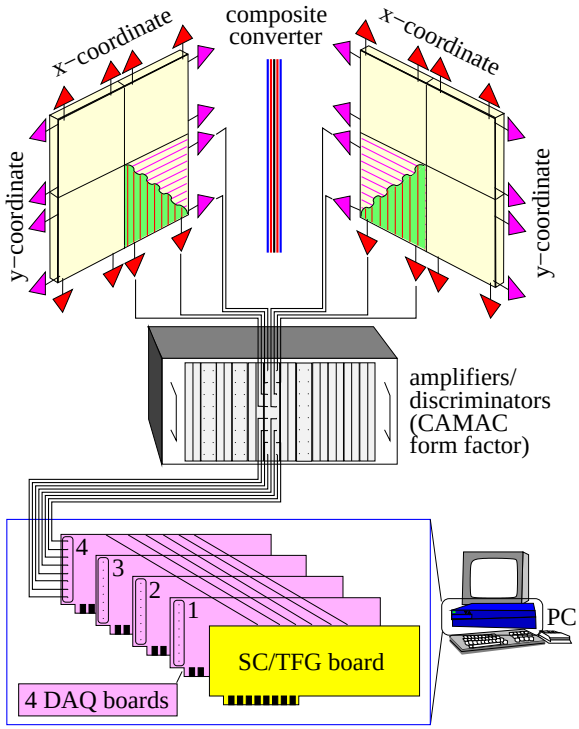

Fig. 1: Schematic sketch of the detector, the electronics and the DAQ system, the latter being comprised of one slow control/time frame generator PCI board and four DAQ PCI boards in a PC. Each DAQ board processes one pair of MSGC segments standing opposite to each other in distances of 4.5 mm from the central converter foil.

Low-pressure operation differs from the normal pressure case in particular by a much longer mean free path for ionization, which is ~40 µm for 20 mbar of isobutane in the microstrip amplification regime in the present detector design [1]. Thus, in order to achieve in the microstrip amplification stage a gain of a few hundred to 1000, i.e. 6-7 gas multiplication steps, in the present MSGC an anode-cathode edge-to-edge distance d_{AC} = 255 µm is used in combination with a surface-conductive DLC-like undercoating of the microstrip plane. The latter delivers constant field strength between the anode-cathode edges and also a maximal and rather homogeneous extension of the high field region into the gas perpendicular to the microstrip plane [1]. Thus, microstrip amplification, which would be restricted to the vicinity of the anode edges without surface resistivity, is taking place with maximal and nearly equal strength for all electron trajectories approaching the anodes [1]. Due to diffusion broadening mainly in the first amplification stage, i.e. in the ~4 mm deep high-E/p constant-field region, the base width of the charge distribution induced on the microstrips corresponds to 3-5 times the pitch, al-

though a large pitch of 635 µm had to be chosen with d_{AC} = 255 µm.

The MSGC design comprises two crossed Ti/Au microstrip patterns for x and y readout, separated by a thin insulating layer and the DLC-like layer, and integrated MΩ resistors and capacitors outside of the active area [1]. This stack of µm thick layers is deposited on a 3 mm thick insulating B270 glass plate, which has little thermal neutron absorption. As shown in [1], for a pad design and strip layout, which is optimized for low-pressure operation, in the lower 'Second Coordinate Pad' (SCP) layer signals are induced, which have about 70% of the height and the same width of 4-5 ns FWHM as the anode signals. This was shown in a comprehensive modeling of the detector functionality [1], using codes for electric field calculations and for simulation of gas multiplication, electron transport (including diffusion) and signal induction and propagation in the microstrip planes and delay lines.

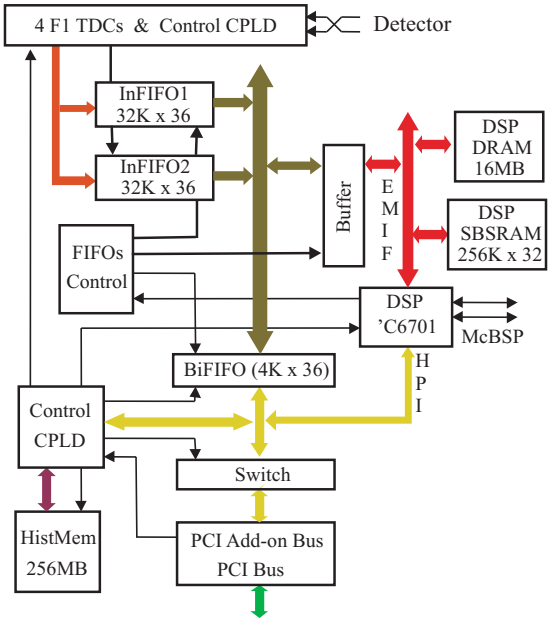

The very high and fast signals are well suited for position encoding via fast, subdivided delay lines (DL). In both readout planes, every second anode or SCP strip, respectively, is connected to a DL tap, but all strips are connected to both neighbors by integrated capacitors. Due to the width of the induced signal distributions, this readout scheme, which is interpolating via the capacitors and in the DL, delivers low differential non-linearity [1] and thus the potential to achieve much better position accuracy than according to the pitch. In order to minimize signal distortion in the DL by separating the DL from the capacitive and inductive loads of the strips, impedance matching amplifiers with 11 kΩ output impedance are inserted between the strips read out and the DL. These loads are due to the strip length and to the crossings with all the strips in the other plane. For each of the four sub-segments of the two readout planes of each geometrical detector segment (i) a position independent Start, a pulse-height (PH) signal and a position code are obtained, and (ii) from both DL ends Stop signals and PH signals are derived via constant fraction and time-over-threshold discriminators, respectively.

Since all signals are fast timing signals, the DAQ system requires only TDCs. On one PCI DAQ board, handling one pair of congruent MSGC segments, four deadtime-less 8-channel multihit TDC chips of the F1 type with 120 ps LSB, FIFOs and CPLDs, a 1 GFLOP digital signal processor (DSP) of the type TMS320C6701 and 256 MByte of histogram memory are installed (see Fig. 2). In addition the DAQ system comprises one slow control board. Using the multihit capability of the TDC in conjunction with a sum check algorithm processed in the DSP, pulses from different events are disentangled to raise the count rate limit. TOF, measured versus a chopper or accelerator pulse with 120 ps bin width in a TDC channel, is extended to the long TOF ranges of thermal neutrons of up to >100 ms by means of a course TOF counter and by synchronizing TDC reset and new-start with a 40 MHz clock. In the DSP the data of the individual coordinates can be calibrated and transformed online, by evaluating position dependent thresholds, from x/y/TOF/PH data into 2D spectra with physical parameters (e.g. 2θ/TOF, with 2θ being the scattering angle). The spectra are accumulated in the HM and dumped into the PC memory after the end of the run. The original or transformed parameters can also be written out via list mode or with reduced statistics in monitoring mode. Two DAQ boards were fabricated and tested so far. With the present DSP computing power histogramming was measured with up to 1.7 MHz per board. Further improvements are in preparation. A more detailed description of the DAQ board is given in [4].

References

[1] B. Gebauer et al., Nucl. Instr. and Meth. A 392 (1997) 68; A 409 (1998) 56; A 471 (2001) 249

[2] N. Chkhalo, B. Gebauer et al., Proc. Int. Workshop on Micro-pattern Gas Detectors, Orsay, France, June 28-30, 1999, p. 47

[3] A. Breskin et al., Nucl. Instr. and Meth A 345 (1994) 205; D.F. Anderson, Nucl. Instr. and Meth A 346 (1994) 102

[4] F.V. Levchanovski, B. Gebauer, Ch. Schulz, Proc. of the 2nd Int. Workshop on Data Acquisition Systems for Neutron Experimental Facilities (DANEF-2000), Dubna, Russia, June 5-7, 2000, JINR E10-2001-11, p. 89

*Work supported by the European Commission under contract no. HPRI-CT-1999-50005

B. Gebauer, Ch. Schulz, G. Richter, F.V. Levchanovski, A. Nikiforov, et al.
(SF7.02 Development of Thermal Neutrons Imaging Detectors)

Division

SE Solar Energy Research

The solar energy division of the HMI concentrates its research activities on the exploration of the potential of highly productive thin-film technologies for solar cells of „tomorrow“ and „beyond“. The main objective is to realize systems which lead to substantial cost reduction at high conversion efficiency. This requires research for improvements of materials and systems which are already at the edge of being industrialized but also research for new materials and innovative solar cell structures. Therefore, the activities reach from basic material research to the development of technologies for solar cells and minimodules on the laboratory scale.

The work is supported by the broad range of analytical methods available in both sections of the HMI, particularly in the field of surface and interface physics, defect spectroscopy, ion-beam techniques and structural characterization, solid states physics, as well as conventional material and device analysis.
The groups collaborate in numerous projects and networks with national and international partners.

The division Solar Energy Research comprises 5 scientific departments:

SE1	**Silicon Photovoltaics**
SE2	**Heterogeneous Materialsystems**
SE3	**Technology**
SE4	**Dynamics and Interfacial Reactions**
SE5	**Solar Energetics**

and the group

SE6	**Electronic Structure of Semiconductor Interfaces.**

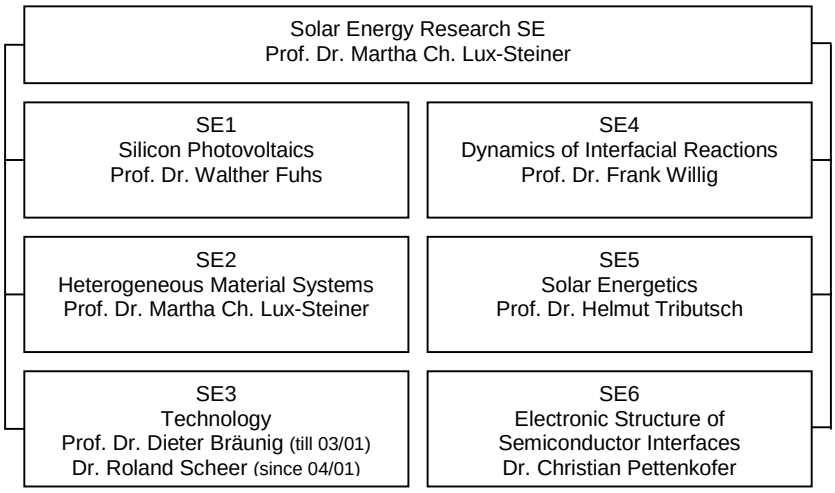

Department

SE1 Silicon Photovoltaics

Pulsed EDMR – New insight into the mechanisms of recombination in thin crystalline silicon films

The characterization of materials for photovoltaic applications depends strongly on methods that allow an assessment of electronic loss mechanisms. The major part of these losses are due to recombination processes of photogenerated charge carriers which are caused by localized bandgap states due to structural defects and impurities. The electronic activity of a certain type of defect is not only related to its density in a given material but also to its cross section which describes the probability for the capture of carriers into a defect state. Traditional methods of defect characterization are unable to provide microscopic information about such parameters for distinct defects. For instance, when the average charge carrier lifetime as well as the defect distributions in a material are known, it is still unclear which of the observed defects is more and which is less active without the knowledge of the respective recombination cross section and hence a systematic improvement of the photo response of a material becomes difficult.

An important part of the activity in our investigations of electron spin resonance (ESR) has therefore been the development of a new characterization method that combines the advantages of ESR, namely the microscopic identification of certain types of defects, with lifetime measurements of photogenerated charge carriers. The product of this development is the "Time domain measurement of spin dependent recombination" (TSR) [1-3], a method strongly related to electrically detected magnetic resonance (EDMR). The method bases on the fact that spin-selection rules determine the recombination probability between two paramagnetic states. For instance, the recombination rate between paramagnetic states that are initially in a triplet state can be by orders of magnitude smaller than between partners in a singlet state.

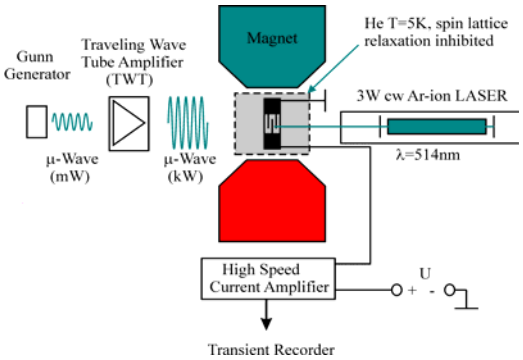

Fig. 1: The experimental principle of TSR: A semiconductor sample with micrometer-structured lateral Al-contact grids in an ESR microwave cavity is continuously exposed to strong LASER light. The transient measurement of the sample resistance after a fast (nanosecond) and strong (kW) ESR excitation of a certain defect type reveals the defects' distinct recombination cross section.

By applying intensive (kW-range) and very short (nanosecond–range) coherent microwave pulses at ESR resonance, the spin state of such recombining pairs can be rapidly altered at rates that are faster then any other process that may determine recombination, e.g., spin relaxation, pair creation as well as recombination or dissociation of electron-hole pairs. The microwave induced change of the spin states rapidly alters the recombination probability which may be observed as a time-dependent photocurrent change. The technical challenge of TSR lies in the implementation of an appropriate time resolution of the measured current changes. After employment of state-of-the-art current amplifier and transient recorder technologies as well as a special interdigited micrometer- structured sample contact system, it was possible to detect relative conductivity changes in the 10^{-8} range at time resolutions of less then 5 μs.

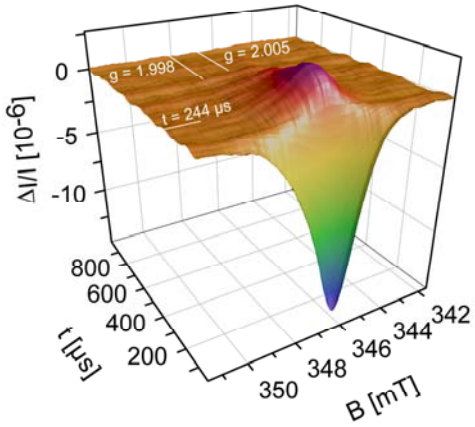

Fig. 2: In contrast to conventional EDMR, TSR not only identifies the states that are involved in recombination but also gives detailed information on their dynamics. The plot shows the time evolution of the ESR-induced current transients as a function of the magnetic field. The field dependence clearly reveals the involvement of dangling bonds (Landé factor g = 2.005) and band tail states (g = 1.998). The time dependence exhibits an initial strong current quenching followed by an enhancing.

As an example for the potential of TSR with regard to the characterization and investigation of recombination processes in semiconductors, the dynamics of recombination between shallow bandtail states (CE) and dangling bond (db) in hydrogenated microcrystalline silicon (μc-Si:H) is discussed in the following. A set of real-time TSR transients measured at various externally applied magnetic fields on a 2.7μm thin film of μc-Si:H is displayed in Fig. 2. The experiment was carried out at a sample current of I_{ph}=100μA. A 320ns pulse at time t = 0 leads to a strong recombination increase* at magnetic fields

* Since the current change ΔI is proportional to negative recombination change -ΔR, current decreases indicate recombination increases and vice versa.

which correspond to the ESR resonance of the CE and db states. After the current quenching signal relaxes, an enhancing signal becomes apparent which has a slower decay constant. Since the magnetic field dependences of the quenching and the enhancing effect are identical, we may conclude that both effects belong to the same recombination process.

As explained in previous publications [1,2], the pulse length dependence of a TSR transient can reveal the spin dynamics of the recombination centers during the resonant microwave interaction. Since microwave pulses can be changed in 2ns steps, the influence of coherent spin motion on recombination which has been predicted just recently [4], can be detected. The first results of this new high-resolution TSR indicate such a fingerprint of coherent spin motion of electrons and holes. The application of two 180° phase shifted 64ns resonant microwave pulses at times t=0 ns and t=64 ns induces a recombination echo a t=128 ns observed as a current spike shown in Fig. 3. By changing the timing of the two pulses the time evolution of the echo (echo decay) may be measured which contains all information on the dynamics of the recombination process.

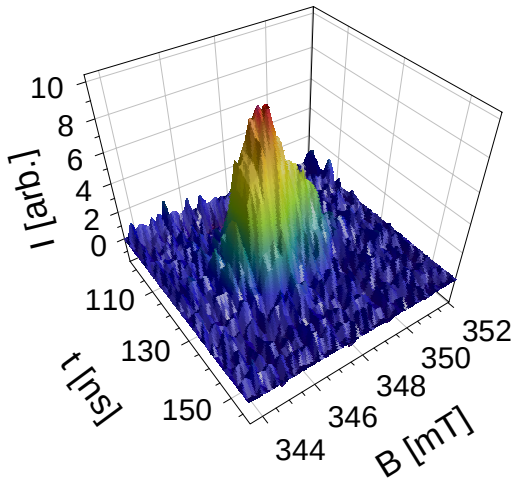

Fig. 3: Indirect TSR of a nanosecond microwave pulse shows the existence of an echo effect in the CE-db recombination rate of µc-Si:H. The current peak is caused by rephasing spins of recombining charge carriers and therefore is evidence for the influence of coherent spin motion on recombination. The recombination rate can be determined from the temporal behavior of the echo.

The fact that the shape of the recombination echo is the same for both quenching and enhancing signals, gives additional support of the fact that both belong to the same recombination process.
The observation that ESR changes of spin dependent recombination can lead to an increase of the photocurrent has never been proven experimentally although it was predicted theoretically for the finite triplet recombination probability. As illustrated qualitatively in Fig. 4, a non vanishing triplet recombination leads to a steady state population of the electron-hole ensemble where the triplet density is much higher than the singlet density, providing that the singlet recombination rate is larger than that of triplets. Under ESR resonance, both singlet and triplet densities are equalized which means that the singlet and triplet densities are enhanced and depleted, respectively leading to a net increase of the recombination. After the end of the ESR pulse, both singlet and triplet densities relax back to their steady state population. Due to the higher singlet recombination, this relaxation is faster for singlet states than for triplets. Therefore, the net recombination will shift temporarily below the steady state value which leads to an increase of the photocurrent (illustrated in Fig. 4 after about 250 µs for µc-Si:H).

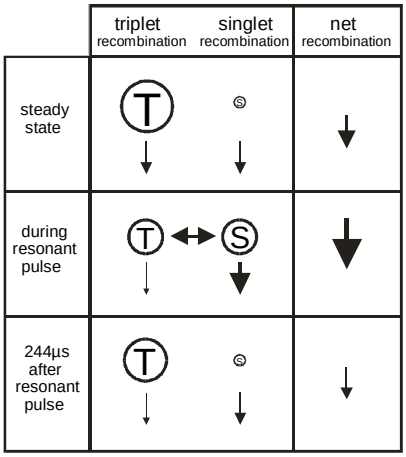

Fig. 4: Qualitative illustration of the dynamics of triplet -recombination. For details see text.

The prove of non-vanishing triplet recombination in µc-Si:H is of importance for the understanding of the recombination mechanism. Our measurements strongly suggest that the recombination cross sections can strongly be determined by spin-spin or spin-dipole interaction, which are related to bonding angles and topologies and hence depend on the microscopic structure of the material.

References
[1] Böhme, C.; Lips, K.:
Time domain measurement of spin-dependent recombination
Appl. Phys. Lett., 79 (26), 2001, pp. 4363-4365

[2] Böhme, C.; Kanschat, P.; Lips, K.:
Time domain measurement of spin-dependent recombination - a novel defect spectroscopy
Nucl. Instr. Meth. B, 186 (1-4), 2002, pp. 30-35

[4] Böhme, C.; Kanschat, P.; Lips, K.:
Quantum-beat recombination echoes
Europhys. Lett., 56 (5), Dec 2001, pp. 716-721

C. Böhme, K. Lips, W. Fuhs
(SE1.01a Crystalline Silicon Thin-film Solar Cells)

Amorphous/crystalline-silicon heterojunction solar cells

a-Si/c-Si heterojunctions are promising candidates for highly efficient solar cells processed at low temperatures. They are attractive as a low-cost alternative to the traditional Si wafer technology. As a bench mark Sanyo Corp. has reported on an efficiency of η=20.7 % for a laboratory cell based on this type of heterojunction with monocrystalline Si and has announced the production of modules of η=15.2 %. It is very interesting to use such low-temperature emitters also with low-cost Si substrates and in particular with polycrystalline Si thin-film solar cells. In spite of the achieved technological progress little is known about the physical properties of the heterojunction interface, in particular about the role of band offsets, the passivation and the effect of interface states.

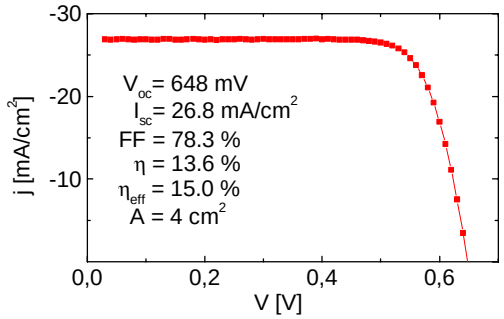

Fig. 1: I-V characteristics of an ITO/a-Si:H(P)/c-Si(p)/BSF heterojunction solar cell under AM1.5 illumination.

A standard preparation procedere was developed for the a-Si/c-Si heterojunction solar cells: The emitter, phosphorus-doped amorphous silicon, a-Si:H(P) about 20 nm thick, was deposited on a p-type Si(111) wafer (350 µm) by standard PECVD at T=210 °C. The c-Si wafers had a back-surface field and were pretreated by a HF-dip (3 % HF:H_2O) prior to the deposition. The front contact was made by a transparent conducting oxide (80 nm of ZnO or ITO) deposited by sputtering. With this standard procedure an efficiency of η=13.6 % was obtained on an area of 4 cm² without adding any additional high-tech feature to cell structure. The good quality of the heterojunction is confirmed by a value of η_{eff}= 15.0 % for the effective area efficiency (Fig.1). The modification of the interface properties by applying various wet- chemical pretreatment procedures led to the result that the lowest interface recombination velocity and the highest efficiency were obtained for the atomically flat and H-terminated Si surface. The electrical and photoelectrical studies of the TCO/a-Si/c-Si structures showed that the optimization of both the interface treatment and the deposition procedure for the a-Si:H(P) film are of crucial importance for the device performance. Since it turned out that the band profile in the c-Si wafer is to some extend determined by the TCO layer the optimization of the emitter must include the entire TCO/a-Si:H/c-Si film structure [1,2].
For a more detailed understanding we have modeled and numerically simulated the device behavior taking into account of the complex electronic structure of a-Si:H(P) and of the c-Si surface. Fig. 2 addresses the question whether there are intrinsic advantages in the use of n- or p-type c-Si wafers by plotting the efficiency as a function of the respective band-offset in the minority carrier bands. Using internal photoemission spectroscopy (IPE) we determined the band offset in the conduction and valence band, ΔE_C for c-Si(p) and ΔE_V for c-Si(n), to about 0.1 eV and 400-500 meV, respectively. If interface states are neglected the efficiencies for a-Si(P)/c-Si(p) and a-Si(B)/c-Si(n) are comparable. However, if interface states are introduced which enhance recombination the efficiency is more strongly reduced for the a-Si(P)/c-Si(p) structure as compared to the opposite configuration. A reasonable explanation for this result is that the higher band offset of the a-Si(B)/c-Si(n) structure causes strong inversion at the interface which results in a considerable reduction of recombination.

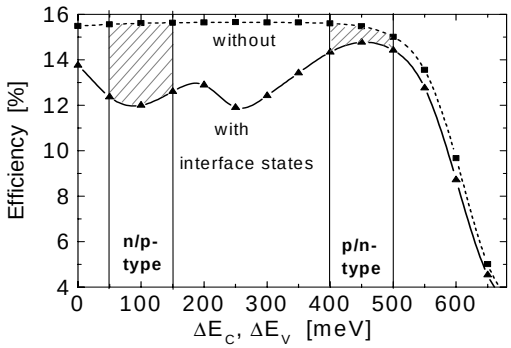

Fig. 2: Influence of the band discontinuity of the minority carrier band of crystalline silicon on the cell efficiency. The ranges of the a-Si:H(P)/c-Si(p) and a-Si:H(B)/c-Si(n) structures are indicated. The two curves have been calculated with D_{it}-values of 0 and 10^{12} $cm^{-2}eV^{-1}$.

References

[1] Schmidt, M.; Froitzheim, A.; Stangl, R.; Elstner, L.; Kliefoth, K.; Fuhs, W.:
Photocurrent Analysis in TCO/a-Si:H/c-Si Solarcell Structures
Proc. of 17th Europ. Photovoltaic Solar Energy Conf. (2001) in press

[2] Stangl, R.; Froitzheim, A.; Elstner, L.; Fuhs, W.:
Amorphous/Crystalline Silicon Heterojunction Solar Cells, a Simulation Study
Proc. of 17th Europ. Photovoltaic Solar Energy Conf. (2001) in press

A. Froitzheim, R. Stangl, H. Angermann, L. Elstner, W. Fuhs, K. Kliefoth, M. Schmidt
(SE1.01b Silicon Heterostructures)

Thin organic layers: a new approach for functionalization of Si surfaces

The recent progress in the development of electronic devices on basis of organic semiconductors has considerably raised the interest in studies which explore the potential of organic materials. It appears particularly attractive to use organic films as buffer layers in heterostructures since the large variety of available compounds is expected to enable a systematic engineering of the junction, for instance by a variation of an external dipole moment on the semiconductor surface.

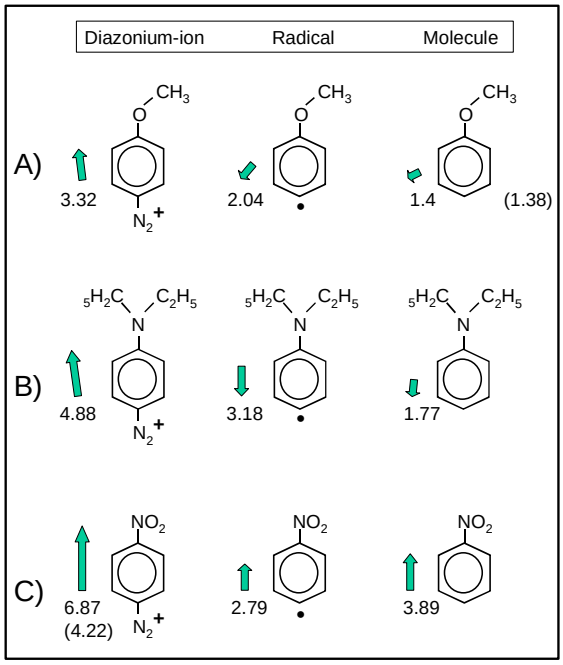

Fig. 1: Changes of the dipole moment and orientation of organic molecules after radical formation during the grafting process as calculated by the DFT method (Dipole strength in units of debye, values in parenthesis are taken from the literature; the orientation is shown by the arrow).

In order to form such organic layers on monocrystalline silicon we used electrochemical grafting of organic molecules on hydrogenated Si surfaces in aqueous electrolytes. The organic molecules consist of a benzene ring with a diazo-group (N_2^+-Ø-G) where G is a variable electron donor or acceptor group which defines the orientation and strength of the dipole moment. Fig. 1 convincingly demonstrates the large variety of available compounds and dipole moments. The deposition process was performed at room temperature by applying a cathodic current to the Si electrode (electron injection into the electrolyte). Cathodic polarization prevents the oxydation of the Si surface. Pulsed in-situ photovoltage (SPV) and an especially designed photoluminescence (PL) techniques, which has been developed in our laboratory, were used to investigate the changes of band bending and of the concentration of active centers for nonradiative recombination. The relative change of the SPV signal by grafting of the organic molecule on the H-terminated Si surface, ΔU_{PV}, is plotted in Fig. 2 as a function of the effective dipole moment perpendicular to the Si(111) surface for various molecules. ΔU_{PV} is a direct measure of the change of the band bending in the c-Si substrate. The grafting of a thin layer of a diazonium compound, diethylaniline or nitrobenzene on atomically flat p-Si(111):H surfaces induces changes of the band bending of about +20 or –110 meV, respectively. The concentration of nonradiative surface defects increases only by a factor of about 3 with respect to the perfect hydrogenated Si surface ($N_s < 10^{11}$ cm^{-2}) which suggests very good passivation of interface states. The changes of band bending are less pronounced when a rough Si surface is used where the dipoles are no longer regularly ordered at the surface [1].

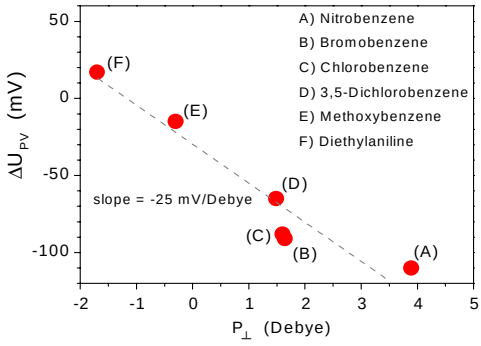

Fig. 2: Change of the photovoltage, ΔU_{PV}, which is directly related to the change in band bending, as a function of the effective dipole moment, p⊥, perpendicular to the Si(111) surface. (A) strongest and (F) weakest electron acceptor group.

These first results are encouraging as they demonstrate good surface passivation and a modification of the electronic structure by thin organic layers. The results show that the band bending in the Si crystal can considerably be modified which possibly is induced by charge transfer via the formed Si-C bonds. A variation in the band offset due to the introduced dipole has still to be shown. The next step will be the formation of electrical contacts on top of these layers in order to study the properties of the films as buffer layers in a device structure.

References

[1] Hartig, P.; Rappich, J.; Dittrich, Th.:
Engineering of Si Surfaces by Electrochemical Grafting of p-Nitrobenzene Molecules
Appl. Phys. Lett 80 (2001) 67-69

J. Rappich, P. Hartig, M. Schmidt
(SE1.01b Silicon Heterostructures)

Department

SE2 Heterogeneous Material Systems

Multi-source evaporation of $Cu(Ga,In)S_2$ for thin-film solar cells

Incorporation of gallium causes a higher absorber band gap. As we have shown in our previous work this leads to a higher open circuit voltage of the solar cell. It was remarkable that the gain in open circuit voltage could be higher than the increase in band gap. The experiments were based on different sequential processes which have in common that metallic precursor films are reacted in a sulfur containing atmosphere. It was found that the reaction kinetics of the sequential processes, via the sequential formation of $CuGaS_2$ and $CuInS_2$, lead to a strong vertical gradient of the [Ga]/[In] ratio in the film. The maximum achievable band gap in the active region of the cell was therefore limited to approximately 1.6 eV, corresponding to a [Ga] / ([In+[Ga]) ratio of 10%. The inherent grading of the gallium content in the active cell region does not allow a full assessment of the electronic influence of Ga. Therefore, we have for the first time used multi-source evaporation to grow $Cu(In,Ga)S_2$ in this reporting period. Four different preparation sequences have been investigated:

- M1: evaporation with constant rates and substrate temperatures,
- M2: evaporation of In,Ga,S at lower substrate temperatures (typically 250 °C) followed by evaporation of Cu,S at higher (typically 500 °C) substrate temperature,
- M3: same as M2 but including a certain amount of Cu (below stoichiometry) already during the first stage,
- M4: same as M3 but with high substrate temperature from the beginning.

Straightforward co-evaporation (M1) resulted in poor reproducibility and unsatisfying material properties. Tentatively, this has been assigned to Cu_xS segregated within the polycrystalline film.

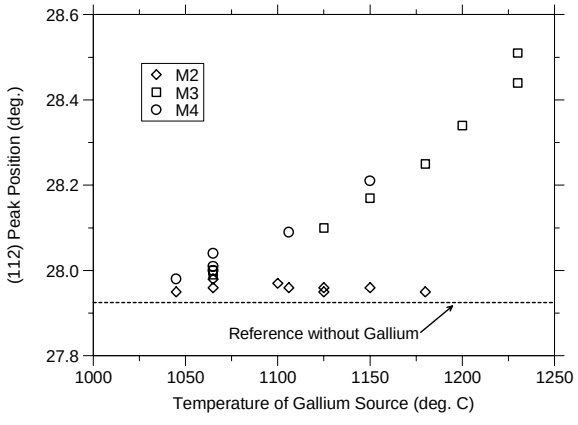

Fig. 1. Position of the (112) reflection in XRD as a function of the gallium source temperature.

The gallium content in the upper part of the film can be judged from its lattice constant. Fig. 1 shows the position of the (112) peak in x-ray diffraction (XRD) as a function of the gallium source temperature. It can be seen that in case of the M2 sequence the lattice constant and hence gallium content of the upper part of the film is almost constant. In general, also taking into account the previous results from sulfurization, there is a certain correlation between the phase formation sequence, the film properties and the homogeneity of Ga distribution.

Sample	E_g eV	V_{oc} mV	j_{sc}* mA/cm^2	ff %	η* %
#94 M2	1.53	776	22.4	74	12.9
#96 M3	1.65	837	18.4	70	10.8
#113 M3	1.74	895	16.2	70	10.1

* Active area

Table 1. Development status of $Cu(In,Ga)S_2$ solar cells (Band gap Eg determined from spectral response).

Re-crystallization, as it must occur in sulfurization and in sequence M2, yields good film properties but as described causes a strong gradient in the Ga distribution perpendicular to the substrate. In M3 and M4, a Cu-poor quaternary chalcopyrite or related compound is already formed during the first stage. This prevents the sequential segregation of $CuGaS_2$ and $CuInS_2$ but also limits the beneficial influence of Cu_xS induced re-crystallization in the second stage. Using sequence M2 we have achieved a new world record for Se-free chalcopyrite solar cells (Table 1, 12.3 % total area efficiency confirmed by the National Renewable Energy Lab, U.S.A.) The more homogeneous Ga profile with M3 and M4 allows higher band gaps, up to values which are suitable for the top cell in a tandem configuration. While the transport properties are clearly inferior compared to the re-crystallized lower band gap material they are still sufficient for more than 10 % efficiency which is a remarkable value at this band gap (Table 1).

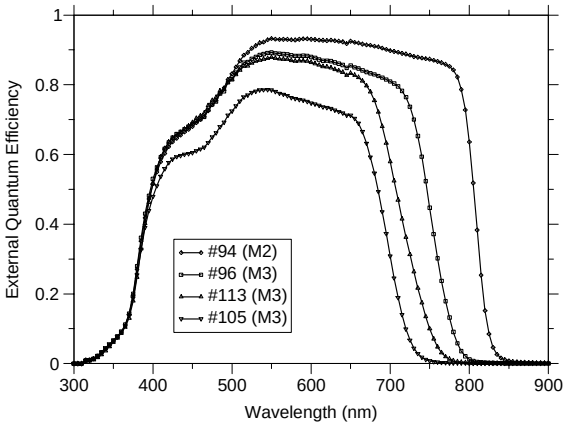

Fig. 2. External quantum efficiency of $Cu(In,Ga)S_2$ solar cells. Homogeneous gallium distribution and hence significantly increased band gap are achieved by using preparation sequence M3.

R. Klenk, R. Kaigawa, C. Kelch, M. Kirsch, A. Neisser, M.Ch. Lux-Steiner
(SE2.05 Chalcopyrite Solar Cells)

(Zn,Mg)O as window layer for Cd-free chalcopyrite solar cells

Current chalcopyrite based thin film solar cells use a complicated three layer window typically consisting of a CdS buffer layer deposited from a chemical bath, an undoped sputtered ZnO layer and a highly doped ZnO:Al or ZnO:Ga layer. The CdS buffer has major drawbacks: it contains Cd and the chemical bath deposition does not integrate well into a production line that is otherwise using only dry vacuum processes. There are indications that the requirement for the undoped ZnO layer is due mostly to technological reasons rather than device physics. Nevertheless, the band line-up at the buffer/ZnO interface could in principle influence the potential drop across the absorber and the Fermi-level position at the absorber/buffer interface. Following a concept proposed by T. Minemoto et al., the band gap of ZnO can be widened by alloying with MgO which should lead to a reduced conduction band cliff. Since band matching is also normally a major task of the buffer layer it might be possible to omit the buffer if an optimized ZnO is used. This would result in a very attractive completely dry cell manufacturing.

We have been able to grow single phase $(Zn_{0.85}Mg_{0.15})O$ films with the expected lattice constant and band gap (Fig. 1) by RF-sputtering from a mixed target. The new TCO has been tested in solar cells based on absorbers with varied band gap between 1.1 and 1.7 eV. The preliminary results can be summarized as follows: substituting the ZnO layer by (Zn,Mg)O has a very small positive influence in cells with a CdS buffer layer for all absorbers. If the CdS buffer is omitted the influence is much more significant. In case of low gap $Cu(In,Ga)(S,Se)_2$ absorbers we have achieved an efficiency of almost 10 % (Fig. 2) which is a remarkable value for completely dry process. With the higher gap absorbers the efficiencies are also increased but still marginal in terms of absolute value.

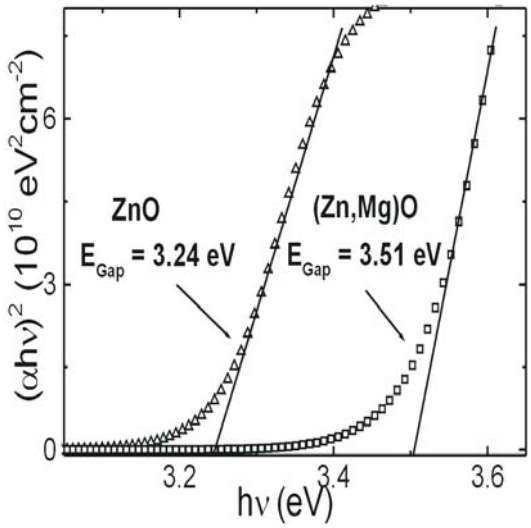

Fig. 1: Determination of the optical band gap of ZnO and (Zn,Mg)O from $(\alpha h\nu)^2$ vs. $h\nu$ plots.

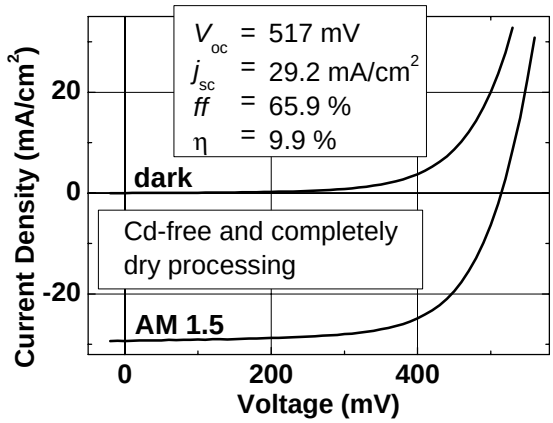

Fig. 2: jV curves of a $Cu(In,Ga)(S,Se)_2$ / (Zn,Mg)O / ZnO solar cell. No wet chemistry was used to prepare this cell.

The expected tendency in band alignment has been confirmed in a model experiment where ZnO, (Zn,Mg)O and ZnO:Ga have been deposited sequentially onto a GaP substrate. A cross section has been prepared by mechanical polishing and investigated in the Kelvin probe force microscope (KPFM) after sputter cleaning (Fig. 3). It is expected that this unique method can assist in developing optimized band alignments throughout the chalcopyrite/buffer/TCO heterostructure.

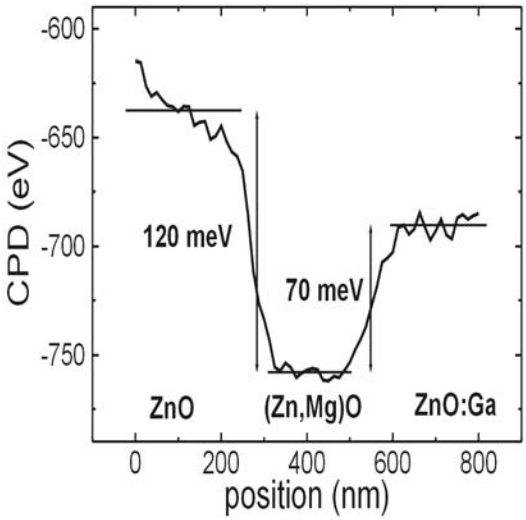

Fig. 3: Contact potential difference CPD as measured by KPFM on the cross section of a polycrystalline film consisting of ZnO, (Zn,Mg)O, and ZnO:Ga deposited sequentially onto a GaP wafer.

Th. Glatzel, R. Klenk, M. Kirsch, S. Sadewasser, M. Ch. Lux-Steiner
(SE2.05 Chalcopyrite Solar Cells)

Analysis of recombination losses in chalcopyrite solar cells

Recombination losses are analyzed by measuring *j(V)* curves as a function of temperature and illumination. The open circuit voltage for state of the art $CuInSe_2$ and $CuGaSe_2$ solar cells from the Ångström Solar Center extrapolates in Fig. 1 for zero Kelvin to values corresponding to the band gap of the considered absorber material, indicating that recombination in the space charge region dominates the current transport. In contrast, this is not the case for our baseline $CuInS_2$ cells. The open circuit voltage extrapolates to values some hundred mV below the value corresponding to the $CuInS_2$ band gap of 1.5 eV, indicating a stronger influence of the $CuInS_2$/CdS interface.

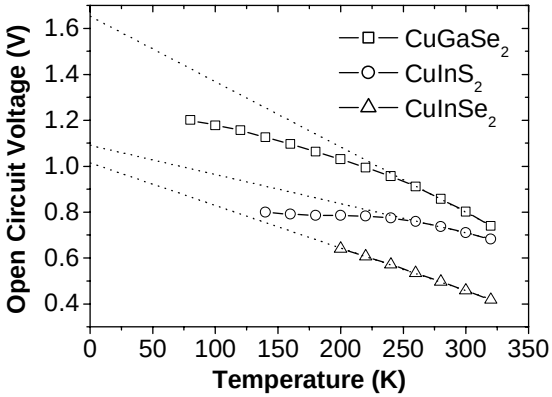

Fig. 1. Open circuit voltage of different chalcopyrite solar cells as a function of temperature

For selenide based cells, different models have been suggested to explain the negligible influence of recombination at the absorber/CdS interface, including a low density of states due to good lattice matching, an n-type ordered vacancy compound (OVC) surface segregation or a buried homojunction by diffusion of Cd into the absorber. We have been able to show, however, that suppression of interface recombination can be a generic feature of any heterojunction if only a few design rules are taken into account. In $CuInS_2$ cells these rules are apparently only partly fulfilled.

The further analysis of the *j(V)* curves in terms of a modified one diode model gives diode quality factors and saturation currents. In contrast to the selenide based cells we learned from the diode quality factors that the dominating recombination mechanism in $CuInS_2$ cells depends on the illumination. For $CuInS_2$ cells in the dark, strongly temperature dependent diode quality factors point to recombination assisted by tunnelling. Under illumination the diode quality factors are significantly lowered, indicating that tunnelling assistance is reduced.

In order to further investigate the illumination induced effects we determine the activation energy of the main recombination in the dark and under illumination, respectively. An Arrhenius plot of the saturation current density with a correction for the temperature dependence of the diode quality factor should yield a straight line where the slope provides the activation energy. For selenide based cells these plots result in activation energies again corresponding to the band gap of the considered absorber material in the dark as well as under illumination. In contrast, we find illumination dependent behavior for $CuInS_2$ cells as shown in Fig. 2. in accordance with our findings from the diode quality factors.

The $CuInS_2$ cells from standard absorber preparations (rapid thermal process RTP) show under illumination activation energies below the band gap, which is believed to be due to recombination at the interface over a barrier which is reduced by the unfavourable band line-up or Fermi-level pinning at the $CuInS_2$/CdS interface. In the dark, the activation energy is at least 0.2 eV higher, with values equivalent to the absorber band gap for cells sulfurized in the conventional thermal process (CTP). These results suggest a change of the dominating recombination mechanism from tunnelling enhanced recombination via traps in the space charge region in the dark to partly tunnelling enhanced recombination via interface states under illumination.

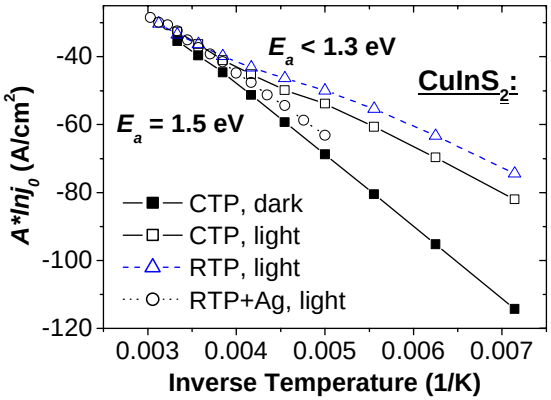

Fig. 2. Corrected saturation currents for $CuInS_2$ cells depending of absorber preparation

As an exception cells where the absorbers were doped with Ag did not exhibit the barrier reduction under illumination. Furthermore, the lateral conductivity of the Ag containing cells is decreased. From these findings we conclude that a reduced net carrier density shifts the dominant recombination away from the interface. Even if this improved open circuit voltages by some 10 mV, the values are still moderate in view of the absorber band gap E_g of 1.5 eV.

J. Reiß, R. Klenk, M.C. Lux-Steiner
(SE2.05 Chalcopyrite Solar Cells)

Transport mechanism of solar cell grade polycrystalline $CuGaSe_2$ thin films

$CuGaSe_2$ as a wide-gap chalcopyrite (Eg=1.68eV) is a promising candidate for high open circuit voltages in solar cells and an ideal partner for copper indium selenide solar cells in tandem photovoltaic devices. However, considerable optimization of $CuGaSe_2$ based solar cells is necessary for this purpose and the limitations of this material in comparison to $CuInSe_2$ are still not clear.
Various studies present transport properties of chalcopyrite single crystals and epitaxial layers but the influence of grain boundaries in device grade polycrystalline material is almost unknown.

Transport studies

In our study the mechanism of charge carrier transport in solar cell grade polycrystalline $CuGaSe_2$ has been studied in the temperature range of 80-350K using Hall effect and conductivity measurements in the dark. Polycrystalline $CuGaSe_2$ layers were grown on soda lime glass substrates by PVD according to our standard process resulting in Mo/$CuGaSe_2$/CdS/ZnO/NiAl solar cells reaching efficiencies of 7.9 % [1]. Figure 1 shows a typical mobility plot of the measured samples.
Mobilities of the polycrystalline films were found to be thermally activated in the temperature range of 150-300K (region II) and are explained by the grain-boundary barrier model developed by Seto [2] for polycrystalline Si assuming thermionic emission of the charge carriers across the grain boundaries. Mobilities are activated according to

$\mu = \mu_0 \exp(E_a / kT)$.

Inter-grain barriers limiting the charge carrier transport and the band bending corresponding to E_a at the grain boundaries were found to vary between 60 and 120meV. Using Poisson's equation a charge density p_t of ~5e11/cm^2 located at the grain boundaries was obtained independent of the doping level i.e. the position of the Fermi-level. Thus a defect state at the grain boundaries above the Fermi-level is concluded.

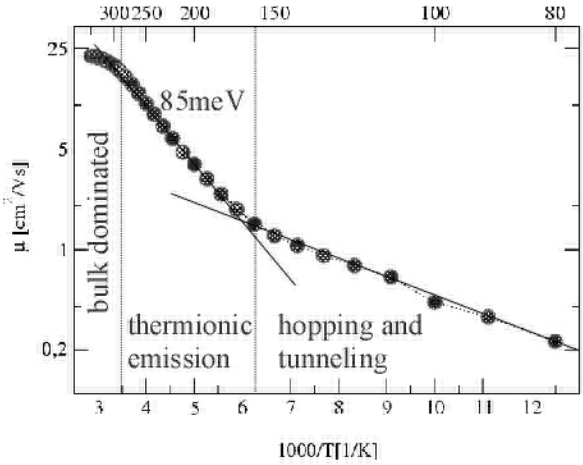

Fig.1: Mobility vs 1/T for typical stoichiometric samples. The regions dominated by different scattering mechanisms are shown.

Above temperatures of 300K (region I) charge transport is not limited by grain boundary scattering, but phonon scattering in the bulk of the grains dominates.
At temperatures below 150K (region III) the activation energy of the mobility lowers indicating a change in the conduction mechanism. Comparison with transport measurements in epitaxial $CuGaSe_2$ films indicates hopping in defect states as the dominating transport path. The resulting grain boundary model is summarized in Fig. 2.

References

[1] S. Schuler, S. Nishiwaki, M. Dziedzina, R.Klenk, S. Siebentritt, M. Ch. Lux-Steiner, Mat. Res. Soc. Symp. Vol.668 (2002) in press

[2] Y. W. Seto, Journal of applied Physics Vol. 46 (75), p.5247

S. Schuler, S. Nishiwaki, N. Rega, S. Brehme, S. Siebentritt, and M.Ch. Lux-Steiner
(SE2.05 Chalcopyrite Solar Cells)

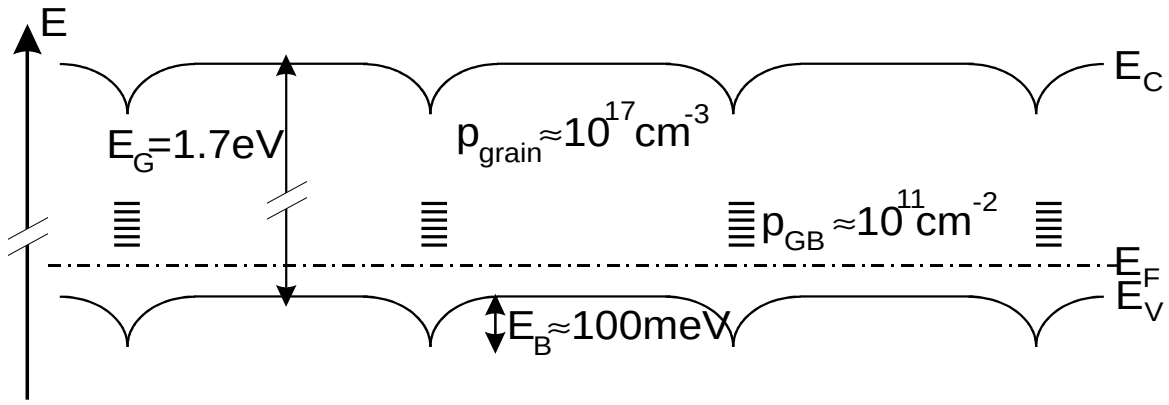

Fig.2: Concluded grain boundary model. E_C, E_V, E_F conduction band, valence band and Fermi-energy-level, E_B grain boundary barrier, E_G band gap, p_{grain} bulk doping density, p_{GB} grain boundary defect density.

$CuGaSe_2$ by Chemical Vapor Deposition (CVD)

Recent improvements of the CVD-process

A stoichiometric volatility and therefore improved material yield of the source material for CGS preparation was achieved by switching from a single $CuGaSe_2$ powder source to two binary sources, Cu_2Se and Ga_2Se_3 [1]. The gas phase composition can be accurately adjusted by modifying the flow of the halide transport agents for Cu_2Se and Ga_2Se_3, HI and HCl respectively. For this set up a two-stage deposition process has been adapted: i) in the first stage nearly stoichiometric CGS is grown during 3-4 hours at a substrate temperature of 500°C and thereafter ii) just Ga_2Se_3 is transported for 20 min to the sample side at 530°C. The first stage provides high-quality crystallites with grain sizes in the range of 1.5 µm. The second stage ensures a final overall slightly Ga-rich composition for optimal device performance.

Photoluminescence of CVD grown $CuGaSe_2$

Different from other deposition methods, the photoluminescence (PL) of CVD grown $CuGaSe_2$ thin films exhibit a deep luminescence peak located around 1.3 eV. This CVD-specific radiative recombination mechanism has been related with a deep acceptor-like defect band around 240 meV, probably caused by V_{Ga} [2]. Chemical calculations assisted with ChemSage software revealed the active role Ga plays in the removal of iodine species from the saturated sample-side atmosphere in the CVD reactor. The thus reduced amount of Ga available for incorporation into the solid film, together with the high growth rate would favor the formation of V_{Ga}. After the second stage leading to an overall Ga-rich composition a significant decrease of the 1.3 eV signal is observed (Fig.1).

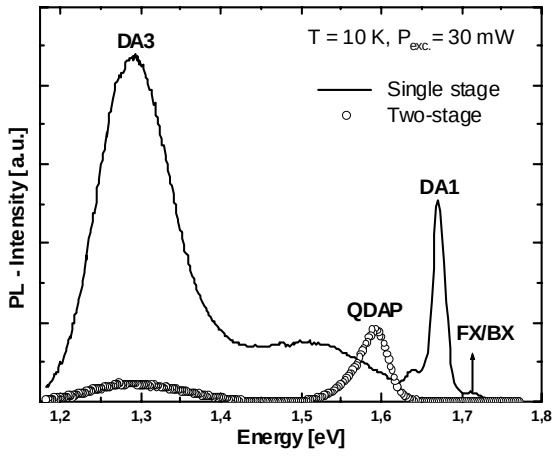

Fig. 1: PL spectra of samples after completion of the first stage (solid line) and after the second stage (dotted). Notation of peaks follows [2].

Device performance

We have recorded a relative improvement of more than 20 % in the efficiency of two-stage grown samples compared to previous cells based on slightly Ga-rich single-stage CGS absorbers (see Table 1).

Sample	Voc (mV)	Jsc (mA/cm2)	FF	Eff (%)
Single-stage	684	11.7	0.51	4.1
Two-stage	804	12.9	0.57	5.9

Table 1: Comparison of PV parameters under AM1.5 illumination of cells grown by single- and two-stage processes, used for the analysis.

The highest efficiency value achieved so far is 6.1% (V_{OC} up to 844 mV) under AM 1.5 illumination Quantum efficiency as well as EBIC (electron beam induced current) measurements reveal an enlarged space charge region for the two-stage processed samples (Fig.2) [3]. This result can be explained by the lower doping level of Ga-rich material due two a higher degree of compensation. In accordance with the enlarged space charge region of two-stage based devices the tunneling contribution to the electronic transport is reduced, identified from the diode ideality factor in current voltage analyses, leading to a better device performance.

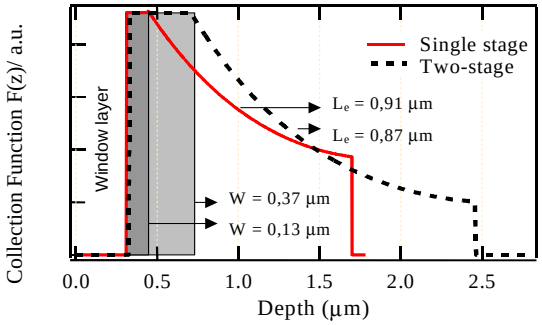

Fig. 2: Collection function profile from EBIC data of single-stage (solid) and two-stage (dotted) samples. The SCR (shaded) is enlarged after the second stage (from 0.13 to 0.37 µm) and the minority carrier diffusion length slightly reduced (from 0.91 to 0.87 µm), compared with single stage sample values.

Microstructure of ZnO/CdS/$CuGaSe_2$/Mo Interfaces

Actual chalcopyrite based solar cells are characterized by a complex polycrystalline structure. Microstructural characterization by transmission electron microscopy (TEM) and scanning probe microscopes assists in refinement of the device models when correlated with electrical measurements.
The microstructural properties of the different interfacial regions have been studied in the CVD-ZnO/CdS/$CuGaSe_2$/Mo solar cell heterostructure in cooperation with SF/BENSC and the Fritz-Haber-Institute of the MPG. The $CuGaSe_2$-film was prepared by the two-stage-process. High-resolution transmission electron microscopy (HRTEM) combined with scanning energy dispersive X-ray detection (EDX) shows the formation of an interfacial

$MoSe_2$-layer (Fig. 3) at the back contact, while, on the other hand, no Cu-Se precipitates have been found neither at the CdS/$CuGaSe_2$-interface nor in the grains of the absorber film, as usually detected in Cu-rich $CuGaSe_2$-thin film solar cells [4].

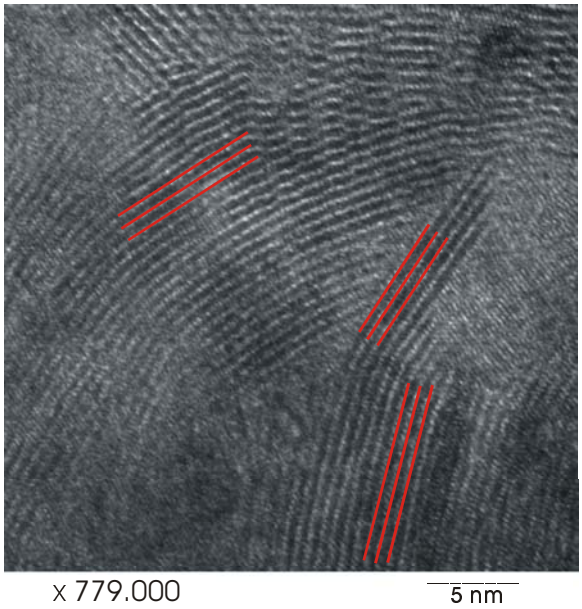

Fig. 3: High-resolution TEM picture of the interfacial $MoSe_2$ film found in the ZnO/CdS/$CuGaSe_2$/Mo solar cell heterostructure.

Thin interfacial $MoSe_2$ films have thickness of ~150 nm and are formed only onto soda-lime glass substrates. This suggests a promoting behavior of the diffusing Na cations in the formation process of the layered structure of $MoSe_2$ onto the metallic Mo film. The $MoSe_2$ layers are stacked together by weak Van-der-Waals forces and, as shown in Fig.3, these layers have a distance of ~6.5 Å in very good agreement with the literature, and are oriented almost perpendicular or tilted to the Mo-back contact plane (i.e. the c-axis of the hexagonal lattice is almost parallel or tilted to the substrate plane).
Kelvin probe force microscopy (KPFM) investigations on the cross-sectional ZnO/CdS/$CuGaSe_2$/Mo heterostructure are shown in Fig. 4 and reveal clear variations of the work function indicating well defined electronic transitions at the interfaces. This is important since a second junction at the back contact of the solar cell would severely reduce the maximum solar-to-electric conversion efficiency. TEM and KPFM reveal that process conditions in the CVD favor the formation of a $MoSe_2$ layer between back contact and absorber. This can be correlated with a roll-over of the jV(T) characteristics at low temperatures (blocking diode) as shown in Fig. 5.

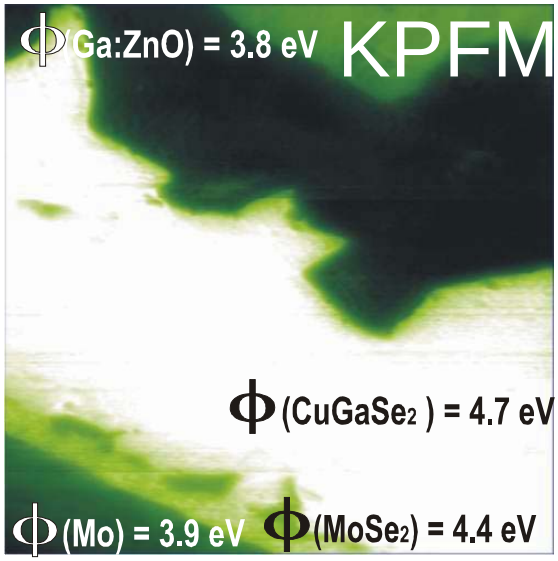

Fig. 4: Kelvin probe force microscopic picture of the ZnO/CdS/ $CuGaSe_2$/Mo solar cell heterostructure.

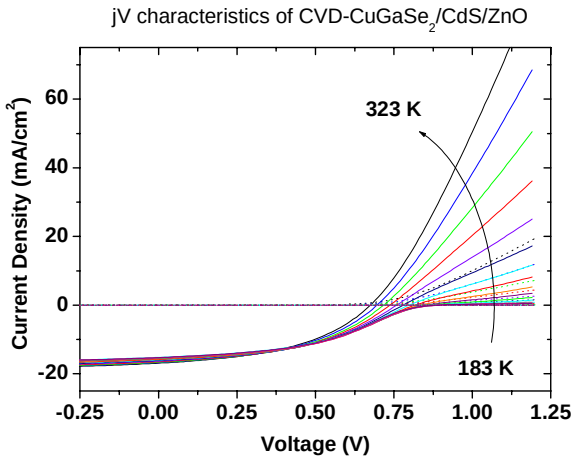

Fig. 5: Temperature-dependent jV-characteristics of the ZnO/CdS/ $CuGaSe_2$/Mo solar cell heterostructure.

References
[1] D. Fischer et al., Solar Energy Mat. Solar Cells 67 (2001) 105.
[2] A. Meeder et al., Thin Solid Films, 403-404 (2002), 495-499.
[3] D. Fuertes Marrón, et al., Proc. 17th Int. PVSEC Conf. Munich.
[4] see, for example: V. Nadenau et al., Journal of Applied Physics 85 (1999) 534.

S.M. Babu, D. Fuertes Marrón, Th. Glatzel, K. Höhn, A. Jäger-Waldau, A. Meeder, T. Münchenberg, A. Rumberg, M. Rusu, Th. Schedel-Niedrig, S. Wiesner, R. Würz, M. Ch. Lux-Steiner (SE2.05 Chalcopyrite Solar Cells) in collaboration with N. Pfänder, H. Sauer (Fritz-Haber-Institute), P. Schubert-Bischoff (SF/BENSC)

Interdiffusion study at the ZnSe / Cu(In,Ga)(S,Se)$_2$ heterojunction by ERDA measurements

A co-operation of the CSVT group and the ERDA group of the ISL is engaged in investigating diffusion processes at the ZnSe / Cu(In,Ga)(S,Se)$_2$ heterosystems. The aim of the project is the quantitative determination of interdiffusion processes of chemical elements at the heterojunction. As previously shown the ZnSe deposition on chalcopyrite absorbers using chemical vapor deposition (CVD) or metal organic CVD (MOCVD) needs a minimal deposition temperature of 280 °C / 265 °C due to reaction kinetics in the gas phase. Additionally, the homogeneity of the coverage and the layer quality increase with increasing temperature. Therefore, one would expect higher solar cell efficiencies with enhanced deposition temperatures. In contrast to this, best results were found for the lowest temperatures and shortest deposition times. The question arises if structural changes may occur during the deposition. Thus, the structural composition of the layers is investigated by means of heavy ion elastic recoil detection analysis (HI-ERDA). From the amount of the scattered atoms detected, the ejectiles, this technique allows to determine the absolute concentration of all chemical elements of the sample simultaneously. Furthermore, the depth distribution of the element concentration can be calculated from the energy of the ejectiles.

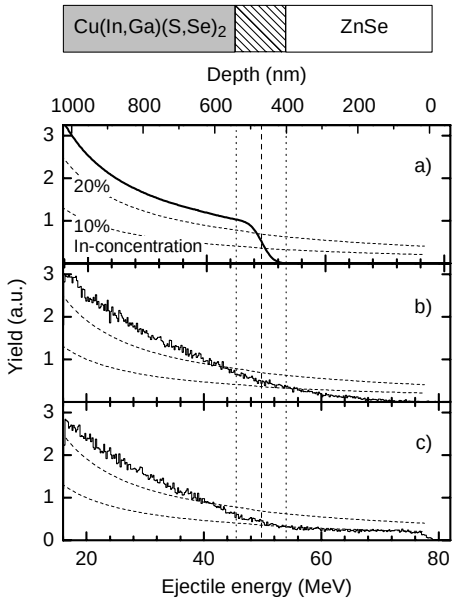

Fig. 1: Qualitative demonstration of In diffusion from the polycrystalline Cu(In,Ga)(S,Se)$_2$ absorber into the ZnSe buffer measured with 143 MeV ^{86}Kr projectiles at a scattering angle of 40 °. (a) Simulation of the In energy spectrum taking into account surface and interface roughness as derived from AFM and the corresponding sulfur spectrum without diffusion. (b) Measured In spectrum of an as grown sample. (c) Measured In spectrum of a sample after annealing for 5h at 400 °C.

Fig. 1 shows an example of In profiles from ZnSe / Cu(In,Ga)(S,Se)$_2$ heterostructures grown by CVD at 350 °C for 3h. Fig. 1a depicts the spectrum as it was expected theoretically without In-diffusion. Fig. 1b and fig. 1c show the measured In spectra of an as grown sample and of a sample which was annealed at 400 °C for 5h, respectively. The occurring of In-ejectiles with energies above 50 MeV indicate the presence of In atoms in the depth region of the ZnSe buffer layer. For the case after annealing the fraction of In is significantly enhanced up to 80 MeV, corresponding to the surface of the samples. This proves the diffusion of the In from the absorber into the buffer layer qualitatively.

For the quantitative discussion of diffusion parameters, it is necessary to understand the effect of surface roughness. As the beam spot has a finite area (some mm^2), roughness results in a distribution of path lengths for the individual projectile/ejectile couples and, therefore, in a broadening of the energy spectra. If this effect is unfolded, the remaining energy broadening corresponds to diffusion.

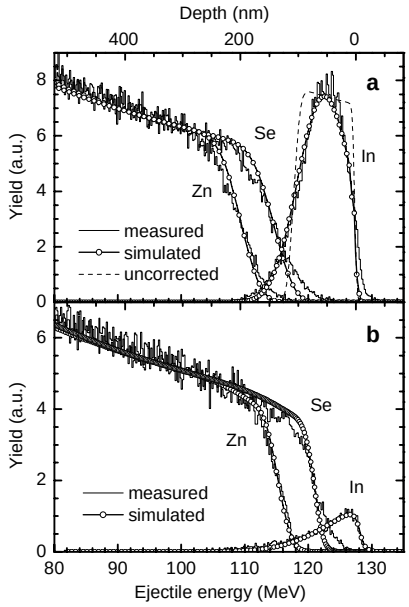

Fig.2: Experimental and simulated spectra obtained from a ZnSe single crystal covered with a 90nm thick In layer, including roughness corrections. The measurements were performed with a 230 MeV ^{129}Xe beam. (a) As grown sample. A mean roughness of ±45nm has been determined by means of AFM. The dashed curve represents the simulation calculation for In without roughness correction. (b) The result for a second part of the sample analyzed after annealing for 5h at 350 °C

S. Lindner (SE2.05 Chalcopyrite Solar Cells) in collaboration with W. Bohne, J. Röhrich, E. Strub (SF4)

Kelvin probe force microscopy

Kelvin probe force microscopy (KPFM) in ultra-high vacuum allows to simultaneously obtain structural as well as electronic information (work function Φ) of a sample's surface with an extremely high lateral (~ 20 nm) and energy resolution (~ 5 meV).
The application of the KPFM to a solar cell absorber material was demonstrated using $CuGaSe_2$ deposited on Mo covered glass by chemical vapor deposition. Figure 1 shows the topography (b) and the work function (a) of the $CuGaSe_2$ film in dark conditions. The work function of the illuminated (20 mW, 675 nm) sample is shown in Fig. 1 (c). In the topography the granular structure of the polycrystalline film is clearly visible. Except for one grain (indicated by the ellipse) at the bottom of the image the work function increases homogeneously under illumination. This becomes clearer in Fig. 1 (d) where a line scan through the images is presented. The major part of the sample shows an 80 meV increase under illumination with only one grain showing a 200 meV decrease, which was attributed to a $CuSe_x$ impurity phase.

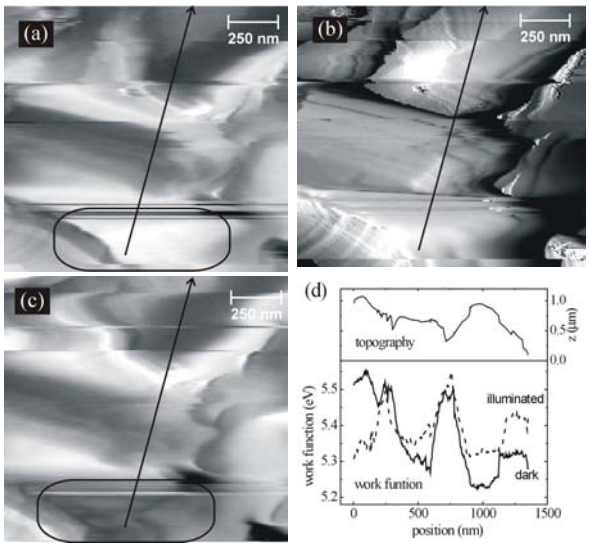

Fig. 1: KPFM measurements of $CuGaSe_2$ on Mo/glass. ***(a)*** *work function image (Φ = 5.14 eV – 5.53 eV) of the surface in the dark,* ***(b)*** *simultaneously measured topography image (gray scale ≈ 1044 nm),* ***(c)*** *work function image of the surface under illumination with 20 mW at 675 nm (Φ = 5.21 eV – 5.53 eV),* ***(d)*** *line scans of the topography and work function.*

The surface of a MOVPE-grown $CuGaSe_2$ film on a ZnSe (110) single crystalline substrate is shown in Figure 2. Again the topography (a) shows the grains of the polycrystalline film. However, x-ray diffraction revealed a film orientation along the (220) direction of the $CuGaSe_2$ unit cell. The corresponding work function image in Fig. 2 (b) clearly shows different areas of constant work function, which coincide with the crystal facets of the grains observed in the topography. In Fig. 2 (c) this is demonstrated more clearly: the topography is represented as the 3D effect and the work function is superimposed on this image represented by the color scale. The observed work function difference in dependence of the orientation of the crystal facets is due to a surface dipole which is characteristic for each orientation. For this oriented film, an analysis of the angles between the facets allows to determine the surface orientation of the facets, as indexed in Fig. 2(b). The observation of such a wide variation (up to 250 meV) of Φ within one surface will influence the band alignment to a subsequently built-up heterostructure and might have a detrimental effect on the solar cell efficiency.

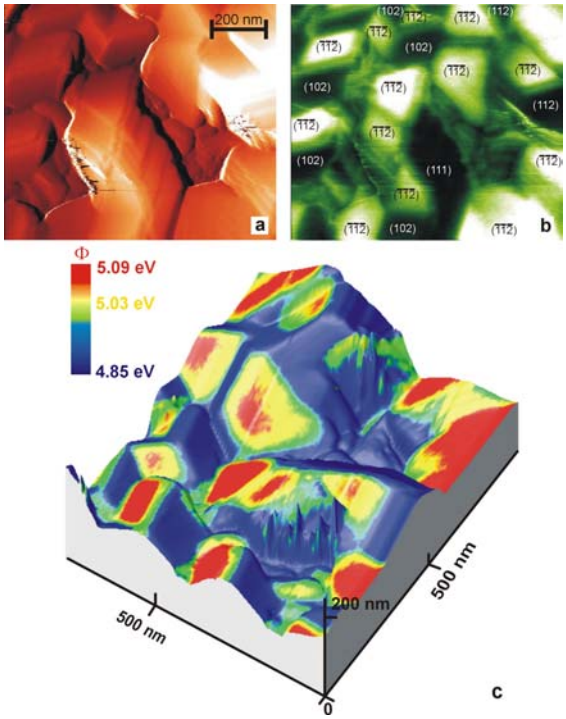

Fig. 2: KPFM measurement of a $CuGaSe_2$ thin film grown on ZnSe(110) by MOVPE. ***(a)*** *The topography image shows distinct crystal facets on the (220) oriented $CuGaSe_2$ film. The colour scale corresponds to height differences of 384 nm.* ***(b)*** *Representation of the simultaneously measured work function (Φ = 4.85 ... 5.09 eV). The crystallographic orientation of the facets is indicated.* ***(c)*** *3-dimensional image merging the topography (as the 3D effect) and the work function represented by the color scale. The origin corresponds to the lower left corner in the 2D images.*

S. Sadewasser, Th. Glatzel, M.Ch. Lux-Steiner (SE2.05 Chalcopyrite Solar Cells)

Chemical and electrochemical deposition of chalcogenides for solar cells

Presently, interest for deposition of chalcogenide semiconductors from solution emerged as competitive techniques for the fabrication of thin films for solar energy conversion. Among the various solution growth methods, chemical bath deposition (CBD) and electrodeposition (ED) techniques can offer convenient, low cost and environmentally compatible tools. The CBD process does not involve electron exchange with a conducting substrate and appears to be the best technique for depositing buffer layers in high efficiency large area thin film chalcogenide devices.

ZnS and ZnSe by CBD

ZnSe and ZnS buffer layers are deposited on $Cu(In,Ga)(S,Se)_2$ (CIGSS) substrate using an aqueous alkaline solution using a solution (A) which consists of metallic cation precursor $ZnSO_4$ and two different ligands NH_2NH_2 (25%), NH_3 (25%) dissolved in tri-distilled water under stirring and heated to the appropriate temperature and the chalcogene source (solution B) containing either $SeC(NH_2)_2$ and Na_2SO_3 or its sulfur analogue $SC(NH_2)_2$ dissolved in tri-distilled water.The CBD consists of a heterogeneous process, where ZnX (X = S, Se) and $Zn(OH)_2$ grows on the substrate surface and a homogenous one which consists of the precipitate of ZnX and $Zn(OH)_2$. We investigated by using HRTEM of the CBD-precipitate after ZnSe deposition. We observed the precipitation of ZnSe nanocrystallites as agglomerates in a cluster structure (see inset in Fig. 1). Fourier analysis yields a lattice plane spacing of d = 3.2 nm. It can be attributed to hexagonal ZnSe [002] and/or cubic ZnSe [111]. Previous results showed that nanoclusters of the same orientation and size could be found in the buffer layer deposited on CIGSS substrate. Since crystallites of the same spacing and dimension are found in buffer layers, we believed that ZnSe precipitates (homogeneous reaction) stick to the surface of the absorber. The mechanism of growth is by colloid aggregation.

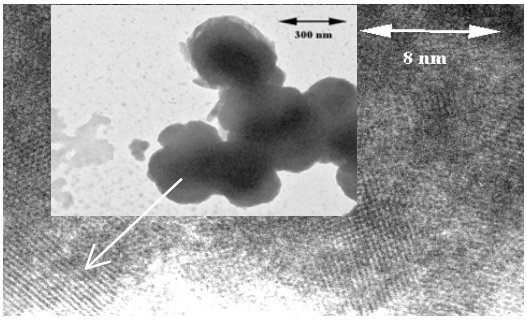

Fig. 1: Remains of the CBD-solution on a Cu grid as revealed by TEM (inset) and HRTEM.

The reactions commonly accepted are:

$$XC(NH_2)_2 + 2OH^- \Rightarrow X^{2-} + CN_2H_2 + 2H_2O$$

$(Zn^{2+})L_n \Rightarrow Zn^{2+} + nL$ and $Zn^{2+} + X^{2-} \Rightarrow ZnX$ The global reaction is:

$Zn(NH_3)_4^{2+} + XC(NH_2)_2 + 2OH^- \Rightarrow ZnX + 4NH_3 + H_2O$

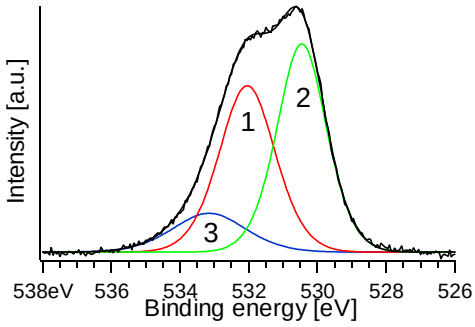

Fig. 2: O_{1s} -XPS spectrum of a CBD-ZnSe on CIGSSe showing ZnO, $Zn(OH)_2$ and C-O.

The ZnSe (or ZnS) film grows with slow release of Se (or S) mainly due to hydrolysis of $SeC(NH_2)_2$ (or $SC(NH_2)_2$) in basic solution. Zn^{2+} ions are released by the decomplexation of $(Zn^{2+})L_n$, where L is the ligand species. When the ionic product of Zn^{2+} and X^{2-} exceeds the solubility product of ZnX, the precipitation of ZnX occurs either in the solution or at surface of the absorber. The formation of ZnSe colloids occurs first in the solution as supported by TEM investigation (Fig. 1). However the hydrolysis of $SC(NH_2)_2$ is rather slow and the formation of ZnS at the surface of the substrates via a heterogeneous process is possible.

The presence of $Zn(OH)_2$ in the deposit is unavoidable due to the aqueous nature of the bath. XPS analysis (Fig. 2) revealed that a large amount of oxygen was included in the CBD-ZnSe film in the form of $Zn(OH)_2$ and H_2O.

The peak located at 531.6 eV – 532 eV is attributed to OH^--groups. the peak at 530.5 eV correspond to O^{2-}compounds and the one at 533.1 eV to water and/or C-O bonds.

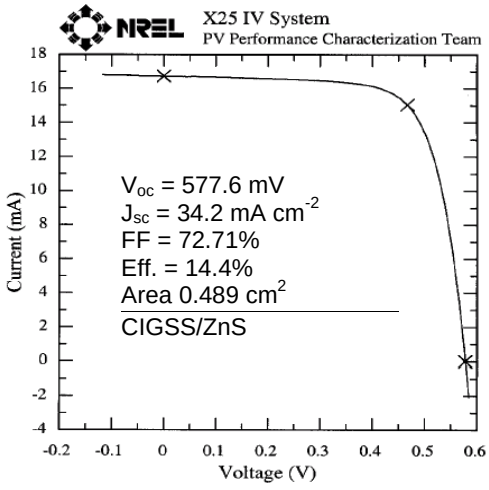

Fig. 3: I-V characteristic of CBD-ZnS/CIGSS solar cell without AR coating.

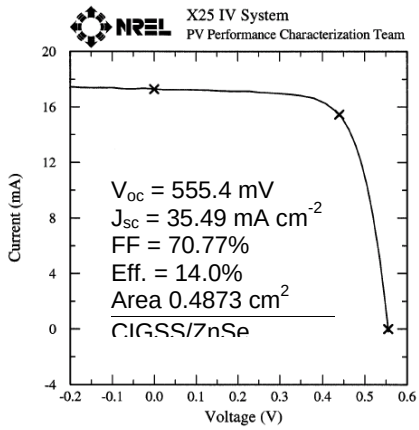

Fig. 4: I-V characteristic CBD-ZnSe/CIGSS solar cell with MgF_2-AR coating

Cell performance

Various photovoltaic devices were fabricated using production scale CIGSS absorber provided by Siemens-Shell. The CBD is a soft process and the CBD-film covers the rough CIGSS surface with a minimum thickness and a high quality pn junction can be formed. Fig. 3 and Fig. 4 show the I-V characteristics of solar cells fabricated using CBD-ZnS and CBD- ZnSe, respectively.
All output characteristics mentioned above were measured by NREL, (Colorado, USA). The devices are submitted to light soaking for 10 minute at P_{max}. under AM1.5, 1000 $W.m^{-2}$ illumination.

Electrodeposition of Cu-In-Ga-Se system

The challenge in this work is to improve the properties of the films prepared already from the electrodeposition step in such a way that they can be used with no or minimal post-treatment.
In order to look for the deposition potential, which will favor the alloy formation, we studied the steady state polarization characteristics of the bath containing $CuCl_2$, $GaCl_3$, H_2SeO_3 and $InCl_3$. Three plateaux are observed at -0,35 to -0,4 V, -0,5 to -0,8 V and -0,9 to -1.2 V corresponding to $Cu_{2-x}Se_2$, $CuInSe_2$ and $CuGa_xIn_{1-x}Se_2$ phases, respectively (see Fig. 5). Above -1.0 V, the current density increases rapidly due to hydrogen evolution. Films deposited at -0.6 V, show the ternary $CuInSe_2$ phase. At -0.9 V, and -1.0 V the film exhibit $CuGa_{0.3}In_{0.7}Se_2$, and $CuGa_{0.5}In_{0.5}Se_2$ phases, respectively.

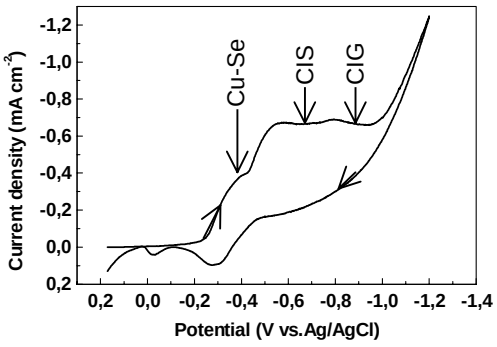

Fig. 5: Cyclic voltammetry on titanium substrate in solution 3mM $CuCl_2$, 50mM $GaCl_3$, 4mM $InCl_3$ and 2mM H_2SeO_3 at pH 2.2.

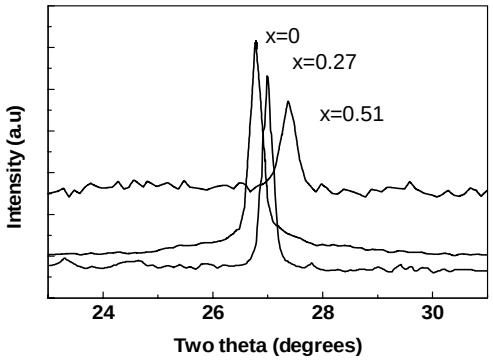

Fig. 6: Bragg peaks (112) positions. The x values represent the Ga content.

All phases are clearly identified by XRD. They show (112), (220, 204), and (116, 312) reflections of the tetragonal structure. Furthermore, we observed a shift of the (112) peaks to larger angles (see Fig. 6). No binary phases such as Cu_xSe and In_2Se_3 are found. Table I gives EDX composition and lattice parameters for as-deposited films grown at various potentials. The composition analysis reveals that the films deposited at potentials -0.6 V, -0.9 V, and -1.0 V on titanium substrates are Se-rich. Diffraction peaks (XRD) from elemental Se cannot be observed in the as-deposited films. This indicates that excess Se in these films is of amorphous phase.

Final Remarks

- ED and CBD are simple and fast, and they can be used for the preparation of binary, ternary and quaternary compounds for subsequent processing into high-quality CIGS thin film absorbers and high efficiency CIGS/ZnX based devices.
- Cd-free devices using production scale absorber are demonstrated and our ZnS and ZnSe buffer layers show efficiencies over 14 % certified at NREL.
- As an initial step, in developing low cost and Cd-free thin film solar cells, it was demonstrated that device quality of single phases $CuGa_xIn_{1-x}Se_2$ can be prepared by electrochemical method at low temperature. The composition is controllable by applied cathode potential and by concentration of elements in the electrolyte.

Table 1: EDX composition and lattice parameters for films electrodeposited at various potentials

E (V vs.Ag/AgCl)		-0.6	-0.9	-1.0
EDX Comopsition (at.%)	Cu	26.36	25.91	22.18
	Ga	0	6.12	12.47
	In	21.35	16.1	11.92
	Se	52.29	51.87	53.43
x = [Ga]/[Ga]+[In]		0	0.27	0.51
Lattice const.				
	a (Å)	5.77	5.73	5.64
	c (Å)	11.68	11.47	11.34
Phase present		$CuInSe_2$	$CuGa_{0.3}In_{0.7}Se_2$	$CuGa_{0.5}In_{0.5}Se_2$

A. Ennaoui, W. Eisele, M.C. Lux-Steiner (SE2.06 New Materials)

Buffer layers, alternative sequential thin layer technology (ILGAR)

The project comprises the development of sequential chemical methods for the deposition of semiconductor thin layers. In the center of interest stands the versatile and robust ILGAR process (Ion Layer Gas Reaction, patents by HMI) featuring low-cost equipment, economical material consumption and low temperature as well as easy controllability of chemical composition, layer thickness and electronic and optical properties.

The ILGAR Process

ILGAR is a sequential and cyclic process which can be fully automated and easily up-scaled. It consists basically of the following steps:

1. Application of a precursor solution on a substrate by dipping or spraying.
2. Reaction of the dry solid precursor layer with a hydrogen chalcogenide gas.

→ Repetition of this process cycle, until the desired layer thickness is obtained.

Sulfide layers are deposited by converting a metal salt by H_2S as reactant gas. Here, selected results from ILGAR oxide layers are presented. A substantial process modification opened the access to these technologically extremely interesting films. A H_2O/NH_3 gas mixture converts the precursor salt to the corresponding hydroxide which undergoes dehydration to the oxide when moderately heated. However, thermodynamic calculations of the system $ZnCl_2$ / H_2O / NH_3 revealed ZnO as the only stable Zn compound under ILGAR conditions even at room temperature (co-operation with Dr. Fiechter, HMI). In spite of this, UV-spectroscopic findings and the absence of any X-ray diffraction signal (XRD) pointed to the formation of meta stable amorphous $Zn(OH)_2$ films at 25°C. Finally, we succeeded in confirming this identity by FTIR reflection spectroscopy (in co-operation with the IWS Dresden, B. Leupolt). Fig. 1 shows the FTIR spectra of ILGAR ZnO layers deposited at various process temperatures: (i) at room temperature, (ii) at 155°C (the typical temperature for window extension layers (WEL) in $Cu(InGa)(S,Se)_2$ („CIGSSe“) solar cells, vide infra) and (iii) at 155°C with an additional annealing at 300°C to ensure complete dehydration. The spectra of bare substrate and a rf-sputtered ZnO sample are given for comparison. The presence or absence of the OH-stretching vibration and the shift in the ZnO-stretching vibration allows a distinction between zinc hydroxide and oxide.

The Window Extension Layer Concept (WEL)

We developed the novel WEL concept for buffer layers. WELs consist of the same material as the sputtered window, but deposited by a mild process. CIGSSe based solar cells with an ILGAR ZnO WEL reached significantly higher efficiencies than the reference cells with the standard CdS buffer (Fig.2). Here the classical cell structure with a sputtered window bilayer consisting of i- ZnO and ZnO:Ga was applied. Even more promising is a novel cell structure with WEL and only the sputtered doped window layer (ZnO:Ga), i.e. one complete sputter step (i-ZnO) can be omitted. This is especially advantageous for the production of solar modules where the substrates have to be removed from the sputter chamber for the scribing in-between the two sputter processes. The cell performance is already comparable with the standard structure (Fig. 2).

With ZnO WELs already a large number of cells has been produced showing statistics and reproducibility. Standard cell concept with sputtered i-ZnO layer: The average efficiency of 80 cells (the 6 best cells out of 8 on each device taken from a series of ten devices) is η_{80}= 13.6 % though the series still contains some process optimization. For the innovative cell concept with ZnO WEL but without *sputtered* i-ZnO layer η_{80}= 13.8 % was achieved. A first up-scaling experiment resulted in a 5x5 cm^2 mini-module with an efficiency η=10.9 %.

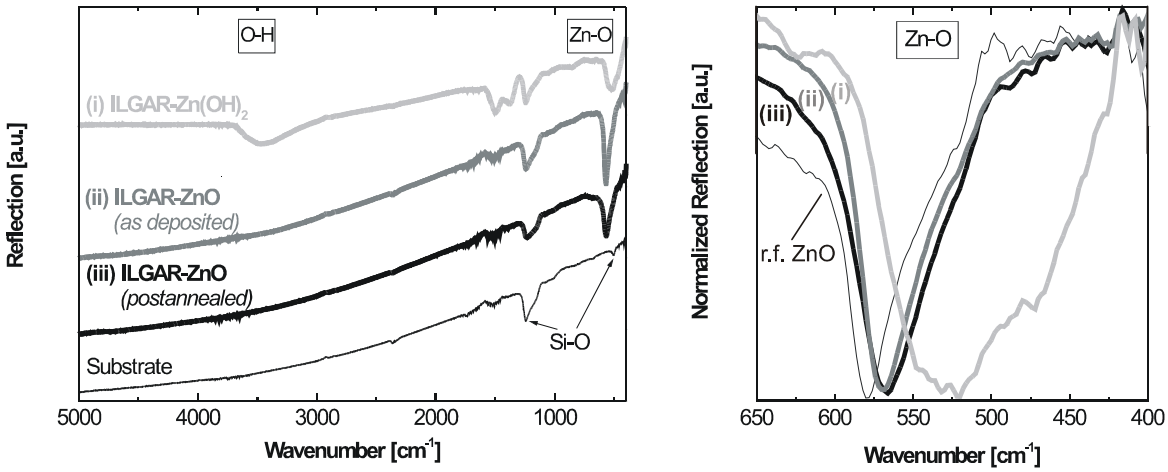

Fig. 1: Left: FTIR reflection spectra (75°/p-polarization) of ILGAR-$Zn(OH)_2$ and ZnO layers, respectively, prepared under different process conditions as described in the text. Right: expended region of the Zn-O-stretching vibration, for comparison the band of a rf-sputtered ZnO sample is shown.

	ILGAR ZnO WEL	Ref. CBD CdS	ILGAR ZnO WEL	Ref. CBD CdS
V_{OC} [mV]	**587**	589	581	**597**
J_{SC} [mA/cm^2]	**35**	33	35	**34**
FF [%]	**72**	73	71	**72**
η [%]	**14.6**	14.1	14.5	**14.7**

Fig. 2: Solar cells with ILGAR ZnO WEL with and without sputtered i-ZnO window layer (CIGSSe absorbers from Siemens&Shell Solar GmbH (SSSG), reference with CBD-CdS buffer)

Absorber Pretreatments

CIGSSe solar cells with ILGAR ZnO WEL reach excellent efficiencies only after a "partial electrolyte" pre-treatment of the absorber similar to that of Ramanathan (i.e., a warm aqueous $CdSO_4$ or $ZnCl_2$/ammonia solution). The nature of surface modifications induced by these treatments is still under debate. In order to gain more insight the absorber surface was investigated by photoelectron spectroscopy after various procedures in a close cooperation with the University of Würzburg (L. Weinhardt, Dr. C. Heske, and Prof. E. Umbach).
First, pure aqueous KCN (3 min, room temperature) or ammonia solutions (10 min, 80°C) were applied to CIGSSe absorbers from Siemens Solar Industries (USA). Both treatments lead to a removal of Na and a strong reduction of oxides. As an example, Fig. 3a shows the complete removal of SeO_2. Moreover, a reduction of In and Cu oxides can be identified. The treatment with NH_3 also leads to a partial removal of the surface C content. In contrast, Fig. 3b shows an increase of the C signal after the KCN treatment, and, furthermore, a deposition of K on the absorber surface. Finally, we observe a strong increase in the S content at the surface after both treatments and, in the case of KCN, a decrease of Cu.
In a second experiment SSSG absorbers were treated with an aqueous NH_3 solution containing $CdSO_4$ or $ZnCl_2$. The survey spectra after both treatments are shown in Fig. 4 in comparison with the spectrum of an untreated absorber. Possible compounds that are compatible with the Cd 3d and Cd MNN line positions are CdS and CdSe, while the Zn-treatment leads to a deposition of $Zn(OH)_2$. To gain further insight into the Cd-treatment process a series of absorbers treated with different $CdSO_4$ concentrations were investigated. We find that the highest $CdSO_4$ concentrations lead to an enhanced Cd deposition and an increase of the oxygen signal. Simultaneously, we observe a shift of the Cd MNN Auger line to lower kinetic energies. The resulting compound can be identified as $Cd(OH)_2$.

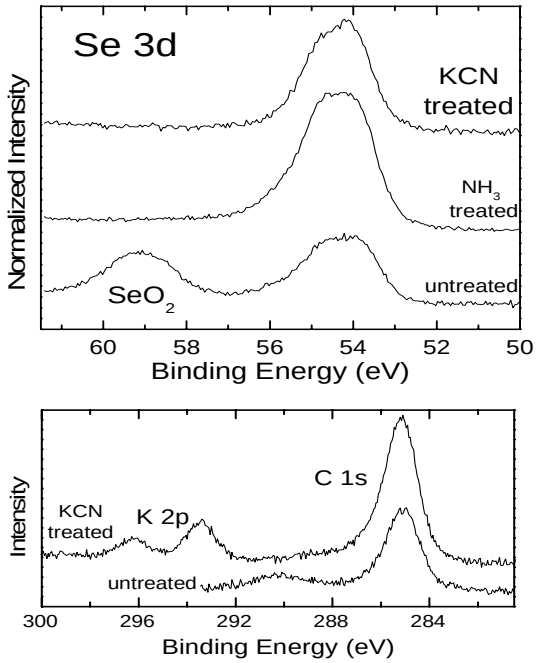

Fig. 3: XPS spectra of CIGSSe absorber surfaces before and after a 10 min treatment with aqueous KCN or ammonia at 80°C, Se 3d (top) C 1s / K 2p (bottom).

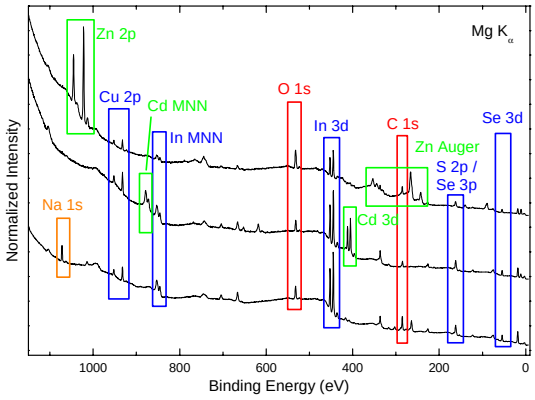

Fig. 4: XPS survey spectra of CIGSSe absorbers before (bottom) and after treatments with aqueous $CdSO_4/NH_3$ (center) or $ZnCl_2/NH_3$ (top).

Ch.-H. Fischer, M.C. Lux-Steiner, H.-J. Muffler, M. Bär, M.C. Lux-Steiner (SE2.08 Buffer Layers, Alternative Thin-film Technology), C. Kelch, M. Kirsch (SE2.05 Chalcopyrite Solar Cells), S. Fiechter (SE5 Solar Energetics) in collaboration with L. Weinhardt, C. Heske, E. Umbach, (Universität Würzburg); B. Leupoldt (Fraunhofer Institut Werkstoff- und Strahltechnik, Dresden); F. Karg, S.Zweigart (Siemens&Shell Solar GmbH, München); B. Gay (Siemens Solar Industries, Camarillo USA)

Eta-solar cell and other applications

Eta-solar cells

In the eta-cells project we aim at the fabrication of solar cells with extremely thin absorber layers. Sufficient absorbance in these cells is ensured by depositing the absorber on a deeply structured substrate with a high surface enlargement. Strong light trapping and short transport paths in the absorber are the key features in this type of cell. Fig. 1a shows a model for such a cell.

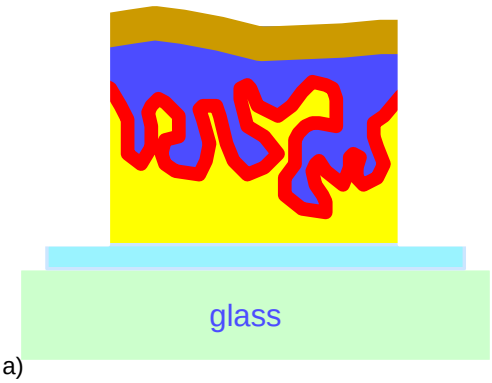

a)

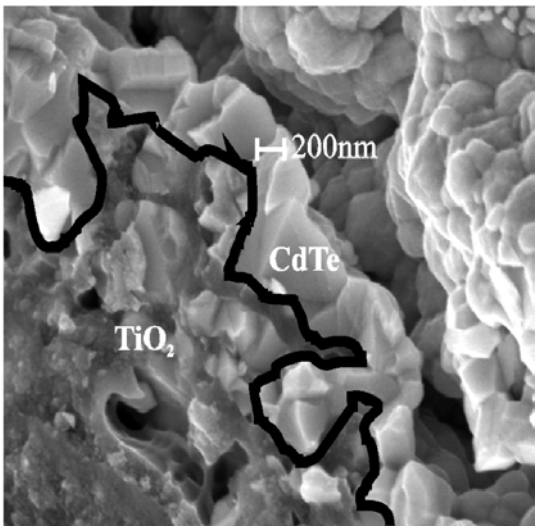

b)

Fig. 1: a) Model of the envisioned eta-solar cell with a thin absorber (red) and back contact (blue) deposited on a nano- or microstructured substrate (yellow). b) ~200nm nano-crystalline CdTe-layer on micro-porous TiO_2 substrate. EDX and electron scattering contrast allow to distinguish the two materials, which are in intimate structural and electrical contact.

So far, the most promising device consists of a CdTe absorber layer deposited in electrodeposition on a micro-porous TiO_2 substrate. Contacts are provided by highly conducting SnO_2/glass on the TiO_2 light entry side and an Au or graphite layer at the back. The CdTe consists of a nano-crystalline layer of approximately 150 nm thickness covering the TO_2 surface as a continuous film.

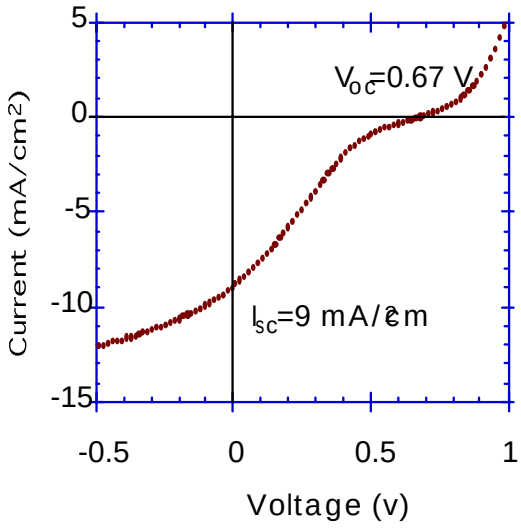

a)

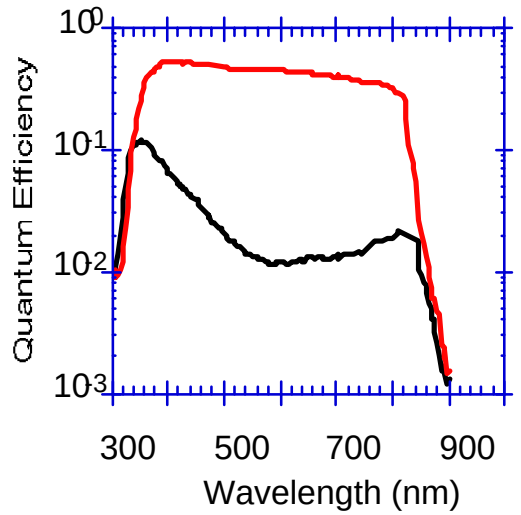

b)

Fig. 2: a) I-V characteristic of eta-cell under 100 mW AM1 illumination. b) Comparison of quantum efficiency for eta-cell (red) and planar reference (black).

A micrograph of the TiO_2/CdTe interface is shown in Fig. 1b. An optimized cell of this type has produced an open-circuit voltage of 0.67 V and a short-circuit current of 9 mA/cm^2 (Fig. 2). When compared to a planar reference cell with CdTe of the same quality and the same total thickness, the eta-cell arrangement shows much superior performance. As shown in Fig. 2b, the quantum efficiency is approximately a factor of 10 higher in the eta-cell than in the planar cell.

In the last year we have carried out a detailed optical, electrical and structural characterization of this cell [1]. XPS/UPS measurements indicated a surprisingly large conduction band off-set of 0.6 eV at the CdTe/TiO_2 interface, which leads to a comparably small band-bending. Numerical simulation of

the electron transport across the interface indicates that the poor fill factor, which presently limits the efficiency of the cell, is a consequence of the small band bending. We will therefore have to address the problem of "band engineering" at nano-structured interfaces in the near future.
A promising alternative to the porous morphology used so far, appears to be given by substrates with columnar crystallites, since the electron transport path will involve fewer grain boundaries. We recently developed ZnO layers with nearly vertically aligned, single-crystalline columns. In these substrates we found electron mobilities as high as 20 cm^2/Vs, confirming this expectation. We therefore started work to implement columnar morphologies in several chalcogenide-based compounds.

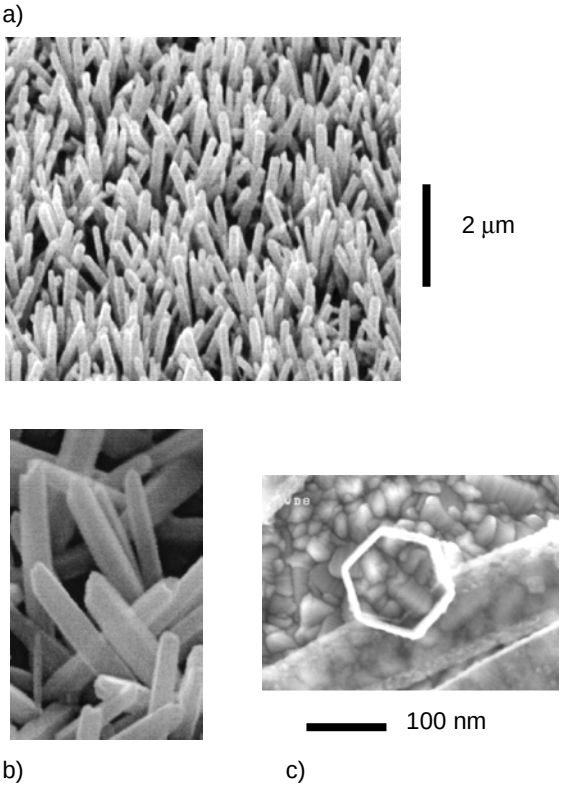

Fig. 3: a) Scanning electron micrograph of single-crystalline ZnO columns. b) The same at higher magnification. c) Hexagonally shaped ZnS tubes prepared by ion exchange from ZnO columns and subsequent etching. The image shows one vertical and two horizontal tubes.

Using sequential ion exchange we were able to transfer the columnar morphology of the ZnO substrates to several other compound semiconductors, such as ZnS, Ag_2S, Cu_2S, Bi_2S_3, Sb_2S_3 and others [2]. We also learnt to manipulate these nano-structures to some extent. Fig. 3 shows hexagonal columnar ZnO crystallites and a hexagonally shaped nano-tube of Zincblende ZnS, which was prepared by partial conversion of a ZnO column and subsequent etching of the core. The tube has a diameter of 150 nm, a wall thickness of 15 nm and can have lengths up to 2 μm.

Other applications

Our experience in nano-scale semiconductor deposition also lends itself to the preparation of devices on flexible substrate. Using irradiation by fast heavy ions and subsequent etching, narrow hollow cylinders can be prepared in μm thick polymer foils. We have applied electrodeposition to fill these cylinders with semiconductor compounds [3]. Fig. 4 shows free-standing CuSCN cylinders which resulted from this work. In this case the CuSCN columns are exposed. While these exposed columns could be used as substrates in solar cell applications, the embedded columns may also become part of a flexible electronic device.

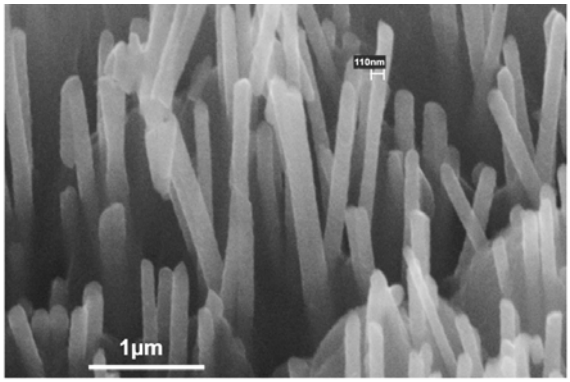

Fig. 4: Free-standing CuSCN columns grown in flexible polymer foils.

References

[1] C. Grasso, K. Ernst, R. Könenkamp, M. Burgelman, M. C. Lux-Steiner, Proc. PVSEC, München 2001

[2] L. Dloczik, R. Engelhardt, K. Ernst, S. Fiechter, I. Sieber, R. Könenkamp, Appl. Phys. Lett. 78, 3687 (2001)

[3] R. Engelhardt and R. Könenkamp, J. Appl. Phys. 90, 4287 (2001)

R. Könenkamp, K. Ernst, L. Dloczik, J. Chen, R. Engelhardt
(SE2.07 Eta-cell)

Alignment of the endohedral fullerenes N@C_{60} and N@C_{70} in liquid crystals

Endohedral fullerenes [1] are envisaged to serve as quantum bit carriers in a quantum computer design [2,3]. For this application, an alignment of fullerene chains is required which is naturally achieved by embedding them in a liquid crystal matrix.
N@C_{60} and N@C_{70} in solution show a three line spectrum in EPR due to the hyperfine interaction of the electrons with the nuclear spin I = 1 of ^{14}N (top of Fig.1). Since the electron spin of nitrogen is S = 3/2, each of these hyperfine lines consists by itself again of three lines which are degenerate for a spherically symmetric electron distribution. However, for non-spherical atoms the degeneracy is lifted and the three lines become visible (see lower part of Fig. 1).

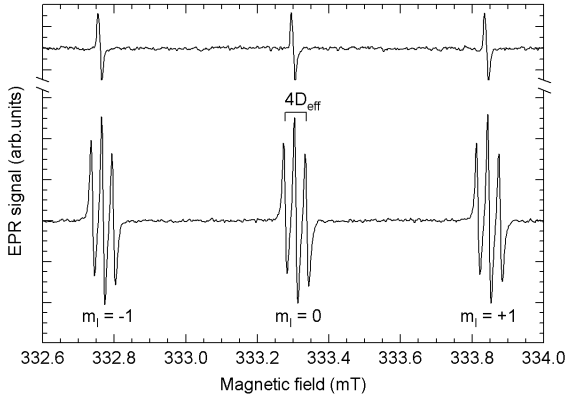

Fig. 1: EPR spectrum of N@C_{70} in toluene solution (upper graph) and N@C_{70} in MBBA liquid crystal (lower graph) at 299 K. The magnetic quantum number m_I of the nuclear spin I = 1 and the splitting of the outer lines by 4D_{eff} (see text) for the m_I = 0 hyperfine line are indicated.

For an axially symmetric interaction and high external field, the splitting $\Delta\nu$ (separation between two successive peaks in each hyperfine multiplet) in the EPR spectrum can be represented as $\Delta\nu = 2\ D_{eff}$, where D_{eff} is an effective interaction for this specific orientation. The fine structure interaction splits each hyperfine line into three lines, one at the original position and one shifted to lower and one to higher fields. Fig. 1 shows this additional line splitting for N@C_{70} in the liquid crystal MBBA [4].
C_{60}, other than C_{70}, has no natural axis for alignment in a liquid crystal. However, as Fig. 2 shows, there is also a splitting of the EPR line, and thus an alignment for N@C_{60}. The observed splitting shows that the spin density distribution of the enclosed nitrogen atom in C_{60} slightly deviates from spherical. The explanation is that the contact of C_{60} with the aligned liquid crystal molecules induces a slight deformation of the electron shell of C_{60}, which in turn affects the electron density distribution of the enclosed nitrogen.

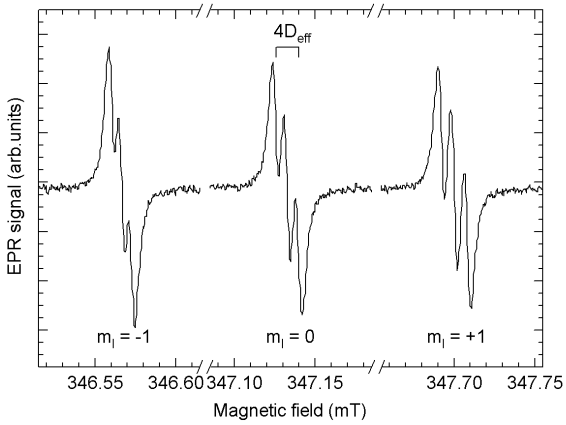

Fig. 2: EPR spectrum of N@C_{60} in MBBA liquid crystal at 296 K. Note that the field axis is interrupted between the lines in order to emphasise the splitting. The magnetic quantum number m_I of the nuclear spin I = 1 and the splitting of the outer lines by 4D_{eff} (see text) for the m_I = 0 hyperfine line are indicated.

The alignment of the endohedral fullerenes in a liquid crystal matrix is of great importance in connection with quantum computing. There, one can construct by chemical means a chain of endohedral fullerenes, e.g. dimers [5] or polymers, and embed them in a liquid crystal. Since the magnetic interaction between the fullerenes is dipolar, the arrangement in a chain and the orientation with respect to the external field ensures that the interaction is unique and even changeable if the angle between the chain axis and the external field is varied. Since the fullerenes are diluted in the liquid crystal, the inter-chain interaction is negligible as required for independent small qubit assemblies.

References

[1] T. Almeida Murphy, T. Pawlik, A. Weidinger, M. Höhne, R. Alcala, J.M. Spaeth, Phys. Rev. Lett. 77 (1996) 1075

[2] W. Harneit, M. Waiblinger, K. Lips, S. Makarov, A. Weidinger, AIP Conf. Proc. 544 (2000) 207

[3] W. Harneit, M. Waiblinger, K. Lips, C. Meyer, A. Weidinger, and J. Twamley, in Experimental Implementation of Quantum Computation, edited by R.G. Clark (Rinton Press Inc., Princeton, NJ, 2001) 38

[4] H. Kelker, R. Hatz, Handbook of Liquid Crystals, Verlag Chemie (Weinheim, Germany, 1980)

[5] B. Goedde, M. Waiblinger, P. Jakes, N. Weiden, K.-P. Dinse, A. Weidinger, Chem. Phys. Lett. 334 (2001) 12

C. Meyer, W. Harneit, R. Döring, B. Mertesacker, K. Lips, A. Weidinger (SE2.02 Fullerenes) n collaboration with P. Jakes, K.P. Dinse (TU Darmstadt)

Synchrotron-diagnostics for cost-efficient photovoltaic devices (CISSY)

Project Goals

This joint project with Universität Würzburg, Siemens & Shell Solar and BESSY aims at the development of optimized chalcopyrite thin film solar cells (CIGSSe). This is achieved through an interplay between various spectroscopic analysis methods and preparation at small and production scale. An experimental set-up is installed at the BESSY synchrotron, which combines sophisticated spectroscopy with the preparation of buffer, window, and absorber layers. Detailed experimental knowledge will be gained about the chemical and electronic structure of buried interfaces, which is of particular importance for the electrical performance of the cells. The results of this work will then directly be fed back into solar cell fabrication, allowing an optimization far beyond the common trial-and-error approach.

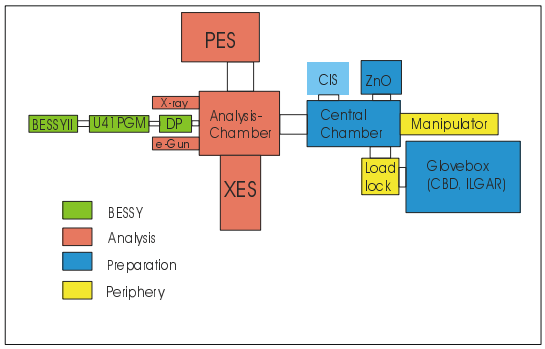

Fig. 1: Block diagram of the experimental endstation (CIS: chalcopyrite module, planned; ILGAR: Ion Layer Gas Reaction; CBD: Chemical Bath Deposition)

Experimental set-up and current status

The set-up of the apparatus is schematically shown in Fig. 1. It consists of an analysis chamber containing the spectrometers, a central main chamber for simple preparation procedures, a sample manipulator, a chamber for ZnO sputter deposition, a glove box for wet-chemical processes, and a load-lock system. The analysis chamber will house an XES 300 Soft X-ray Emission Spectrometer and a high-resolution electron analyzer. The central chamber allows ion sputter treatments, sample annealing and sample storage. Various preparation procedures will be implemented into several side-chambers: chemical conditioning of the absorber, including etching and ion exchange treatments, chemical bath deposition (CBD), ion layer gas reaction (ILGAR) for deposition of buffer layers, and sputtering deposition of selected window layers. The experimental set-up is complete and initial experiments have been performed: various layers were prepared both on glass and CIGSSe absorbers using chemical methods like ILGAR and CBD. An explorative spectroscopic analysis was carried out at the Advanced Light Source (ALS) in Berkeley.

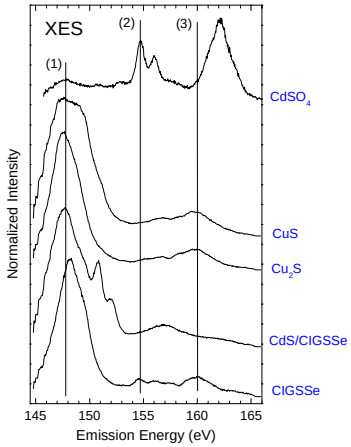

Fig. 2: XES-spectra of different sulfur compounds with characteristic peaks. The marked peaks are attributed to the following electronic transitions:
(1): S 3s → S 2p (sulfide environment)
(2): S 3s → S 2p SO_x (x≤2)
(3): Cu 3d → S 2p Cu-S bonds

The XES-spectra (Fig. 2) show characteristic peaks which identify the local chemical environment of the sulfur atoms. The spectra in Fig. 3 were taken on a $Cu(In,Ga)(S,Se)_2$-sample in contact with water using a wet cell with a polymide window. With increasing exposure to the x-ray beam the data indicate a formation of sulfate.

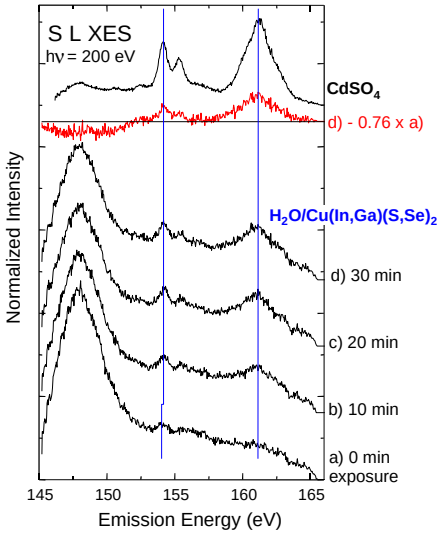

Fig. 3: S Lα-XES spectra of a $Cu(In,Ga)(S,Se)_2$-sample in contact with water after different exposure times compared to $CdSO_4$ (above).

M. Ch. Lux-Steiner, Ch. H. Fischer, A. Grimm, I. Kötschau, I. Lauermann, J. Reichard, S. Sokoll (SE2.08 Synchrotron Analytics) in collaboration with E. Umbach, C. Heske (Universität Würzburg); W. Gudat, Ch. Jung (BESSY Berlin) and F. Karg (Siemens&Shell Solar, München)

Department

SE3 Technology

Chalcopyrite solar cells and monolithically integrated test modules

This project aims at the development of a technological process for the preparation of modules and solar cells based on the chalcopyrite semiconductor $CuInS_2$ with an efficiency of 10 % and above. Development targets are: reproduceable efficiency, high process and material yield, compatibility with the specifications of inexpensive substrates as well as suitability for industrial environment (scalability and throughput). The project forms the scientific basis for the scaling-up effort of a start-up company. The baseline supports internal and external research on $CuInS_2$ solar cells and on other chalcopyrite semiconductors.

Producing a ternary compound semiconductor on large areas requires to overcome the stoichiometry problem. The process developed at HMI is specific in the sense that it uses growth of the chalcopyrite $CuInS_2$ from non-stoichiometric precursors (Cu/In>1) and the chemical stoichiometry adjustment by chemically etching of a surplus CuS layer after sulfurization [1]. This approach results in an inherent process stability as will be shown below.

Fig. 1 gives the dependence of the open circuit voltage and fill factor on top temperature (Fig. 1a) and the amount of sulfur in the sulfurization containment (Fig. 1b). A broad maximum in the temperature dependence is found. Also the amount of added elemental sulfur can be varied in a wide range. The latter result reflects the well known property of chalcopyrite materials which is the self-adjustance of the group VI element. A plot of the cell data vs the deposited Cu/In ratio is given in Fig. 1(c). The Cu/In ratio can be varied from about 1.2 up to 1.8 without a strong effect on the cell parameters.

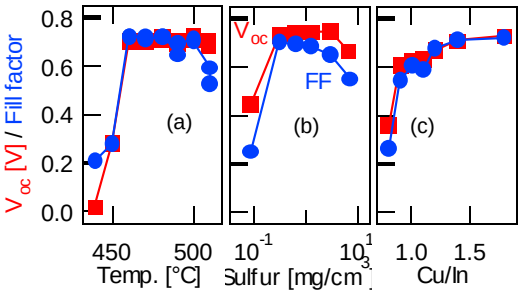

Fig.: 1 Dependence of V_{oc} and fill factor on the RTP process parameter top temperature (a) amount of sulfur (b) and precursor Cu/In ratio (c)

With aid of the $CuInS_2$ baseline the reproducibility of the process was investigated. Fig. 2 gives a direct print-out of the baseline performance over a period of 6 months. For 114 samples processed in this period, a narrow distribution of the cell efficiency peaking at 10.7 % (total area) has been found. The absolute FWHM of this curve is 1.35 %. In accordance with physical arguments, the chemical stoichiometry adjustment of the absorber layer (etching of Cu-rich prepared absorber) is the key factor of the process robustness.

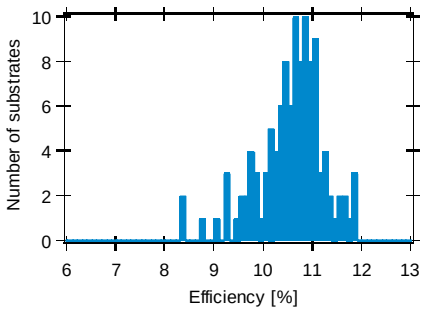

Fig. 2: Direct print-out of the $CuInS_2$ cell baseline statistic from the period Jan-Jul 2001 showing the efficiency distribution from 114 processed samples. Each data point represents the average of up to 6 cells (0.5 cm^2) on one glass substrate

The $CuInS_2$ cell base line has recently been extended to a module baseline (5×5 cm^2, 20 cm^2 aperture area). The module baseline currently delivers efficiencies up to 10.2 % on an aperture area basis. An encapsulated module sample is shown in Fig. 3. Parameters of the champion module are V_{oc}=5.1 V, j_{sc}=21 mA cm^{-2} , FF=66.6 %. Less efficient modules still suffer from inferior fill factors. Fill factors less than 65 % could each be related to pin holes or shunts mainly at the interconnects by use of lock-in thermography.

A critical dimension of integrated modules is the cell width. Two general dependencies have to be considered: A too small cell width increases the relative area of the interconnect, thereby increasing current losses. A too large cell width increases the series resistance due the sheet resistance of the window layer. Using test structures, an optimum cell width of 6 mm has been derived based on the currently realized material parameters. In order to increase this cell width, these material parameters have to be newly optimized; for instance the sheet resistances have to be reduced.

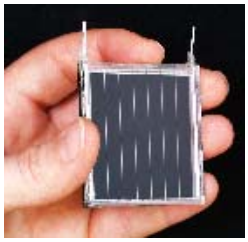

Fig.3: Encapsulated $CuInS_2$-based monolithically integrated test module

References

[1] R. Scheer, T. Walter, H.W. Schock, M.L. Fearheiley and H.J. Lewerenz, Appl. Phys. Lett. **63**, 3294 (1993)

J. Klaer, I. Luck, A. Boden, A. Werner, I. Gavilanes-Perez, R. Klenk, R. Scheer (SE3.01a Monolithically Integrated Test Modules)

Quality control and reliability of thin film solar cells

For a reliable production process of thin film solar cells, quality control of different constituents of the cells are desired. Concerning quality assessment of chalcopyrite thin films there is a general lack of appropriate methods. This is mostly due to a missing correlation to solar cell parameters. In order to assess the quality of the $CuInS_2$ absorber layer, Raman spectroscopy has been tested. This method is particularly interesting as it allows fast access to absorber properties at room temperature without fabricating complete solar cells.
In collaboration with the University of Barcelona (UB), a Raman data base from samples with different structural quality has been generated in order to study the influence of film properties on the Raman modes. These experiments aim at establishing a quality assessment method for chalcopyrite absorbers. Therefore, a relation between solar cell parameters and structural data is the final goal. Fig. 4 shows Raman spectra of two $CuInS_2$ thin films prepared on Si(111). The totally symmetric chalcopyrite A1 mode can be observed together with additional modes at 60 cm^{-1} and 305 cm^{-1}. Since the structural quality as well as the solar cell parameters of Cu-poor films are inferior than those of Cu-rich films, the presence of the additional modes, which is more intense for Cu-poor films, can tentatively be interpreted as a marker for crystal defects. The origin of these modes, however, previously was not known.

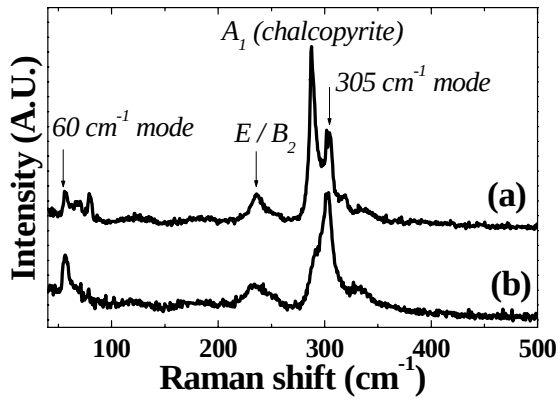

Fig.4: Raman spectra of Cu rich (Cu/In>1, curve a) and Cu poor (Cu/In<1, curve b) epitaxial films showing the presence of the additional non-chalcopyrite bands at 60 cm^{-1} and 305 cm^{-1}.

An assignment of the additional modes was recently achieved by a HMI-UB collaboration. Samples epitaxially grown on Si(111) were investigated using Raman spectroscopy and XRD. In XRD, the occurrence of the $CuInS_2$ (100) diffraction was observed which is related to a defect ordering of cations in the lattice. This so-called CuAu ordering has been theoretically predicted [2] and has first been found by our group [3]. Combined XRD and Raman data of films with different structural quality (due to the deposition temperature) are given in Fig.5. Clearly, a relation between the CuAu related XRD peak and the additional Raman modes are revealed [4]. Hence, the additional Raman modes are due to the defect ordering of CuAu. First principle calculations support this interpretation [4]. More detailed analysis showed that the FWHM of the chalcopyrite A1 mode is also correlated with the CuAu content. This is important for samples which are apt for highly efficient solar cells having only a small CuAu Raman intensity. The next step was to investigate the correlation between the CuAu related Raman intensity of different samples and the solar cell parameters. Preliminary results indeed point out this inverse relation: the lower the CuAu related Raman features the higher the cell's open circuit voltage. This correlation may be used for later material assessment and the prediction of solar cell efficiency based on the quality of the constituent.

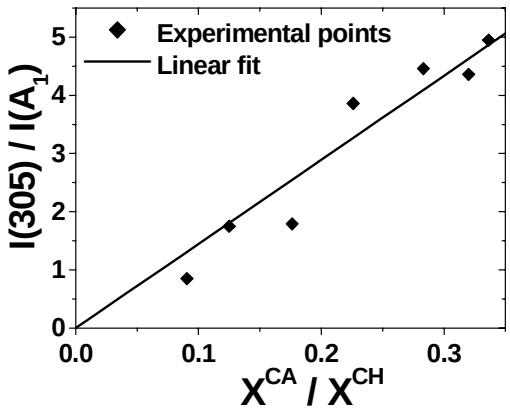

Fig. 5: Correlation between Raman relative intensity of the 305 cm^{-1} mode and the estimated amount of Cu-Au ordered phase.

References

[2] S.-H. Wei, S.B. Zhang and A. Zunger, Phys. Rev. B **59**, R2478 (1999)

[3] D.S. Su, W. Neumann, R. Hunger, P. Schubert-Bischoff, M. Giersig, H.J. Lewerenz, R. Scheer and E. Zeitler, Appl. Phys. Lett. **73**, 785 (1998).

[4] J. Alvarez-Garcia, A. Perez-Rodriguez, B. Barcones, A. Romano-Rodriguez, J.R. Morante, A. Janotti, S.-H. Wei and R. Scheer, Appl. Phys. Lett. **80**, 562 (2002)

R. Scheer, E. Rudigier, A. Perez-Rodriguez, A. Romano-Rodriguez, J. Alvarez-Garcia, B. Barcones (SE3.01b Quality Control and Reliability of Thin-film Solar Cells)

In-situ process monitoring

In the last annual report, we presented the method of diffuse laser light scattering (LLS) for monitoring the sulfurization process of metallic Cu/In precursor layers. LLS transients recorded during the sulfurization showed distinct intensity features which were tentatively assigned to phase transitions or previously could not be related to any kind of precursor transformation at all. The task thus was to find out the structural origin of LLS transient features in order to establish this method for a future industrial process control.

LLS experiments have been conducted at Hasylab while simultaneously recording energy dispersive X-ray diffraction (EDXRD) spectra. With a time resolution of 15 s, EDXRD is able to resolve phase transitions which occur during the sulfurization of metallic Cu/In layers. Fig. 6 gives a series of EDXRD spectra recorded during the sulfurization of the metallic precursor. The graphs depict the time evolution of several peaks during a sulfurization experiments (bottom trace represents the ramp-up start). Clearly, the evolution of the $CuInS_2$ (112) diffraction is visible. This diffraction occurs already in the ramp-up period of the substrate and comes along with a strong decrease of the LLS intensity.

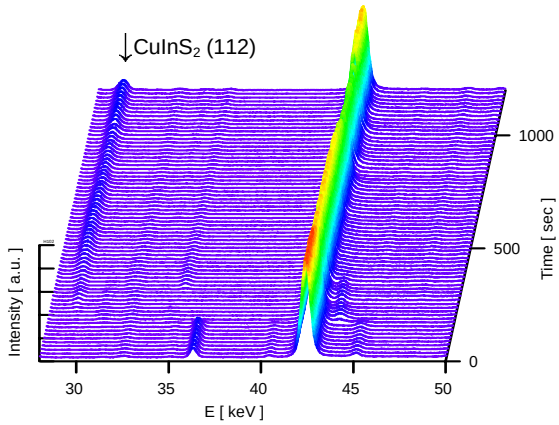

Fig.6: Time series of EDXRD spectra during the sulfurization of a Cu-rich CuIn precursor on a molybdenum coated soda lime glass, 5 min heat up time, T_{Sub} = 500 °C

The area of the diffraction peaks is determined for each spectrum in Fig. 6 and is plotted as a function of time in Fig. 7. The graph also contains the substrate temperature during the course of the sulfurization process. Due to the penetration depth of X-rays in the investigated wavelength range, the area of the diffraction peaks can in a first approximation be considered as an indicator of phase volume fraction. From Fig. 7, a variety of phase transitions can be appreciated. These are intermetallic transitions and metal-semiconductor transitions. In addition, the position of the EDXRD peaks can be used to determine stress development in the layers. Fig. 7 gives the example of the Mo (110) lattice spacing as a function of time.

The combination of both optical and structural techniques has allowed the assignment of the following laser light transient features. The assignments, derived from Fig. 7, were:

α: $CuIn_2 \rightarrow Cu_{11}In_9$
β: surfacial $CuInS_2$
χ: $Cu_{11}In_9 \rightarrow Cu_{16}In_9$

These assignments are very useful for the application of the LLS method for process control and were the basis for a patent application for an optically controlled chalcogenization process. We prepared solar cells from $CuInS_2$ films formed in the *in-situ* EDXRD chamber. Since they exhibited up to 10.6% efficiency, the relevance of these model experiments is demonstrated.

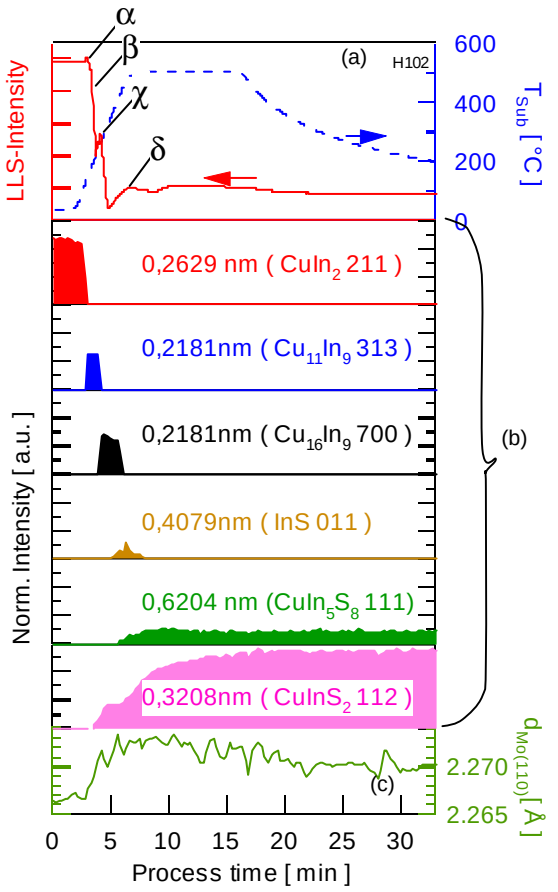

Fig. 7: (a) Temperature profile and LLS intensity, (b) intensity of characteristic diffraction peaks and (c) EDXRD lattice spacings of Mo from the annealing of a Cu,In precursor (Cu/In=0.7) on Mo/glass. Phases identified are given in parenthesis. Details of the process are 5 min heating-up, 10 min hold, and passive cooling. The d-spacing of the Mo 110 peak reveals stress release in the ramp-up period.

Ch. Pietzker, E. Rudigier, R. Scheer
(SE3.01c In-situ Process Control and Doping)

Doping

The formation of local pn-junctions in chalcopyrite thin films would allow the combination of solar cells and electronics on a single substrate. However, this formation was previously not possible. In a joint research effort, the Weizmann Institute of Science, Israel, and HMI have recently invented the method of electric field induced junction formation.
Epitaxial layers of $CuInSe_2$ grown on n-type Si(111) were mounted on a base electrode. An electric field was applied to the surface of the $CuInSe_2$ film via a second contact which is a movable tungsten tip. Beyond a certain negative threshold voltage, a pn-junction was created in the film and a laterally extended junction could be scribed by moving the tip [5]. The p- and n-regions are laterally formed in the layer as can be appreciated from the EBIC image of Fig.8 where bright areas represent the n-type region. By scribing the junction up to a predefined gold pad on the $CuInSe_2$ surface, it was possible to contact the junction.
The origin of the electric field induced junctions can at the moment only tentatively be described: Mobile Cu ions move towards the tip and form an n-type region in the direct vicinity of the tip. In the former host area of the Cu atoms Cu vacancies are formed and this area is converted into a p^+-type region. The basic idea of the process can be apprehended from Fig.9. The process is temperature activated by the current flow from the tip to the back contact. Since the $CuInSe_2$/Si interface forms a blocking contact, lateral current densities occur.
The persistence of the formed junctions has been tested one year after formation. No relaxation of the pn-junction was found. Also the surface of the $CuInSe_2$ layer was proven to be unaffected by the scribing process. The next step will be the application of the electric field through rigid contacts. A patent application has been filed.

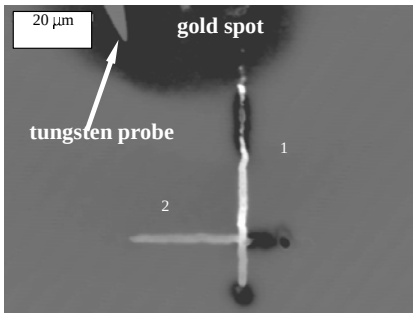

Fig.8: EBIC image of a pn-junction scribed into the surface of a $CuInSe_2$ thin film deposited on Si(111). Two perpendicular junction scribes were performed, one being connected to a gold spot on top of the surface. The EBIC current is flowing through the n-region of the pn-junction to the gold spot. Thus the n-region is electrically connected.

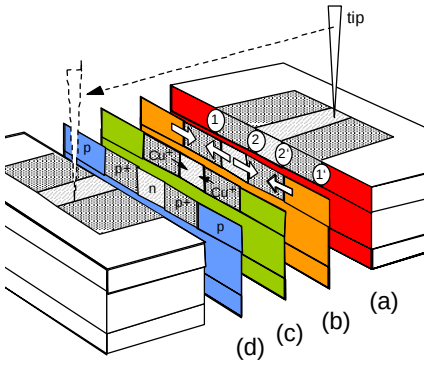

Fig.9 : Tentative model of junction region creation within $CuInSe_2$ epilayers. (a) Four junctions can be derived. (b) Electric fields are driving the EBIC currents. Electric field vectors can be drawn between dashed and dotted as well as dotted and white zones. The white zone is the pristine p-$CuInSe_2$ layer. (c) Application of negative bias (-100 V) leads to migration of Cu^+ ions towards the tip. There Cu_i defects act as donors forming an n-type region (d). Cu depletion leads to V_{Cu} in adjacent zones (dotted) which become more p-type. As a consequence, junction regions are formed between depleted and non-depleted zones. Moving the biased tip creates a patterned junction within the sample.

References

[5] K. Gartsman, D. Cahen and R. Scheer, Appl. Phys. Lett. **79**, 2919 (2001)

R. Scheer, K. Gartsman
(SE3.01c In-situ Process Control and Doping)

Department

SE4 Dynamics of Interfacial Reactions

Time-resolved dynamics of hot electrons in InP(100)

The actual efficiency of a solar cell is always significantly lower than the maximum value derived from thermodynamic considerations. This holds true also for the most efficient solar cells (above 30 percent conversion efficiency) that can be realized with III-V materials. Efficient recombination paths, i.e. loss mechanisms, are known to arise for III-V materials at surfaces and interfaces. Hitherto, such loss mechanisms have generally been considered only for thermalized charge carriers on longer time scales, i.e. nano-seconds or longer. Recombination of thermalized charge carriers can be studied with several conventional measuring techniques. It is well known, however, that already hot carriers can reach a nearby surface or interface prior to thermalization. This holds true in particular in III-V materials with high absorption coefficients and good transport properties. The surface of a III-V-semiconductor in contact with ultra-high-vacuum is the simplest interface that can be realized with different atomic reconstructions. The pioneering work of Bokor [1] and Haight [2] has shown that interfacial reactions of hot carriers can be studied employing time-resolved two-photon-photoemission (2PPE). The principle of this 2PPE method is illustrated in Fig.1. Electrons are photo-emitted into vacuum and the distribution over kinetic energy is measured. A narrow kinetic energy window can be addressed (in our case about 100 meV wide) that probes the corresponding intermediate states (Fig.1). Time-resolution is achieved by varying the time-delay between the two consecutive laser pulses. This way, the dynamics of hot carriers are time-resolved for specific intermediate states. The latter are occupied due to photon absorption and are emptied via subsequent relaxation and scattering processes. Fig.2 shows the disappearance of hot electrons from intermediate states about 1.15eV above the lower edge of the conduction band of InP(100) [3]. Hot electrons were generated by the first femtosecond laser pulse (2.52eV photon energy) and photo-emitted by the second laser pulse (4.66eV photon energy) with variable delay. The crystal surface was prepared with an ordered In-rich reconstruction. The instrumental cross correlation function (inset in Fig.2) was measured as two-photon-photoemission involving virtual intermediate states at the Cu(111) surface. The main part of the signal in Fig.2 decayed faster than our presently available time resolution of about 30fs. The origin of the slower tail is not yet clear.

One possibility is the return of hot electrons back to the Γ-valley, where the intermediate states are probed, from different k-states where they had been scattered after being generated initially by the first laser pulse near the Γ-valley.

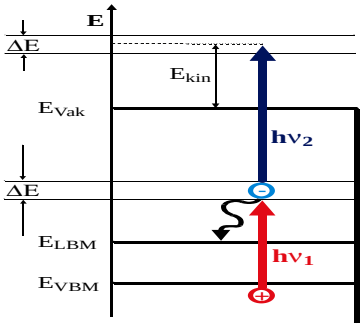

Fig.1: Illustration of femtosecond two-photon-photoemission. The first laser pulse (photon energy hν1) lifts electrons to unoccupied electronic states. The second laser pulse (photon energy hν2) promotes these electrons into vacuum.

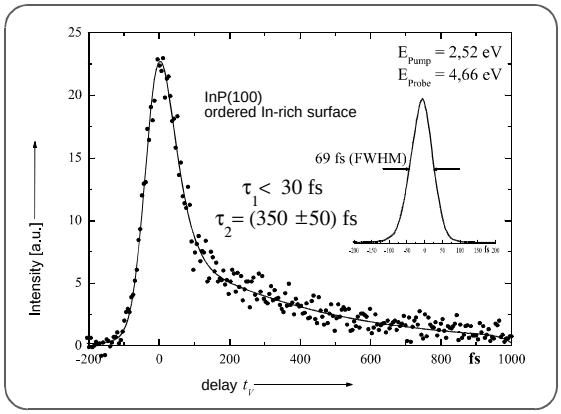

Fig.2: Decay of hot electrons about 1.15eV above the lower conduction band edge of InP measured via femtosecond two-photon-photo-emission.

References

[1] J. Bokor, Science 246 (1989) 1130

[2] R. Haight, Chem. Phys. 205 (1996) 231

[3] L. Töben, PhD Thesis, Technical University of Berlin, 2002

L. Töben, R. Eichberger, L. Gundlach, T. Hannappel, K. Möller, R. Ernstorfer, F. Willig
(SE4.01 Dynamics of Light-induced Charge Transfer)

Preparation and characterization of the n-SnO_2/p-InP heterocontact

Formation of the heterocontact n-SnO_2/p-InP(100) via spraypyrolysis was accomplished without excessive loss of phosphorus. InP develops a deficit in its phosphorus content once it is brought to a temperature higher than the congruent evap-oration temperature (350°C). Such a high tem-perature is required, however, for forming the contact with n-SnO_2 via spraypyrolysis. Its simplicity makes the latter preparation technique attractive. If an excess of phosphorus leaves the InP wafer In droplets will be left behind on the surface. They can give rise to excessive recombination losses for the photocurrent. It was at hand to minimize the time during which InP is exposed to the high tem-perature. It turned out that preventing excessive loss of phosphorus required a further protective preparation step. Prior to forming the heterocontact via spraypyrolysis a few atomic layers of Sn were deposited onto the freshly grown surface of the InP wafer. For this preparation step the group's patented contamination free sample transfer had to be employed [1]. Fig. 1 shows TEM images of cross sectional preparations. The formation of an unwanted thick amorphous layer of mixed phosphate and oxide can be seen in panel a if the Sn layer was absent. In contrast, this thick amorphous layer was not formed (panel b) if Sn was deposited prior to applying spraypyrolysis [2]. Sn forms chemical compounds with phosphorus that can stop the loss of phosphorus. A possible excess of Sn is converted to SnO_2 during spraypyrolysis. The photo-electrical behavior of the heterointerface improved significantly for the interface illustrated in panel b compared to that of panel a. Improvements were seen in the onset voltage of the photocurrent and in the capacitance determined from a Mott-Schottky plot. An abrupt interface was suggested firstly by SIMS signals, secondly by the spectral dependence of the photocurrent at the blue edge, and thirdly by the spatial onset of an EBIC signal.

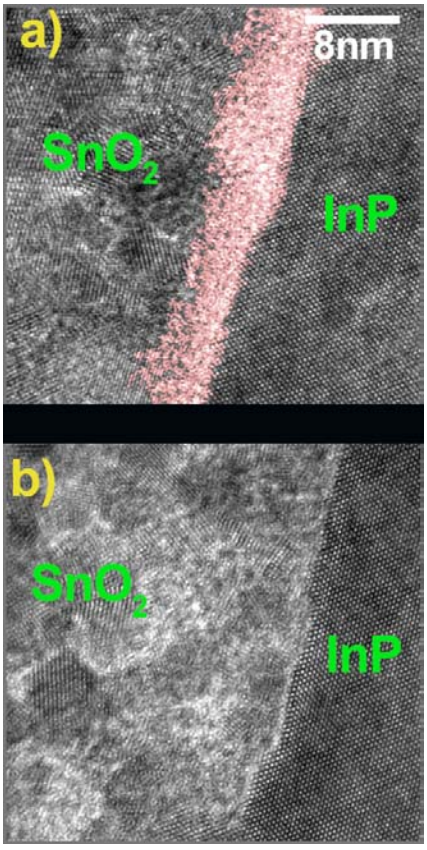

Fig. 1: TEM images of cross sections of the hetero-interface: SnO2:F/InP:Zn(100) in the absence (panel a) and presence (panel B) of a thin layer of Sn.

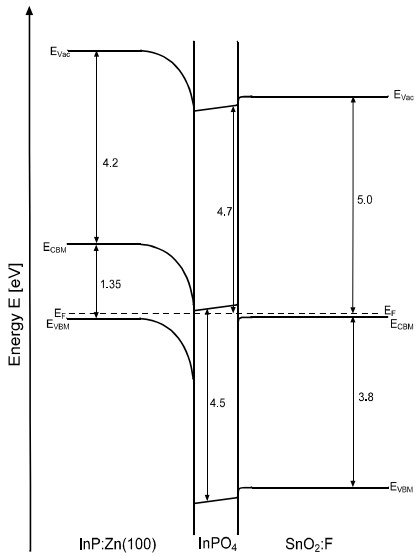

Fig. 2: Banddiagram for p-doped(Zn) InP(100) covered by an amorphous layer of mixed oxide/phosphate (labeled InPO4 here, compare panel a in Fig.1) followed by a polycrystalline layer of n-doped SnO2:F.

The banddiagram shown in Fig. 2 is in agreement with the measured electrical signals. The band bending is already established at the p-InP/vacuum interface irrespective of whether the surface is P-terminated or In-terminated. The corresponding Fermi-level pinning has been found to be very robust and to remain at the surface independent of the material that is deposited on top.

References
[1] T. Hannappel, F. Willig, DPMA Munich, Patent No. 19837851
[2] Dirk Herrmann, PhD Thesis, Technical University of Berlin, 2001

D. Herrmann, L. Toeben, K. Schwarzburg, T. Hannappel, M. Neges, K. Möller, U. Bloeck, F. Willig (SE4.02 Preparation and Characterization of III-V-Semiconductors)

Department

SE5 Solar Energetics

Platinum-free catalysts for the reduction of oxygen

The aim of this project is to develop platinum free catalysts for the electroreduction of oxygen in acidic media and to optimize them with respect to their catalytic activity and morphology for an application as gas-diffusion-cathode in proton exchange membrane (PEM) fuel cells. Starting from own results [1], we were able to improve a Ru-Se based catalyst by developing several new preparation strategies and by optimizing the catalysts composition. Fig. 1 shows the achieved progress indicated by H_2-PEM fuel cell measurements. Although the catalytic activity of the best preparation (colloidal techniques) remained below the output characteristic of platinum using hydrogen as fuel the Ru-Se catalyst has advantages using methanol as fuel in Direct Methanol Fuel Cells (DMFCs). This is because the Ru-Se catalyst is stable against depolarization by methanol. Due to the leaking of methanol from the anode to the cathode in direct methanol fuel cells the Ru-Se catalyst exhibits a better performance than platinum. This was verified under laboratory conditions. DMFC measurements under industrial conditions are in progress.

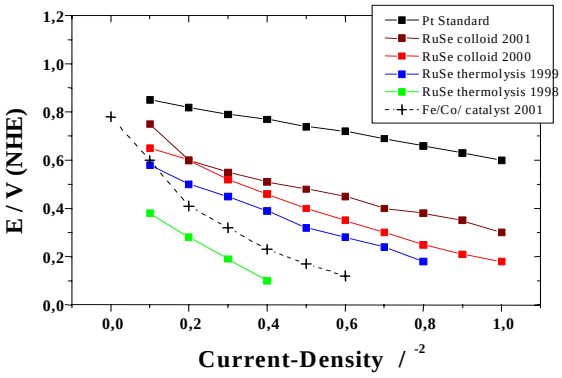

Fig. 1: Current-voltage-characteristic of H_2-PEM fuel cells using Ru-Se and Fe/Co catalysts at the cathode site (cathode: C / Ru_xSe_y (20%Ru / C, load 0.14mg/cm^2); Fe/Co (5 %Co/C, load 0,2mg/cm^2) operation pressure 3bar of compressed air; anode: Pt, load 4mg/cm^2, fuel: H_2; operation temperature: 80°C, active area: 50cm^2.

Rotating disc electrode (RDE) experiments, applying a Fe-Co-N catalyst, revealed that the kinetic parameters are close to those of platinum (Fig.2). However under fuel cell conditions, the efficiencies remained up to now behind the platinum standard (dotted line in Fig. 1) presumably due to the coarse mesoscopic shape of the carbon supported catalyst and the relative low catalyst-loading onto the carbon support. The aim of our work is to develop new preparation strategies to overcome this disadvantage.

Ruthenium based catalysts

It was demonstrated in earlier work from the department (Alonso-Vante and Solorza)[1] that catalysts based on Ru, Se and Mo can be used for the oxygen reduction in acidic solutions. The catalysts were prepared from $Ru_3(CO)_{12}$ and $Mo(CO)_6$ by thermolysis in a selenium saturated organic solution. Carbon supported catalysts could be formed by addition of carbon black to the reaction mixture. The parameters of this preparation procedure (several organic precursors and organic solvents, variation of the selenium concentration, subsequent activation by heat treatment steps) to optimize the catalytic activity and the morphology of the Ru-Se catalyst were investigated.

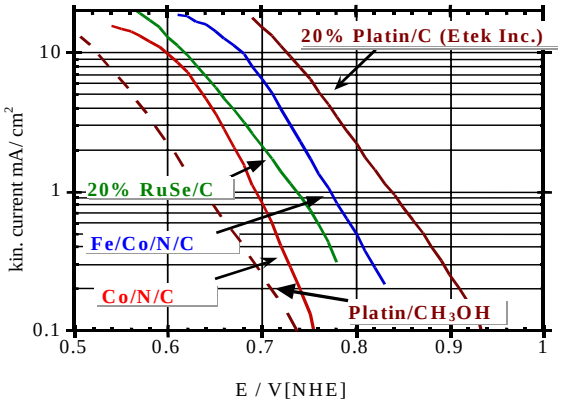

Fig. 2: Tafel plots of Ru-Se/C and Co-Fe-N/C catalysts obtained from rotating disc electrode measurements. Please, note the shift of the platinum curve in the presence of methanol.

Our results show that molybdenum is not necessary in the catalyst composition to obtain an effective four-electron-reduction process of oxygen. Therefore, further experiments were done without any molybdenum. Although even with a selenium free ruthenium catalyst, prepared by thermolysis, oxygen reduction was achieved, addition of selenium increased the catalytic activity and stabilized the catalyst against oxidation. The highest activities were obtained with a Se amount of 14.5 % (related to the content of ruthenium). Further addition of selenium led to a decrease of the activity, may be due to the formation of elementary selenium as it was detected by XRD measurements.

To get a deeper insight into the structure of the Ru-Se catalyst measurements with Thermo-Gravimetry TG, X-Ray Diffractometry XRD, Extended X-ray Absorption Fine Structure EXAFS Analysis, Transition Electron Microscopy TEM and X-ray Photoelectron Spectroscopy XPS were performed.

XRD and TEM measurements revealed that the catalyst prepared from $Ru_3(CO)_{12}$ by thermolysis in the presence of an optimized selenium concentration consists of metallic Ru-particles with a particle size of about 2-6 nm. No other crystalline compounds, such as $RuSe_2$ or RuO_2, could be detected. In TG-measurements, it was found that the samples release considerable amount of the gas species CO and CO_2 (Fig. 3) upon heating in vacuum, which belongs to an amorphous layer covering the metallic

core of the Ru nano-particles. A release of selenium is observed at 800°C and at about 1100°C. However, only the latter led to a decrease of the catalytic activity. To elucidate Ru-Se, Ru-O and Ru-C distances of the amorphous part of the catalyst EXAFS measurements were performed using synchrotron radiation (RÖMO II X1.1 station at HASYLAB) (Fig. 4).

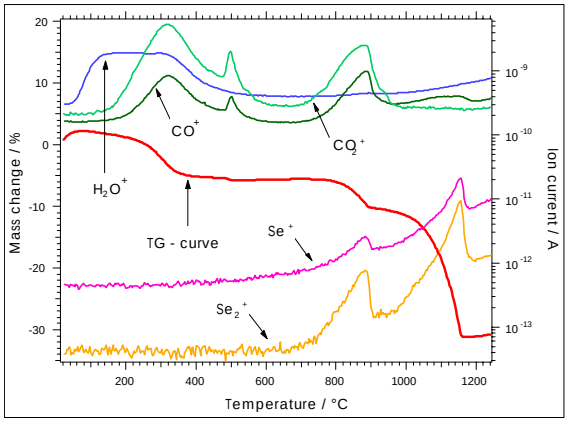

Fig. 3: Thermogravimetric curve of a Ru-Se catalyst heated under argon gas flow. The red curve indicates the stepwise release of CO_2 and CO (200-350°C) and the loss of selenium in a first step as SeO_2 (700-900°C) and in a second step as Se_2 (1000-1200°C).

All Ru-Se catalysts weakly showed the EXAFS pattern of Ru metal and additional features that can be addressed as Ru-Se, Ru-C and Ru-O bondings. Inferring the Ru-Se distance by adjusting EXAFS profiles it was found that the distance in the as grown material amounts to a value of $d_{Ru\text{-}Se} \approx 2.56$Å which is typical for metal organic compounds such as $Ru_4Se_4(CO)_{12}$. The Ru-C and Ru-O distances are 1.95Å and 1.97Å, respectively. This behavior can be explained by the presence of amorphous ruthenium oxides or hydroxides and metal organic complexes covering the surface of the Ru nano-particles.
After annealing of the unsupported catalysts at 450°C and 900°C both distances become close to those found in $RuSe_2$ and RuO_2 and the Ru EXAFS pattern becomes dominant. Obviously the amorphous Ru-oxides were disproportionated to metallic Ru and RuO_2 during the heat treatment step and stoichiometric but catalytic inactive $RuSe_2$ was formed. From XRD measurements it is known that with increasing temperature the unsupported Ru particles coalesce increasing from 4nm to 20nm in size. All this changes led to a decrease of the observed current density obtained from unsupported catalysts after the heat treatment.
During the annealing of the carbon supported samples the amorphous ruthenium oxides and hydroxides were reduced by carbon to metallic ruthenium. Howeve, the Ru-Se distance remained unchanged and no stoichiometric $RuSe_2$ compound could be detected. Additionally, no growth of the particle size was observed. Obviously the ruthenium particles were stabilized by the carbon support.
The observation that the catalytic activity of the carbon supported catalysts can be increased by heat treatment of the catalyst in vacuum, where the most of the surface complexes thermally decompose, might be an indication that the presence of these complexes is sufficient but not necessary to achieve high catalytic activity of the catalyst. However, the modification with selenium led to a chemical stabilization of the metallic ruthenium particles and to a high catalytic activity towards the oxygen reduction.

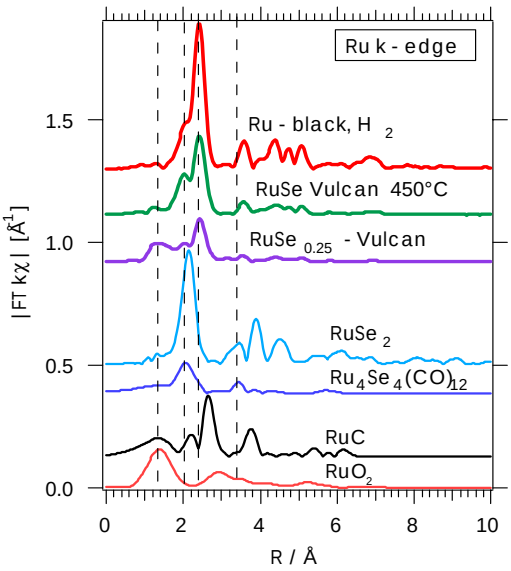

Fig. 4: Fourier transformed EXAFS spectra of as grown and heat treated Ru catalysts in comparison with $RuSe_2$, RuO_2, RuC and Ru_4Se_4 $(CO)_{12}$.

In order to improve the current densities for the application in industrial fuel cell systems three additional methods for the preparation of carbon supported catalysts were developed: formation of ruthenium particles as a precursor by the reduction of ruthenium oxalate (cheap chemical compounds and aqueous solutions), impregnation of carbon black with $Ru_3(CO)_{12}$ (best cost-performance analysis) and the formation of ruthenium colloids as precursor by a micelle technique described by Bönnemann [2] (highest electrochemical performance). The morphology of the different Ru-nano-particle were analyzed by transmission electron microscopy (TEM) and X-ray diffraction (XRD), which shows that the different catalysts consist of crystalline ruthenium particles with a good dispersion over the applied carbon substrate. Smallest particles were found using Bönnemann´s colloidal technique (2.5nm) while the thermolysis method formed particles of 4nm size. Largest particles were obtained using ruthenium oxalate (7nm). Several techniques for the subsequent modification of the Ru-particles with selenium were developed to obtain the high catalytic activity and the chemical stability against oxidation. An increase of the current densities obtained by RDE measurements by a factor of 2 to 3 was found after this treatment.
As expected from the particle size analysis the catalysts prepared by the micelle technique showed the highest current densities. However, with decreasing particle size the apparent overvoltage for the oxygen reduction decreases less significant as expec-

ted from the increase in relative surface area from the respective catalysts. These results suggest that the concentration of surface sites on the carbon substrate, which bond catalytic particles, is limiting the overall current density. Catalysts loading higher than 20 % ruthenium / 80 % carbon did not lead to a further increase of the current density. However, the presence of selenium was found to have a significant effect on current density and may act as an electron transfer bridge between substrate and catalytic center. Furthermore, the surface of the ruthenium nano-particles is chemically modified by selenium and become stable against oxidation.
In co-operation with DaimlerChrysler/Ulm these optimized catalysts were used to prepare Gas Diffusion Electrodes GDEs and Membrane Electrode Arrays MEAs for the application in PEM fuel cells. Fig. 1 shows some results obtained from fuel cell measurements.
Nevertheless, under the best conditions achieved the overvoltage obtained from our catalysts by RDE and fuel cell measurements in alkanol free acid media is approximately 0.12 V higher than for a comparable platinum catalyst. This could be explained by an activation barrier for the overall oxygen reduction that is approximately 0.15 V higher than for platinum.
However, in the presence of alkanols the Ru-Se catalysts is more effective than platinum (Fig. 1). Therefore, it could be used in DMFCs or as a sensor-material for oxygen in alkanol containing media. Both applications are still under investigation.

Iron-cobalt based catalysts

Iron-cobalt catalysts were prepared by pyrolysis at 840°C under argon atmosphere using a mixture of cobalt tetramethoxyphenylporphyrin (CoTMPP), as a nitrogen-containing organic transition metal complex, and iron oxalate ($Feox_2$). During the heating process, $Feox_2$ first releases water prior to decomose into FeO under CO_2 and CO gas evolution. Melting and decomposition of CoTMPP occurs in the same temperature range (250-500°C). At 900°C the pyrolytic reaction is completed. Carbon, generated during the decomposition of CoTMPP, reduces FeO particles to metallic iron. After cooling the sample, the iron particles were removed by etching in an acidic solution. SEM and TEM images reveal that this procedure led to an in situ generation of carbon black with a very high porous structure (Fig. 5).
According to the literature it is assumed that the catalytic centers consist of metal atoms integrated into the surfaces of the carbon support by pyridinic-type nitrogen. Even after the complete removal of metallic iron, a residual amount of iron was found by EXAFS, Energy Dispersive X-ray EDX analysis and Neutron Activation Analysis NAA in the samples. Obviously, beside the cobalt atoms also a small amount of iron atoms are incorporated into the carbon structure. From EXAFS measurements a Co/Fe ratio = 20:1 and a Co-N distance of 1.97Å were inferred.

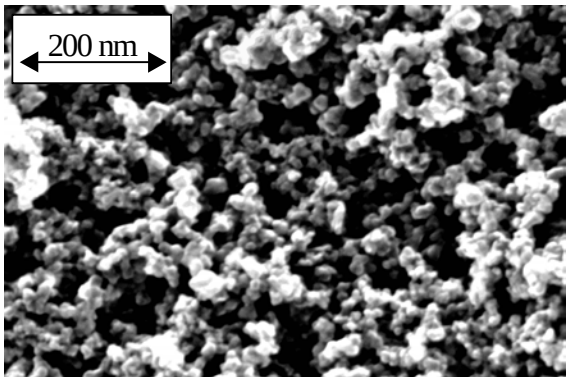

Fig. 5: SEM image of the porous Co-Fe-C catalyst prepared from Co TMPP and $Feox_2$ by pyrolysis.

The Tafel-plots obtained by RDE measurements reveal the high catalytic activity of the Co/Fe samples, which comes close to that of the Pt-standard. Interestingly our Co/Fe catalysts yielded higher current densities than a comparable sample prepared from CoTMPP without any iron (Fig. 2). Further investigations have to clarify if this is due to the incorporated iron atoms or to a morphological effect caused by the decomposition of the iron-oxalate.

References

[1] Solorza-Feria, O.; Ellmer, K.; Giersig, M.; Alonso-Vante, N.: Novel Low-Temperature Synthesis of Semiconducting Transition Metal Chalcogenide Electrocatalyst for Multielectron Charge Transfer: Molecular Oxygen Reduction. Electrochim. Acta 39 (1994) 1647.

[2] Bönnemann, H., Brijoux, W., Brinkmann, R., Dinjus, E., Joußen, T., Korall, B., Angew. Chem. 103 (1991) 1344-1346.

M. Hilgendorff, M. Bron, H. Schulenburg, I. Dorbandt, P. Bogdanoff, S. Fiechter, H. Tributsch (SE5.01b Platnium-free Catalysts for the Reduction of Oxygen in Fuel Cells)

Interface engineering

The project aims at optimization of optoelectronic properties of semiconductor interfaces and at directed band alignment in semiconductor heterocontacts by (photo)electrochemical and chemical techniques. This includes the investigation of structure formation phenomena induced by electrochemical treatments. Accompanying photoelectron spectroscopy and in-situ/ex-situ scanning probe microscopy investigations serve for the understanding of the reaction mechanisms occurring during the interface modifications. Priority objectives are

- development and optimization of photoelectrochemical, electrochemical and chemical processes for the surface conditioning of relevant photovoltaic materials;
- electrochemical preparation of alternative buffer layers;
- influencing the band alignment by adsorption of atoms, ions and molecules;
- investigation and influencing of self-organized and scanning probe microscopy induced structure formation for light-coupling systems and photonic structures.

The investigated materials were $CuInS_2$, Si and InP.

The original electrochemical method for the removal of deleterious CuS from Cu-rich prepared CIS surfaces was further developed and simplified (two electrochemical steps instead of three). The new procedure for replacement of the KCN etch by non-toxic electrochemistry is based on a transformation of CuS to Cu_2S and its partial dissolution in alkaline solutions; addition of small amounts of In ions to the electrolyte leads to a removal of CuS and Cu_2S.

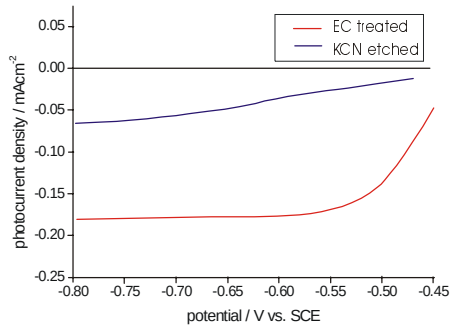

Fig. 1: Photocurrents obtained for an electrochemically (EC) treated and KCN etched CIS sample in S^{2-}_x/S^{2-} redox electrolyte.

In redox electrolytes, the photocurrents obtained for electrochemically prepared samples are now larger than for KCN etched samples (Fig. 1). The electrochemical reduction of CuS to Cu_2S is confirmed by XPS measurements: the Cu line has shifted to the value for Cu in Cu_2S. In addition, a pronounced decrease in the FWHM for S and a simultaneous decrease in the FWHM of Cu indicate a reduction of the different bonding sites after the transformation. The addition of small amounts of In ions to the solution leads to the dissolution of CuS and Cu_2S and obviously also to a chemical change of the CIS surface: after the treatment, the Cu and In lines correspond to the respective line positions in CIS while the S line position is located at a binding energy lowered by 1 eV compared to the S line position in CIS. From this and the intensity ratios of the Cu, In and S lines, a coverage of CIS with a few ML of an In-S phase can be concluded. The chemical surface change also affects the valence band position relative to EF, as obtained with synchrotron radiation: $E_F - E_V = 0.9$ eV ($E_F - E_V = 0.5$ eV for KCN etched samples).

The investigation of alternative possibilities for directed structure formation at silicon surfaces necessitates fundamental studies of dissolution at a molecular level. In the acidic processing regime, the divalent dissolution leading to porous Si can be induced by holes, for instance in n-Si under illumination. We have found, however, that pit formation leading to porous structures occurs also on highly n-doped Si in the dark at neglegible hole concentration (Fig. 2). So far, no plausible explanation for this finding has been given. In a sytematical study using variably doped n^+-Si

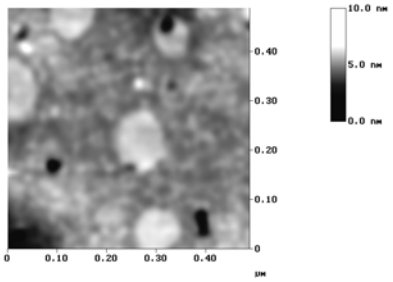

Fig. 2: In-situ AFM micrographs of n-Si (111) ($N_D = 2 \cdot 10^{18}$ cm^{-3}) obtained after reaching the first dark current maximum.

we observe that for decreasing doping level the current onset connected with por-Si formation is shifted towards anodic potentials. It is found that the relative potential drop in the Helmholtz layer always amounts to the same value of 0.5 V. The shift of the current onset is interpreted by assumption of an interface state 0.3 – 0.5 eV below the conduction band edge, extending some Å into the Helmholtz layer. The state is shifted energetically proportional to the potential drop ΔV_{HH} in the Helmholtz layer. For sufficiently large ΔV_{HH} electron injection becomes possible (Fig. 3). Since the injected electron is delocalized in the conduction band local corrosion is assumed as a result of subsequent chemical steps. Either surface atoms are attacked by decomposition products of the oxidised surface complex (radicals) and/ or bond rupture results in local dissolution of Si atoms.

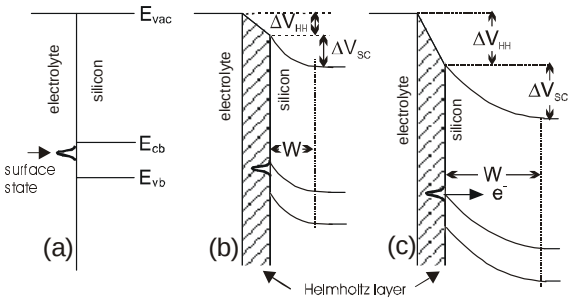

Fig. 3: Energetic position of the suggested surface state; (a) flatband condition; (b) anodic polarization; (c) electron injection.

Investigation of electrochemical processes with synchrotron radiation

Photoelectron spectroscopy investigations related with the project, which cannot be carried out with the necessary degree of resolution and surface sensitivity by use of common XPS/UPS systems are performed with synchrotron radiation at BESSY (cooperation with the Cooperating Research Group (CRG)).

In the search for self-organized and SPM induced microtopography alterations, initial phases of por-Si formation in dilute ammonium fluoride solution were investigated by synchrotron radiation and AFM. Fig. 4 shows AFM data for the Si(111):H(1x1) surface (Fig. 4a) and in Fig. 4b the onset of pit formation at step edges of atomic terraces after anodic processing at + 0.1 V from the rest potential.

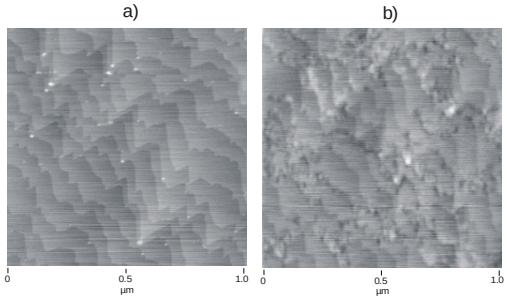

Fig. 4: AFM images of a Si(111) surface (a) before and (b) after initial corrosion reaction

Fig. 5 displays PES data obtained after emersion close to the first photocurrent maximum where divalent dissolution still takes place. Five features are discernible: the core level signal (signal A), a surface core level shift indicating residual H-termination (0.35 ML; signal B) and mainly two oxidized species shifted by 1 eV (C) and 4 eV (E). The former is attributed to a = Si-H-F species. DFT calculations yield a Si partial charge of $\rho = 0.54$ for the = Si-H-F species. Signal D is too small for serious evaluation; signal E can only be evaluated under consideration of the O 1s and F 1s lines (not shown). The former shows O in OH^- and H_2O but not O in SiO_2. The latter shows predominantly F in $Si\text{-}F_x$. In conjunction with DFT calculations we attribute the 4 eV shifted signal to $SiOHF_3$, a precipitate from the dissolution reaction. The presence of species C indicates that solvolytic splitting of backbonds is rate determining, possibly due to the complex chemical reactions involved.

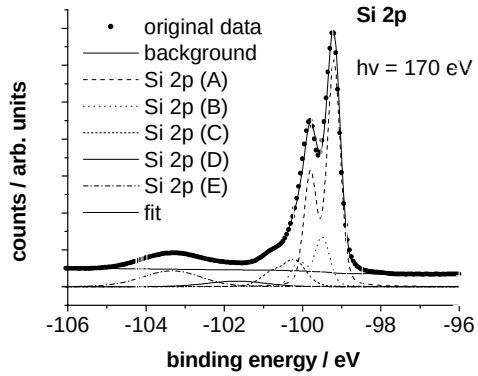

Fig. 5: Si 2p line after sample emersion at the first current maximum in the i-V characteristic (cf. Fig. 7) including deconvoluted signals.

H. J. Lewerenz (SE5.02 Surface Engineering), M. Aggour (guest scientist), C. Murrell, H. Jungblut, M. Kanis, J. Jakubowicz (DFG Priority Program: Fundamentals of Electrochemical Nanotechnology)

Work Group

SE6 Electronic Structure of Semiconductor Interfaces

TGM7, Transfer of a VUV monochromator to a BESSY II dipole beamline

With closing of BESSY I in 1999 it was decided to transfer the monochromator TGM7 to BESSY II. The instrument was used for the characterization of semiconductor interfaces and the electronic structure of materials relevant for solar energy conversion. The TGM7 had been designed in 1988 to deliver photons in the range of 6-120 eV with a resolution of about 250 meV and reasonable intensity in a photoemission experiment. To cover the photon energy range two gratings are installed ranging from 120-16 eV and from 30-6 eV.

Fig. 1: Location of TGM7 at BESSY II

With the transfer the beamline had to be adapted to the new dipol and the beam characteristics at BESSY II. Due to the lower ring current a focussing mirror of ca. 500x220 mm was chosen and the angle of incidence was decided to be slightly smaller. It was suggested to gain a little in resolution by maintaining about the same intensity as at BESSY I.

Fig. 2: Focussing mirror, cooling facilities and mechanics installed in the new vacuum chamber.

With the new focusing mirror the beamline from the outlet system up to the slit section of the monochromator had to be redesigned. Especially a completely remote controlled mirror adjustment of all 6 degrees of freedom had to be realized. Within two years the design and fabrication of the chamber, the mechanics, and the prefabrication of the mirror substrates took place. In December 2001 after installing the components and preadjusting the optics, for the first time the beamshutter was opened. Severe outgasing of the new components hidden by the intense white synchrotron light restricted the first operations to low ring currents. After the final adjustment of the focussing mirror by the help of the motor driven mechanics was achieved and first spectra were taken. Fig. 3 displays the transmission spectrum of an Al foil in the range of the LII/III edge. The resolution obtained here with 100 µm slits was at BESSY I only obtained with much smaller slits (50 µm, hence lower intensity), showing nicely the improvement in resolution. A resolving power of $E/\Delta E = 880$ was reached for 20 µm slits, the limit of the instrument.

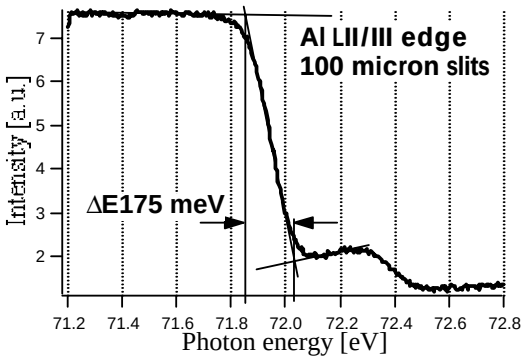

Fig: 3. Absorption spectrum of an Al foil at the LII/III edge

Far more important are the obtained photoemission spectra as an overall resolution of about 200 meV for monochromator and electron spectrometer for an Al2p core level were obtained at 95 eV photon energy.

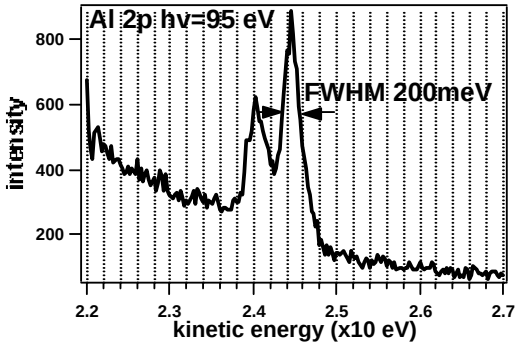

Fig. 4: Photoemission of Al 2p level

The yield curve of the instrument will give an intensity of a factor 2-3 above the value reached at BESSY I, normalized to 100 mA ring current. As the maximum current at BESSY II is about a factor 3 lower, the overall intensity is of the same order as obtained at BESSY I.

C. Pettenkofer, S. Tiefenbacher
(SE6.01: Electronic Structure of Semiconductor Interfaces)